Technische Universität München

TUM School of Medicine and Health

Interrogation of neural and astrocytic circuitry in sleep homeostasis

Chia-Luen Leu

Vollständiger Abdruck der von der TUM School of Medicine and Health der Technischen Universität München zur Erlangung eines

Doctor of Philosophy (Ph.D.)

genehmigten Dissertation.

Vorsitz: Prof. Dr. Ruben Portugues

Betreuerin: Prof. Dr. Juliane Winkelmann

Prüfer der Dissertation:

1. Prof. Dr. Konrad Oexle

2. Prof. Dr. Ali Ertürk

Die Dissertation wurde am 16.08.2023 bei der Technischen Universität München eingereicht und durch die TUM School of Medicine and Health am 16.10.2023 angenommen.

Declaration of Originality

I hereby declare that all data presented in this thesis were collected during my PhD study, under the supervision of Dr. Rhîannan H Williams and Prof. Dr. Juliane Winkelmann. Any collaborative works were properly acknowledged, and any works presented from published literature were fully referenced.

Copyright Declaration

Funding

The studies in the thesis were supported by the European Research Council (ERC) under the European Union's Horizon 2020 Research and Innovation Program Grant Agreement No. 715933 to Dr. Rhîannan H Williams (Chapter 3 - 6), and internal funding (Helmholtz Munich) to Prof. Dr. Juliane Winkelmann (Chapter 6).

Acknowledgements

This thesis becomes a reality with the great help and support from many individuals. Here, I would like to thank Dr. Rhîannan H Williams and Prof. Dr. Juliane Winkelmann for having me as a PhD student. During my PhD study, Dr. Rhîannan H Williams provided years of supervision, guidance, training, experimental support, as well as brilliant insights into my research, writing, and presentation. Prof. Dr. Juliane Winkelmann provided an amazing platform and environment to gain the latest knowledge in neuroscience and genetics. Because of these, my knowledge in neuroscience has grown dramatically. Their expertise and support would be a key to the success of this thesis.

I would like to thank Prof. Dr. Konrad Oexle and Prof. Dr. Ali Ertürk, who provided valuable suggestions and feedback in the thesis committee meetings. The same thanks go to Dr. Melissa Chee and Ms. Nikita Koziel Ly (Carleton University, Canada) for the collaboration, Mr. Mikołaj Miękus for supporting analysis, and Dr. Daniel Lam for providing insights for the experiments and data from time to time.

I would also like to express my special gratitude and thanks to all the members in our group, especially for Dr. Serena Antonio, Dr. Margarita Hessel, and Ms. Elisabeth Stephan. Not only did they help me through my academic difficulties and support experiments, but also brought plenty of joy and laugh to my life. The same thanks go to all the members from the Institute of Neurogenomics at Helmholtz Zentrum München. They treated me as family and the warmth they brought to me was unforgettable.

None of this would be possible without the funding of the European Research Council (ERC) under the European Union's Horizon 2020 Research and Innovation Program Grant Agreement No. 715933 to Dr. Rhîannan H Williams. The grant it provided gave me the opportunity to pursue my scientific career in such an extraordinary establishment, and made this thesis possible. The academic resources from Helmholtz Zentrum München and Technical University of Munich facilitated my PhD study and scientific career. I would also like to thank Dr. Barbara Schormair for the administrative support at Helmholtz Zentrum München, as well as Ms. Bettina Kratzer and Ms. Raphaela Blum for the guidance and support for the PhD program in Medical Life Science and Technology at Technical University of Munich.

Last but not least, I would like to express my sincere gratitude to my parents, my siblings, and my friends. They have always been supportive and encouraged me to finish my PhD study. I would have never finished it without them. Thank you all.

Thesis Abstract

Sleep is very important for our life, having insufficient or bad quality of sleep could increase risks of developing diseases such as hypertension and impaired cognition. Hence, we studied sleep homeostasis to understand how the brain controls sleep based on neuronal and astrocytic mechanisms. However, sleep can be recorded by different methods such as electroencephalogram/electromyography (EEG/EMG) and piezo sleep screen (piezo), and sleep deprivation (SD) can be performed in different ways (manual and treadmill) and durations (4h and 6h). In order to ensure the validity of the methodology used in the studies, we compared different sleep recording and SD methods and found out there was no significant difference between EEG/EMG and piezo recordings. There was also no significant difference for sleep in the recovery period after using different SD methods and durations. Therefore, this showed our methodology is valid for sleep studies. However, whole brain mapping showed some brain regions such as tuberomammillary nucleus (TMN) had significantly different activities after manual and treadmill SD, suggesting different SD methods caused similar sleep drives but did not have the exact same brain activity. Therefore, if the purpose of the study is to examine the brain activity, it would be important to choose the most appropriate SD method.

After finishing the comparison of different SD methods, we wanted to examine the brain regions that may have contributed to sleep homeostasis. Therefore, we did whole brain mapping on SD, recovery sleep (RS), and undisturbed mice (ZT4 and ZT6) to find out how brain activity changed in sleep homeostasis. We found out several amygdala regions, especially basolateral amygdalar nucleus (BLA) and basomedial amygdalar nucleus (BMA) were significantly active after both manual and treadmill SD compared to undisturbed mice. Therefore, they are the potential regions to do functional study on and investigate their roles in sleep homeostasis.

Astrocytes are macroglial cells and recently reported to play a role in sleep. On the other hand, the cortical nNOS/NK1R neurons (nNOS neurons) have also been suggested to play a role in modulating sleep.Therefore, we were interested in the interaction between astrocytes and nNOS neurons in the cingulate cortex, and the functionality of cortical astrocytes in sleep homeostasis. We analyzed their anatomical pattern and found out the number of astrocytes reduced significantly only between the distance in 300-600 μm from nNOS neurons after SD compared to undisturbed condition. Therefore, this suggested the interaction between astrocytes and nNOS neurons might be different in this range. Chemogenetic activation of astrocytes in cingulate/motor cortex promoted sleep when they were undisturbed, but showed no difference after SD. This suggested cortical astrocytes might already be activated by high sleep drive, so supplemental activation of astrocytes was no longer effective in modifying sleep state. Therefore, this showed a possible role that cortical astrocytes might play in sleep.

Apart from sleep homeostasis, we were also interested in restless legs syndrome (RLS), because it is a sensorimotor disorder and could cause sleep disturbance. In order to facilitate the future RLS studies, we aimed to validate

a new RLS mouse model (Meis1$^{R272H/R272H}$ mice) and examine the brain regions that might cause the sleep disturbance. Integrating phenotypes (based on phenotypic assessment) reveals an overall phenotypic shift in Meis1$^{R272H/R272H}$ mice. Meis1$^{R272H/R272H}$ mice also sleep significantly less at the end of active period (dawn) which is similar to RLS human patients. Therefore, these supported Meis1$^{R272H/R272H}$ mice to be a mouse model for future RLS studies. Whole brain mapping of Meis1$^{R272H/R272H}$ mice showed the connectivity between midbrain and hypothalamus changed significantly at dawn (ZT0) compared to wildtype mice. Therefore, this suggested the potential brain regions that caused hyperactivity, and the candidate regions to study sleep homeostasis in RLS.

Table of Contents

List of Figures and Tables

List of Abbreviations

5HT	serotonin
$A_{2a}R$	A_{2a} receptor
AAA	anterior amygdalar area
AAV	adenoassociated virus
ARA	Allen brain reference atlas
Aβ	amyloidβ
BA	bed nucleus of the accessory olfactory tract
BF	basal forebrain
BLA	basolateral amygdalar nucleus
BLAa	basolateral amygdalar nucleus, anterior part
BLAp	basolateral amygdalar nucleus, posterior part
BLAv	basolateral amygdalar nucleus, ventral part
BMA	basomedial amygdalar nucleus
BMAa	basomedial amygdalar nucleus, anterior part
BMAp	basomedial amygdalar nucleus, posterior part
CaM	calcium-binding protein calmodulin
CEA	central amygdalar nucleus
CEAc	central amygdalar nucleus, capsular part
CEAl	central amygdalar nucleus, lateral part
CEAm	central amygdalar nucleus, medial part
ChAT	choline acetyltransferase
ChR2	channelrhodopsin-2
CNO	clozapine-N-oxide
CNS	central nervous system
DA	dopamine
DDC	DOPA decarboxylase
Dim	dimension
DPGi	dorsal paragigantocellular reticular
DREADDs	designer receptors exclusively activated by designer drugs
DRN	dorsal raphe nuclei
EEG	electroencephalogram
EMG	electromyography
EOG	electrooculograms
FDR	false discovery rate
fMRI	functional magnetic resonance imaging
FN	false negative
FP	false positive
GECIs	genetically encoded calcium indicators
GFP	green fluorescent protein
HOM	homozygote
IA	intercalated amygdalar nucleus

iDISCO+	immunolabeling-enabled three-dimensional imaging of solvent-cleared organs plus
ISF	interstitial fluid
LA	lateral amygdalar nucleus
LC	The locus coeruleus
LDT	laterodorsal tegmental nuclei
LPGi	lateral paragigantocellular nuclei
LPT	lateral pontine tegmentum
LSFM	light sheet fluorescence microscopy
MCH	melanin concentrating hormone
MEA	medial amygdalar nucleus
MEAad	medial amygdalar nucleus, anterodorsal part
MEAav	medial amygdalar nucleus, anteroventral part
MEApd-a	medial amygdalar nucleus, posterodorsal part, sublayer a
MEApd-b	medial amygdalar nucleus, posterodorsal part, sublayer b
MEApd-c	medial amygdalar nucleus, posterodorsal part, sublayer c
MEApv	medial amygdalar nucleus, posteroventral part
MnPO	median preoptic nucleus
MRN	median raphe nuclei
NA	noradrenaline
NK1R	neurokinin-1 receptor
NMDA	N-methyl-D-aspartate
nNOS	neuronal nitric oxide synthase
NO	nitric oxide
NpHR	halorhodopsin
NREM	non-rapid eye movement
OSA	obstructive sleep apnea
PA	posterior amygdalar nucleus
PB	parabrachial nucleus
PCA	principal component analysis
peri-Lca	peri-locus coeruleus alpha
PET	positron emission tomography
PFA	paraformaldehyde
PH	posterior hypothalamus
Piezo	piezo sleep screen
POA	preoptic area
PPI	replicable prepulse inhibition
PPT	pedunculopontine
PZ	parafacial zone
REM	rapid eye movement
RLS	restless legs syndrome
ROIs	regions of interest

RS	recovery sleep
RT	room temperature
SC	subcoeruleus
SCN	suprachiasmatic nucleus
SD	sleep deprivation
SEM	standard error of the mean
SLD	sublaterodorsal nucleus
SSRIs	selective serotonin reuptake inhibitors
SWA	slow wave activity
SWS	slow-wave sleep
TMN	tuberomammillary nucleus
TN	true negative
TP	true positive
Veh	vehicle
vGluT2	vesicular glutamate transporter
vlPAG	ventrolateral periaqueductal gray matter
VLPO	ventrolateral preoptic area
VMM	ventromedial medulla
VTA	ventral tegmental area
WT	wildtype
ZT	zeitgeber time

Chapter 1
Sleep science, techniques, and neuronal circuits

Daily cycles of sleep and wake occur in all complex lifeforms, highlighting their central importance. In 1989 the importance of sleep to health and life has been illuminated by Rechtschaffen *et al*. when his experiment showed that all rats die within 2-3 weeks after the total sleep deprivation[1]. During the progressive sleep deprivation, the rats developed skin lesions, had erosions of the gastrointestinal tract, became hypermetabolic, and lost weight before they die. Most rats died of sepsis implying that their immune system were attenuated and were more easily to get infection due to sleep deprivation[2].

Furthermore, a large body of knowledge has accumulated over the past quarter century documenting the adverse consequences of short-term, total or partial sleep deprivation on human learning, mood, memory, behavior, performance, and organ-system function[3,4]. For example, increasing inability to write down the items they see while the items are being presented has been observed in 1 night sleep loss subjects. The decreases in immune cells (such as natural killer cell) and increase of infection rates are observed after short periods of sleep deprivation. Epidemiologic studies performed by Kripke *et al* on more than 1 million human subjects show that mortality rates after 6 years of follow-up were significantly increased for subjects reporting less than 4 hours or more than 10 hours of sleep per night at baseline. The consistency of these reports suggests that deviations in sleep duration from the normal range (4-10 hours per day) may adversely influence human longevity[5,6].

Development of Sleep Science

Before 1952, it was assumed that sleep occurred when sensory stimulation to the brain was rendered insufficient to maintain a waking level of brain activity. Thus sleep usually occurred at night, in darkness for humans. This theory is often called the “passive process theory”, which described sleep could be regarded as an entirely homogeneous state, and that a single observation could be generalized to the entire sleep period[7].

In 1937 Dr. A. L. Loomis and his lab in Tuxedo Park, New York first documented the characteristic electroencephalogram (EEG) patterns from humans, which is now called Non-rapid eye movement sleep (NREM sleep): vertex waves, sleep spindles, K complexes, and delta slowing. He divided sleep into 5 stages of increasing depth from A through E, which form the basis for the current classification of NREM sleep[8].

In 1952 the binocularly synchronous rapid eye movements occurred during sleep was observed by Eugene Aserinsky and Nathaniel Kleitman[9]. The eye movements were recorded quantitatively as electrooculograms (EOG) by employing one pair of leads on the superior and inferior orbital ridges of one eye, and another pair of leads on the internal and external canthi of the same eye. Monopolar EEG was recorded simultaneously from the frontal and occipital areas, which were invariably of low amplitudeand irregular frequency. The fact that these eye movements and EEG pattern are significantly related and do not occur randomly suggest that these physiological phenomena are very likely all manifestations of a particular level of cortical activity which is

encountered normally during sleep, as we now know the rapid eye movement sleep (REM sleep)[9].
In the following 20 years, scientists investigated the whole night sleep, and finally the basic sleep cycle and characteristic all-night sleep stage architecture were built, which consist of four stages of NREM sleep and REM sleep, a schema still used today with very few alterations. The major advance was the concept of the duality of sleep—that is, sleep consists of two entirely different organismic states, REM sleep and non-REM sleep[10,11].
Since 1965, the experimental study of sleep and its disorders has developed rapidly. This has permitted the development of sleep medicine and sleep mechanism studies as the sleep disorders started to be considered a new clinical discipline, and more sleep related associations were founded[12].

One Model of Controlling Sleep: Circadian Rhythm

Circadian rhythms are intrinsic oscillations in organisms of approximately 24 hours in length that exist in virtually all cells[13]. Although circadian rhythms are endogenous they are adjusted (entrained) by factors known as ‘zeitgebers’ ("time giver"), the most potent being light[14].
In 1963, Wurtman *et al* reported that melatonin synthesis in the pineal gland was under the inhibitory control of light[15]. Anatomic destruction of the suprachiasmatic nucleus (SCN) located in the hypothalamus showed that the neural pathway by which output from the SCN reaches the pineal gland. This pioneering work completed our understanding of how light reaching the retina could produce suppression of melatonin secretion from the pineal gland[16].
Moore and Lenn identified the retinohypothalamic tract that serves the important function of connecting the SCN with the photic environment, which accelerated the investigation of SCN in circadian rhythm[17].
In 1972, more SCN destruction studies showed that destruction of SCN eliminate circadian rhythms in adrenal corticosterone and drinking and locomotor activity in rats. Hence, the scientific investigation and understanding of these rhythms dramatically accelerated with the discovery of the SCN as the site of the biologic clock[18,19].
The central role played by the SCN in mediating circadian rhythmicity was further supported in 1995 by the finding that individual neurons dissociated from the SCN were capable of maintaining rhythmic circadian firing patterns when cultured in vitro[20].

Development of Sleep Homeostasis and Two-process Model

Generally speaking, a homeostatic control system implies the existence of a negative feedback loop. There must be some variable whose level is sensed by a group of, usually, specialized cells. Changes in the activity of these cells are registered by a control center which activates effector systems that return the value of the variable being sensed to within an acceptable range. In the case of sleep/wake regulation, we may hypothesize that prolonged waking causes progressive changes in the value of some as yet undetermined physiological variable probably on the brain[21].
The most obvious evidence that sleep is homeostatically regulated is the simple observation that sleep loss leads to an increased propensity to sleep and that sleep lasts longer following a period of sleep deprivation[22,23]. Lost sleep is not recovered minute-for-minute, but there is evidence that recovery

sleep following sleep deprivation is “deeper” and more “restorative” than normal sleep[24,25].

In 1982, the two-process model of sleep regulation was proposed by Borbély, and it has served as a major conceptual framework in sleep research since[25]. The two-process model posits that the interaction of a homeostatic process depending on sleep and wake (Process S) with a process controlled by the circadian pacemaker (Process C) determines salient aspects of sleep regulation (**Fig. 1.1**)[26].
Process S, representing sleep debt, increases during wakefulness and declines during sleep, within a value-range that oscillates with a periodicity that is normally entrained to day and night by the circadian pacemaker. When S approaches the range’s lower boundary it triggers awakening; near the upper boundary it triggers sleep. Non-rapid eye movement (NREM) sleep electroencephalography (EEG) slow wave activity (SWA) represents the principal marker of process S during sleep; theta activity in waking is a marker of the rising limb of process S. Core body temperature and melatonin rhythms are markers of process C[26]. In animals rendered arrhythmic by lesioning the suprachiasmatic nuclei (SCN), sleep homeostasis is not disrupted. This indicates that the two processes are regulated separately[27,28].
In process S, prolonged periods of wake are followed by long periods of deep NREM sleep, and this homeostatic response is likely mediated by NREM sleep-promoting substances (somnogens), including adenosine, prostaglandin D2, and cytokines such as interleukin-1 and tumor necrosis factor-a. In general, somnogens increase during wake and act as paracrine mediators to promote sleep, which can be markers for sleep pressure[29].

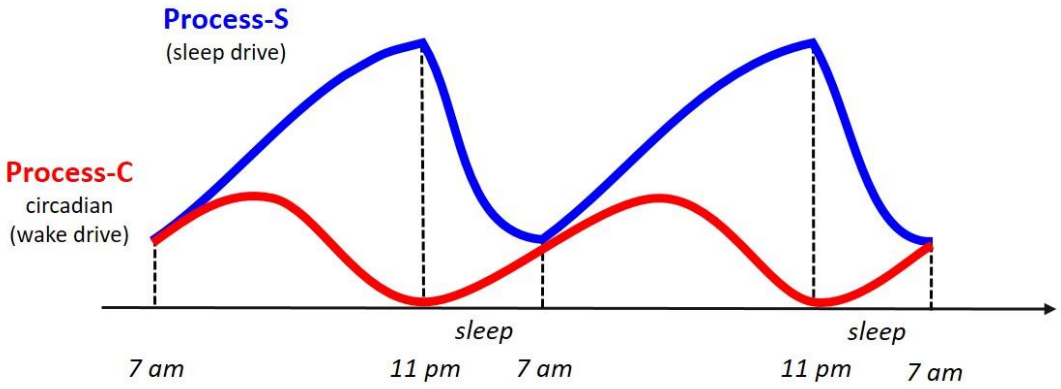

Figure 1.1 Schematic of the two-process model[26]

Techniques for Sleep Science

It was only since the middle of the 19th century that sleep became an object of experimentation[12,30]. In the following decades physiological processes during sleep, such as the distribution of blood volume[31], muscular fatigue[32], and the 24-hour rest-activity cycle[33] have been investigated.
However, since the brain is the essential organ for the regulation of sleep, systematic investigations of sleep had to wait for techniques that enabled the study of brain activity during sleep. Such a method became available with the invention of the electroencephalogram (EEG). Caton was the first to record brain electrical activity of animals in England in 1875[34], but it was Berger who

discovered and reported the “electroencephalogram of man” in Germany in 1929[35]. EEG is also the technique to characterize the NREM sleep and REM sleep as describe previously.
The EEG is still being used nowadays. It is the central device in a sleep laboratory and is considered the gold standard for identifying sleep. Neural oscillations, or brainwaves, are rhythmic or repetitive patterns of neural activity in the central nervous system which can be characterized by their frequency, amplitude and phase. These signal properties can be extracted from neural recordings using Fourier transform, which decomposes a function of time (a signal) into the frequencies that make it up, and transforms the signal from time domain to frequency domain[36]. The spectrum means the distribution of power into frequency components composing that signal, which is commonly used in EEG. The spectral content of EEG is divided into bands by frequency, and each has been associated with specific vigilance states. Delta, the range between 0.5–4.0 Hz, is associated with NREM sleep, also known as slow-wave sleep (SWS), and aids in characterizing the depth of sleep[37]. Delta power is also used as an index of homeostatic sleep pressure, as it declines across a sleep period but increases in recovery sleep[25].

A century ago Bremer, Jouvet, and other researchers used knife-cuts to transect the brain at various levels to identify the nature of sleep[38]. These transaction studies were eventually replaced by electrolytic lesions of specific brain areas. Researchers then started to make region-specific lesions by injecting neurotoxins into specific regions[39], monitoring cellular electrophysiology, and measuring neurotransmitters by employing the microdialysis technique in conjunction with high-performance liquid chromatography methods for the quantification of neurotransmitters release[40]. All of these are meant to understand how candidate neurochemicals and the activity of restricted cells groups were associated with sleep–wake behaviors. Recent advances in molecular biology have created new genetically engineered tools that are allowing researchers to understand sleep control. They are discussed below

Genetically engineered tools for sleep research

Cre-loxP system

Cre gene encodes a protein of 343 amino acids, cycle recombinase (cre), that recognizes two sites, called LoxP (locus of X-over P1) sites, and the cre enzyme will very efficiently recombine essentially any DNA substrates which contain these sites. Mice and rats can express Cre in specific cells and neurons by using genetic engineering to insert Cre to the gene locus of cell specific marker. They can be used when the objective is to deliver specific genes of interest (e.g., channelrhodopsin-2 or ChR2) in specific cells (e.g., hypocretin or MCH). The specific genes of interest (e.g., ChR2) can be inserted into Cre-expressing cells by stereotaxically injecting ready-made viruses (e.g., recombinant adenoassociated virus, AAV) into region of interest[41,42]. The advantage of Cre-loxP system is that it can combine with either optogenetics or chemogenetics to study neuronal circuits. The genes of interest are activated only in the cells which express Cre, but not in the cells which do not contain Cre, enabling manipulation of specific cells and/or

neurons to study their neuronal circuits.

Optogenetics

Optogenetics is a technique by which fine temporal control is achieved over a distinct population of cells by selective expression of a light-sensitive opsin[43]. It uses the light-sensitive proteins channelrhodopsin-2 (ChR2) and halorhodopsin (NpHR) to either activate (photoactivation) or inhibit (photoinhibition) respectively the activity of neurons in which they are targeted to test the functionality of circuits. The fast temporal kinetics of light-sensitive opsins makes it possible to reliably drive trains of high-frequency action potentials in ChR2-expressing cells or suppresses action potentials in NpHR-expressing neurons. These two types of light-sensitive proteins can be inserted and expressed in specific cells by using Cre-loxP system, allowing researchers the ability to manipulate the activity of specific cells with millisecond precision. Thus, by delivering a specific wavelength of light, it is possible to control specific circuits in a neural network.

To manipulate either ChR2 or NpHR, a fiber-optic probe is stereotaxically placed over the candidate cells. Blue light (~473 nm) is used to activate ChR2, causing opening of the ChR2 ion channel, allowing Na+ to flow into cells and depolarization of the cell membrane[44]. On the other hand, yellow light (~590 nm) is used to activate NpHR. NpHR is a light-gated chloride pump causing hyperpolarized of cells when exposed to yellow light[45]. This can be used to evoke neurotransmitter release via both soma and terminal light stimulation.

The first published study that used optogenetic methods to examine behavior in intact mice used photic manipulation of hypocretin cells to identify their role in arousal. This landmark paper used a lentivirus to drive ChR2 expression in hypocretin neurons in mice. 5–30 Hz blue-light stimulation triggered arousal from both NREM and REM sleep, suggesting that hypocretin cells function to promote arousal[46].

Chemogenetics

Chemogenetics relies on ‘Designer Receptors Exclusively Activated by Designer Drugs’, known as DREADDS[47]. Those most commonly published are hM3Gq and hM4Gi, which are engineered G-protein coupled receptors (modified muscarinic M3 and M4 receptors). hM3Gq muscarinic receptor that acts to excite cells by a Gαq signaling pathway, whereas the hM4Gi muscarinic receptor that inhibits cells by a Gαi pathway. The modification permits selective activation only by the exogenous ligand clozapine-N-oxide (CNO). Since CNO crosses the blood brain barrier, it can be delivered by intraperitoneal injection or by putting CNO in an animals drinking water[48]. In contrast to ChR2, the activation kinetics of these DREADDS are much slower and cannot be temporally defined since it is influenced by the bioavailability of the CNO (systemic vs. directly to brain). Once the ligand is bound, there is no ability to ‘turn off’ the receptor activation until it is metabolized (~6 h). Therefore this method is often used for behavioural experiments due to the longer lasting effects of manipulation[49]. One advantage of chemogenetics is that it can activate or suppress the activity of broadly scattered neuron populations, making it a more useful approach than optogenetics for manipulating distributed cell groups[48].

The chemogenetic approach has been used to determine how wake-active cells group participate in behavioral control. For example, Sasaki *et al.* used CNO-induced activation of hM3Gq receptors on hypocretin neurons to show they increase wakefulness, whereas CNO-induced activation of hM4Gi receptors increases sleep for 4 h[50].

Deep Brain Imaging

Currently, activity in brain regions can be detected using positron emission tomography (PET) scanning or functional magnetic resonance imaging (fMRI). However, these methods cannot identify the phenotype of the cells, which hinders the ability to understand how the brain processes complex information to trigger behaviors, such as sleep.

Deep brain imaging can go deep to cellular level and measures changes in calcium dynamics in cells using fluorescent probes[51]. New genetically encoded calcium indicators (GECIs) can measure calcium influx in astrocytes[52] and neurons[53]. The most widely used GECI are GCaMPs, consisting of the calcium-binding protein calmodulin (CaM) fused to green fluorescent protein (GFP), and a linker peptide M13. Each successive generation of GCaMPs has been improved to yield better speed, sensitivity, intensity, and durability of the fluorescent signal. The current versions of GCaMP6 (6s, 6m, 6f for slow, medium, fast) can detect single action potentials in neurons[53]. The fluorescence of a GECI changes when it binds calcium, providing a readout of intracellular changes in calcium levels. As calcium waves are the main read-out of astrocytic activity and the mode of communication to neurons, and calcium is also required for neuronal generation of action potentials, GECIs can be used to determine both astrocytic and neuronal activity[54].

The fluorescence of GCaMP6-expressing cells can be monitored in virtually any brain region. This is achieved by placing a tiny endoscope (0.5–1.0 mm diameter) in the vicinity of targeted cells. The endoscope transmits the fluorescent signal to a miniature fluorescence microscope (2 g) mounted atop the animal's head[55]. The significant advantage is that the endoscope-microscope combination can image many individual neurons at the same time, thereby providing unprecedented data on the behavior of individual neurons during a specific behavior[56]. Moreover, these neurons can be followed for many days.

An alternative approach is not to use the microscope but instead, gather the signal with a fiber-optic line from the endoscope in the brain. This approach is referred to as "fiber photometry". The rationale is that since the GCaMP is in phenotype-specific neurons, then it is possible to measure the collective output of this population. The serious limitation of "fiber photometry" is that it cannot isolate the activity of single neurons or locate the source of the fluorescence signal[57].

Recently, Cox *et al.* used GCaMP6s to identify the activity patterns of different cell types in the dorsal pons—a region hypothesized to regulate REM sleep. They found that glutamate cells in this region were most active during REM sleep, whereas GABA cells were most active during wakefulness[58].

New Histochemical Tissue-Clearing Methods and Circuit Mapping Tools

In addition to genetically engineered tools, new histological methods are

emerging that provide a new option apart from the familiar cryostat and sliding microtome. The new approach is to make the tissue transparent, scan it with a laser from a light sheet microscope, and then use software to render a 3D image of the scanned images. These methods are known by various names (3DISCO, CLARITY, CUBIC, SCALE) depending on the process (passive vs. electrochemical) and type of chemicals (hydrogels, organic solvents, and detergents) that are used to stabilize proteins, remove lipids, and render the tissue, such as the brain, transparent[59].

The enormous appeal of the new histoclearing methods is that they allow visualization of the underlying cytoarchitecture in great detail[60]. If the brain contains fluorescent markers in phenotype-specific neurons, the 3D image will depict the distribution of their somata along with the neural pathways throughout the brain. This allows for visualization of the relationship between cell types in a way that has not been possible before. For instance, it will be useful in reconstructing visual maps of sleep–wake circuitry to understand how different circuits communicate with one another and where they are anatomically located in the central nervous system (CNS). This method can be used in combination with neuronal activity markers such as c-Fos to determine when particular neuron networks are activated and where they project[59]. This also allows researchers to position the probes better for optogenetic stimulation and deep brain imaging of specific clusters.

The power to image the intact brain can be further enhanced by the use of new retrograde tracers. New genetically assisted circuit mapping tools have been developed that can be used in conjunction with optogenetics in cre-transgenic animals. The new tracers allow researchers to identify, manipulate, and map the projections of genetically targeted neurons[61]. For example, the tracer AAVEF1alpha–mCherry—IRES-WGA-Cre (WGA is the plant lectin in WGA-HRP used for tract tracing) can be injected into a target site such that Cre is then retrogradely transported to neurons that project to the injection site. It is very likely that multiple phenotypes of neurons project to the target site, all of which will express Cre. The gene of interest, such as ChR2, can be inserted into Cre-expressing neurons at a specific site by injecting AAV-DIO-ChR2-Cre at that site. All neurons containing Cre and that project to the target site will now contain ChR2. Thus, projection specific neurons can be stimulated[62,63].

Neuronal Circuits for Wake

About 100 years ago, an epidemic of encephalitis lethargica swept through Europe, and affected patients would often sleep more than 20 hr/day for months on end[64]. The Viennese neurologist Constantin von Economo discovered that these patients often had lesions in the midbrain and posterior hypothalamus, and he proposed that these regions contain vital wake-promoting circuitry[64]. Moruzzi and Magoun later showed that electrical stimulation of the reticular formation in anesthetized cats shifts the EEG from the slow activity typical of anesthesia to fast activity similar to that seen during wake[65].

Over the last few decades, researchers established that the major influences on arousal arise from neurochemically distinct systems (**Fig. 1.2**). These nuclei are:

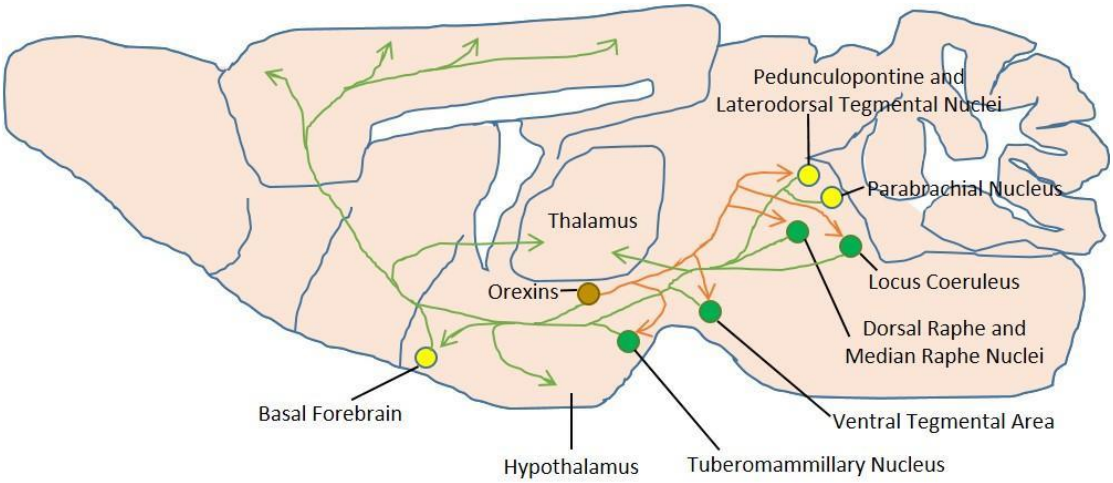

Figure 1.2 Wake-promoting pathways

Several neurochemical systems promote arousal and the fast cortical activity typical of wakefulness. These include noradrenergic neurons of the locus coeruleus, serotonergic neurons of the dorsal and median raphe nuclei, dopaminergic neurons of the ventral tegmental area, histaminergic neurons of the tuberomammillary nucleus, glutamatergic neurons of the *parabrachial nucleus, cholinergic regions including the pedunculopontine and laterodorsal tegmental nuclei and basal forebrain, and orexin neuropeptides.*

Locus Coeruleus

The locus coeruleus (LC) is the major source of forebrain noradrenaline (NA). LC neurons promote arousal in general and are essential for the high levels of arousal required when responding to salient stimuli and stressors. NA agonists (e.g., alpha-1 adrenergic agonists) increase wake, and photoactivation of the LC rapidly wakes mice from sleep. Conversely, drugs that reduce NA release such as alpha-2 adrenergic agonists are sedating, and photoinhibition of noradrenergic LC neurons promotes transitions into NREM sleep and mildly reduces wake[66].

Dorsal Raphe and Median Raphe Nuclei

Most forebrain serotonin (5HT) arises from the dorsal raphe nuclei (DRN) and median raphe nuclei (MRN). 5HT directly excites other wake-promoting neurons, and drugs that increase 5HT tone, such as selective serotonin reuptake inhibitors (SSRIs), which increases the levels of 5HT in the brain, generally increase wakefulness in both humans and rodents. Photoactivation of 5HT neurons for 1 hr in mice during inactive periods doubles the amount of wake and fragments NREM sleep during the optical stimulation[67]. Male C57BL/6 J mice and Tph2- ChR2 transgenic mice were used in the study.

Ventral Tegmental Area

Dopamine's capacity to drive arousal is clear from the potent effects of drugs that increase or decrease dopamine (DA) signaling. Amphetamines and modafinil strongly promote wake, mainly by increasing synaptic concentrations of DA[68]. However, the source of this wake-promoting DA has been a mystery as many brain regions produce DA. Chemogenetic inhibition of DA ventral tegmental area (VTA) neurons reduced wake during baseline

conditions and especially under conditions of high motivation such as seeking palatable food or a potential mate[69]. Tyrosine hydroxylase knock-in mice (Th-IRES-Cre; EM:00254) were used in the study. Cre-inducible recombinant AAV vectors carrying chemogenetic and optogenetic transgenes were stereotaxically infused to the VTA[69]. Conversely, photoactivation of these neurons or their terminals in the nucleus accumbens or the central nucleus of the amygdala rapidly wakes mice from sleep[69].

Tuberomammillary Nucleus

The tuberomammillary nucleus (TMN) is the sole neuronal source of histamine in the brain. TMN neurons excite neurons in the cortex, thalamus, and other arousal-promoting regions during wake. Centrally acting histamine H1 antagonists are sedating, and mice lacking histamine or the H1 receptor have less wakefulness at the beginning of the dark period and less wake in response to the stress of a novel environment[70]. Histamine likely promotes generalized arousal as histamine levels are consistently high during wake, and chemogenetic stimulation of the TMN increases locomotion[71]. Optogenetic inhibition of ventral TMN histamine neurons during wakefulness promotes slow-wave sleep, but not rapid eye movement sleep, during a period of low sleep pressure[72]. Together, these data suggest that histamine neurons is necessary for the maintenance of wakefulness.

Monoaminergic cell groups consist of locus coeruleus (LC), dorsal raphe nuclei (DRN), median raphe nuclei (MRN), ventral tegmental area (VTA), and tuberomammillary nucleus (TMN). They drive arousal by producing noradrenaline (NA), serotonin (5HT), dopamine (DA), or histamine, and they diffusely innervate the cerebral cortex, basal forebrain (BF), lateral hypothalamus, thalamus, and many other regions[73].

Basal Forebrain

The basal forebrain (BF) is defined by fields of cholinergic neurons extending from the medial septum back to the substantia innominata, and this region also contains neurons producing GABA and glutamate. BF neurons project topographically to distinct regions of cortex[74]. Selective lesions or inhibition of the BF cholinergic neurons using optogenetic or chemogenetic techniques mainly increase slow EEG rhythms and reduce awakenings from NREM sleep, but they do not reduce the amount of wake[75,76]. Conversely, chemogenetic activation of these neurons suppresses slow EEG activity during NREM sleep and destabilizes NREM sleep for several hours but with little effect on the amount of wake[76,77]. Photoactivation similarly suppresses slow waves, but after a few seconds it also wakes mice from NREM sleep and then prolongs the subsequent period of wake[78,79]. These results consistently show that the BF cholinergic neurons promote fast cortical activity, but it is less clear whether these neurons are necessary for wakefulness itself.
In contrast to the cholinergic neurons, GABAergic BF neurons are clearly capable of promoting wake. Chemogenetic activation of GABAergic BF neurons dramatically increases wake and fast EEG activity for many hours[77], whereas inhibition increases NREM sleep for about 3 hr[77]. In the study, Vgat-IRES-Cre mice were used, and AAV vector expressing hM3Dq or hM4Di was stereotaxically injected into the BF. These cells promote cortical activation by

reducing the activity of inhibitory cortical interneurons, and they may have indirect effects via projections to the thalamus and many other subcortical regions[77].
Much less is known about the glutamatergic BF neurons, but they also seem to promote cortical activation[79]. Photoactivation of these cells consistently wakes mice from NREM sleep, and though chemogenetic activation slightly reduces slow EEG rhythms, it does not increase wake[77,79].

Pedunculopontine and Laterodorsal Tegmental Nuclei
The pedunculopontine (PPT) and laterodorsal tegmental nuclei (LDT) are clusters of cholinergic neurons at the junction of the pons and midbrain, and like the BF, these nuclei also contain separate populations of GABAergic and glutamatergic neurons[80]. PPT/LDT cholinergic neurons innervate many subcortical regions that influence arousal, but unlike the BF cholinergic neurons, their innervation of the cortex is sparse[81]. Selective chemogenetic activation of PPT cholinergic neurons strongly suppresses slow EEG activity during NREM sleep[82]. In the study, ChAT-Cre mice were used and AAV-M3-mCherry was microinjected into PPT. CNO was administered in saline afterward. Photostimulation of these cells reduces slow wave activity during seizures[83]. Thus, much like BF cholinergic neurons, PPT/LDT cholinergic neurons can suppress slow cortical activity, but it remains unknown whether they promote wake itself. Chemogenetic activation of the glutamatergic PPT neurons markedly increases wake for several hours, and chemogenetic inhibition of glutamatergic PPT neurons mildly reduces wakefulness during the dark period[82]. On the other hand, chemoactivation of hM3-expressing GABAergic PPT neurons mildly reduces REM sleep and shortens latency to sleep onset[82].

Parabrachial Nucleus
The parabrachial nucleus (PB) is crucial for regulating arousal as injury to the PB region produces coma or persistent vegetative state in both animals and humans[84,85]. Glutamatergic neurons of the medial PB may be especially important for wake as this region heavily innervates the BF, and destruction of medial PB neurons or local deletion of the vesicular glutamate transporter (vGluT2) reduces wake and increases EEG delta power during NREM sleep[85,86].

Orexins/ Hypocretins
Orexin-A and orexin-B (also known as hypocretin-1 and hypocretin-2) are neuropeptides that produced by neurons in the lateral hypothalamus and excite neurons in the cortex, midline thalamus, and all wake-promoting brain regions. Photoactivation of the orexin neurons rouses mice from sleep[46], and chemogenetic activation of the orexin neurons increases wake and strongly suppresses REM sleep[50]. The importance of the orexin system is most obvious in narcolepsy, a common sleep disorder caused by selective loss of the orexin-producing neurons. People with narcolepsy have chronic, often severe sleepiness and dysregulated REM sleep, and animals with disrupted orexin signaling have a very similar phenotype, with wake bouts much shorter than usual and sudden transitions from wake into REM sleep-like states[87]. This role in maintaining wake is evident in mice with acute loss of the orexin

neurons, which lose their ability to produce long bouts of wake. Mice were more likely to wake during the first 30 sec of NREM sleep and then less likely to return to sleep during the first 60 sec of wakefulness[88]. Orexin signaling also helps maintain arousal when animals are stressed, seeking reward, or responding to homeostatic challenges[89]. For example, food deprivation markedly increases wake in wild-type mice, probably to encourage foraging, but mice lacking the orexin neurons show very little arousal with hunger[90].

Neuronal Circuits for NREM Sleep

In his research on encephalitis lethargica, von Economo found that most patients had severe sleepiness caused by lesions in the posterior hypothalamus, but some had just the opposite—unrelenting insomnia with lesions in the preoptic area (POA), the most rostral part of the hypothalamus[64]. He proposed that the POA contains neurons that promote sleep. Afterward, more sleep-promoting areas have been identified (**Fig. 1.3**):

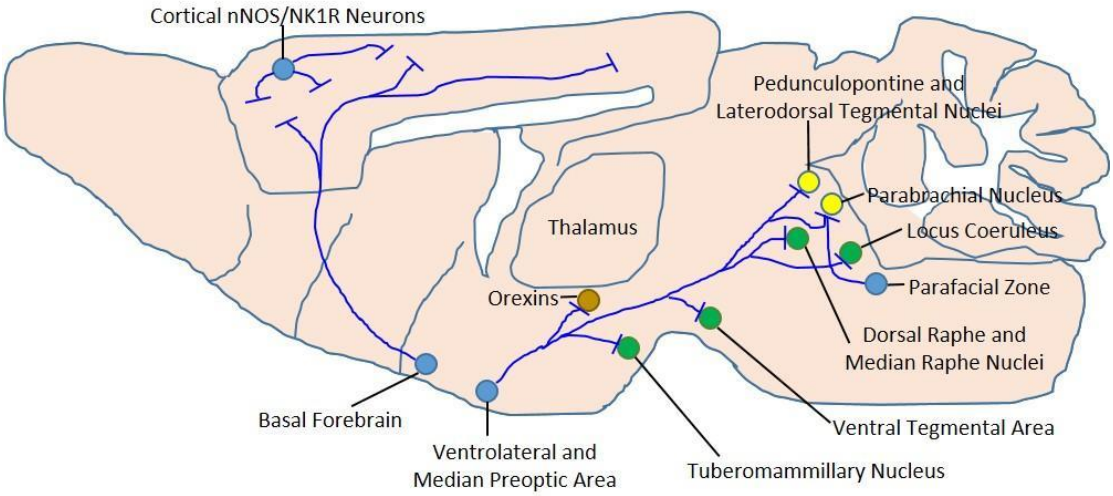

Figure 1.3 NREM sleep-promoting pathways

Most sleep-promoting neurons are GABAergic neurons. GABAergic neurons in the ventrolateral preoptic area and median preoptic nucleus promote sleep by inhibiting wake-promoting neurons. The GABAergic neurons in the basal forebrain also contains sleep-active neurons that may promote sleep via projections within the BF and direct projections to the cortex. GABAergic neurons of the parafacial zone may promote sleep by inhibiting the parabrachial nucleus. The cortex contains scattered Cortical nNOS/NK1R Neurons that contain both GABA and neuronal nitric oxide synthase.

Preoptic Area

Researchers have now established that the ventrolateral preoptic area (VLPO) and median preoptic nucleus (MnPO) contain neurons essential for promoting NREM sleep. VLPO and MnPO sleep-active neurons are GABAergic, and VLPO neurons also produce the neuropeptide galanin. Both cell groups strongly innervate and inhibit arousal-promoting brain regions, including the cholinergic neurons of the BF, orexin neurons, TMN, DRN, MRN, and LC[91,92]. With rising sleep pressure, neurons in both regions fire faster during the sleep deprivation period and during the subsequent sleep[93]. The VLPO may contain two types of sleep-active neurons: one population is

excited by adenosine and may promote sleep in response to homeostatic sleep pressure, and the other population does not respond to adenosine but is inhibited by acetylcholine, NE, and 5HT, suggesting it may help consolidate sleep once the arousal systems are inactive[94]. Chemogenetic activation of sleep-promoting preoptic neurons produced abundant EEG slow waves and reduced body temperature[95]. However, the precise identity and function of these neurons is only partially understood.

Basal Forebrain
Though most neurons in the BF are wake-active, others are mainly active in NREM sleep. These neurons are mostly GABAergic, and they usually begin to fire a few seconds before NREM sleep onset and then fire at their maximal rate throughout NREM sleep[96]. Optogenetic stimulation of this population mildly increases NREM sleep, perhaps via inhibition of other wake-active BF neurons producing acetylcholine, parvalbumin/GABA, and glutamate[97]. In addition, some of these sleep-active neurons innervate the cortex, so they may promote NREM sleep via direct inhibition of cortical neurons[98].

Parafacial Zone
Using a combination of chemogenetic techniques and lesions, researchers recently identified a cluster of NREM sleep-active neurons in the parafacial zone (PZ), a region just dorsal and lateral to the facial nerve in the rostral medulla[99]. These GABAergic/glycinergic neurons express Fos during NREM sleep, and directly inhibit PB neurons, including those that project to the BF[99]. Chemogenetic activation of these neurons rapidly induces sustained periods of NREM sleep with high EEG delta power similar to that seen after sleep deprivation[99]. Conversely, chemogenetic inhibition of PZ GABAergic neurons strongly decreases NREM sleep, even during times of high sleep drive, indicating that these neurons are necessary for NREM sleep[99].

Cortical Sleep-Active nNOS Neurons (Cortical nNOS/NK1R Neurons)
Though most cortical neurons are wake-active, one population is especially active during NREM sleep. These cells are called sleep-active nNOS cells, corresponding to type I nNOS neurons, which are larger and less numerous than type II cells. Type I cortical nNOS neurons are primarily found in the deep layers of the cerebral cortex, which produce neuronal nitric oxide synthase (nNOS), express the neurokinin-1 receptor (NK1R), and are a small subset of the broader population of GABAergic cortical interneurons[100]. Because of its ability to co-express nNOS and NK1R, it is also called cortical nNOS/NK1R neurons. Fos expression in cortical nNOS/NK1R neurons correlates with the amounts of NREM sleep and slow wave activity during NREM sleep[101]. The cortical nNOS/NK1R neurons are thought to respond to homeostatic sleep drive and synchronize slow cortical rhythms via long-range, intracortical projections and release of GABA and nitric oxide (NO). In support of this idea, mice constitutively lacking cortical nNOS have shorter NREM sleep bouts, less total NREM sleep, and a blunted homeostatic response to sleep deprivation[102].

NREM sleep clearly relies on neurons in the POA, BF, brainstem, and possibly the cortex, but how these generate transitions into NREM sleep and

how they sustain NREM sleep is still being established. One model proposes that mutual inhibition between wake-promoting neurons and sleep-promoting neurons generates patterns of activity akin to an electrical flip-flop switch[103].

Neuronal Circuits for REM Sleep

Neural circuits in the pons are required for REM sleep. Early studies showed that when in REM sleep, animals with a knife cut at the caudal edge of the pons show the usual low amplitude, fast EEG activity but lack muscle atonia, whereas transections at the rostral edge of the pons preserve the atonia of REM sleep but eliminate the fast EEG activity[104,105]. In the late 1970s, many researchers thought REM sleep was controlled by reciprocal connections between the REM sleep-promoting cholinergic LDT/PPT neurons and the REM sleep-suppressing monoaminergic neurons[106]. Over the last several years, another REM sleep model has taken hold in which glutamatergic neurons in the sublaterodorsal nucleus of the pons play a central role in generating REM sleep since they contribute to the muscle atonia of REM sleep[107] (**Fig. 1.4**):

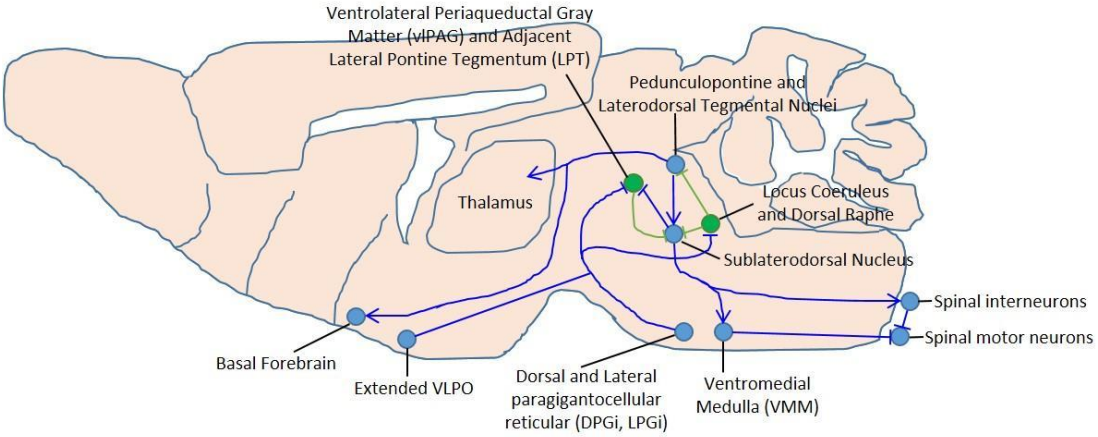

Figure 1.4 REM sleep-promoting pathways

Glutamatergic neurons of the sublaterodorsal nucleus produce the muscle paralysis of REM sleep by exciting GABAergic/glycinergic neurons in the ventromedial medulla and spinal cord that hyperpolarize motor neurons. Cholinergic neurons of the pedunculopontine and laterodorsal tegmental nuclei also promote REM sleep. During wake and NREM sleep, the SLD is inhibited by GABAergic neurons of the ventrolateral periaqueductal gray and adjacent lateral pontine tegmentum as well as locus coeruleus and raphe nuclei. During REM sleep, the ventrolateral periaqueductal gray is inhibited by GABAergic neurons of the SLD, DPGi, LPGi, and extended VLPO.

Pedunculopontine and Laterodorsal Tegmental Nuclei

PPT/LDT cholinergic neurons begin firing just before REM sleep or wake[81], suggesting they may help promote transitions into these states. In line with this idea, optogenetic activation using ChR2 under PPT/LDT cholinergic neurons promotes transitions from NREM to REM sleep[108]. In the study, adult male transgenic mice expressing ChR2 under the choline acetyltransferase (ChAT) promoter (stock no. 014546; The Jackson Laboratory) were used. Recent studies have begun to shed light on the non-cholinergic neurons of the PPT/LDT. Most glutamatergic neurons in this region begin firing just before

and continue during REM sleep, and many also fire during wake. The GABAergic neurons in the PPT/LDT region seem mainly wake-active, but some may be more active during REM sleep than in NREM sleep[58].

Sublaterodorsal Nucleus

This region lies just ventral to the caudal LDT and LC and is named the sublaterodorsal nucleus (SLD) (equivalent to the subcoeruleus (SC) or peri-locus coeruleus alpha (peri-LCa) of the cat brain)[109]. Considerable research indicates that glutamatergic neurons of the SLD are essential for generating the muscle atonia of REM sleep[110]. SLD neurons are active during REM sleep as demonstrated by c-Fos immunoreactivity and by single-unit recordings[111]. Animals with focal lesions of the SLD or deletion of glutamate signaling in the SLD often have a state much like REM sleep but without atonia, during which they twitch, jump, and sometimes exhibit complex motor behaviors[107]. SLD lesions that extend into adjacent regions can also shorten REM sleep bouts and reduce the total amount of REM sleep[107]. Researchers continue to debate the mechanism by which the SLD generates muscle atonia. One model proposes that the SLD excites neurons in the ventromedial medulla (VMM) that inhibit spinal motor neurons[112]. Another model proposes that the SLD neurons bypass the medulla and directly excite spinal interneurons that use glycine and/or GABA to inhibit motor neurons[111].

REM Sleep-Suppressing Neurons in the Pons

Several neuronal populations in the pons are thought to suppress REM sleep during wake, including the monoaminergic neurons of the LC and DRN. These neurons are very active during wake but nearly silent during REM sleep. They project to the SLD where NA inhibits REM sleep-active neurons and suppresses REM sleep[113]. In addition, NA and 5HT inhibit cholinergic neurons of the PPT/ LDT[114].

The pons contains another population of REM sleep-suppressing neurons in the ventrolateral periaqueductal gray matter (vlPAG) and the adjacent lateral pontine tegmentum (LPT), a region also known as the deep mesencephalic reticular nucleus[115]. The vlPAG/LPT sends GABAergic projections to the SLD, and lesions or pharmacological inactivation of the vlPAG/LPT region increase REM sleep[116]. Chemogenetic activation or inhibition of GABAergic vlPAG/LPT neurons reduces or increases REM sleep, respectively[117]. In addition to the glutamatergic, REM sleep-promoting neurons described above, the SLD also contains REM sleep-active, GABAergic neurons that innervate the vlPAG/LPT[111,118]. Therefore, the vlPAG/LPT and SLD may form a mutually inhibitory circuit that regulates REM sleep, much like the wake-NREM sleep flip-flop model introduced above.

Medullary Reticular Formation

In addition to VMM, there are other medullary neurons may promote REM sleep by inhibiting REM sleep-suppressing neurons of the pons such as the LC, DRN, and vlPAG/LPT. These neurons are GABAergic neurons and reside in the dorsal paragigantocellular reticular (DPGi) and lateral paragigantocellular (LPGi) nuclei. Photostimulation of neurons in the LPGi and adjacent regions or their terminals in the vlPAG can prolong REM sleep or trigger transitions into REM sleep, whereas chemogenetic inhibition of

these neurons decreases REM sleep[119].

Hypothalamic Control of REM Sleep
Though the neurochemical identity of most of these neurons remains unknown, two specific groups have been identified.
One cluster of REM sleep-active neurons is located just dorsal and medial to the VLPO, in a region referred to as the extended VLPO. These GABAergic/galaninergic neurons are active during REM sleep, and lesions of the extended VLPO reduce REM sleep. These cells innervate the DR, LC, and vlPAG/ LPT, suggesting that the extended VLPO may promote REM sleep by inhibiting brainstem neurons that suppress REM sleep[120].
Another group of REM sleep-promoting neurons is scattered across the lateral hypothalamus (LH) and posterior hypothalamus (PH) and produces the neuropeptide melaninconcentrating hormone (MCH). Several studies show that photoactivation or chemoactivation of the MCH neurons increases REM sleep[121,122].

Orexins/ Hypocretins
Photoactivation of the orexin neurons awakens mice from REM sleep[46]. Similarly, chemogenetic activation of the orexin neurons robustly suppresses REM sleep[50], whereas orexin receptor antagonists increase REM sleep and decrease REM sleep latency[123]. The orexin receptor antagonist SB-649868 was effective in promoting REM sleep following oral dosing (10 and 30 mg/kg) at the onset of the dark phase in male Sprague–Dawley rats (Harlan Laboratories, weighing 350–450 g)[123]. The precise regions through which orexins inhibit REM sleep are still being mapped, but the orexin neurons heavily innervate REM sleep-suppressing regions such as the LC, DR, vlPAG/LPT[124].

Astrocytes and Sleep

The classical view that astrocytes merely provide structural support was first challenged in 1994 when it was demonstrated that Ca^{2+} signals in astrocytes induced the release of the chemical transmitter glutamate, which in turn caused a NMDA (*N*-methyl-D-aspartate) receptor mediated increase in neuronal calcium[125]. This suggested that astrocytes regulate neuronal calcium levels through the calcium-dependent release of glutamate.
During the last few years an interesting observation has been made concerning the importance of sleep for the export of chemicals from the brain. Santiago Ramón y Cajal found that there was a close association between astrocytes and brain vasculature, and hypothesized that the astrocytes regulated nutrient flow to the brain by contracting and relaxing[126]. New evidence is now revealing that the astrocytes are a key component of a glymphatic system in the CNS that is responsible for waste disposal and distribution of lipids, glucose, and other nutrients[127]. During wakefulness there is little exchange between the CNS and the glymphatic pathway; however, during sleep solutes from the interstitial fluid (ISF), including amyloidβ (Aβ), clear rapidly through the glymphatic pathway[128].
Optogenetic stimulation (10 Hz) of the astrocytes in the posterior hypothalamus significantly increases both NREM and REM sleep[129]. This is the first time that optogenetic activation of non-neural structures has been

shown to influence sleep. In another study, astrocytes were optogenetically stimulated *in vivo* while the activity of associated neurons was recorded[52]. When astrocytes were stimulated neurons were found to transition to slow oscillations.
It is unclear how astroglial stimulation increased sleep, but astrocytes are a major source of ATP, which is converted to extracellular adenosine (regulated by adenosine kinase) that stimulates sleep via adenosine A1 receptors[130]. It was well known that adenosine acts through adenosine A1 receptors to cause presynaptic inhibition, but the source of adenosine was assumed to be neuronal. However, Pascual *et al.,* clearly showed that astrocytes are a source of this presynaptic inhibition[131]. In 2005 a novel mouse model was developed in which astrocyte-specific expression of the dominant-negative SNARE domain of a vesicle protein was expressed to impair exocytosis and block the release of transmitters from these glial cells[131]. When this molecule was expressed selectively in astrocytes the tonic adenosine-mediated presynaptic inhibition of excitatory synaptic transmission was relieved, suggesting that astrocytes are a source of the presynaptic inhibition.

In the BF, cortex, and hippocampus, extracellular levels of adenosine increase across prolonged periods of wake and decline during sleep[132]. Injections into the brain of adenosine receptor agonists increase NREM sleep, whereas adenosine antagonists, such as caffeine, promote wake[133]. Adenosine can promote sleep by directly inhibiting wake-promoting neurons and by activating sleep-promoting neurons[134].

Summary

Ever since the Two-process Model had been proposed in 1982 (**Fig 1.1**), more and more research focused on sleep homeostasis. We now know that prolonged periods of wake (sleep deprivation) are followed by long periods of deep NREM sleep, and this homeostatic response (process S) is likely mediated by NREM sleep-promoting regions. The NREM sleep EEG slow wave activity represents the principal marker of process S during sleep, so researcher can use this as a marker for measure sleep pressure and try to find out what might cause and/or control the sleep homeostasis. In additional to EEG slow wave activity, somnogens such as adenosine and prostaglandin D2 are also considered marker of sleep pressure and can be used in sleep homeostatic research. As a result, by monitoring the EEG slow wave activity and/or the level of somnogens after sleep deprivation, we can decide if specific brain areas or neurons are involved in the sleep homeostatic process.

However, in order to propose the brain areas or neurons which might involve in sleep homeostasis, we need to look into all the brain areas and neuronal circuits related to wake, NRME sleep, and REM sleep. As mentioned above (**Fig 1.2-1.4**), the noradrenergic neurons of LC, serotonergic neurons of DRN and MRN, dopaminergic neurons of VTA, histaminergic neurons of TMN, glutamatergic neurons of PB, cholinergic regions of BF, PPT, and LDT, as well as orexin neuropeptides are critical wake-promoting regions and neurons. On the other hand, the GABAergic neurons of VLPO, MnPO, BF, and PZ, as well as cortical nNOS/NK1R neurons are critical for promoting NREM sleep. REM sleep is a trickier one, but we know that the cholinergic neurons of PPT

and LDT, glutamatergic neurons of SLD, GABAergic neurons of vlPAG, LPT, SLD, DPGi, LPGi, and extended VLPO, as well as orexin neuropeptides are involved in REM sleep-promoting pathways.

The improvement of techniques have pushed the neuroscientific research to a higher advanced level. In additional to the conventional EEG, genetically engineered tools such as Cre-loxP system, optogenetics, chemogenetics, and deep brain imaging (calcium imaging) have allowed researchers to understand sleep control in systematically and specific ways. Cre-loxP system allows us to activate the genes of interest only in specific cells of interest which makes to selective expression possible. Optogenetics and chemogenetics allow us to manipulate (either activate or inhibit) neurons/cells of interest in specific areas so that we can record and observe the projected neuronal activity accordingly due to the activation of inhibition. The deep brain imaging then allows us to capture the neurons/astrocytes activity by measuring the changes in calcium dynamics in cells, which is now a useful tool to determine both astrocytic and neuronal activity. In addition to genetically engineered tools, new histochemical tissue-clearing methods and circuit mapping tools provide us a new way to visualize the underlying cytoarchitecture in great detail and relationship between cell types within a 3D image.

Chapter 2
Materials and Methods

1. Mice for experiments

Summary of experimental cohorts in different chapters and experiments
The background, mouse line (genotype), sex, age, and sample size of each experimental cohort were summarised in **Table 2.1** and **Table 2.2**.

Chapter	Chapter 3 Sleep deprivation methodology		Chapter 4 Identification of amygdala neurons activated by sleep loss	Chapter 5 Astrocyte–neuron interactions in sleep homeostasis	
Experiments	*in vivo* EEG/EMG and piezo recording	iDISCO+ whole brain mapping	iDISCO+ whole brain mapping	IHC proximity analysis and quantification	*in vivo* chemogenetics and piezo recording
Background	C57BL/6J		C57BL/6J	C57BL/6J	
Mouse line (Genotype)	Wildtype		Wildtype	Aldh1l1-creERT2:Ai14 (Het:Het)	Wildtype
Sex	Equally mixed		Equally mixed	Equally mixed	Female
Age	6-9 months	4-8 months	4-8 months	2-9 months	8-9 months
Sample size	9-10	8-10 per group	8-10 per group	6-7 per group (proximity analysis) 8-11 per group (quantification)	Virus injection group: 3-4 Non-viral injection group: 5

Table 2.1 Summary of experimental cohorts in chapter 3-5

Chapter	Chapter 6 Phenotypic assessment and neural activity mapping of *MEIS1* point mutation mice				
Study	A			B	
Experiments	Open field, indirect calorimetry, rotarod, and hot plate test	Wheel-running and *in vivo* piezo recording (young adult)	Wheel-running and *in vivo* piezo recording (aged adult)	The second *in vivo* piezo and EEG/EMG recordings	iDISCO+ whole brain mapping
Background	C57BL/6J				
Mice line (Genotype)	$Meis1^{R272H/R272H}$ (HOM) Wildtype littermates (WT)				
Sex	Female				
Age	2-5 months	2-3 months (wheel-running) 4-6 months (piezo)	10-11 months (wheel-running) 12-14 months (piezo)	8-9 months (young adult) 12-14 months (aged adult)	7-10 months
Sample size	15 per genotype	7-11 per genotype	7-11 per genotype	4-5 per genotype	5-7 per group

Table 2.2 Summary of experimental cohorts in chapter 6

Mouse husbandry

Mice were kept in solid-bottomed cages with environment enrichment and sawdust bedding. They were available to *ad libitum* food and water and maintained on a regular light/dark 12h:12h cycle (standard lights-on hours: 08:30-20:30, ZT0 to ZT12) at constant temperature (22±2 °C) and humidity (55±10 %).

Wildtype mice

Wildtype mice were either purchased from The Jackson Laboratory, or bred on site at Helmholtz Zentrum München in Germany by mice purchased from The Jackson Laboratory.

Aldh1l1-creERT2:Ai14 mice

Aldh1l1-creERT2:Ai14 mice were bred on site by crossing male heterozygotic Aldh1l1-creERT2 with homozygotic females Ai14 mice, both with C57BL/6J background. The Aldh1l1-creERT2 and Ai14 mice were either purchased from The Jackson Laboratory, or were bred on site at Helmholtz Zentrum München in Germany by mice purchased from The Jackson Laboratory.

Generation of $Meis1^{R272H/R272H}$ Mice

$Meis1^{R272H/R272H}$ mice were generated to include a point mutation at p.Arg272His (G815A) in *MEIS1* on a C57BL/6N background[140], and were developed collaboratively by Institute of Neurogenomics, Institute of Developmental Genetics, and German Mouse Clinic at Helmholtz Zentrum München in Germany. Specifically, C57BL/6N wildtype zygotes were microinjected with Cas9, a Meis1-specific sgRNA (protospacer AAAAAGCGTCACAAAAAGCG), and a single-stranded oligodeoxynucleotide as repair template for homology-directed repair. The oligonucleotide carried

the intended R272H substitution as well as four silent mutations for genotyping purposes. The point mutation aimed at the nucleotide at position 815 within the gene *MEIS1*, and replaced nucleotide guanine by adenine. This resulted in the change of amino acid from arginine to histidine at position 272 in the MEIS1 protein. A mutant founder animal was crossed to C57BL/6N wildtypes to establish the mouse line. Afterwards, the line was maintained by crossing to wildtype C57BL/6JOlaHsd (Harlan) mice every 10 generations. Experimental cohorts were generated by breeding hetereozygote x hetereozygote carriers to obtain homozygote (HOM, Meis1$^{R272H/R272H}$ mice), and non-carrier littermates (WT, wildtype mice). Genotypes were confirmed by sequencing targeted at position 815 within the gene *MEIS1.*

2. Techniques

Summary of techniques used in different chapters and experiments

The techniques (including *in vivo*, *ex vivo*, and analysis) used in the experiments were summarised in **Table 2.3** and **Table 2.4**.

Chapter		Chapter 3 Sleep deprivation methodology		Chapter 4 Identification of amygdala neurons activated by sleep loss	Chapter 5 Astrocyte–neuron interactions in sleep homeostasis	
Experiments		*in vivo* EEG/EMG and piezo recording	iDISCO+ whole brain mapping	iDISCO+ whole brain mapping	IHC proximity analysis and quantification	*in vivo* chemogenetics and piezo recording
in vivo	Piezo recording and vigilance states analysis	Y				Y
	EEG and EMG recording and vigilance states analysis	Y				
	Sleep deprivation and recovery sleep	Y	Y	Y	Y	Y
	Tamoxifen injection					Y
	AAV transgene plasmid and stereotaxic injection					Y
	Chemogenetic activation					Y
ex vivo	Transcardial perfusion		Y	Y	Y	Y
	iDISCO+ (Tissue clearing)		Y	Y		
	Light sheet fluorescence microscopy imaging		Y	Y		
	Microtome sectioning			Y	Y	Y
	Parcellation			Y		
	Immunohistochemistry				Y	Y
	Microscope slide scanner imaging				Y	
Analysis	ClearMap		Y	Y		
	ImageJ		Y	Y	Y	
	Python		Y			
	IHC quantification and analysis				Y	

Table 2.3 Summary of techniques used in chapter 3-5

Chapter		Chapter 6 Phenotypic assessment and neural activity mapping of *MEIS1* point mutation mice				
Study		A			B	
Experiments		Open field, indirect calorimetry, rotarod, and hot plate test	Wheel-running and *in vivo* piezo recording (young adult)	Wheel-running and *in vivo* piezo recording (aged adult)	The second *in vivo* piezo and EEG/EMG recordings	iDISCO+ whole brain mapping
in vivo	Piezo recording and vigilance states analysis		Y	Y	Y	
	EEG and EMG recording and vigilance states analysis				Y	
	Wheel-running		Y	Y		
	Indirect calorimetry	Y				
	Open field	Y				
	Hot plate	Y				
	Rotarod	Y				
ex vivo	Transcardial perfusion					Y
	iDISCO+ (Tissue clearing)					Y
	Light sheet fluorescence microscopy imaging					Y
Analysis	ClearMap					Y
	ImageJ					Y

Table 2.4 Summary of techniques used in chapter 6

Piezo recording and vigilance states analysis

Piezo sleep screen (piezo) is a transducer that transforms mechanical pressure into electrical signal with a voltage proportional to the compressive mechanical strength. When it is placed at the bottom of an animal cage, the piezo transducer can detect body movements by the pressure signals[135]. Mice were placed in a customized cage (piezo sleep cage) with piezo bed located on the bottom of the cage (Signal Solutions, LLC), and the pressure signals were recorded by PiezoSleep2 (Signal Solutions, LLC) for four days, from light-on time to the light-on time after 4 days (ZT0 to ZT0 on the fifth day).

The piezo pressure signals were then analyzed by software SleepStats Data Explorer (v2.181, Signal Solutions, LLC) based on signal amplitude, quasi-periodicities, and regularity/consistency of the signal amplitudes. Relatively low amplitudes imply smaller/weaker movements typical for sleep, and small amplitude with signal regularity (quasi-periodic signal with consistent amplitudes) implies regular breathing with no conscious activity. This pattern is critical for distinguishing sleep from quiet wake or rest. These signal features form a model for sleep-like and wake-like behavior which referred to the decision statistics. Afterwards, a histogram of the decision statistics was

made to show the distribution of sleep-like and wake-like decision statistics. The histogram is typically bimodal and assumes the decision statistics are clustering around two dominant behaviors. Based on the bimodal histogram, the threshold was calculated and typically falls in the saddle point between the two modes. The sleep and wake states were decided based on the value of decision statistics and the threshold. If the decision statistics is higher than the threshold, it is classified as sleep state. If the decision statistics is lower than the threshold, it is classified as wake state (User manual of SleepStats Data Explorer, Signal Solutions, LLC. 2020).
Subsequently, SleepStats Data Explorer can compute and export the sleep percent time, sleep mean bout duration, and the breathing rate in sleep based on the given duration of time for further analysis.

EEG and EMG recording and vigilance states analysis

For EEG (Electroencephalography) and EMG (Electromyography) recording, mice were implanted with wireless telemeter (HD-X02, Data Sciences Inc) in abdominal cavity (intraperitoneal placement) connected with two stainless-steel wires (covered with insulation layer) for EEG recording and two stainless-steel wires for EMG recording. The skull was exposed and two holes of 1-2 mm deep were drilled with automatic drill by the following coordinates: 1.0 mm anterior and 1.0 mm lateral to Bregma for the negative lead, and 3.0 mm posterior and 3.0 mm lateral to Bregma on the contralateral side for the positive lead. The installation layer at the terminal end of the two EEG wires/leads was removed and the exposed wires inserted into the skull perforation. The dental acrylic was applied sparingly to the wire entry holes and the surrounding bone to ensure electrical isolation from surrounding tissues. The installation layer at the terminal end of the two EMG wires/leads was removed and were slid into the dorsal muscles with the help of 18-gauge needle. The two EMG wires/leads were 1-2 mm apart along the same bundle of muscle fibers. The open head and abdominal incisions were closed with an absorbable suture. Mice were monitored daily and allowed at least two weeks for recovery in their home cage before *in vivo* recording.

In each condition, the EEG and EMG were recorded for 24 hours, from light-on time to the next light-on time (ZT0 to ZT0 on the following day).
The signals recorded by telemeter were transmitted to receiver boards wirelessly, allowing the mice to move freely during the recordings. The signals were then transmitted to the computer by ethernet cables and saved in the computer by using software Ponemah (v5.32, Data Sciences Inc). The mice were also monitored by infrared camera (Axis Communications). The videos were run on Media Recorder (v2.6) and saved automatically by Ponemah.
The EEG and EMG signals were processed automatically by software NeuroScore (v3.3.1, Data Sciences Inc). The EEG signal, EMG signal, delta power (0.5-4 Hz) of EEG, and theta (6-10 Hz) to delta power of EEG were displayed and the vigilance states (WAKE, NREM sleep, and REM sleep) were scored manually into 10s epochs by an experienced expert.

Sleep deprivation and recovery sleep

The Sleep deprivation (SD) methods and durations used in each experiment are summarised in **Table 2.5**.

Chapter	Chapter 3 Sleep deprivation methodology		Chapter 4 Identification of amygdala neurons activated by sleep loss	Chapter 5 Astrocyte–neuron interactions in sleep homeostasis	
Experiments	*in vivo* EEG/EMG and piezo recording	iDISCO+ whole brain mapping	iDISCO+ whole brain mapping	IHC proximity analysis and quantification	*in vivo* chemogenetics and piezo recording
SD method and duration	Manual 4h Manual 6h Treadmill 4h Treadmill 6h	Manual 4h Treadmill 4h	Manual 4h Treadmill 4h	Manual 4h	Manual 4h
Experimental type	*in vivo*	*ex vivo*	*ex vivo*	*ex vivo*	*in vivo*

Table 2.5 Summary of SD methods and durations used in chapter 3-5

The start time of SD was zeitgeber time zero (ZT0), which is the light-on time and the start of the light period. The SD ended at either ZT4 (4 hours SD) or ZT6 (6 hours SD). For manual SD, mice were disturbed by gently tapping the cage, adding novel objects into the cage, and moving/redistributing the bedding materials in the cage when the mice appeared inactive or drowsy to keep the mice awake. The physically handlings were kept to minimum to avoid stress. After the SD, mice were undisturbed in their home cages to have recovery sleep (RS). For treadmill SD, mice were placed on a home-made treadmill with customized perspex holding zones (3 spaced 8cm apart) to separate mice. The speed for the treadmill was 3 cm per second, permitting the mouse to travel from one side of the holding space to the other if not walking which prevented a sleep period greater than 50% of an epoch[204]. After the SD, mice were moved back to their home cages to have undisturbed RS.

In the *in vivo* studies, mice continued the piezo (and EEG/EMG) recordings after SD. In the *ex vivo* studies, mice were sacrificed and transcardially perfused immediately after SD or RS.

Tamoxifen injection

Tamoxifen (Sigma-Aldrich, T5648) was administered to mice by i.p. injection to activate CreER^{T2}. The injection dose was 100mg/kg and dissolved in corn oil (Sigma-Aldrich) with concentration 15mg/ml.

AAV transgene plasmid and stereotaxic injection

The AAV transgene plasmid used in the experiment was pAAV-GFAP-hM3D(Gq)-mCherry purchased from Addgene (Plasmid #50478).

A robot stereotaxic instrument and system (StereoDrive, Neurostar) were used for surgery, which allowed smart bregma finding, robotic drilling, and robotic injection. The skull was exposed and holes were drilled by robotic drill, then a glass capillary nanoinjector was used for AAV viral delivery with

injection rate 10nL/min. The injection coordinates (bilateral) were AP: 0.02-0.1 mm, ML: ± 0.6-0.8 mm, DV: 1.5 mm relative to bregma. 100nl of virus was injected to each hemisphere targeting L5/6 anterior cingulate cortex. The open head was closed with an absorbable suture. Mice were monitored daily and allowed at least 7 days for recovery and virus incubation in their home cage before *in vivo* recording.

Chemogenetic activation

For chemogenetic activation of astrocytes, mice were split into random groups that received either clozapine-N-oxide (CNO, Enzo Life Sciences, BML-NS105) with injection dose 3mg/kg or saline (NaCl, B. Braun) by i.p. injection in the same volume for an unambiguous comparison. CNO was dissolved in saline with concentration 0.3mg/ml. Both CNO and saline were injected at ZT4.

Transcardial perfusion

Mice were placed in a CO_2 cage filled by CO_2 for 5 minutes. Once the mice lost the paw reflexes, they were transcardially perfused.
The thoracic cavity were opened by thoracotomy, and the heart was exposed after cleaning out the fat tissues. A butterfly needle connected with 20 mL syringe was inserted into the left ventricle. Afterwards, a small incision on the top side of the right atrium was made by micro spring scissor. 20-40 mL of 0.01M PBS (Sigma-Aldrich) was then perfused throughout the whole body with a flow rate around 3.5 mL per minute until the liver looked clear (yellow-grey). Then 20-40 mL of 4% paraformaldehyde (PFA, w/v, diluted in PB, Sigma-Aldrich) was perfused throughout the whole body until the mice were fixed. The brain was dissected and kept in 4% PFA at 4 °C overnight. The brains were then transferred to PBS with azide solution (0.2% azide in PBS, w/v) until the following step (tissue clearing).

iDISCO+ (Tissue clearing)

The iDISCO+ protocol used in the study was slightly modified from the original protocol[136]. The protocol includes three parts: pretreatment, immunolabeling, and clearing.

Pretreatment: Brains were washed in PBS (Sigma-Aldrich) with shaking: RT 30min x 3 times. Then dehydrated with methanol (AppliChem) /H_2O series: 20%, 40%, 60%, 80%, 100%; 1h each. Then washed with 100% methanol for 1h and then chilled the sample at 4°C. Afterwards, overnight incubation with shaking, in 66% DCM (Sigma-Aldrich) /33% Methanol at RT. The next day, brains were washed twice in 100% Methanol at RT, then chilled the sample at 4°C. Then bleached in chilled 5%H_2O_2 (Merck Millipore) in methanol overnight at 4°C. The next day, brains were rehydrated with methanol /H_2O series: 80%, 60%, 40%, 20%, PBS; 1h each at RT. Then washed in PTx.2 1h for two times at RT.

Immunolabeling: Brains were incubated in Permeabilization Solution, 37°C for 3-4 days. Then Incubated in Blocking Solution, 37°C for 3-4 days. Afterwards, brains were incubated with primary antibody in PTwH with 5%DMSO (Sigma-Aldrich) and 3% Goat Serum (Life Technologies), 37°C for 7 days. Followed

by washing in PTwH for 4-5 times until the next day. Then brains were incubated with secondary antibody in PTwH with 3% Goat Serum, 37°C for 7 days. Followed by washing in PTwH for 4-5 times until the next day.

Clearing: Brains were dehydrated in methanol /H_2O series: 20%, 40%, 60%, 80%, 100%, 1hr each at RT. Then changed to fresh 100% methanol and left it overnight at RT. The next day, brains were incubated with shaking in 66% DCM /33% Methanol for 3 hours at RT. Then washed the brains in 100% DCM 15 minutes twice with shaking. For the final step, brains were incubated in DiBenzyl Ether (Sigma-Aldrich) for 4-5 days before the imaging.
All steps were performed in small brain jars with solutions around 7-8mL.

List of buffers and antibodies:
PTx.2 (1L): 100mL PBS 10X + 2mL TritonX-100 (Cayman Chemical Company), then filled to 1L with MilliQ H_2O
PTwH (1L): 100mL PBS 10X + 2mL Tween-20 (Sigma-Aldrich) + 0.01g Heparin (Sigma-Aldrich), then filled to 1L with MilliQ H_2O
Permeabilization Solution (500mL): 400mL PTx.2 + 11.5g Glycine (ChemCruz™) + 100mL of DMSO
Blocking Solution (50mL): 42mL PTx.2 + 3mL Goat Serum + 5mL of DMSO
Primary antibody: Rabbit anti-cFos polyclonal purified antibody (1:2k, Synaptic Systems, 226 003)
Secondary antibody: Goat anti-Rabbit IgG (H+L) Highly Cross-Adsorbed Secondary Antibody, Alexa Fluor™ Plus 647 (1:500, Invitrogen, AB_2633282)

Light sheet fluorescence microscopy imaging

The cleared samples from iDISCO+ were imaged by light sheet fluorescence microscope through the horizontal plane. The microscope used in the study is Olympus MVX10 with objective lenses MV PLAPO 2XC (Olympus) at Research Unit Analytical Pathology, Helmholtz Zentrum München. The ventral side of the brains were mounted on the holder by few spikes, then the holder with brain was placed in the imaging chamber filled with DiBenzyl Ether. The magnification was 0.63X in order to image the whole brain. The laser power (NKT Photonics) was 95% and the sheet numerical aperture (NA) was 0.103. For autofluorescence signal, laser sheets with wavelength 520±40 nm were used for excitation, and 584±40 nm wavelength filter was used to acquire the emission light. For c-Fos signal, laser sheets with wavelength 640±30 nm were used for excitation, and 690±50 nm wavelength filter was used to acquire the emission light. The resolution for one horizontal 2D image is 2048*2048 pixels (4.79µm*4.79µm per pixel) and 16-bit grayscale. The imaging z-step was 7 µm in chapter 3 and 4, and was 10 µm in chapter 6. The laser sheets started at the top of the brain to make the first horizontal 2D image, then the sample holder moved up 7 µm every time to make the next horizontal 2D image until the whole brain was imaged. The microscope was linked to a computer and the imaging was operated under ImSpector Pro[64] (LaVision BioTec). The images from the right and the left laser sheets were combined based on embedded algorithm on ImSpector Pro[64] (contrast mode). It generated 600-1000 horizontal 2D images (900-1000 in chapter 3 and 4, 600-700 in chapter 6) for one channel from one brain. The images were stored in a computer for further analysis.

Microtome sectioning

The fixed brains were transferred to sucrose solution for few days before the microtome sectioning. Afterwards, brains were mounted onto a sliding microtome (Leica Biosystems, SM 2010 R) and frozen with dry ice. 30-µm-thick coronal sections were sliced and kept in cryoprotectant solution (50% 0.1M PBS, 20% Glycerol, 30% Ethylene glycol, Sigma-Aldrich) at -20°C until immunohistochemistry.

Parcellation

Parcellation is a manual quantification method for immunohistochemistry images based on the brain regions from brain atlas. First, sections were incubated in peroxidase (0.3% H_2O_2 in PBS, Merck Millipore) for quenching for 30 minutes. Then the sections were washed in 0.01M PBS three times, each for 5 minutes. Sections were then incubated in blocking buffer (3% donkey serum in PBx) for 30 minutes, followed by washing in 0.01M PBS three times, each for 5 minutes. Afterwards, sections were incubated with primary antibodies in blocking buffer overnight. On the next day, sections were washed in 0.01M PBS three times, each for 5 minutes. Then sections were incubated with secondary antibodies in blocking buffer for one hour. Subsequently, the secondary antibody was washed off with 0.01M PBS three times, each for 5 minutes. Then sections were incubated with ABC-HRP kit (VECTASTAIN, PK-6100) in blocking buffer for one hour, followed by washing in 0.01M PBS three times, each for 5 minutes. All steps above were performed on an orbital shaker (IKA Labortechnik MTS 4) at room temperature (RT). Afterwards, sections were incubated with DAB substrate kit (Vector Laboratories, SK-4100) in MilliQ H_2O for 10-20 minutes. Then DAB substrate was washed off with MilliQ H_2O three times with shaking, each for 5 minutes. Sections were transferred to PBS until mounting. Primary antibody: Rabbit anti-cFos polyclonal antibody (1:2k, Proteintech, 26192-1-AP). Secondary antibody: Biotin-SP-conjugated AffiniPure Donkey Anti-Rabbit IgG (1:1k, Jackson ImmunoResearch Laboratories, 711-065-152).

Sections were then mounted on microscope slides (25*75*1.0 mm, Thermo Scientific), followed by Nissl staining. Sections were submerged in Kresylviolett for 10-15 minutes, then submerged in aqua dest. Sections were then submerged in 70% Ethanol two times, each for 2 minutes. Afterwards, sections were submerged in 96% Ethanol (with acetic acid) for 15-30 seconds to reduce intensity. Subsequently, sections were submerged in 96% Ethanol two times, each for 1 minute. Followed by submerged in 100% Ethanol two times, each for 2 minutes. Then sections were submerged in Xylol two times, each for 3 minutes. Afterwards, covered the slides immediately in DPX by cover slips (24*60 mm, Hirschmann). The slides were put in fume hood for 1-2 days before imaged by microscope under brightfield.

After the imaging, the regions of interest (ROIs) were first parcellated (drawing the boundary of brain regions on the images based on Allen Brain Reference Atlas). Afterwards, manually counted the DAB positive cells in ROIs, then transferred the results to Allen Brain Reference Atlas (ARA) template and added up the cell numbers in the same region.

Immunohistochemistry

For the proximity analysis (of cortical nNOS neurons and astrocytes) and quantification in chapter 5, sections were washed in 0.01M PBS three times, each for 5 minutes. Sections were then incubated with primary antibodies in PBx (0.1% Triton™ X-100 (Sigma-Aldrich) in PBS) overnight. On the next day, sections were washed in 0.01M PBS three times, each for 5 minutes. Then sections were incubated with secondary antibodies in PBx for one hour. Subsequently, the secondary antibody was washed off with 0.01M PBS three times, each for 5 minutes. All steps were performed on an orbital shaker (IKA Labortechnik MTS 4) at room temperature (RT). Primary antibodies: Goat anti-nNOS (1:500, Abcam, #GR3309597-1) and Chicken anti-RFP (1:1k, Rockland, #30830). Secondary antibodies: Donkey anti-Goat IgG (H&L) - Alexa Fluor™ 488 (1:1k, Invitrogen, #1463163) and Donkey anti-Chicken IgG (H&L) - Alexa Fluor™ 594 (1:1k, Invitrogen, #139055).

Sections were then mounted on microscope slides (25*75*1.0 mm, Thermo Scientific) with mounting medium (VECTASHIELD® Antifade Mounting Medium with DAPI, H-1200), and covered by cover slips (24*60 mm, Hirschmann) before imaging.

Microscope slide scanner imaging

Microscope slide scanner is a high-performance and fast automated scanning microscope that allows scanning up to 100 slides in a single run. It can operate in fluorescence, brightfield and polarization modes.
The microscope slide scanner used in the study was Axioscan 7 (ZEISS) from Research Unit Analytical Pathology, Helmholtz Zentrum München. The imaging was operated in fluorescence mode with filters for GFP, RFP, and DAPI excitation and emission.

ClearMap

ClearMap is a Python-based automatic analytical tool for cleared mouse's brain developed by Renier N. in 2016[136]. It is a published free source and available online. The code was slightly adjusted and run in Linux system. The brain atlas (for reference) used in the study was developed by Perens J. in 2020[137]. All the settings on ClearMap remained unchanged except for the thresholds. The size threshold was set 5-1000, and the intensity threshold varied based on the averaged intensity of the whole brain and adjustment after subjective evaluation on the results of cell check. The details of deciding brain atlas and intensity threshold were described in Result in chapter 3 Sleep deprivation methodology.

ImageJ

ImageJ (National Institutes of Health, USA, v1.53f51) was used for whole brain intensity calculation, cell check, orthogonal transformation, and image evaluation.

Python

Python (Python Software Foundation, v3.7) was used for exporting the grey value/intensity of the pixels from brain samples and the three brain atlases for

the mapping comparison. The Pearson correlation coefficient and linear regression in this part were computed in Python.

IHC quantification and analysis

For the proximity analysis between astrocytes and nNOS neurons, 3-4 nNOS neurons in cingulate cortex were selected from each mouse without any overlap. Then three concentric circles with diameter 300μm, 600μm, and 900μm, respectively, were placed on the nNOS neurons (with center of circle). The astrocytes in the upper half of the three circles were counted manually by experienced personnel. All steps were done on ZEN 3.1 (blue edition, ZEISS).

For the quantification of astrocytes in sleep homeostasis in cortex, several patches were extracted in cingulate/motor cortex by the algorithm. Then three patches from each mice, without overlapping each other, were selected manually. These patches then went through automatic cell counting algorithm and the astrocytes were counted automatically. The algorithms were based on a publication in 2018[139], where they extracted patches and detected c-Fos positive cells automatically. The algorithms were modified and tested by Mikołaj Miękus in order to detect astrocytes more accurately. Algorithms were run on Python, ImageJ, and MATLAB.

Wheel-running

Mice were given access to a running wheel in the homecage to run voluntarily for three weeks. The running-wheel activity was recorded during the entire period. Mice were kept at room temperature (23°C) with a 12:12 hours light/dark cycle in the room. Wood shavings and paper tissue were provided as bedding material. Each mouse was placed individually in the cage with free access to food and water.

Indirect calorimetry

The determination of energy expenditure was based on indirect calorimetry[141]. High precision CO_2 and O_2 sensors measure the difference in CO_2 and O_2 concentrations in air flowing through control and animal cages. The rate of oxygen consumption taking into account the air flow through the cages that is measured in parallel. Data for oxygen consumption were expressed as ml $O_2*h^{-1}*animal^{-1}$. The system also monitors CO_2 production, therefore, the respiratory exchange ratio (RER) can be calculated (VCO_2/VO_2). The test was performed at room temperature (23°C) with a 12:12 hours light/dark cycle in the room. Wood shavings and paper tissue were provided as bedding material. Each mouse was placed individually in the chamber for a period of 21 hours, from ZT7 to ZT28 (ZT4 on the next day) with free access to food and water. Metabolic cuvettes were set up in a ventilated climate room continuously supplied with fresh air from outside. Distance traveled was also measured by the system per time interval.

Open field

The Open Field test was carried out according to the standardized phenotyping screens developed by the IMPC partners (http://www.empress.har.mrc.ac.uk). The test apparatus (from ActiMot, TSE) was a square-shaped frame with two pairs of light-beam strips, each pair

consisting of one transmitter strip and one receiver strip. These basic light barrier strips were arranged at right angles to each other in the same plane to determine the X and Y coordinates of the animal, and thus its location (XY frame). Each strip was equipped with 16 infrared sensors with a distance between adjacent sensors of 28 mm.The light barriers were scanned with a frequency of 100 Hz each on fast computer platforms. Whenever an even number of light beams was interrupted, the centre of gravity was calculated to lie between adjacent sensors. The test apparatus where the mouse was placed consisted of a transparent and infrared light permeable acrylic test arena (internal measurements: 45.5 x 45.5 x39.5 cm) with a smooth floor. The illumination levels were set at approximately 150 lux in the corners and 200 lux in the middle of the test arena.

At the beginning of the experiment, all animals were transported to the test room and left undisturbed for at least 30 minutes before the testing started. Then each animal was placed individually into the middle of one side of the arena facing the wall and allowed to explore it freely for 20 min. The distance traveled was recorded during the test, and percentage time spent in the centre was calculated. After each trial, the test arena was cleaned carefully with a disinfectant.

Hot plate

Mice were placed on a metal surface maintained at 52 ± 0.2°C (TSE GMBH, Germany)[142]. Locomotion of the mouse on the hot plate was constrained by 20 cm high Plexiglas wall to a circular area with a diameter of 28 cm. Mice remained on the plate until they performed one of three behaviors regarded as indicative of nociception: hind paw lick (licking), hind paw shake/flutter (shaking) or jumping. Only hind paw, and not front paw responses were evaluated, since fore paw licking and lifting are components of normal grooming behavior. The latency was recorded to the nearest 0.1s. To avoid tissue injury 30s cut-off time was used.

Rotarod

The rotarod (Bioseb, Chaville, France) was used to measure forelimb and hindlimb motor coordination, balance and motor learning ability[143]. The machine was set up in an environment with minimal stimuli such as noise and movement. The rotarod device was equipped with a computer controlled motor-driven rotating rod. The unit consists of a rotating spindle and five individual lanes for each mouse. Magnetic sensors were used to detect when a mouse falls from the rotarod. In general, the mouse was placed perpendicular to the axis of rotation, with the head facing the direction of the rotation. All mice were placed on the rotarod at an accelerating speed from 4 to 40 rpm for 300 sec with 15 min between each trial. In motor coordination testing, mice were given three trials at the accelerating speed at one day. The reason for the trial end (falling, jumping or rotating passively) was recorded and used in subsequent analysis.

3. Statistics

Summary of statistics used in different chapters and experiments

The statistics used in each experiment were summarised in **Table 2.6** and **Table 2.7**.

Chapter	Chapter 3 Sleep deprivation methodology		Chapter 4 Identification of amygdala neurons activated by sleep loss	Chapter 5 Astrocyte–neuron interactions in sleep homeostasis	
Experiments	*in vivo* EEG/EMG and piezo recording	iDISCO+ whole brain mapping	iDISCO+ whole brain mapping	IHC proximity analysis and quantification	*in vivo* chemogenetics and piezo recording
Paired Student's t-test	Y				
Two-way ANOVA	Y				
Pearson correlation coefficient	Y	Y	Y		
Linear regression	Y	Y	Y		
Student's t-test with multiple correction (FDR)		Y	Y		
cocor (A comprehensive solution for the statistical comparison of correlations)[138]		Y	Y		
PCA			Y		
Student's t-test			Y	Y	
Wilcoxon signed-rank test					Y

Table 2.6 Summary of statistics used in chapter 3-5

Chapter	Chapter 6 Phenotypic assessment and neural activity mapping of *MEIS1* point mutation mice		
Study	A	B	
Experiments	Open field, indirect calorimetry, rotarod, hot plate test, wheel-running, *in vivo* piezo recording	The second *in vivo* piezo and EEG/EMG recordings	iDISCO+ whole brain mapping
Student's t-test	Y	Y	
Wilcoxon rank sum test	Y	Y	
Pearson correlation coefficient	Y		Y
Linear regression	Y		Y
PCA	Y		
Two-way ANOVA with multiple correction (FDR)			Y
cocor (A comprehensive solution for the statistical comparison of correlations)[138]			Y

Table 2.7 Summary of statistics used in chapter 6

Details of statistics used in each experiment and test

In the *in vivo* EEG/EMG and piezo recording in chapter 3, the sleep percent time between baseline and sleep deprivation period was tested by paired Student's t-test after confirming equal population distribution. The sleep percent time in 4 SD conditions was tested by Two-way ANOVA with SD time and SD duration after confirming equal population distribution. The Pearson correlation coefficient and linear regression was computed on R. In the iDISCO+ whole brain mapping study, the number of c-Fos positive cells was tested by Student's t-test with multiple testing correction by False Discovery Rate (FDR) after confirming equal population distribution. The Pearson correlation coefficient between two regions was tested by cocor (A Comprehensive Solution for the Statistical Comparison of Correlations, 2015)[138].

In the iDISCO+ whole brain mapping study in chapter 4, The number of c-Fos positive cells was tested by Student's t-test with multiple testing correction by False Discovery Rate (FDR) after confirming equal population distribution. The Pearson correlation coefficient between two regions was tested by cocor[138]. The linear regression and PCA were computed on R. The mean neuronal activity heatmaps and voxel p-value heatmaps were produced by ClearMap. For the p values in the voxel p-value heatmaps, Student's t-test was run based on the intensity (grey value) of each voxel.

In the IHC proximity analysis and quantification study in chapter 5, the number of astrocytes between different groups was tested by Student's t-test after confirming equal population distribution. In the *in vivo* chemogenetics and piezo recording study, the sleep percent time and sleep mean bout duration in different conditions was tested by Wilcoxon signed-rank test due to unequal

population distribution.

In chapter 6, the distance traveled (open field), wheel-running, indirect calorimetry, and hot plate test, genotype effects were examined by Student's t-test after confirming equal population distribution. In rotarod and piezo recording, genotype effects were examined by Wilcoxon rank sum test (Mann Whitney U test) due to unequal population distribution. The Pearson correlation coefficient, regression, and PCA for phenotypic assessment were computed on R. PCA was performed based on 6 phenotypic results: hot plate reaction time, distance traveled, falling proportion from the rotarod, time spent in center, RER (VCO_2/O_2) in light period, and RER (VCO_2/O_2) in dark period. In the second *in vivo* piezo and EEG/EMG recordings, the sleep percent time between $Meis1^{R272H/R272H}$ mice and wildtype mice was tested by Student's t-test after confirming equal population distribution, and the breathing rate in sleep was tested by Wilcoxon rank sum test (Mann Whitney U test) due to unequal population distribution. In the iDISCO+ whole brain mapping study, the number of c-Fos positive cells was tested by Two-way ANOVA with multiple testing correction by False Discovery Rate (FDR) after confirming equal population distribution. The Pearson correlation coefficient between two regions was tested by cocor[138]. The linear regression was computed on R.

All statistical tests were run on R (R Foundation for Statistical Computing, v4.1.1) with statistical significance set to $p < 0.05$.

Chapter 3
Sleep deprivation methodology

Introduction

Sleep is important for our life. A lot of sleep studies were done to find out mechanisms of sleep or solutions for sleep disorders. Electroencephalogram (EEG) with Electromyography (EMG) are generally used to record the physiological signals of mice, it is considered the gold standard of deciding that sleep states (Wake, NREM sleep, and REM sleep). However, EEG/EMG requires invasive surgery to put the electrodes on the skull or muscle. If the device is a wireless system, the telemeter needs to be placed in the abdominal area which is a huge ratio of the body size and could cause more burden to the animal[144]. Piezo sleep screen (piezo) is used as an alternative to record sleep when EEG/EMG is not preferred. Piezo can transform mechanical pressure into electrical signals, and acquire the activity pattern of mice. The activity pattern can then be analyzed and used to distinguish sleep from wakefulness in mice based on the amplitude and regularity of the signal[145]. One previous study showed that piezo can be a reliable alternative to EEG/EMG recording. They observed a strong positive correlation between the amounts of sleep obtained with the two recording techniques, even though piezo tends to overestimate the sleep time, especially in the light period.[135] Here we wanted to also compare the sleep results between two recording techniques to make sure that our piezo system is similar to what they have observed and can be a reliable alternative to EEG/EEM recording.

Sleep deprivation is a commonly used technique to increase animal's sleep drive in order to study sleep homeostasis. Different methods and durations were used for the studies. Manual disturbance (gentle handling by experienced staffs), treadmill, orbital shaker, rotating drum, and (multiple) platform over water were all used for sleep deprivation[146,147]. Manual disturbance was commonly used in sleep studies. However, it requires experienced staffs to gently handle the cages during the whole experiment time, and it can be labor and time consuming. Hence, a more automatic alternative could be helpful for large-scale study. Here we set up the treadmill and aim to use it as one of our sleep deprivation methods. A comparison will be needed to show the efficiency of treadmill sleep deprivation.
Another difference when doing sleep deprivation is the duration. Some people did 4 hours, and some people did 6 hours sleep deprivation for rodent studies[148,149]. Most of our sleep studies were done in 4 hours sleep deprivation. Therefore, we also wanted to compare the efficiency of 4 hours and 6 hours sleep deprivation.

Apart from the sleep pattern that might be different while using different sleep deprivation methods, the brain activity might also be different. Hence, we wanted to examine if the two different sleep deprivation methods (manual and treadmill) will change the activity of brain regions. Traditionally, tissue sectioning and imaging have been the standard procedure for investigating tissues for several decades. However, it is time-consuming and labor-intensive to do a whole organ investigation. Tissue clearing is a technique that

enables whole brain imaging by using chemical process that aims to match refractive indices throughout intact tissue[150,151]. The tissue becomes nearly transparent afterwards and allows deep-tissue fluorescent microscopy imaging[152]. In the study, I used iDISCO+ (immunolabeling-enabled three-dimensional imaging of solvent-cleared organs plus), a method of tissue clearing, combined with light sheet fluorescent microscopy to acquire the whole brain image with immunolabeling of c-Fos positive neurons[136].

c-Fos is a protein with 380 amino acids, and it is involved in cellular functions such as cell proliferation, differentiation, and changes of gene expression[153]. It is generally rapidly induced and can be detected 15 minutes after the stimulation[154]. It is also generally one of the first proteins that are expressed in cellular functions. Hence, its gene, *c-fos*, is also known as immediate early gene. c-Fos is an indirect marker of neuronal activity because it is often expressed during action potential[155]. In immunohistochemistry, c-Fos has been widely used as the marker of neuronal activity[155]. In the study, I also use c-Fos to indicate the neuronal activity throughout the whole brain.

Whole brain analysis of histological tissues has always been challenging. Even though we got the whole brain image by using tissue clearing, it would still be very time-consuming and labor-intensive to manually count the c-Fos positive neurons and annotate them to brain regions. Hence, I used ClearMap to perform automatic cell detection and annotation. ClearMap is a Python-based free pipeline that is specifically developed to perform c-Fos positive cells detection after tissue clearing, and it is also able to annotate the cell counts to brain regions[136]. Therefore, I used ClearMap to automatically count the c-Fos positive cells (active neurons) and annotate them to different brain regions.

Aims and objectives

We aimed to examine the accuracy of piezo sleep recording (compared to EEG/EMG), as well as the efficiency of sleep deprivation when using different methods (manual and treadmill) and duration (4 hours and 6 hours). We also wanted to examine the brain activity while using different sleep deprivation methods (manual and treadmill). The detailed aims included:

- Record sleep by using both EEG/EMG and piezo system, and compare the results of the sleep states (wakefulness and sleep).
- Record sleep and perform sleep deprivation by using different methods (manual and treadmill) and durations (4 hours and 6 hours). Then compare the efficiency of sleep deprivation.
- Use tissue clearing (iDISCO+) to do whole brain imaging, then use ClearMap to detect active neurons and annotate them to different brain regions. Afterwards, observe the differences between manual and treadmill sleep deprivation (SD) groups, as well as manual and treadmill recovery sleep (RS) groups.

Results

Comparison of sleep states between piezo and EEG/EMG sleep recordings

The first comparison we wanted to do was the sleep states from piezo and EEG/EMG recordings. In order to compare the two recordings, mice were recorded by piezo and EEG/EMG for 24 hours at the same time without disturbance or intervention (**Fig. 3.1**).

The sleep states from EEG were determined by experienced sleep expert based on the signal patterns of EEG and EMG. 10 seconds time bin was used for our study to decide sleep states which means the temporal resolution was 10 seconds. Piezo recording was analyzed by software SleepStats Data Explorer (from Signal Solutions, LLC. 2020). The software has algorithms that can determine the sleep states based on signal amplitude, quasi-periodicities, and regularity/consistency of the signal amplitudes. The sleep states from EEG included wake, NREM sleep, and REM sleep. However, the sleep states from piezo and SleepStats Data Explorer only had sleep and wake. The algorithm for distinguishing NREM and REM sleep based on piezo recording was not available during the analysis time. Since we wanted to compare the results between piezo and EEG/EMG recordings, we needed to make the data format identical. First, the data time bin (temporal resolution) needed to be the same. Since the temporal resolution from EEG/EMG was 10 seconds, I adjusted the piezo data and made the temporal resolution also 10 seconds. Second, the sleep states needed to be the same. Our piezo data did not show difference between NREM and REM sleep. Therefore, for the EEG/EMG data, we combined NREM and REM sleep, and made the states only sleep and wake. Then both data were ready for comparison.

First, I did a heatmap to visualize the comparison result (**Fig. 3.2**). Yellow means wake and purple means sleep. X-axis is time. On the Y-axis, each row represents a mouse, and within a row, the upper panel is the sleep recording from piezo, the bottom panel is from EEG/EMG. The heatmaps between piezo and EEG recordings show high similarity, even though some differences can be seen. The accuracy of piezo sleep recording is 89.29 ± 0.68% (compared to the gold standard: EEG/EMG). This is very similar to the published data (90.0 ± 0.9%)[135].

After checking the accuracy based on 10 seconds temporal resolution, we wanted to see if the trend remained the same in 1 hour temporal resolution, and in the entire light period (12 hours temporal resolution). Therefore, the 10 seconds time bins were collapsed to 1 hour time bins (**Fig. 3.3 A**) to show the hourly wake percent time, as well as to 12 hours time bins to show the wake percent time in light period (**Fig. 3.3 B**). There is no significant difference at both hourly wake percent time and the wake percent time in light period (43.26 ± 7.48% from EEG and 42.35 ±1.60% from piezo). However, we did notice that the EEG recording has slightly lower wake percent time in both hourly wake percent time and the wake percent time in light period. This is similar to the previous study, which suggested piezo recording tended to overestimate the sleep time[135].

In order to evaluate the correlation between piezo and EEG/EMG recordings, the Pearson correlation coefficient based on hourly wake percent time was calculated and the linear regression was plotted (**Fig. 3.3 C**). The result showed that there is a strong positive correlation between the amounts of hourly wake percent time with the two recording methods. The Pearson correlation coefficient is 0.97 with p-value < 0.0001 in light period. This result is also similar to the previously published study[135].

Additionally, we wanted to check if the piezo recording can reflect accurate sleep time during the SD intervention period. Hence, we compared the sleep percent time during 4 hours manual sleep deprivation and 6 hours manual sleep deprivation (**Fig. 3.3 D**). The sleep percent time was 3.22 ± 0.37% during 4 hours manual SD, and 4.70 ± 0.98% during 6 hours manual SD. Both are under 5% and show significant difference (p-value < 0.0001) compared to baseline (58.60 ± 3.04% for 4 hours and 60.30 ± 2.35% for 6 hours), which suggests that the piezo recording can reflect the sleep time during SD intervention.

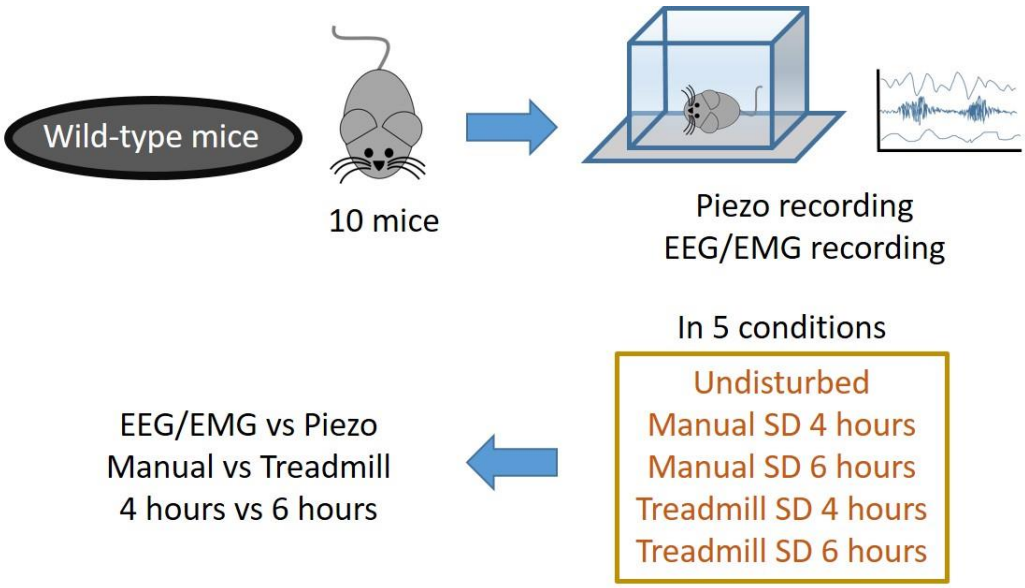

Figure 3.1 Experimental design for the comparison of different sleep recording methods. The flowchart of experiment for the comparison of different sleep recording methods and the SD efficiency based on different SD methods.

Figure 3.2 Heatmaps of the comparison between EEG/EMG and piezo recordings. The heatmaps of the sleep/wake states based on 12 hours recording from EEG/EMG and piezo. The accuracies are between 86% and 91%. Yellow: wake, purple: Sleep. Upper panel: piezo recording, bottom panel: EEG recording. X-axis: ZT hour. Data were from 7 mice.

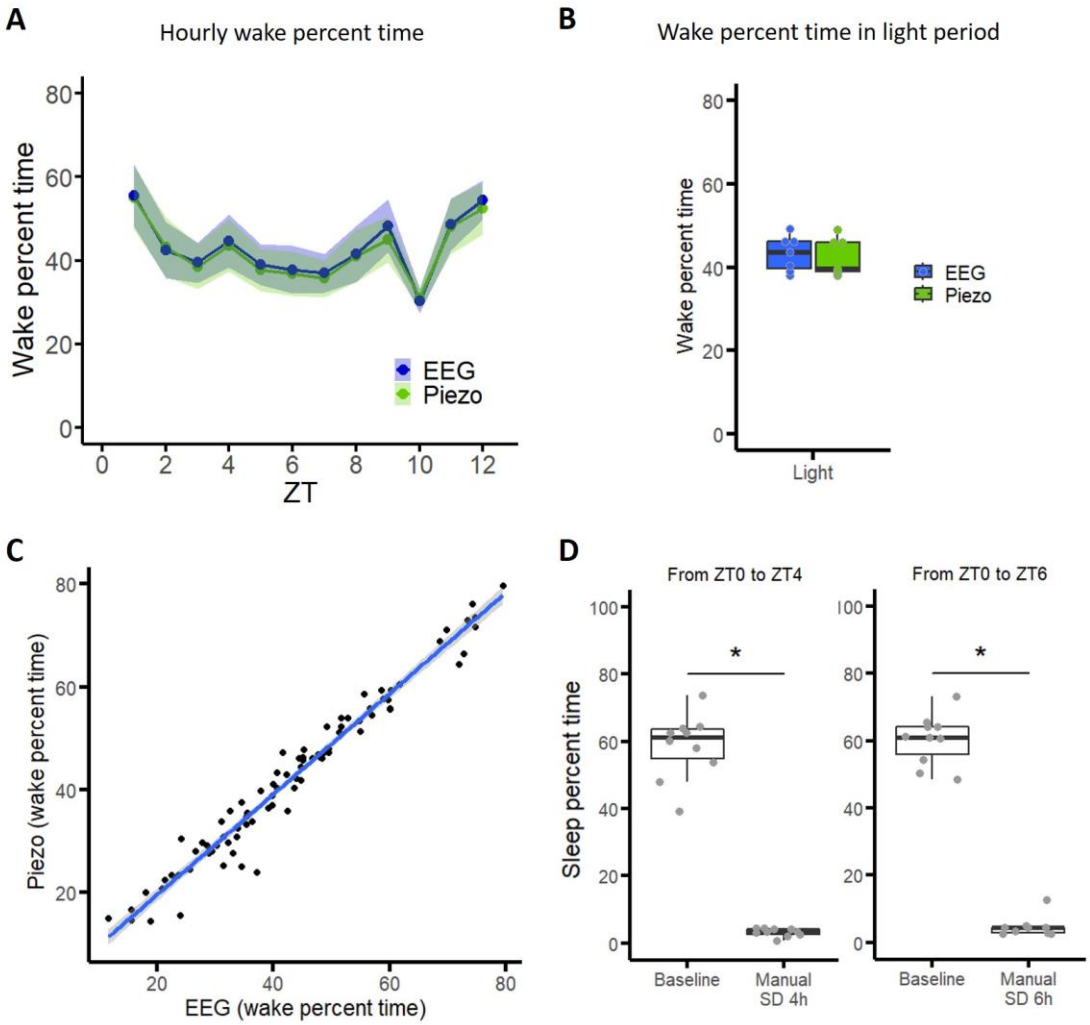

Figure 3.3 Comparison of wake/sleep percent time between EEG/EMG and piezo recordings. (A) The hourly wake percent time between EEG/EMG and piezo recording. No significant difference between two recordings. Line: Mean ± SEM. Statistics: paired Student's t-test. (B) The wake percent time between EEG/EMG and piezo recording in light period. No significant difference. Statistics: paired Student's t-test. (C) The correlation and linear regression between EEG/EMG and piezo hourly wake percent time. The Pearson correlation coefficient is 0.97 with p-value < 0.0001 in light period. (D) The sleep percent time during manual 4 hours SD and manual 6 hours SD. The sleep percent time in both SD periods are lower than 5%, and have significant difference compared to baseline. *p <0.0001 after paired Student's t-test. n=7-10.

Comparison of SD efficiency by different methods (manual and treadmill) and durations (4 hours and 6 hours)

The second comparison we wanted to do was the SD efficiency between different methods (manual and treadmill) and durations (4 hours and 6 hours). Hence, 4 hours manual sleep deprivation from ZT0 to ZT4, 4 hours treadmill sleep deprivation from ZT0 to ZT4, 6 hours manual sleep deprivation from ZT0 to ZT6, and 6 hours treadmill sleep deprivation from ZT0 to ZT6 were applied separately in different recording days. For each condition, 24 hours EEG/EMG and piezo recordings were made.

There are normally two ways to evaluate the efficiency of SD. The first way is examining the delta power from EEG after SD. Delta power from EEG represents sleep drive, and should increase during the SD period. The second way is examining the sleep time during the recovery period, which is defined as the rest of the day after SD (18-20 hours)[149]. After SD, animals should sleep more in the recovery period. In our result, the sleep percent time (recorded by piezo) in the recovery period after 4 different SD conditions (48.48 ± 3.52% after 4 hours manual SD, 46.02 ± 1.36% after 4 hours treadmill SD, 49.13 ± 2.52% after 6 hours manual SD, 48.16 ± 2.00% after 6 hours treadmill SD) do not show significant difference, suggesting the SD efficiencies between different methods (manual and treadmill) and durations (4 hours and 6 hours) are not significantly different (**Fig. 3.4**).

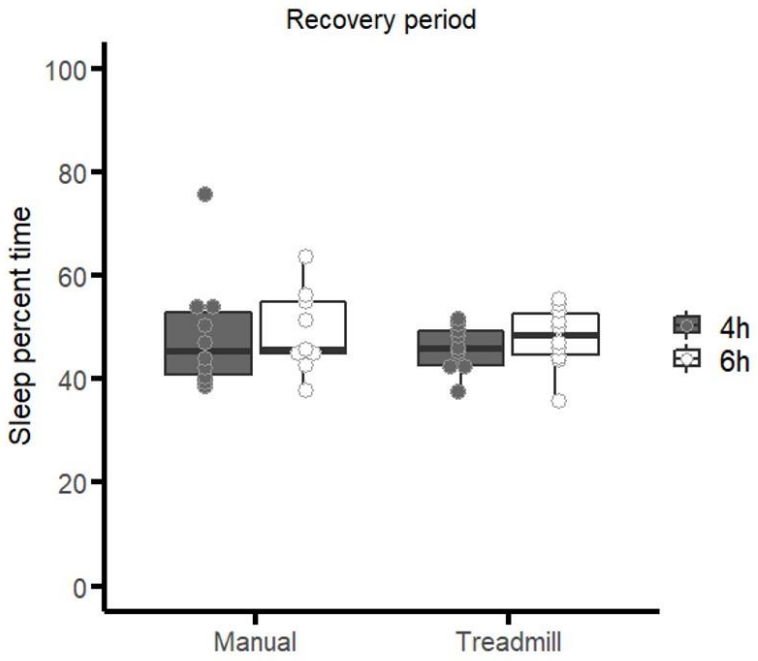

Figure 3.4 Comparison of SD efficiency between different SD methods and durations based on piezo recording. The sleep percent time in the recovery period after 4 different SD: 4 hours manual sleep deprivation, 4 hours treadmill sleep deprivation, 6 hours manual sleep deprivation, and 6 hours treadmill sleep deprivation. There is no significant difference between SD methods and durations. Statistics: Two-way ANOVA. n=9-10.

Calculate and annotate active neurons by ClearMap

In order to evaluate the possible differences of brain activity by using different SD methods, we divided mice into 4 groups. 2 groups of mice went through 4 hours of sleep deprivation (either manual or treadmill) before the brain tissue was taken out at ZT4. Another 2 groups of mice also went through 4 hours sleep deprivation (either manual or treadmill), but followed by 2 hours undisturbed recovery sleep. Then the brain tissue was taken out at ZT6. iDISCO+ was then performed to clear the tissues, as well as immunolabeling c-Fos positive neurons. Afterwards, samples were imaged by light sheet microscopy and ClearMap was run for automatic cell counting and annotation (**Fig. 3.5 A**).

ClearMap is an automatic analytical tool that was developed by Renier N. in 2016. It was designed to detect c-Fos positive neurons specifically based on iDISCO+ cleared at mouse brain. Since we were doing iDISCO+ tissue clearing with c-Fos positive neurons detection, it was the ideal tool for analysis.

However, there were two issues for ClearMap:
First, the parameters for cell detection needed to be set up manually. Even though ClearMap was designed to detect c-Fos positive neurons, the fluorescent signals could vary in different conditions. Possible factors contributing to the differences include biological diversity of different mouse strains, efficiency of tissue clearing, and different antibodies. Therefore, parameters such as the threshold of the intensity (grey value) to define positive objects need to be adjusted accordingly.

At the beginning, the thresholds were determined one by one without any reference number. The steps to determine the thresholds were:

1. Enter the threshold randomly and run ClearMap.
2. Check the cell detection results at 2-3 small regions, and (subjectively) decide if the threshold needs to be adjusted.
3. Adjust the threshold based on experience.
4. Repeat the steps of cell check and threshold adjustment (step 2 and 3), until the results of cell check look reasonable.

However, there were few issues for this method:
First, it showed a strong batch effect. This suggested that the thresholds should be determined and adjusted separately in different batches. Second, the thresholds were not decided in a systematic way, which could lead to strong diversity even in the same batch. Third, the cell check was based on 2-3 small regions which were not objective enough.

I then found out that the average intensities were very different among batches. For example, one batch has the average intensity around 1500-2500, and another batch has the average intensity around 4000-5000. However, the intensity of the samples within the same batch have similar intensity. This is of course not always true, because sometimes there are 1-2 samples in the same batch that show very different intensity, or the intensities

of the samples in the same batch show a bimodal distribution.

Since the average intensity varies among samples, using the same intensity threshold for all samples could cause analytical bias. This difference is even stronger among batches. Hence, I decided to define the intensity threshold by the average intensity of each sample, and adjusted within each batch.

In order to overcome the above issues and determine the threshold more objectively, the criteria were modified as described below:

1. Use the average intensity of each sample as the starting value instead of a random value.
2. Adjust the threshold in a systematic way instead of deciding the adjustment based on experience.
3. Decide the threshold batch by batch instead of sample by sample.
4. The cell check is done in three horizontal slides instead of 2-3 small regions.

The reason for the adjustment 1 and 2 was to reduce the subjectivity when deciding the threshold for each sample. The reason for adjustment 3 was to make the decision at batch level (batch by batch) and reduce the variability among batches. The last but not the least, the reason for adjustment 4 was to make the cell check based on larger areas and increase the objectivity.

The exact optimized steps were (**Fig. 3.5 B**):

1. Check the average of the intensity throughout the whole brain.
2. Use the average intensity at each sample as the threshold and run ClearMap.
3. Check the cell detection results at three horizontal slides, and (subjectively) decide if the threshold needs to be adjusted
4. The thresholds were then adjusted by either adding or subtracting one fourth of the standard deviation of the intensity at each sample.
5. Repeat the steps of cell check and threshold adjustment (step 3 and 4), until the results of cell check look reasonable. This was done batch by batch, so the samples in the same batch will have the same equation to calculate the thresholds.
6. Choose the threshold batch by batch. If the intensity patterns are different in the same batch, decide the threshold differently from these two groups.

After the threshold optimization steps were finalized, ClearMap was run based on the chosen thresholds. Then I wanted to compare the results between the cell counts from ClearMap and cell counts from human (manual counts). However, manually counting the whole brain is very time-consuming, and would be difficult to do it on all samples. Hence, I chose one small region in the cortex, and evaluated the accuracy of ClearMap cell counting in this region. The steps of accuracy evaluation (**Fig. 3.6 A**):

1. Choose a small region in the cortex.
2. Manually count the c-Fos positive cells.
3. Run ClearMap and get the results of automatic cell detection.
4. Compare the results (from step 2 and 3), and calculate the numbers of true positive (TP) cells, false positive (FP) cells, and false negative

(FN) cells.

5. Calculate Precision, Recall, and F1 score based on TP, FP, and FP.

The definition of TP, FP, FN, Recall, Precision, and F1 score was defined in **Fig. 3.6 B**. In general, precision refers to the accuracy of the positive cells detected by the algorithm, so a higher Precision means the positive cells that counted by ClearMap are more likely to be real. On the other hand, Recall indicates how many true positive cells were detected by the algorithm, so a higher Recall means more c-Fos positive cells were counted by ClearMap. F1 score is the harmonic mean of Precision and Recall, and it is widely used as a measure of a test's accuracy. The median of Precision, Recall, and F1 score for our 43 samples are 92%, 66%, and 77%, respectively (**Fig. 3.6 C**).

We have a lower value of Recall, but a higher value of Precision, this is because of the high number of false negative (FN), and low number of false positive (FP) cells. The thresholds for ClearMap were determined in a more conservative way, which means ClearMap only counted the more obvious c-Fos+ cells, and excluded the cells that have weaker c-Fos signal. This resulted in a higher number of false negative (FN) but lower number of false positive (FP) cells. In this way, we are more confident that the c-Fos positive cells counted by ClearMap are real. By doing this assessment, we have a better idea about the accuracy of ClearMap cell detection, and will help us elaborate the results more precisely.

The second issue was the accuracy of annotation. The annotation of ClearMap is based on the brain atlas. The coordinates from the detected sample are projected to the brain atlas and annotate the cell counts to different brain regions. Therefore, using a precise brain atlas as reference is crucial. Originally ClearMap used the brain atlas developed by the Allen's Institute of Brain Science which is a standard brain atlas for histology (Allen Brain Atlas). However, the cleared tissues were imaged by light sheet fluorescence microscopy (LSFM) which had different tissue contrast and morphology compared to the bright field microscopy imaging for standard histology. Therefore, Perens J. developed a brain atlas based on hydrophobic cleared (iDISCO+) and LSFM-imaged brains, and it showed more precise mapping to the hydrophobic cleared brains[137]. In 2021, Young D.M. developed another brain atlas for whole brain mapping. This brain atlas was developed based on hydrophilic cleared (CUBIC) brains, and it showed better mapping to the Hydrophilic cleared brains[156].

Theoretically speaking, the atlas brain developed by Perens J. should be a better atlas brain for our project, since we used hydrophobic tissue clearing (iDISCO+) which was the same reference they used for development. However, in order to confirm that the newly developed atlas brain fits our brains, I ran ClearMap whole brain mapping with all three brain atlases.

I therefore compared the results of mapping visually and mathematically. **Figure 3.7** shows the composite images of the brain atlas and two of our brain samples. The magenta channel represents the brain atlas (either from Allen Brain Atlas, Perens J., or Young D.M.), green channel represents the brain sample.

The first step of the visual check to examine the mapping precision was to look at the outline of morphology. The outline of morphology should match as much as possible between sample and brain atlas.

The brain atlas from Allen Brain Atlas (**Fig. 3.7 A for sample 1 and D for sample 2**) and Perens J. (**Fig. 3.7 B for sample 1 and E for sample 2**) showed good morphology outline matching. On the other hand, brain atlas from Young D.M. (**Fig. 3.7 C for sample 1 and F for sample 2**) showed some misalignment at the lateral side of the brain.
The second step of the visual check to examine the morphology was to look at the color of the sample. According to the theory of color mixing, colocalization of green pixel and magenta pixel leads to white. However, this only happens when both green channel and magenta channel have very strong intensity. In most of the cases, both the green and magenta channels are not that strong. A better way to examine this is comparing the predominance of magenta and green pixels throughout the whole image. More prominent green and magenta pixels suggest higher misalignment. On the contrary, less prominent green and magenta pixels (or even close to white) suggest better misalignment.

In general, brain atlas from Young D.M. (**Fig. 3.7 C and F**) showed more prominent green and magenta pixels suggesting a poorer alignment. The brain atlas from Allen Brain Atlas (**Fig. 3.7 A and D**) and Perens J. (**Fig. 3.7 B and E**) showed less prominent green and magenta pixels suggesting a better alignment. However, if we examine the images closely, brain atlas from Allen Brain Atlas showed stronger green tendency, whereas brain atlas from Perens J. showed stronger white tendency.

Visual check provided us some ideas about how accurate the brain atlas was. However, it was not an objective method, so using another objective (mathematical) way to evaluate the brain atlas would be preferred. Therefore, I ran the Pearson correlation coefficient for the pixels between the sample and three brain atlases. The pixels from the sample and three brain atlases were exported and their intensity (grey value) were recorded, then the Pearson correlation coefficient was calculated based on the comparison between the pixels at the same coordinate from the samples and one of the brain atlases. The brain atlas from Perens J. showed the highest Pearson correlation coefficient (0.9046 for sample 1 and 0.8882 for sample 2). The brain atlas from Allen Brain Atlas showed the second highest Pearson correlation coefficient (0.7525 for sample 1 and 0.8174 for sample 2). The brain atlas from Young D.M.showed the lowest Pearson correlation coefficient (0.5870 for sample 1 and 0.6114 for sample 2) (**Fig. 3.7 M**).The p-value for above Pearson correlation coefficients were all lower than 0.05. This result is similar to what we have seen from the visual check.

In order to have a better look at the distribution of pixels and the correlation between the samples and three brain atlases, the pixels and their linear regression were plotted. The plots between sample and brain atlas from Perens J. showed higher correlated distribution (**Fig. 3.7 H for sample 1 and**

K for sample 2). On the contrary, the plots between samples and brain atlas from Allen Brain Atlas (**Fig. 3.7 G for sample 1 and J for sample 2**), as well as the plots between sample and brain atlas from Young D.M. (**Fig. 3.7 I for sample 1 and L for sample 2**) showed lower correlated distribution.

Hence, based on all above conclusions, I decided to use the brain atlas from Perens J. for our samples to increase the precision of whole brain mapping.

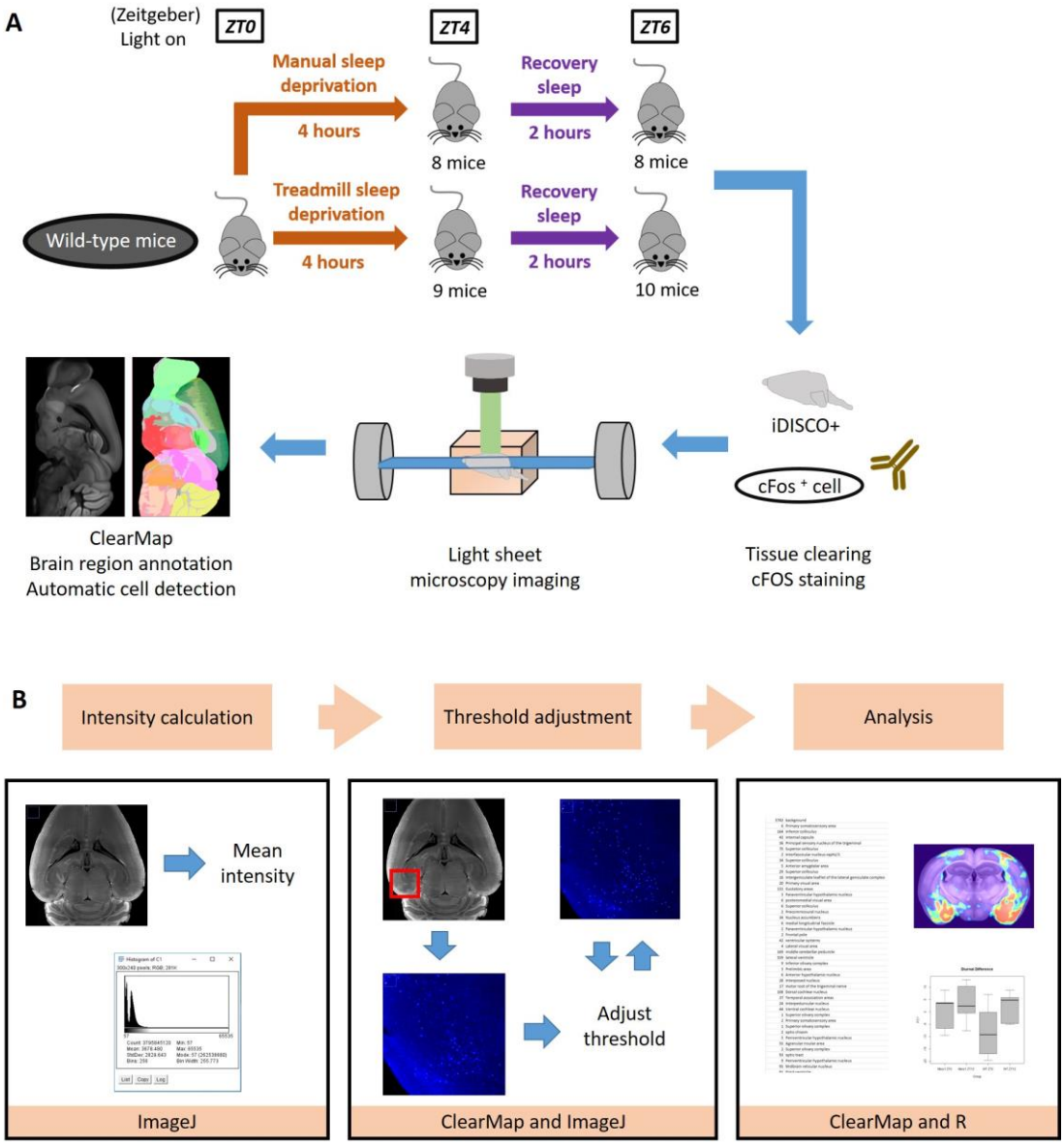

Figure 3.5 Experimental design and analysis steps for the comparison of whole brain activity between manual and treadmill SD/RS. (A) The flowchart of the experiment for the comparison of whole brain activity between manual and treadmill SD/RS. (B) Steps of analysis for whole brain mapping.

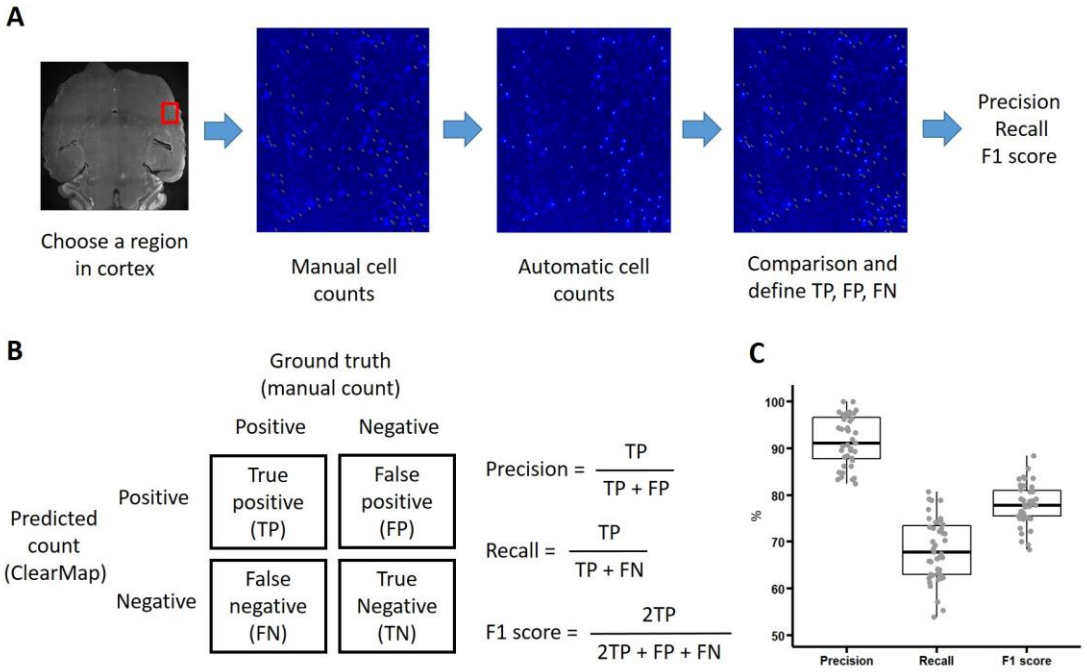

Figure 3.6 Comparison between automatic and manual cell counts. (A) The steps to compare automatic counts and manual counts. (B) The definition of TP, FP, FN, Recall, Precision, and F1 score. (C) The median of Precision, Recall, and F1 score are 92%, 66%, and 77%, respectively in the chosen areas. n=35.

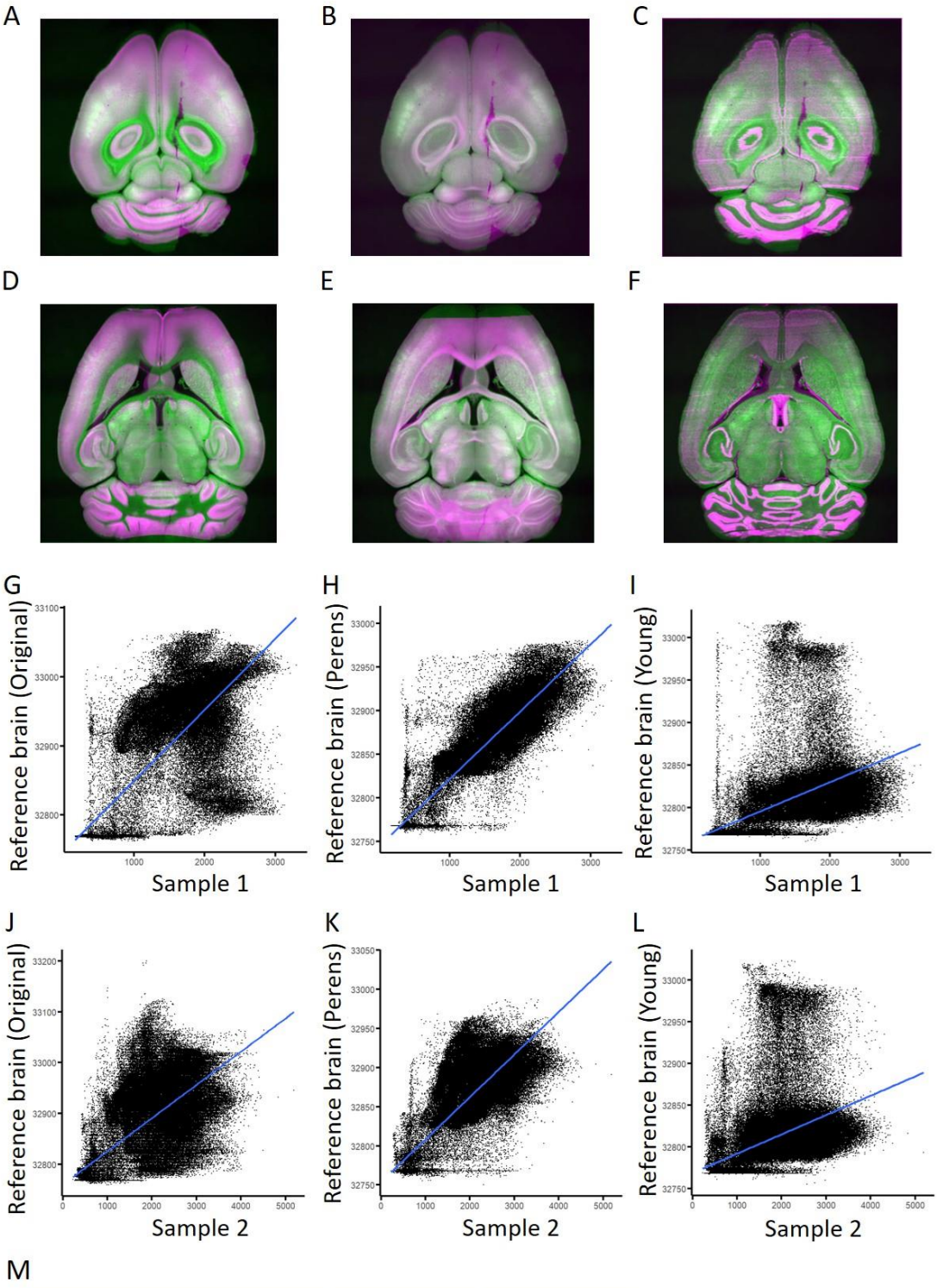

M

Brain atlas reference	Sample 1	Sample 2
from Allen Brain Atlas	0.7525	0.8174
from Perens J.	0.9046	0.8882
from Young D.M.	0.5870	0.6114

Figure 3.7 Mapping comparison between different brain atlases and samples.

(A) The composite image between sample 1 and brain atlas from Allen Brain Atlas. (B) The composite image between sample 1 and brain atlas from Perens J. (C) The composite image between sample 1 and brain atlas from Young D.M. (D) The composite image between sample 2 and brain atlas from Allen Brain Atlas. (E) The composite image between sample 2 and brain atlas from Perens J. (F) The composite image between sample 2 and brain atlas from Young D.M. The magenta channel represents the brain atlas (either from Allen Brain Atlas, Perens J., or Young D.M.), green channel represents the brain sample. (G) The pixel's intensity (grey value) plot between sample 1 and brain atlas from Allen Brain Atlas and the linear regression. (H) The pixel's intensity (grey value) plot between sample 1 and brain atlas from Perens J. and the linear regression. (I) The pixel's intensity (grey value) plot between sample 1 and brain atlas from Young D.M. and the linear regression. (J) The pixel's intensity (grey value) plot between sample 2 and brain atlas from Allen Brain Atlas and the linear regression. (K) The pixel's intensity (grey value) plot between sample 2 and brain atlas from Perens J. and the linear regression. (L) The pixel's intensity (grey value) plot between sample 2 and brain atlas from Young D.M. and the linear regression. (M) The Pearson correlation coefficient of the pixels at the same coordinate from the samples and three brain atlases. All 6 Pearson correlation coefficients have p values lower than 0.05.

Comparison of brain activity between manual and treadmill SD

After the thresholds and brain atlas were decided, I ran ClearMap on the tissue cleared samples. We wanted to see which regions show strong difference between manual and treadmill SD, as well as between manual and treadmill RS. Therefore, I plotted the volcano plot to find out the regions that show low p-value and high fold change after sleep deprivation and recovery sleep. Piriform area, tuberal nucleus, tuberomammillary nucleus, and postpiriform transition area showed higher activity in treadmill SD group compared to manual SD group (low p-value and high fold change; -log10(p-value) > 5.1 and log2(fold change) < -1.2) (**Fig. 3.8 A**).

On the other hand, tuberal nucleus, superior olivary complex, and entorhinal area showed higher activity in treadmill RS group compared to manual RS group (low p-value and high fold; -log10(p-value) > 3.2 and log2(fold change) < -0.9)) (**Fig. 3.8 B**). However, the p-value in RS groups were not as significant as the SD groups. The regions mentioned in this paragraph and last paragraph were selected based on their distribution in the volcano plots, where they showed low p-value compared to other brain regions, but not based on specific thresholds.

I then plotted the box plot to have a closer look for the regions that mentioned above. In the SD groups, piriform area, tuberal nucleus, tuberomammillary nucleus, postpiriform transition area, as well as superior olivary complex and entorhinal area all showed significant difference between manual SD and treadmill SD (FDR adjusted p-value < 0.001 for piriform area, tuberal nucleus, tuberomammillary nucleus, and postpiriform transition area. FDR adjusted p-value = 0.005 for superior olivary complex and entorhinal area) (**Fig. 3.9 A**).

However, in the RS groups, only tuberal nucleus and superior olivary complex showed significant difference between manual RS and treadmill RS (FDR adjusted p-value = 0.03 for both tuberal nucleus and superior olivary complex) (**Fig. 3.9 B**). This suggested that manual RS and treadmill RS may not have too much difference, but manual SD and treadmill SD certainly have some differences. This also suggested that apart from sleep disturbance, two SD methods may have affected the brain activity differently. This is especially intriguing in tuberomammillary nucleus since it is a wake-promoting area but it showed significantly different activity between manual SD and treadmill SD.

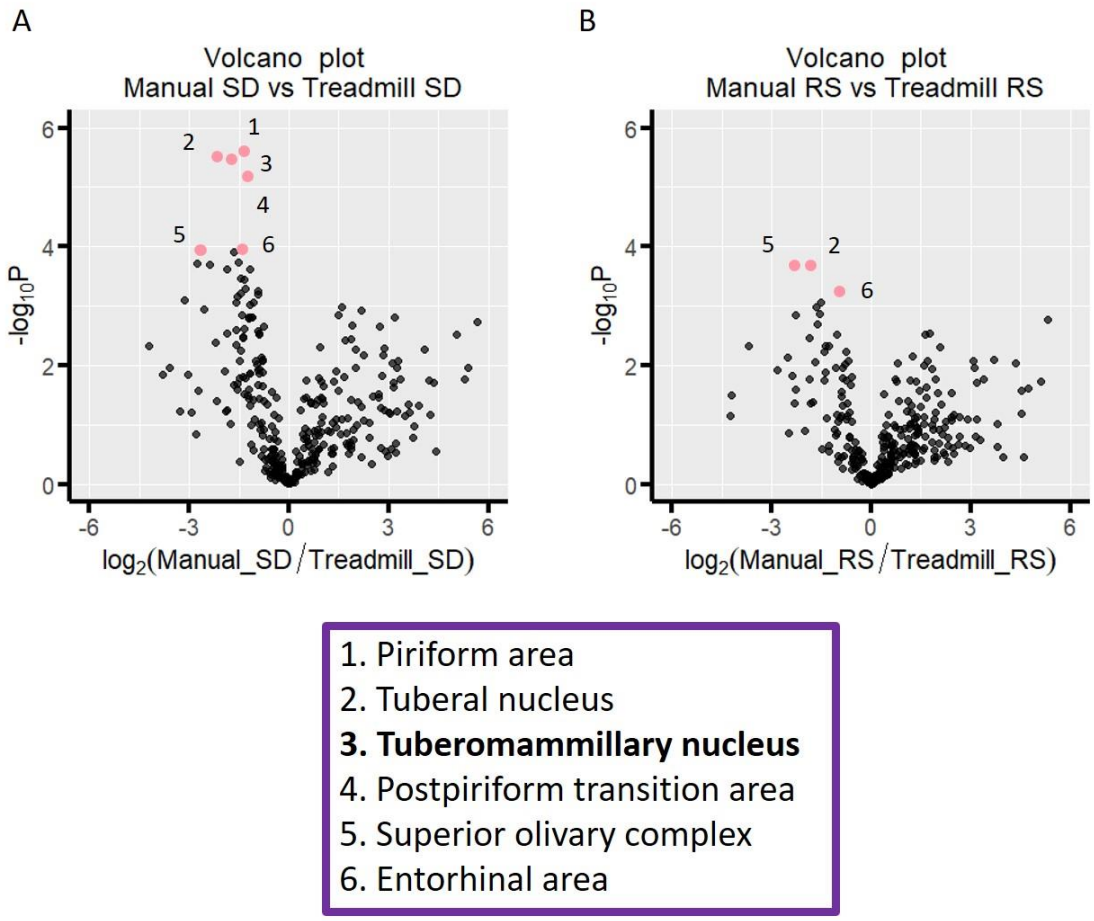

Figure 3.8 Volcano plot of c-Fos positive neurons for manual and treadmill SD/RS mice. (A) Volcano plot between manual SD and treadmill SD groups. Piriform area, tuberal nucleus, tuberomammillary nucleus, and postpiriform transition area showed low p-value and high fold change. (B) Volcano plot between manual RS and treadmill RS groups. tuberal nucleus, superior olivary complex, and entorhinal area showed low p-value and high fold change. p-values were calculated by Student's t-test. n=8-10 per group.

Regions: 1. Piriform area, 2. Tuberal nucleus, 3. Tuberomammillary nucleus, 4. Postpiriform transition area, 5. Superior olivary complex, 6. Entorhinal area.

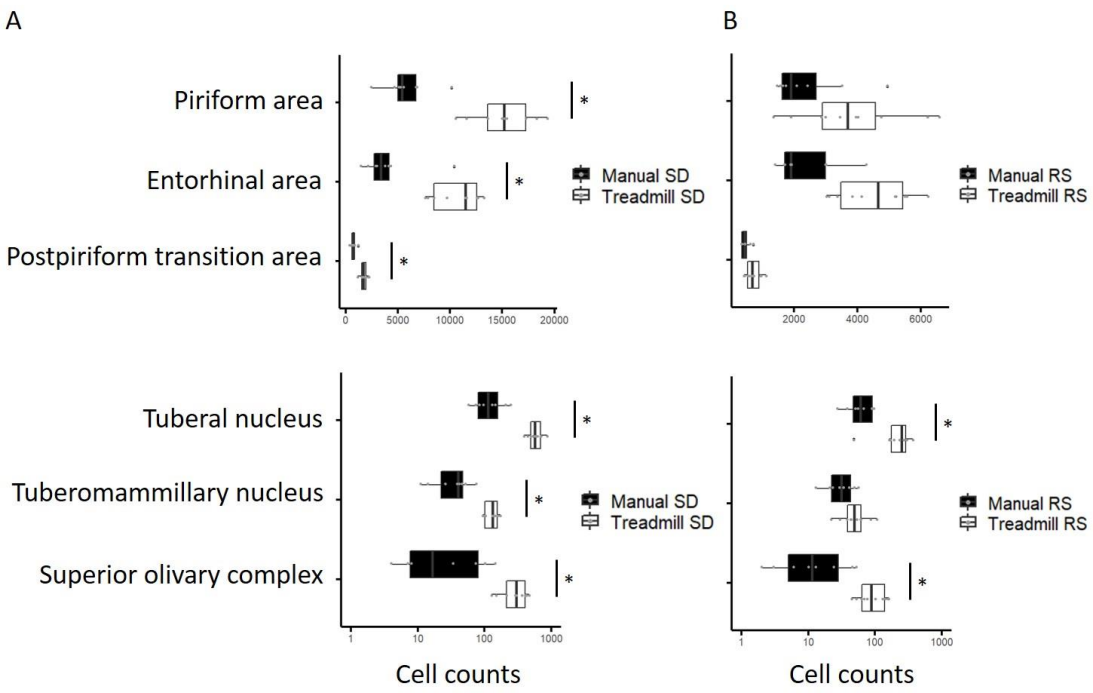

Figure 3.9 Numbers of c-Fos positive neurons in brain regions from figure 3.7. (A) Numbers of active neurons in manual SD and treadmill SD groups. All 6 regions showed significantly higher activity in treadmill SD compared to manual SD. (B) Numbers of active neurons in manual RS and treadmill RS groups. Tuberal nucleus and superior olivary complex showed significantly higher activity in treadmill RS compared to manual RS. *FDR adjusted p-value (after Student's t-test) <0.05 between manual SD/RS and treadmill SD/RS. FDR: False Discovery Rate for multiple testing correction. n=8-10 per group.

Examine the neuronal activity in previously suggested wake-promoting and NREM/REM sleep-promoting regions

In the last few decades, some brain regions have been suggested to promote wake, such as LC, DRN/MRN, VTA, TMN, PPT/LDT, PB, and basal forebrain[66,67,69–71,74,76,77,80,82–86]. There are also some brain regions, such as VLPO/MnPO, basal forebrain, and parafacial zone have been suggested to promote NREM sleep[91–94,96–99]. Since we were comparing two different SD methods, we wanted to examine if these previously suggested wake-promoting and NREM sleep-promoting regions showed different brain activities by using different SD methods.

For the wake-promoting regions, tuberomammillary nucleus (TMN) and substantia innominata (part of basal forebrain[74]) showed significantly higher activity in treadmill SD group compared to manual SD group (FDR adjusted p-value < 0.001 for TMN. FDR adjusted p-value = 0.02 for Substantia innominata). On the other hand, pedunculopontine nucleus (PPT) showed significantly higher activity in manual SD group compared to treadmill SD group (FDR adjusted p-value = 0.03). The rest of the 6 wake-promoting regions did not show significant difference (**Fig. 3.10 A**).

For the 3 NREM sleep-promoting regions (VLPO, MnPO, and parafacial zone), they did not show significant difference, but paragigantocellular reticular nucleus, which may promote REM sleep by inhibiting REM sleep-suppressing neurons of the pons,[119] showed significantly higher activity in treadmill SD group compared to manual SD group (FDR adjusted p-value = 0.03) (**Fig. 3.10 B**). Therefore, some regions did show difference between manual and treadmill SD. However, all wake-promoting and NREM/REM sleep-promoting regions did not show significant difference between manual and treadmill RS groups (**Fig. 3.10 C and D**)**.**

We were not sure about the reasons that caused the different activities of these regions between 2 SD methods. If the two SD methods had similar efficiency of sleep deprivation on mice, it was more likely that the difference was from other aspects of the methods apart from sleep disturbance. For example, the physical activity and locomotion were higher for mice in treadmill SD compared to manual SD since mice were forced to move consistently on treadmill. Stress could also be a potential reason. During the treadmill SD, mice were moved from their homecages to treadmill, which was a new environment for them, whereas mice only needed to stay in their homecages during the manual SD. However, further studies will be required to reveal the reasons that caused the difference.

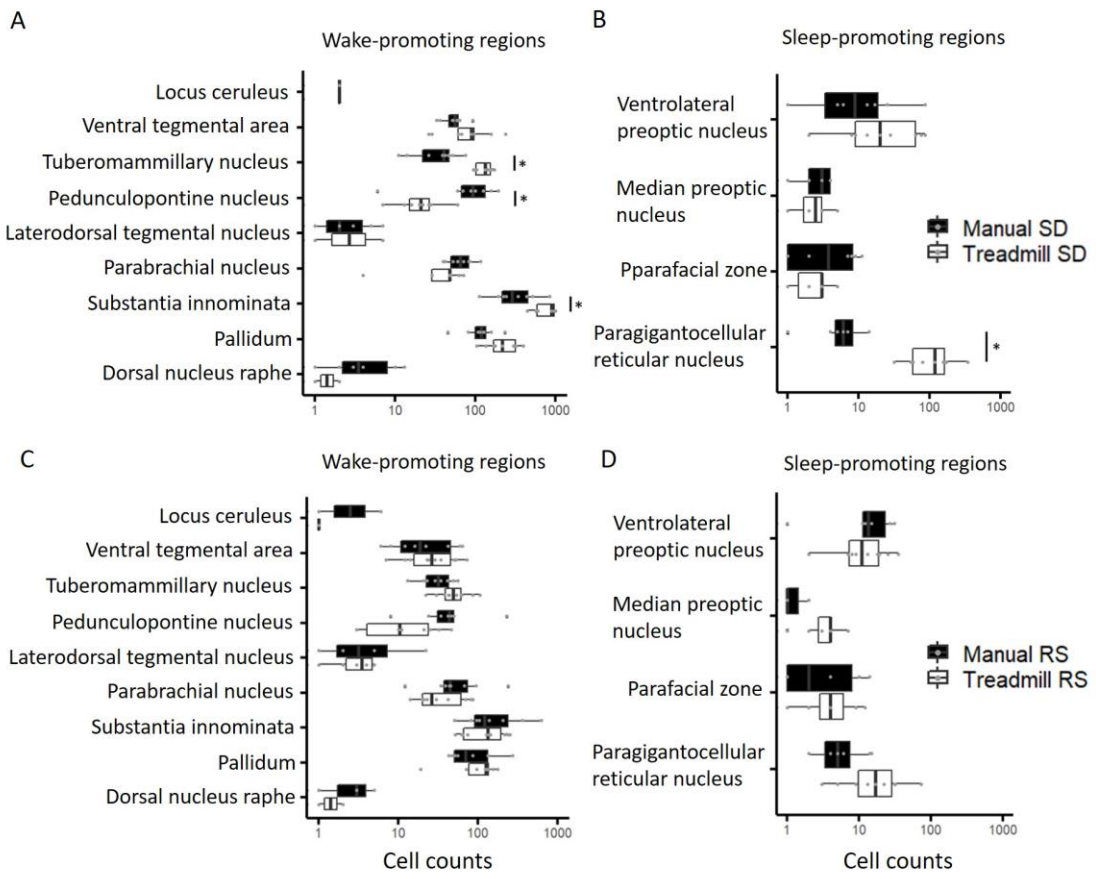

Figure 3.10 Numbers of c-Fos positive neurons in previously suggested wake-promoting and NREM/REM sleep-promoting regions. (A) Number of active neurons in manual SD and treadmill SD groups at wake-promoting regions. Tuberomammillary nucleus and substantia innominata showed significantly higher activity in treadmill SD group compared to manual SD group. Pedunculopontine nucleus showed significantly higher activity in manual SD group compared to treadmill SD group. (B) Numbers of active neurons in manual SD and treadmill SD groups at NREM/REM sleep-promoting regions. Paragigantocellular reticular nucleus showed significantly higher activity in treadmill SD group compared to manual SD group. (C) Numbers of active neurons in manual RS and treadmill RS groups at wake-promoting regions. No significant difference between two groups. (D) Numbers of active neurons in manual RS and treadmill RS groups at NREM/REM sleep-promoting regions. No significant difference between two groups. *FDR adjusted p-value (after Student's t-test) <0.05 between manual SD/RS and treadmill SD/RS. FDR: False Discovery Rate for multiple testing correction. n=8-10 per group.

Examine the neuronal activity and connectivity in high-level brain regions

Apart from the changes of neural activity in small brain regions, we also wanted to see the changes in high-level brain regions and their connectivity in different conditions. This could provide additional information about the activity difference between two SD methods. Therefore, I collapsed the brains regions into 11 high-level brain regions (olfactory areas, cerebral nuclei, isocortex, hippocampus, cortical subplate, thalamus, hypothalamus, midbrain, pons, medulla, and cerebellum) based on the hierarchical structure from the Allen Mouse Brain Atlas[157] (**Fig. 3.11 A**). Olfactory areas, hypothalamus, pons, and medulla showed significantly higher activity in treadmill SD group compared to manual SD group (FDR adjusted p-value < 0.0001 for olfactory areas. FDR adjusted p-value = 0.008, 0.005, 0.02 for hypothalamus, pons, and medulla, respectively) (**Fig. 3.11 B**). On the other hand, thalamus showed significantly higher activity in manual SD group compared to treadmill SD group (FDR adjusted p-value = 0.01). For the RS groups, there was no significant difference between manual and treadmill RS (**Fig. 3.11 C**). This suggested that treadmill and manual SD did cause different activities in some high-level brain regions.

Next, I examined the connectivity of the brain regions between manual and treadmill SD/RS. The cell counts were first scaled and the Pearson correlation coefficients were computed in all 11 brain regions. Then the heatmaps were plotted to show the Pearson correlation coefficient. The heatmaps from manual and treadmill SD, as well as from manual and treadmill RS were subtracted to show the differences. In the heatmaps, yellow means the correlation is more positive in manual group compared to treadmill group. On the contrary, blue means the correlation is more positive in treadmill group compared to manual group (**Fig. 3.12**).

We found out that the Pearson correlation coefficients between some regions were significantly different between manual and treadmill SD groups. That included the Pearson correlation coefficient between olfactory areas and three different regions: cerebral nuclei (r = -0.51 in manual SD group, r = 0.76 in treadmill SD group, p = 0.008), isocortex (r = -0.13 in manual SD group, r = -0.88 in treadmill SD group, p = 0.03), and cortical subplate (r = -0.27 in manual SD group, r = 0.75 in treadmill SD group, p = 0.03). The correlation between hypothalamus and medulla also showed significant difference between the two SD groups (r = 0.04 in manual SD group, r = 0.87 in treadmill SD group, p = 0.03) (**Fig. 3.12 A**).

Surprisingly, the Pearson correlation coefficients between some regions also showed significant difference between manual and treadmill RS groups. This included the correlation between olfactory areas and midbrain (r = 0.40 in manual SD group, r = -0.81 in treadmill SD group, p = 0.006), hippocampus and cerebellum (r = 0.93 in manual SD group, r = 0.45 in treadmill SD group, p = 0.03), cortical subplate and midbrain (r = 0.01 in manual SD group, r = -0.81 in treadmill SD group, p = 0.04), thalamus and pons (r = 0.90 in manual SD group, r = 0.09 in treadmill SD group, p = 0.01), as well as cerebellum and

pons (r = -0.52 in manual SD group, r = 0.60 in treadmill SD group, p = 0.02) (**Fig. 3.12 B**).

For the SD groups, the connectivity between olfactory areas and three regions were significantly different between manual and treadmill SD. This suggested that olfactory areas may react differently by the two different SD methods, and could be a crucial region to look at different SD methods. For the RS groups, we did not see significant changes in the brain activity between manual RS and treadmill RS, but there were significant changes about the correlation for some brain regions. This suggested that the connectivity might still be impacted and showed different patterns even though the activity itself did not change significantly.

A

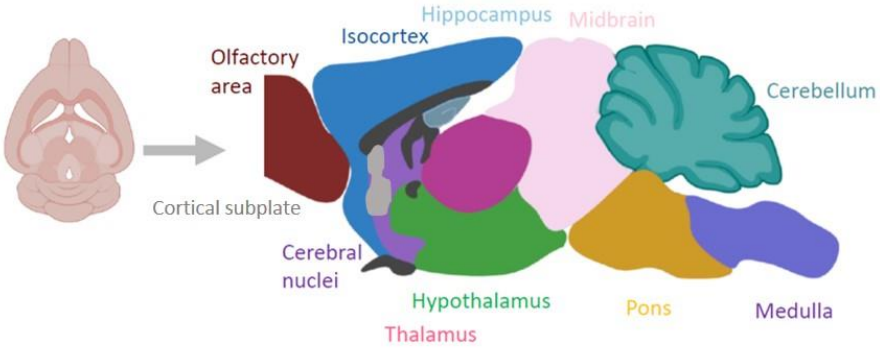
Hippocampus
Midbrain
Isocortex
Olfactory area
Cerebellum
Cortical subplate
Cerebral nuclei
Hypothalamus
Pons
Medulla
Thalamus

B

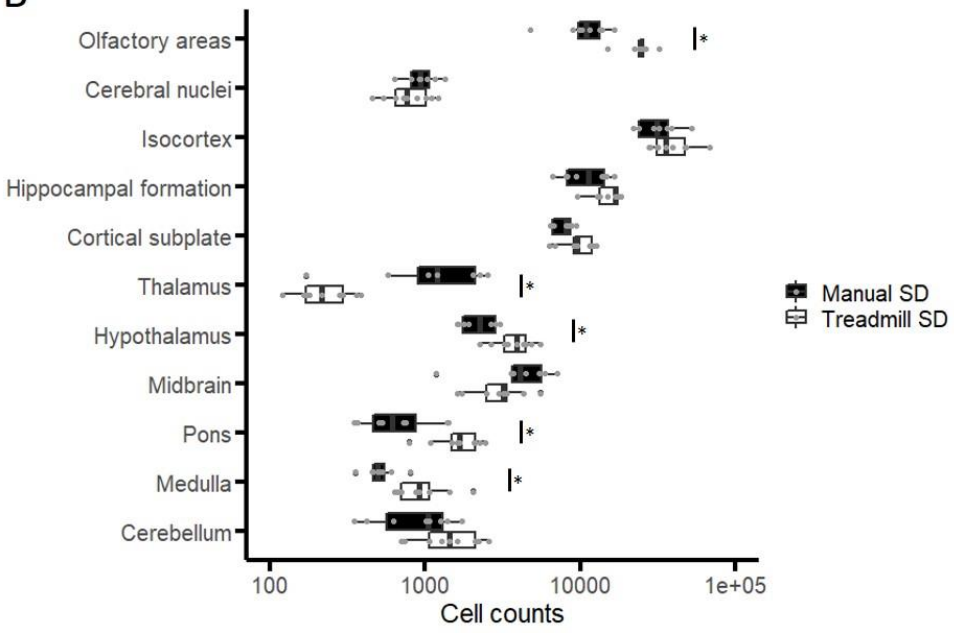
Olfactory areas
Cerebral nuclei
Isocortex
Hippocampal formation
Cortical subplate
Thalamus
Hypothalamus
Midbrain
Pons
Medulla
Cerebellum
*
100
1000
10000
1e+05
Cell counts
Manual SD
Treadmill SD

C

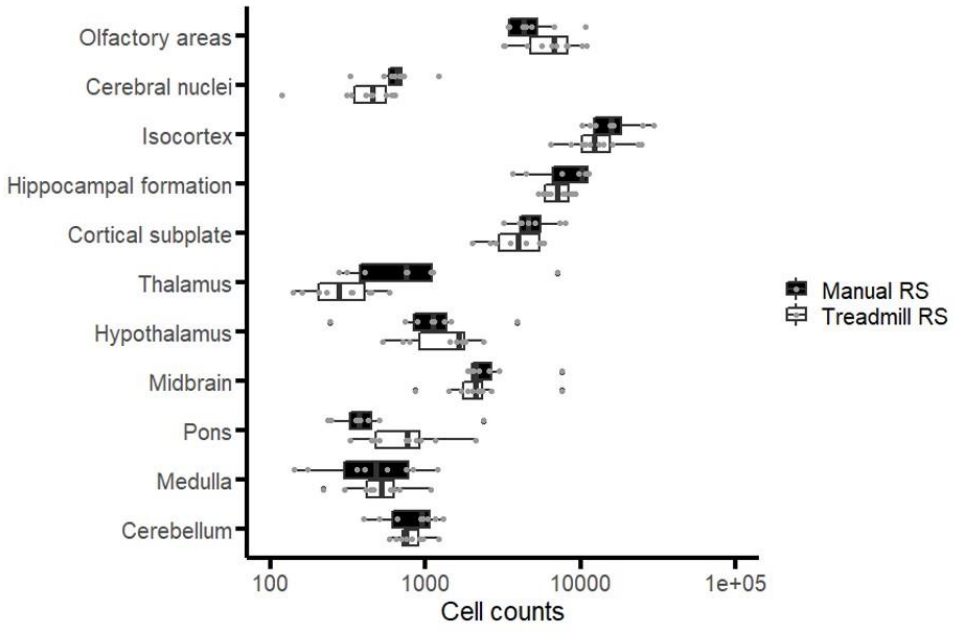
Olfactory areas
Cerebral nuclei
Isocortex
Hippocampal formation
Cortical subplate
Thalamus
Hypothalamus
Midbrain
Pons
Medulla
Cerebellum
100
1000
10000
1e+05
Cell counts
Manual RS
Treadmill RS

Figure 3.11 Numbers of c-Fos positive neurons in high-level brain regions for manual and treadmill SD/RS mice *(figure 3.11 (A) was made by Dr. Rhîannan H Williams)*. (A) 11 high-level brain regions based on the hierarchical structure from the Allen Mouse Brain Atlas.[157] (B) Numbers of c-Fos positive neurons in manual SD and treadmill SD groups. Olfactory areas, hypothalamus, pons, and medulla showed significantly higher activity in treadmill SD group compared to manual SD group. Thalamus showed significantly higher activity in manual SD group compared to treadmill SD group. (C) Numbers of c-Fos positive neurons in manual RS and treadmill RS groups. No significant difference between two groups. *FDR adjusted p-value (after Student's t-test) <0.05 between manual SD/RS and treadmill SD/RS. FDR: False Discovery Rate for multiple testing correction. n=8-10 per group.

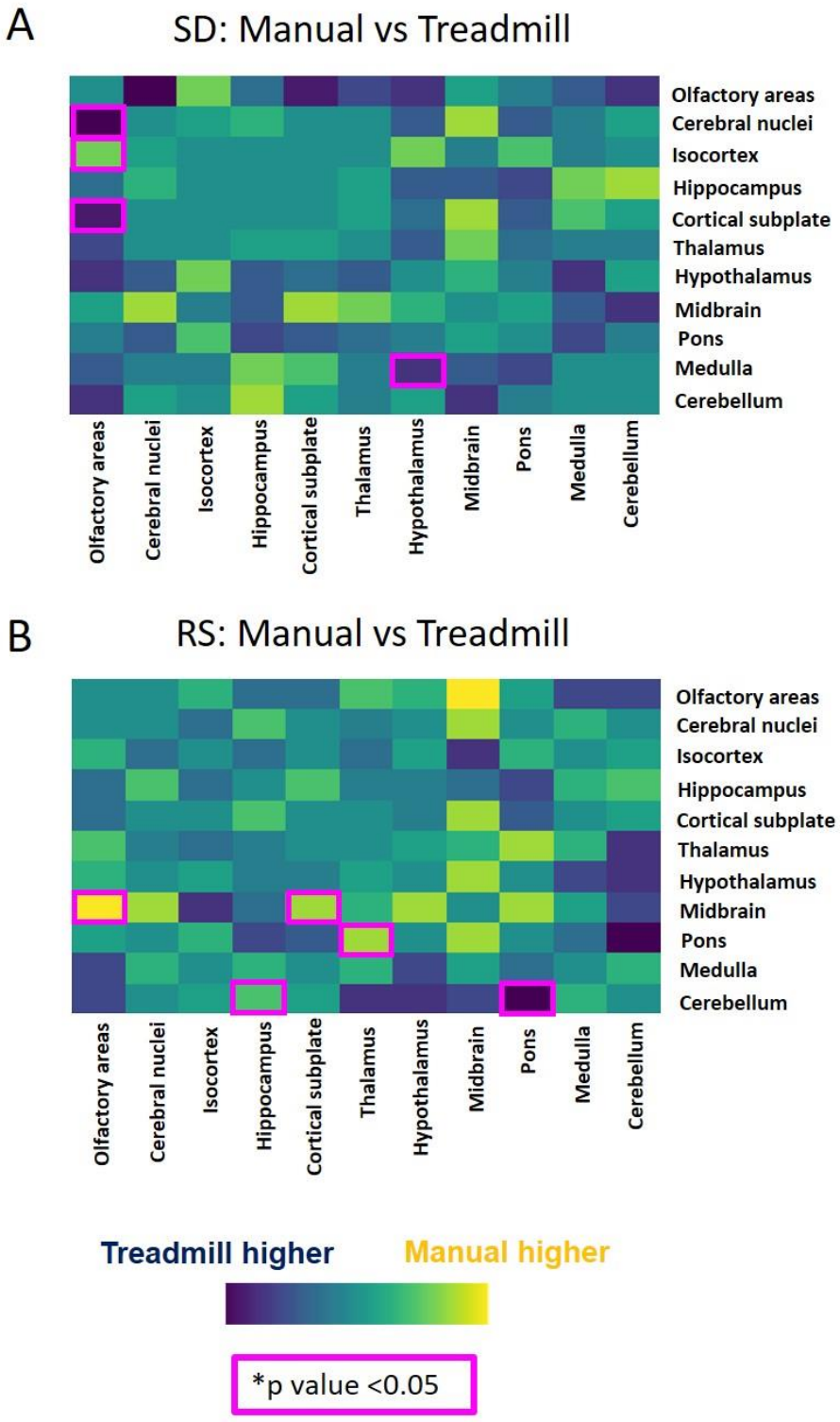

Figure 3.12 The connectivity in high-level brain regions for manual and treadmill SD/RS mice. (A) The subtraction heatmap of Pearson correlation coefficient between difference regions between manual and treadmill SD. The correlation between olfactory areas and three different regions (cerebral nuclei, isocortex, and cortical subplate) showed significant difference between the two SD groups. The correlation between hypothalamus and medulla also showed significant difference. (B) The subtraction heatmap of Pearson correlation coefficient between difference regions between manual and

treadmill RS. The correlation between olfactory areas and midbrain, hippocampus and cerebellum, cortical subplate and midbrain, thalamus and pons, as well as cerebellum and pons showed significant difference between the two RS groups. Magenta square: p-value lower than 0.05 after statistical test by cocor (A Comprehensive Solution for the Statistical Comparison of Correlations, 2015)[138]. n=8-10 per group.

Discussion

The first part of the study was to compare the sleep recording results between piezo and EEG/EMG. The comparison of EEG/EMG and piezo recording suggested that there was no significant difference for wake percent time in the light period, even though piezo recording showed subtle trend toward lower wake percent time (**Fig. 3.3**). In another study, Géraldine et al. also compared the recording between EEG/EMG and piezo[135]. In their study, the total sleep time didn't have difference in the dark period, but piezo recording showed significantly longer total sleep time in the light period, which is similar to our study. Additionally, the correlation between the amounts of sleep obtained with the two recording techniques was similar. Géraldine et al. showed that the Pearson correlation was 0.96 in the light period, and 0.97 in the dark period. In our study, the Pearson correlation was 0.97 in the light period (**Fig. 3.3**). This suggested that the sleep monitoring results from our piezo system were similar to the published piezo system, which gave us more confidence for our sleep data from piezo.

The second part of the study was to examine the efficiency of different SD methods (manual, treadmill, 4 hours, 6 hours). The different methods of sleep deprivation did not show significant difference for the sleep percent time in the recovery period, suggesting the different sleep deprivation methods did not cause longer rebound sleep (**Fig. 3.3**), and had similar SD efficiency.

The third part of the study was to check the reliability of ClearMap automatic cell detection and choose the most appropriate brain atlas. The median of precision, recall, and F1 score of CleapMap cell detection were 92%, 66%, and 77%, respectively in the chosen areas (**Fig. 3.6**). In the original paper where ClearMap was developed, they chose to use stricter thresholds and led to higher precision and lower recall. The precision they had was at least 99%, and the recall was 20-30%, leading to a F1 score around 45-50%[136]. The thresholds in our study were different, resulting in lower precision, but higher recall and F1 score. A higher recall could spot more real cells, and the thresholds we used (recall: 66%) can spot almost doubled amount of real cells compared to the original paper (recall: 20-30%). This also reflected on F1 score where we had a higher F1 score (77%) compared to the original publication (45-50%). The brain atlas from Perens J. was selected for the study because it showed the highest Pearson correlation coefficient to the samples (0.9046 for sample 1 and 0.8882 for sample 2) compared to the brain atlas from Allen Brain Atlas (0.7525 for sample 1 and 0.8174 for sample 2) and the brain atlas from Young D.M. (0.5870 for sample 1 and 0.6114 for sample 2) (**Fig. 3.7**). Therefore, we think the thresholds and brain atlas we used for ClearMap were reasonable.

The last part of the study was to check the difference of brain activity between manual and treadmill SD as well as between manual and treadmill RS. We noticed that tuberomammillary nucleus (TMN) showed significantly higher activity in treadmill SD group compared to manual SD group (**Fig. 3.8 and 3.10**). Since TMN is a wake-promoting area[70,71], it would be interesting to know why TMN showed different activity between two SD methods. However, TMN is also involved in control of learning, memory and reinforcement

processes[158], which suggested that TMN could also be activated by these reasons during SD. For other well-known wake-promoting regions such as locus coeruleus, ventral tegmental area, LDT, parabrachial nucleus, and DRN, they did not show difference between manual and treadmill SD. This was the same for the NREM sleep-promoting regions such as VLPO, MePO, and parafascicular nucleus (**Fig. 3.10**).

The results of the high-level brain regions were intriguing because 5 of them (olfactory areas, thalamus, hypothalamus, pons, and medulla) showed significant difference between two different SD methods (**Fig. 3.11**). Olfactory areas was especially interesting since the connectivity between olfactory areas and three other regions (cerebral nuclei, isocortex, and cortical subplate) showed significant difference between two different SD methods (**Fig. 3.12**).This suggested the levels of locomotion and stress might be causing the changes of neuronal activity and connectivity in different brain regions. If the SD study is for examining the neuronal activity and connectivity in the regions that mentioned above, it might be important to choose the most appropriate SD method and bear in mind that the experiment results could be different when the SD method is different.

(The studies in this chapter were supported by the ERC under the European Union's Horizon 2020 Research and Innovation Program Grant Agreement No. 715933 to Dr. Rhîannan H Williams.)

Chapter 4
Identification of amygdala neurons activated by sleep loss

Introduction

The brain regions that contributed to sleep homeostasis were studied widely in the last few decades. As described in chapter 1, LC, DRN/MRN, VTA, TMN, PPT/LDT, PB, and basal forebrain were suggested to promote wake from sleep[66,67,69–71,74,76,77,80,82–86]. On the other hand, GABAergic neurons in VLPO/MnPO, basal forebrain, and parafacial zone were suggested to be NREM sleep-promoting regions[91–94,96–99].

Even though some regions were suggested to mediate the sleep-wake cycle, the whole mechanism of sleep homeostasis is still unclear, and it is possible that more brain regions or cell populations are involved. Hence, we wanted to examine the brain activity throughout the whole brain with an unbiased method to find out the regions that may have also contributed to sleep homeostasis. Therefore, we used tissue clearing combined with light sheet fluorescence microscopy to get the whole brain images with immunolabeling of c-Fos positive neurons. This allowed us to reveal the whole brain activity under high sleep-drive condition (after sleep deprivation), and indicate the brain regions that may contribute to sleep homeostasis. These regions could be the candidate regions to do the functionality study and prove their roles in sleep homeostasis.

Aims and objectives

We aimed to do unbiased whole brain activity mapping to find out the regions that showed strong neuronal activity in high sleep-drive condition (after sleep deprivation). The detailed aims included:

- Use tissue clearing (iDISCO+) to do whole brain imaging, then use ClearMap to detect active neurons and annotate them to different brain regions. Afterwards, observe the regions that show high neuronal activity after sleep deprivation (high sleep-drive condition) and after recovery sleep. We expected to see some regions that were not well studied previously for sleep homeostasis.
- Collapse all brain regions into 11 high-level brain regions, and examine the changes of connectivity between (manual and treadmill) SD, (manual and treadmill) RS, and undisturbed control (ZT4 and ZT6) groups.

Results

Calculate and annotate active neurons by ClearMap

In order to evaluate the whole brain activity under different sleep-drive conditions, we divided mice into 6 groups. 2 groups of mice went through 4 hours sleep deprivation (either manual or treadmill) before the brain tissue was taken out at ZT4. Another 2 groups of mice also went through 4 hours sleep deprivation (either manual or treadmill), but followed by 2 hours undisturbed recovery sleep. Then the brain tissue was taken out at ZT6. Additional 2 groups of undisturbed mice were sacrificed and the brain tissue was taken out at either ZT4 or ZT6. iDISCO+ was then performed to clear the tissues, as well as immunolabeling c-Fos positive neurons. Afterwards, samples were imaged by light sheet microscopy and ClearMap was run for automatic cell detection and annotation (**Fig. 4.1 A**).

The same analysis method from chapter 3 “Sleep deprivation methodology” was used in this study, including the decision making of intensity threshold for cell detection. Similar to chapter 3, after the threshold optimization steps were finalized, ClearMap was run based on the chosen thresholds, and I compared the results between ClearMap automatic cell detection and human manual cell counting at small areas in the cortex. The median of Precision, Recall, and F1 score for our 51 samples were 92%, 67%, and 76%, respectively (**Fig. 4.1 B**).

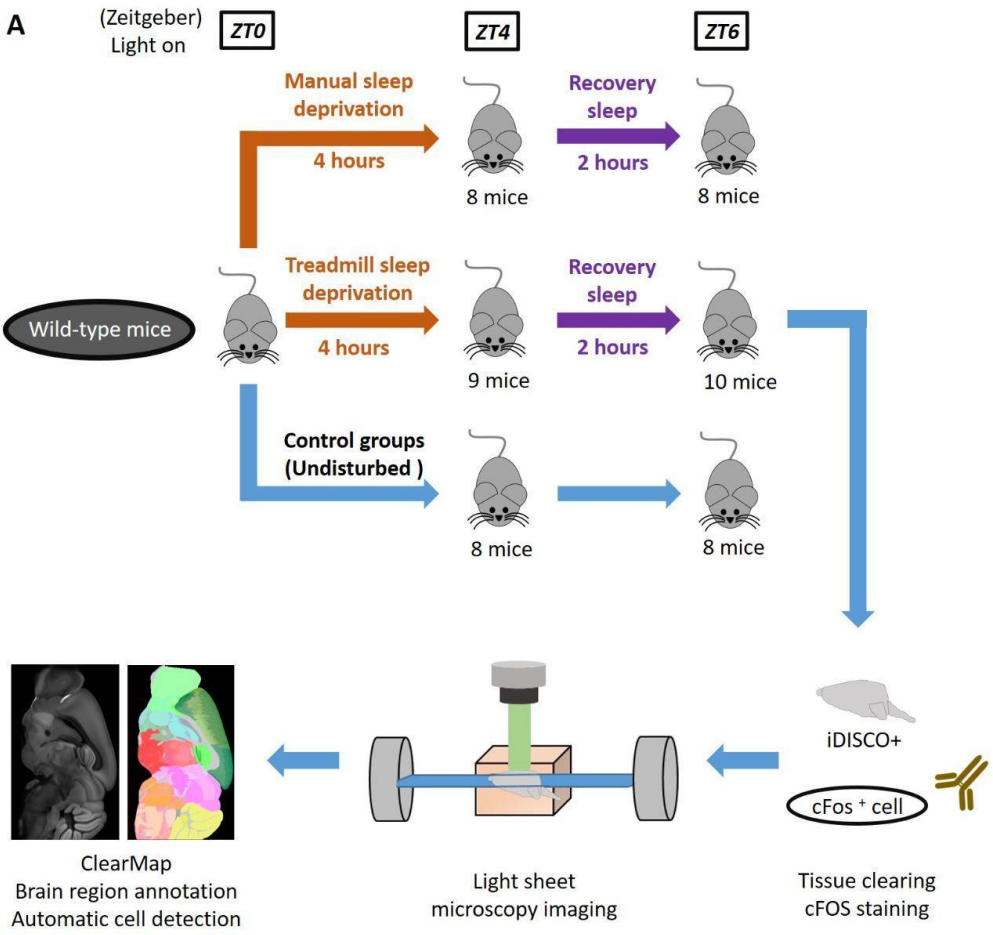

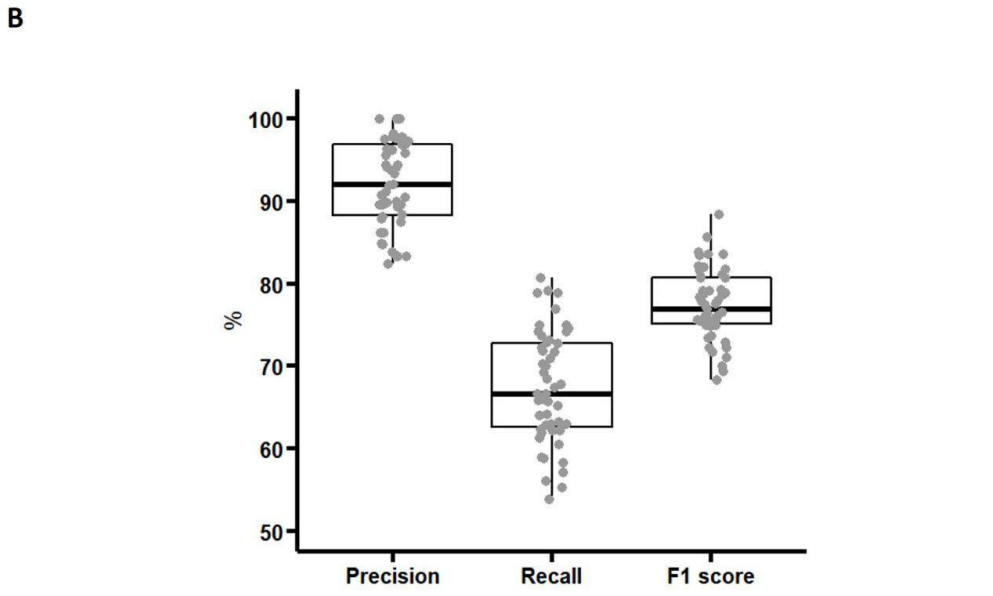

Figure 4.1 Experimental design for iDISCO+ and comparison between automatic and manual cell counts. (A) The flowchart of experimental design. (B) The median of Precision, Recall, and F1 score were 92%, 67%, and 76%, respectively between the automatic and manual cell counts in the chosen areas. n=51.

Whole brain mapping suggests amygdala regions are active after sleep deprivation

After using ClearMap for whole brain mapping and automatic cell detection, we got the cell counts for over 250 regions (**Supplementary table 1 in Appendices**). In order to have an overview for the cell counts from all brain regions across all 6 groups, the original cell counts were scaled to the percentage of active cells in the whole brain (cell count in one region/cell count in the whole brain), and the brain regions were arranged based on 9 high-level brain regions (**Fig. 4.2**).

Then volcano plots were made to find out the regions that showed low p-value and high fold change after sleep deprivation and recovery sleep. Three amygdala regions (basolateral, basomedial, and intercalated amygdala) and cortical subplate showed higher activity in manual SD group compared to control ZT4 group (low p-value and high fold change; -log10(p-value) > 6.1 and log2(fold change) > 1.7)) (**Fig. 4.3 A**). On the other hand, two amygdala regions (basolateral and basomedial) showed higher activity in treadmill SD group compared to control ZT4 group (low p-value and high fold change; -log10(p-value) > 5.1 and log2(fold change) > 2.2)) (**Fig. 4.3 B**). Apart from that, four regions (piriform area, postpiriform transition area, entorhinal area, and nucleus of the lateral olfactory tract) showed similar activity trend.

The results were very different when we compared manual RS and control ZT4. Most regions did not show low p-value and high fold change. However, postpiriform transition area showed relatively low p-value compared to other regions (-log10(p-value) > 4 and log2(fold change) > 1.7)) (**Fig. 4.3 C**). This suggested that postpiriform transition area was more active in manual RS group compared to control ZT6 group. The effect was similar when we compared treadmill RS and control ZT4. Entorhinal area and postpiriform transition area showed relatively low p-value compared to other regions (-log10(p-value) > 5 and log2(fold change) > 2.1)) (**Fig. 4.3 D**), suggesting these 2 regions were more active in treadmill RS group compared to control ZT6 group. Interesting we found out that postpiriform transition area showed significant difference in all four conditions (-log10(p-value) > 4), suggesting it could be triggered by sleep deprivation and last for the whole recovery sleep (**Fig. 4.3 A-D**). We also found out that entorhinal area showed relatively low p-value in both treadmill SD and RS groups (-log10(p-value) > 5.9) compared to manual SD and RS groups (-log10(p-value) < 2.3) (**Fig. 4.3 A-D**). The regions mentioned in this paragraph and last paragraph were selected based on their distribution in the volcano plots, where they showed low p-value compared to other brain regions, but not based on specific thresholds.

Since several amygdala regions showed more active neurons in both manual and treadmill SD groups compared to control ZT4 group, we then decided to focus on amygdala regions and check if the differences were significant. 9 out of 10 amygdala regions (basolateral amygdalar nucleus, basomedial amygdalar nucleus, intercalated amygdalar nucleus, central amygdalar nucleus, medial amygdalar nucleus, posterior amygdalar nucleus, anterior amygdalar area, cortical amygdalar area, piriform-amygdalar area) showed

significant increase of active neurons in manual SD group compared to control ZT4 group (FDR adjusted p-value < 0.0001 for basolateral amygdalar nucleus, basomedial amygdalar nucleus, and intercalated amygdalar nucleus. FDR adjusted p-value = 0.008, 0.01, 0.003, 0.04, 0.01, 0.006 for central amygdalar nucleus, medial amygdalar nucleus, posterior amygdalar nucleus, anterior amygdalar area, cortical amygdalar area, piriform-amygdalar area, respectively). 8 out of 10 amygdala regions (basolateral amygdalar nucleus, basomedial amygdalar nucleus, intercalated amygdalar nucleus, medial amygdalar nucleus, posterior amygdalar nucleus, anterior amygdalar area, cortical amygdalar area, piriform-amygdalar area) also showed significant increase of active neurons in treadmill SD group compared to control ZT4 group (FDR adjusted p-value < 0.001 for basolateral amygdalar nucleus, basomedial amygdalar nucleus, medial amygdalar nucleus, posterior amygdalar nucleus, anterior amygdalar area, and cortical amygdalar area. FDR adjusted p-value = 0.001 for intercalated amygdalar nucleus, and 0.003 for piriform-amygdalar area). Lateral amygdalar nucleus did not show significant difference between manual/treadmill SD group and control ZT4 group. Central amygdalar nucleus only showed significant increase of active neurons in manual SD group (compared to control ZT4 group), but not in treadmill SD group (**Fig. 4.4 A**).

On the contrary, no amygdala region showed significant difference between manual RS group and control ZT6 group, as well as between treadmill RS group and control ZT6 group (**Fig. 4.4 B**). This suggested that most amygdala regions were significantly active under high sleep-drive condition, but became less active after 2 hours of recovery sleep when sleep drive dropped.

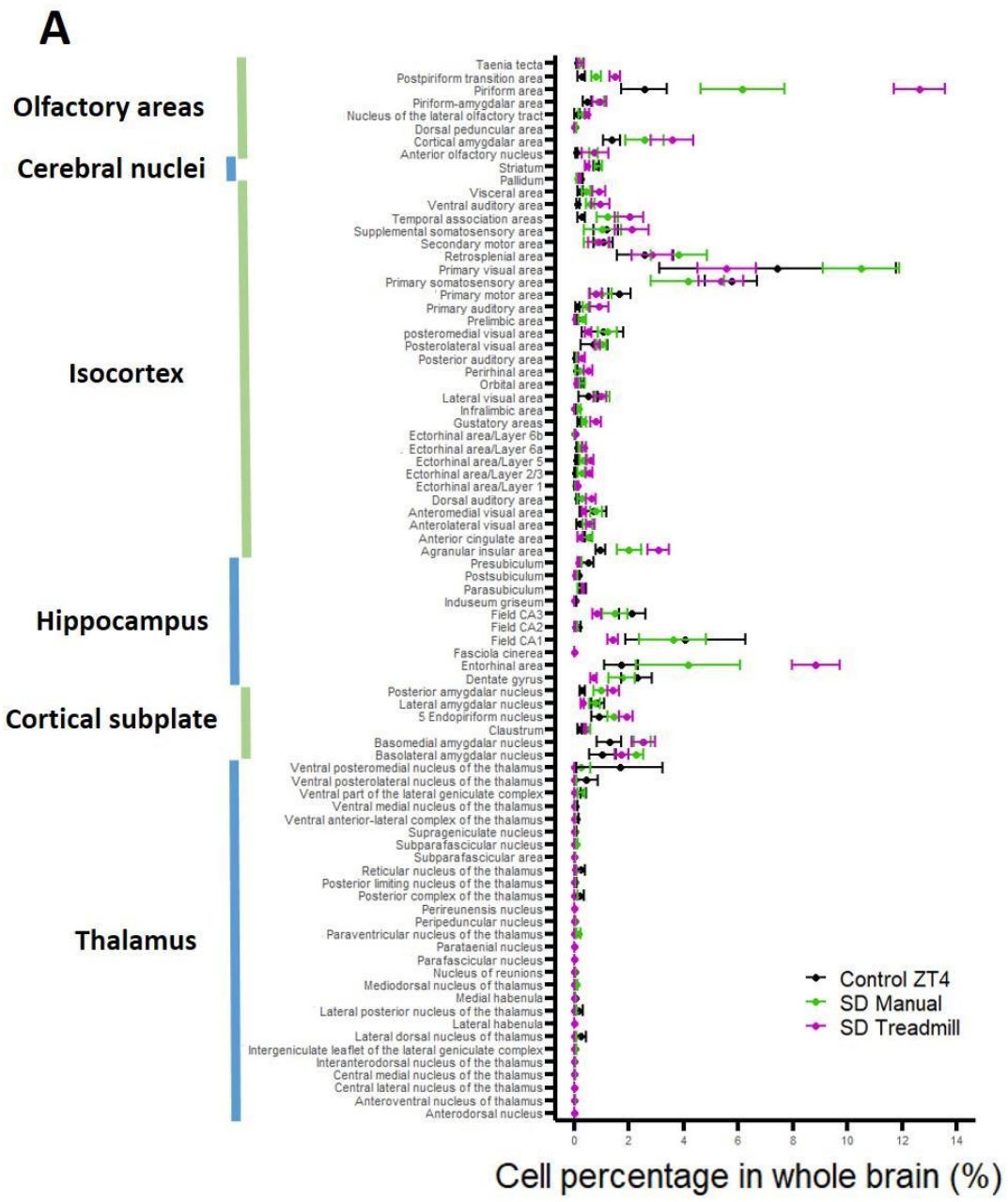

Figure 4.2 (A) Cell percentage of c-Fos positive neurons in olfactory areas, cerebral nuclei, isocortex, hippocampus, cortical subplate, and thalamus in manual SD, treadmill SD, and control ZT4 groups. Line: Mean ± SEM. n=8-10 per group.

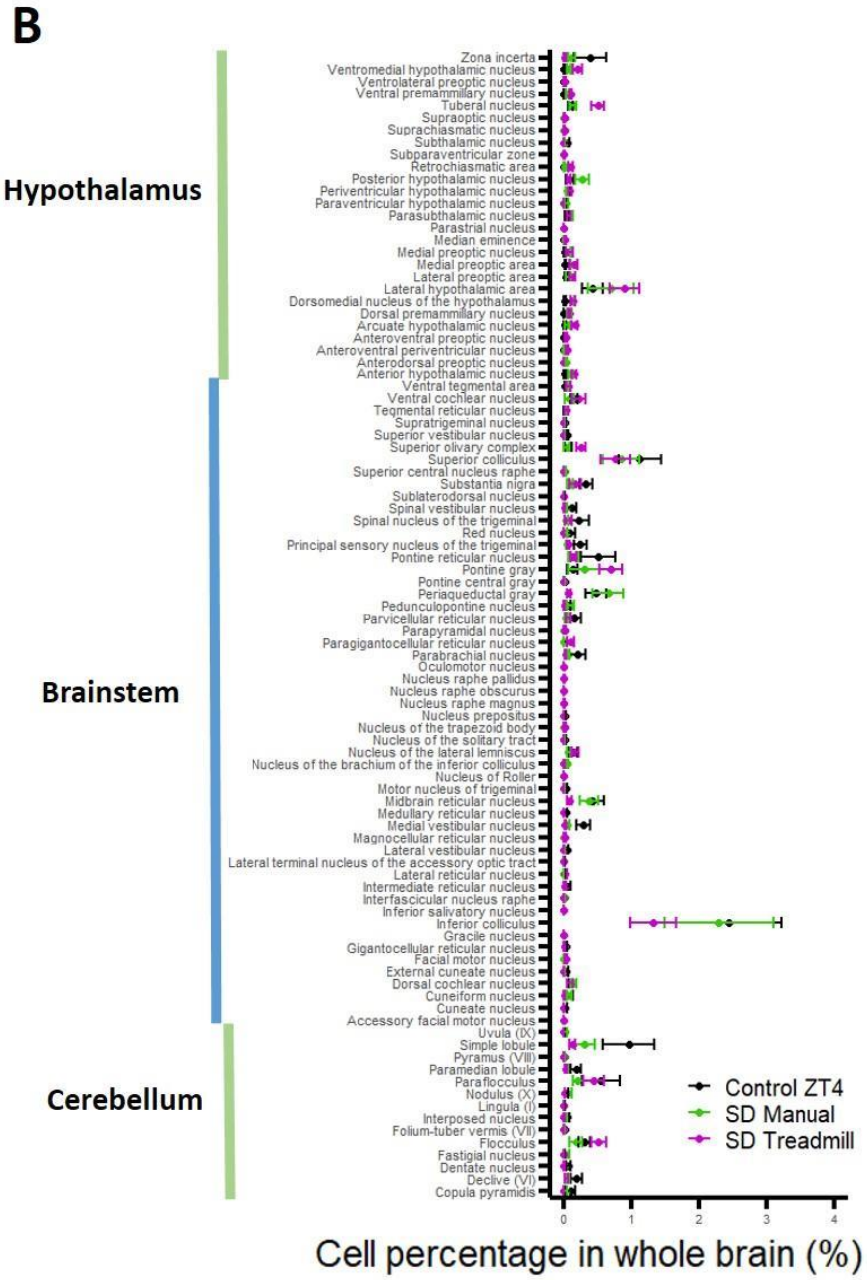

Figure 4.2 (B) Cell percentage of c-Fos positive neurons in hypothalamus, brainstem, and cerebellum in manual SD, treadmill SD, and control ZT4 groups. Line: Mean ± SEM. n=8-10 per group.

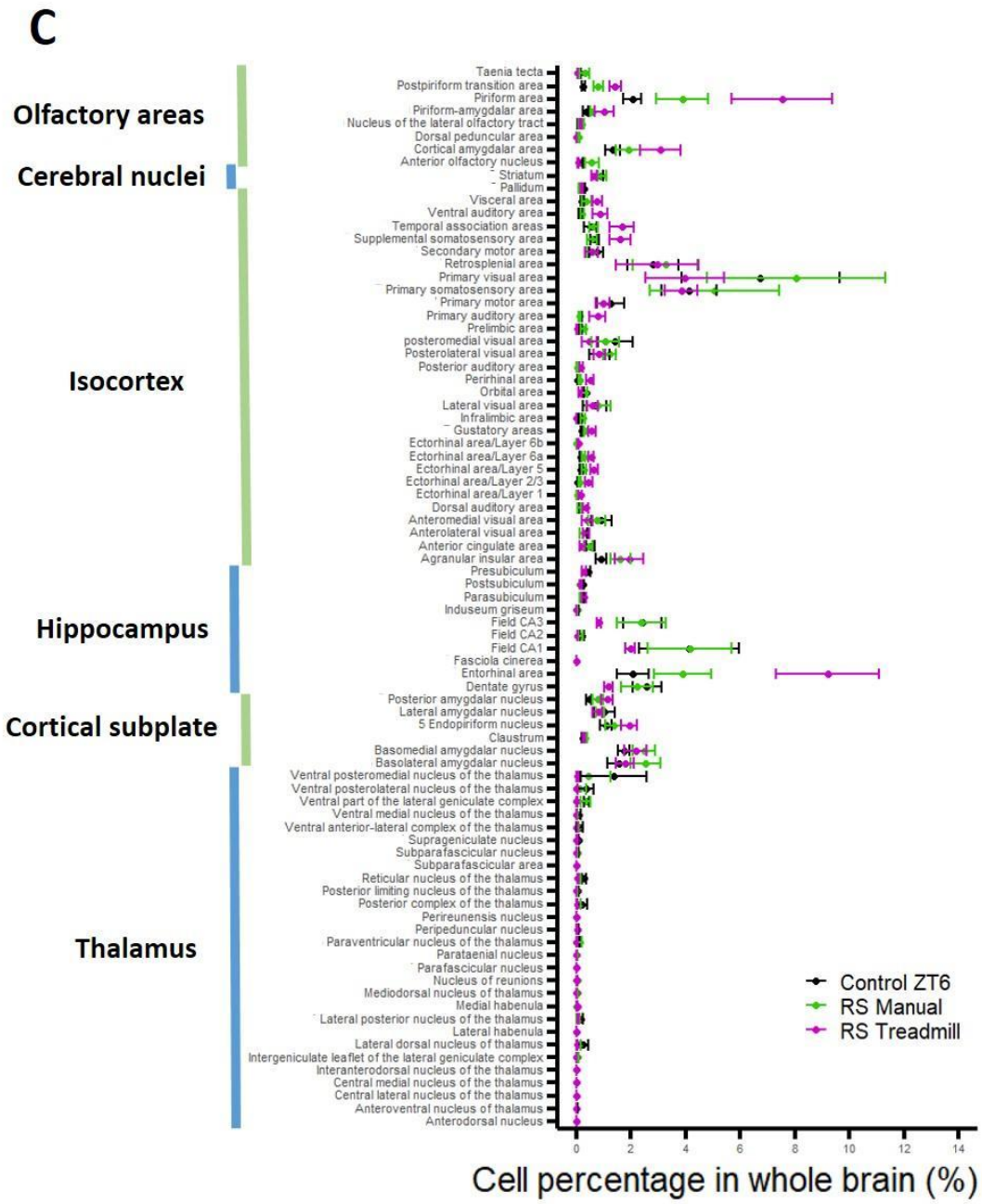

Figure 4.2 (C) Cell percentage of c-Fos positive neurons in olfactory areas, cerebral nuclei, isocortex, hippocampus, cortical subplate, and thalamus in manual RS, treadmill RS, and control ZT6 groups. Line: Mean ± SEM. n=8-10 per group.

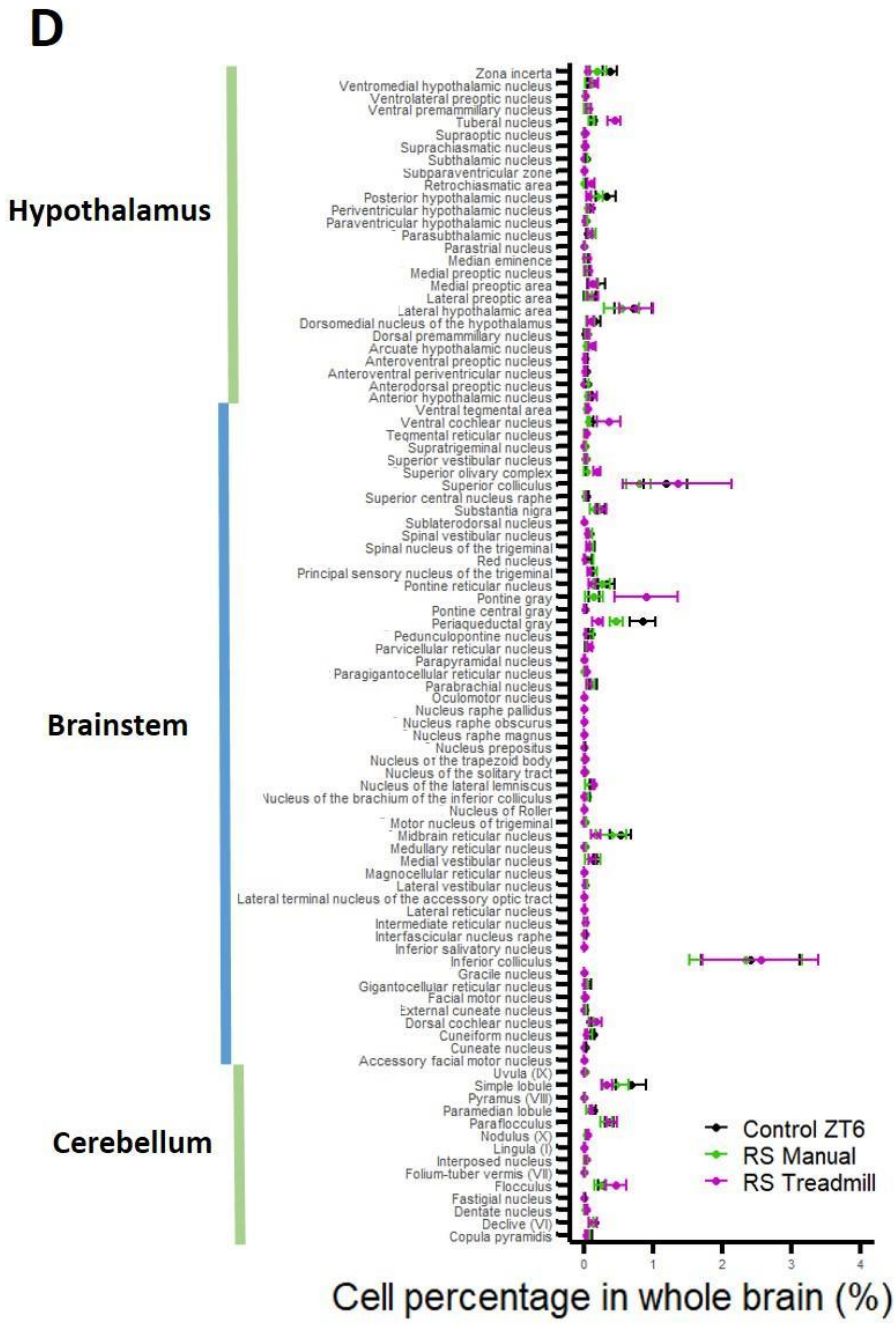

Figure 4.2 (D) Cell percentage of c-Fos positive neurons in hypothalamus, brainstem, and cerebellum in manual RS, treadmill RS, and control ZT4 groups. Line: Mean ± SEM. n=8-10 per group.

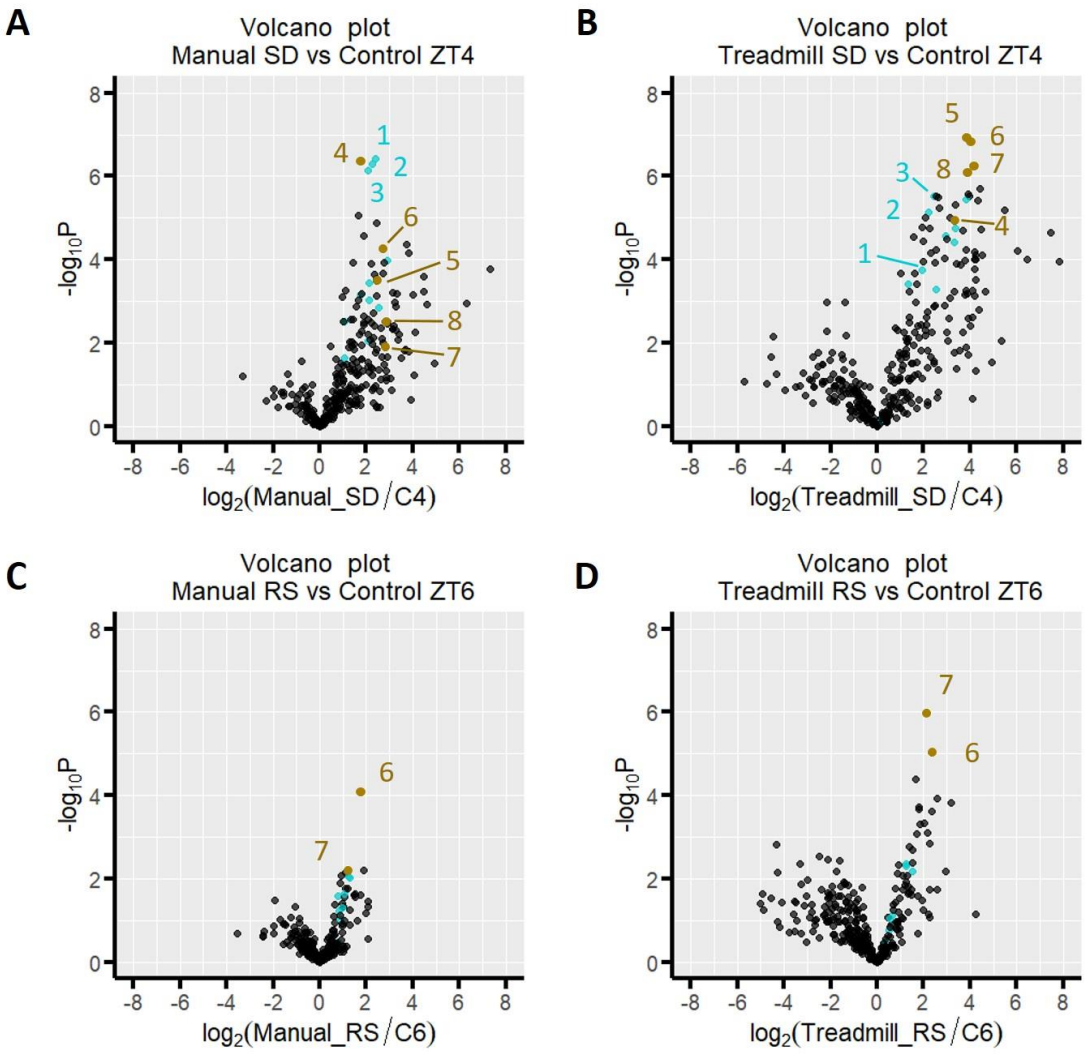

1	Intercalated amygdalar nucleus
2	Basolateral amygdalar nucleus
3	Basomedial amygdalar nucleus
4	Cortical subplate
5	Piriform area
6	Postpiriform transition area
7	Entorhinal area
8	Nucleus of the lateral olfactory tract

Figure 4.3 Volcano plot of c-Fos positive neurons for SD, RS, and control mice. (A) Volcano plot between manual SD and control ZT4 groups. Basolateral, basomedial, and intercalated amygdala, as well as cortical subplate showed low p-value and high fold change. (B) Volcano plot between treadmill SD and control ZT4 groups. Basolateral and basomedial amygdala showed low p-value and high fold change. Piriform area, postpiriform transition area, entorhinal area, and nucleus of the lateral olfactory tract also showed similar trend. (C) Volcano plot between manual RS and control ZT6 groups. Postpiriform transition area showed relatively low p-value compared

to other regions. (D) Volcano plot between treadmill RS and control ZT6 groups. Entorhinal area and postpiriform transition area showed relatively low p-value compared to other regions. The p-values were calculated by Student's t-test. Blue dot: amygdalar area. Brown dot: Non-amydalar area. n=8-10 per group.

Regions: 1.Intercalated amygdalar nucleus, 2. Basolateral amygdalar nucleus, 3. Basomedial amygdalar nucleus, 4. Cortical subplate, 5. Piriform area, 6. Postpiriform transition area, 7. Entorhinal area, 8. Nucleus of the lateral olfactory tract.

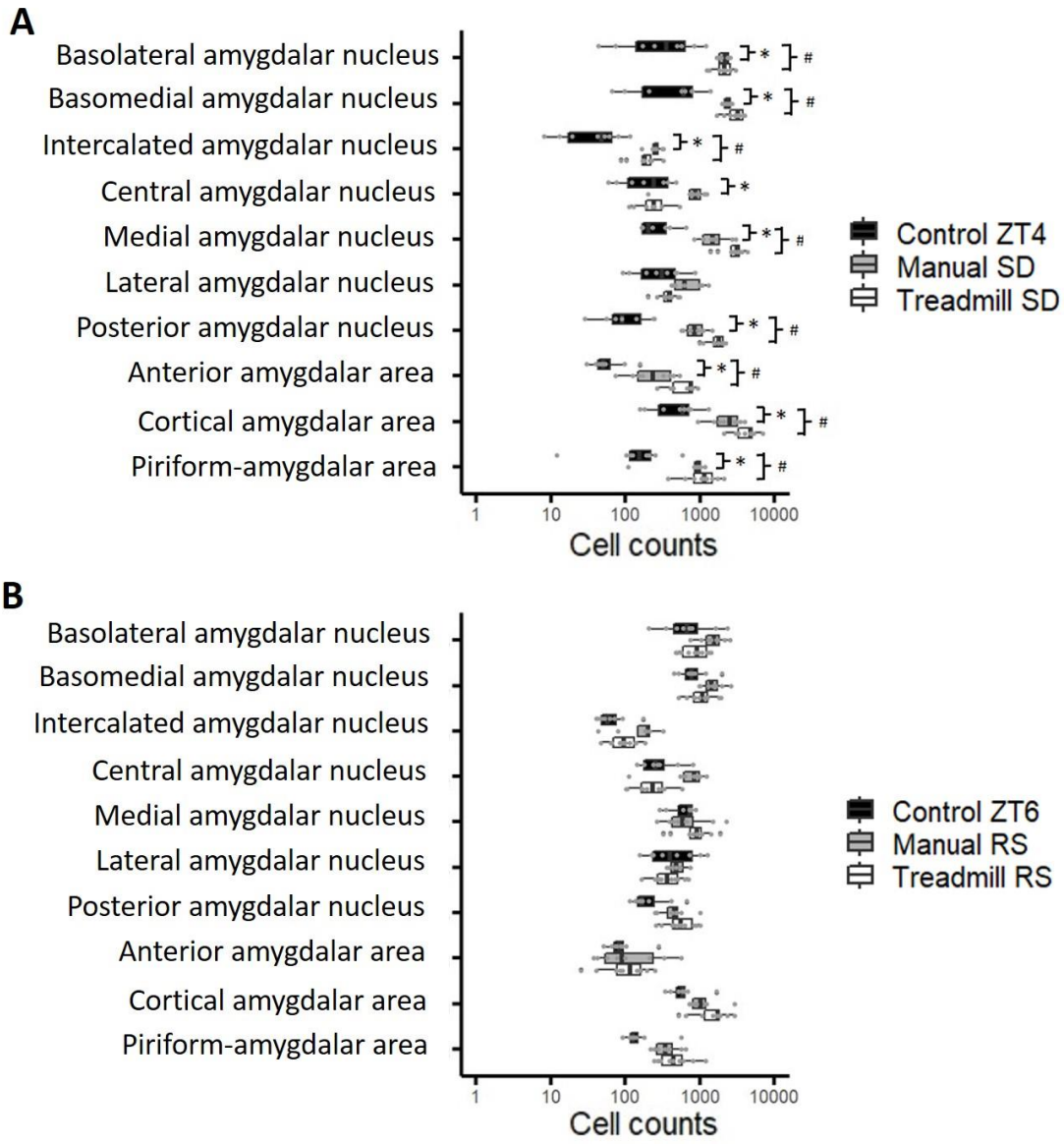

Figure 4.4 Numbers of c-Fos positive neurons in Amygdala regions. (A) Cell counts of active neurons in control ZT4, manual SD, and treadmill SD groups. 9 out of 10 amygdala regions (basolateral amygdalar nucleus, basomedial amygdalar nucleus, intercalated amygdalar nucleus, central amygdalar nucleus, medial amygdalar nucleus, posterior amygdalar nucleus, anterior amygdalar area, cortical amygdalar area, piriform-amygdalar area) in manual SD group showed significant increase of active neurons compared to control ZT4 group. 8 out of 10 amygdala regions (basolateral amygdalar nucleus, basomedial amygdalar nucleus, intercalated amygdalar nucleus, medial amygdalar nucleus, posterior amygdalar nucleus, anterior amygdalar area, cortical amygdalar area, piriform-amygdalar area) in treadmill SD group showed significant increase of active neurons compared to control ZT4 group. (B) Cell counts of active neurons in control ZT6, manual RS, and treadmill RS groups. No amygdala region showed significant difference between manual RS group and control ZT6 group, as well as between treadmill RS group and control ZT6 group. *FDR adjusted p-value (after Student's t-test) <0.05 between manual SD/RS and control ZT4/ZT6 groups, #FDR adjusted p-value (after Student's t-test) <0.05 between treadmill SD/RS and control ZT4/ZT6

groups, FDR: False Discovery Rate for multiple testing correction. n=8-10 per group.

Examine the neuronal activity in previously suggested wake-promoting and NREM/REM sleep-promoting regions

Previous studies have revealed some wake-promoting regions and NREM/REM sleep-promoting regions. Therefore, it would be interesting to see if we can observe activity changes in these regions by using whole brain mapping after either sleep deprivation or recovery sleep.

In the wake-promoting regions, ventral tegmental area was significantly active in manual SD and treadmill SD groups compared to control ZT4 group (FDR adjusted p-value = 0.003 in manual SD group, and 0.02 in treadmill SD group). Tuberomammillary nucleus was significantly active in treadmill SD group compared to control ZT4 group (FDR adjusted p-value < 0.001), but not in manual SD group. Substantia innominata, which is one of the regions of basal forebrain, was significantly active in manual SD and treadmill SD groups compared to control ZT4 group (FDR adjusted p-value = 0.04 in manual SD group, and 0.001 in treadmill SD group). Pallidum, which includes some regions of basal forebrain, was significantly active in treadmill SD group compared to control ZT4 group (FDR adjusted p-value = 0.005), but not in manual SD group (**Fig. 4.5 A**). On the contrary, no wake-promoting region showed significant difference between manual RS group and control ZT6 group, as well as between treadmill RS group and control ZT6 group.

In the NREM sleep-promoting regions, median preoptic nucleus was significantly active in treadmill SD group compared to control ZT4 group (FDR adjusted p-value = 0.04), but not in manual SD group (**Fig. 4.5 B**). On the other hand, one of the REM sleep-promoting regions, paragigantocellular reticular nucleus, was also significantly active in treadmill SD group compared to control ZT4 group (FDR adjusted p-value = 0.02), but not in manual SD group (**Fig. 4.5 C**). On the contrary, no NREM/REM sleep-promoting region showed significant difference between manual RS group and control ZT6 group, as well as between treadmill RS group and control ZT6 group (**Fig. 4.5 D**).

The whole brain mapping was able to reveal some wake-promoting and NREM/REM sleep-promoting regions, but not all of them. This was probably due to different experimental designs and approaches. However, this still showed that our experimental design and approach were able to show some previously suggested wake-promoting and NREM/REM sleep-promoting regions, and the active regions we observed from the whole brain mapping could be the candidate regions to do the functionality study to prove their roles in sleep homeostasis.

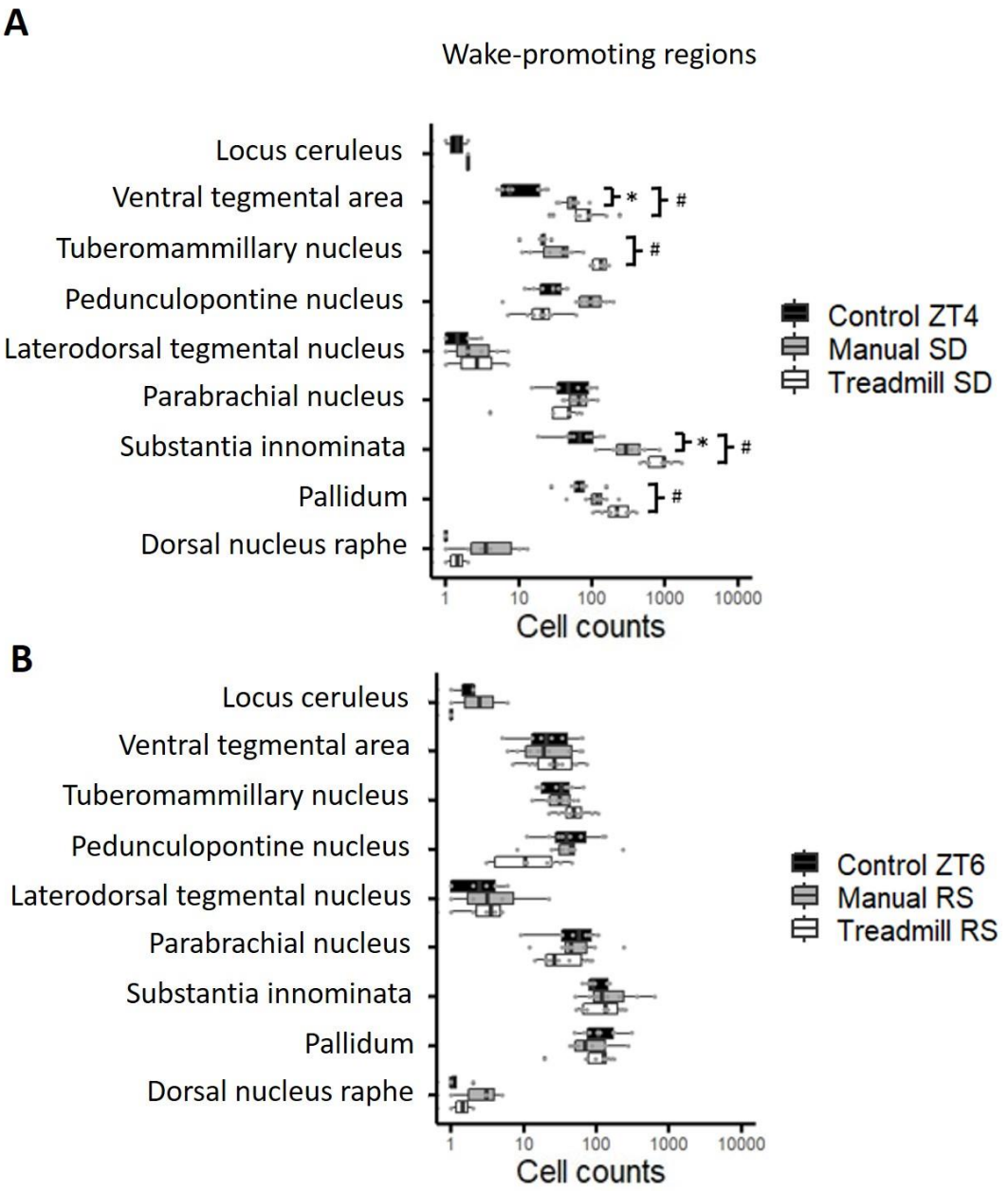

Figure 4.5 Numbers of c-Fos positive neurons in previously suggested wake-promoting and NREM/REM sleep-promoting regions. (A) Cell counts of active neurons in control ZT4, manual SD, and treadmill SD groups at wake-promoting regions. Ventral tegmental area and substantia innominata were significantly active in manual SD and treadmill SD groups compared to control ZT4 group. Tuberomammillary nucleus and pallidum were significantly active in treadmill SD group (compared to control ZT4 group), but not in manual SD group. (B) Cell counts of active neurons in control ZT6, manual RS, and treadmill RS groups at wake-promoting regions. No wake-promoting region showed significant difference between manual RS group and control ZT6 group, as well as between treadmill RS group and control ZT6 group. *FDR adjusted p-value (after Student's t-test) <0.05 between manual SD/RS and control ZT4/ZT6 groups, #FDR adjusted p-value (after Student's t-test) <0.05 between treadmill SD/RS and control ZT4/ZT6 groups, FDR: False Discovery Rate for multiple testing correction. n=8-10 per group.

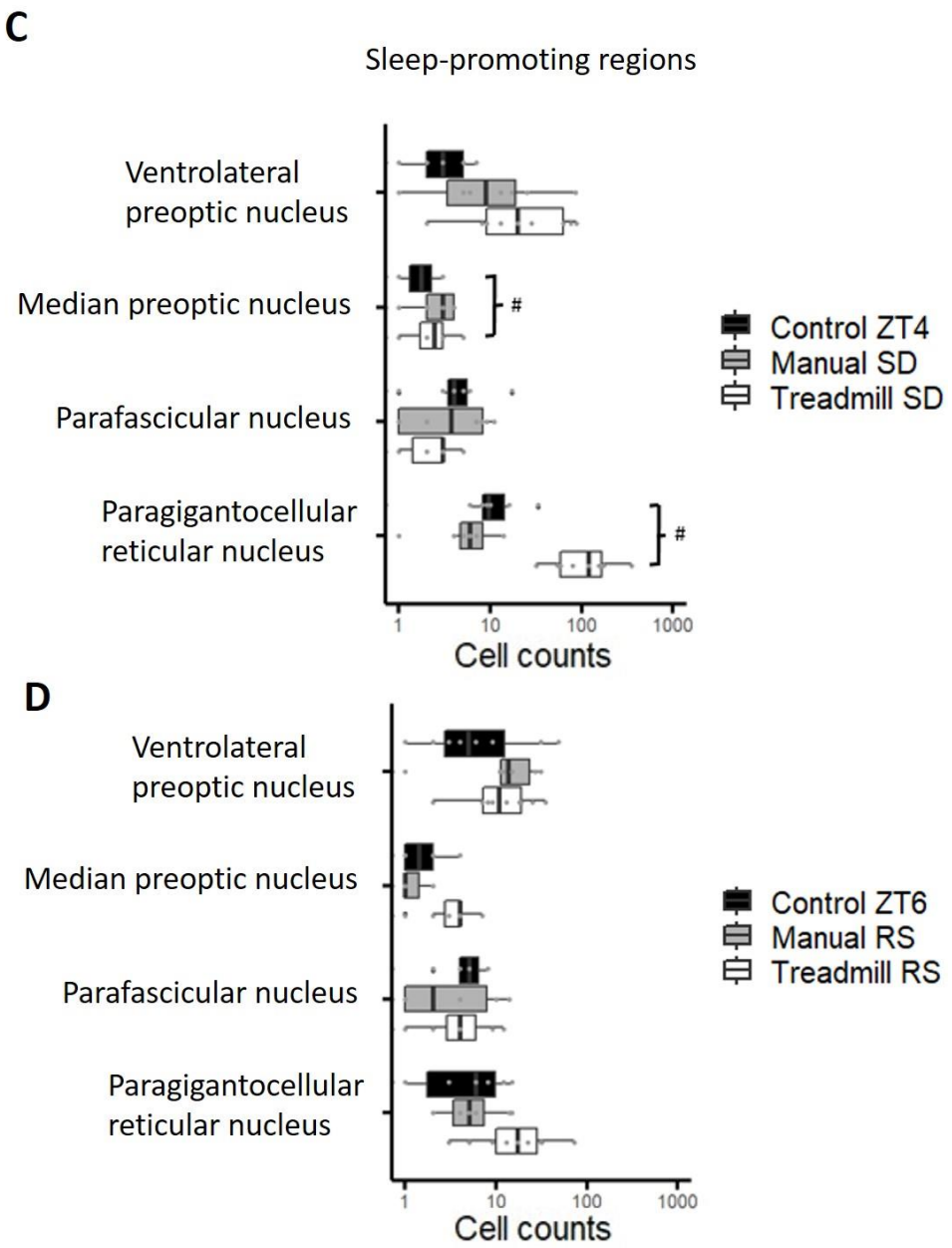

Figure 4.5 Numbers of c-Fos positive neurons in previously suggested wake-promoting and NREM/REM sleep-promoting regions. (C) Cell counts of active neurons in control ZT4, manual SD, and treadmill SD groups at NREM/REM sleep-promoting regions. Median preoptic nucleus and paragigantocellular reticular nucleus were significantly active in treadmill SD group (compared to control ZT4 group), but not in manual SD group. (D) Cell counts of active neurons in control ZT6, manual RS, and treadmill RS groups at NREM/REM sleep-promoting regions. No NREM/REM sleep-promoting region showed significant difference between manual RS group and control ZT6 group, as well as between treadmill RS group and control ZT6 group. #FDR adjusted p-value (after Student's t-test) <0.05 between treadmill SD/RS and control ZT4/ZT6 groups, FDR: False Discovery Rate for multiple testing correction. n=8-10 per group.

Examine the neuronal activity and connectivity in high-level brain regions

Apart from the changes of neural activity in small brain regions, we also wanted to see the activity changes in high-level brain regions and their connectivity in different conditions (SD, RS, and control). Brain regions were collapsed into 11 high-level brain regions (olfactory areas, cerebral nuclei, isocortex, hippocampus, cortical subplate, thalamus , hypothalamus, midbrain, pons, medulla, and cerebellum) as described in chapter 3. Sleep deprivation methodology.

Olfactory areas, cerebral nuclei, isocortex, hippocampus, cortical subplate, hypothalamus, and midbrain were significantly active in manual SD group compared to control ZT4 group (FDR adjusted p-value < 0.001 for olfactory areas, cerebral nuclei, isocortex, cortical subplate, and hypothalamus. FDR adjusted p-value = 0.003 for hippocampus, and 0.007 for midbrain). On the other hand, 10 out of 11 regions (except for thalamus) were significantly active in treadmill SD group compared to control ZT4 group (FDR adjusted p-value < 0.001 for olfactory areas, isocortex, hippocampus, cortical subplate, hypothalamus, and pons. FDR adjusted p-value = 0.001, 0.01, 0.03, 0.04 for cerebral nuclei, midbrain, medulla, and cerebellum, respectively). Thalamus showed significantly lower activity in treadmill SD group compared to control ZT4 group (FDR adjusted p-value = 0.04), which was different from other regions (**Fig. 4.6 A**).

For the RS groups, no region showed significant difference between manual RS group and control ZT6 group. However, olfactory areas was significantly active in treadmill RS group compared to control ZT6 group (FDR adjusted p-value = 0.004), and thalamus showed significantly lower activity in treadmill RS group compared to control ZT6 group (FDR adjusted p-value = 0.02) (**Fig. 4.6 B**). The significantly low activity of thalamus might be caused by locomotion or stress by treadmill, since it was inactive in both treadmill SD and RS groups, but not in both manual SD and RS groups. In general, SD groups showed more active brain regions (7 regions in manual SD and 10 regions in treadmill SD) compared to control ZT4 group, but only 1 region showed significantly higher activity in RS groups compared to control ZT6 group. This suggested that the brain was in general more active under high sleep-drive condition compared to a lower sleep-drive condition, and the wake-promoting mechanism could be more complex than we thought.

Next, we examined the connectivity between the high-level brain regions. The cell counts were first scaled and the Pearson correlation coefficients were computed in all 11 brain regions. Then the heatmaps were plotted to show the Pearson correlation coefficient. The heatmaps from SD (both manual and treadmill) and control ZT4, as well as from RS (both manual and treadmill) and control ZT6 were subtracted to show the differences. In the heatmap, yellow means the correlation is more positive in either SD or RS group compared to control ZT4 or control ZT6 group. On the contrary, blue means the correlation is more positive in control ZT4 or control ZT6 group compared to SD or RS group (**Fig. 4.7**).

We found out that the Pearson correlation coefficients between some regions changed significantly in both SD and RS groups compared to the control groups. For the comparison between manual SD group and control ZT4 group, the Pearson correlation coefficients between cerebral nuclei and thalamus, thalamus and cortical subplate, cortical subplate and midbrain, as well as midbrain and pons showed significant difference (p-value < 0.05) (**Fig. 4.7 A**). For the comparison between treadmill SD group and control ZT4 group, the Pearson correlation coefficients between olfactory areas and 4 regions (cerebral nuclei, isocortex, hypothalamus, pons), cerebral nuclei and 2 other regions (thalamus and hypothalamus), cortical subplate and 3 regions (thalamus, hypothalamus, pons), as well as midbrain and 2 regions (hypothalamus and pons) showed significant difference (p-value < 0.05) (**Fig. 4.7 B**).

Particularly, the Pearson correlation coefficients changed dramatically between midbrain and pons in both manual SD, and treadmill SD groups compared to control ZT4 group ($r = 0.05$ in manual SD group, $r = -0.14$ in treadmill SD group, $r = 0.97$ in control ZT4 group, $p < 0.001$). This was the same between cortical subplate and thalamus, both manual SD and treadmill SD groups showed p-value lower than 0.001 compare to control ZT4 group ($r = 0.41$ in manual SD group, $r = 0.18$ in treadmill SD group, $r = -0.94$ in control ZT4 group, $p < 0.001$) (**Fig. 4.7 A and B**). This suggested that the connectivity between midbrain and pons, as well as between cortical subplate and thalamus might be affected strongly by sleep deprivation, and could imply potential projection routes that were involved in sleep homeostasis. Additionally, the Pearson correlation coefficient between thalamus and cerebral nuclei also changed significantly in both manual SD and treadmill SD groups compared to control ZT4 group ($r = 0.82$ in manual SD group, $r = 0.85$ in treadmill SD group, $r = -0.07$ in control ZT4 group, $p < 0.05$) (**Fig. 4.7 A and B**).

On the other hand, for the comparison between manual RS group and control ZT6 group, the Pearson correlation coefficients between cortical subplate and hippocampus ($r = 0.40$ in manual RS group, $r = 0.93$ in control ZT6 group, $p = 0.04$), as well as hippocampus and cerebellum showed significant difference ($r = 0.93$ in manual RS group, $r = 0.33$ in control ZT6 group, $p = 0.03$) (**Fig. 4.7 C**). For the comparison between treadmill RS group and control ZT6 group, the Pearson correlation coefficients between cortical subplate and olfactory areas ($r = 0.90$ in treadmill RS group, $r = 0.24$ in control ZT6 group, $p = 0.03$), cortical subplate and hippocampus ($r = -0.01$ in treadmill RS group, $r = 0.93$ in control ZT6 group, $p = 0.004$), cerebellum and thalamus ($r = 0.37$ in treadmill RS group, $r = -0.74$ in control ZT6 group, $p = 0.02$), cerebellum and pons ($r = 0.60$ in treadmill RS group, $r = -0.43$ in control ZT6 group, $p = 0.04$), as well as isocortex and hippocampus ($r = -0.33$ in treadmill RS group, $r = -0.90$ in control ZT6 group, $p = 0.04$) showed significant difference (**Fig. 4.7 D**). In general, both RS groups showed fewer significant changes at connectivity. However, The Pearson correlation coefficient changed significantly between cortical subplate and hippocampus in both manual RS and treadmill RS

groups compared to control ZT6 group (p-value < 0.05). This suggested that the connectivity change between these 2 regions might be particularly specific to sleep homeostasis since it changed in both RS groups (**Fig. 4.7 C and D**).

In order to have a better look at the correlation in each group and the distribution of the data, linear regression between two regions was computed and plotted. Only the regions that showed significantly different correlation between both SD groups (manual and treadmill) and control ZT4 group were shown (mentioned above). The correlation between midbrain and pons was strongly positive in control ZT4 group ($r = 0.97$, $p < 0.001$), and was absent in manual SD ($r = 0.05$, $p = 0.89$) and treadmill SD groups ($r = -0.14$, $p = 0.71$) (**Fig. 4.8 A**). On the other hand, the correlation between cortical subplate and thalamus was strongly negative in control ZT4 group ($r = -0.94$, $p < 0.001$), and was positive in manual SD ($r = 0.41$, $p = 0.049$) and treadmill SD groups ($r = 0.18$, $p = 0.13$) (**Fig. 4.8 B**). Last but not least, the correlation between thalamus and cerebral nuclei was strongly positive in manual SD ($r = 0.82$, $p = 0.01$) and treadmill SD groups ($r = 0.85$, $p = 0.003$), and was absent in control ZT4 group ($r = -0.07$, $p = 0.86$) (**Fig. 4.8 C**).

The linear regression was mainly to examine the correlation in each group and the distribution of the data, and further support the changes of connectivity in the heatmaps above.

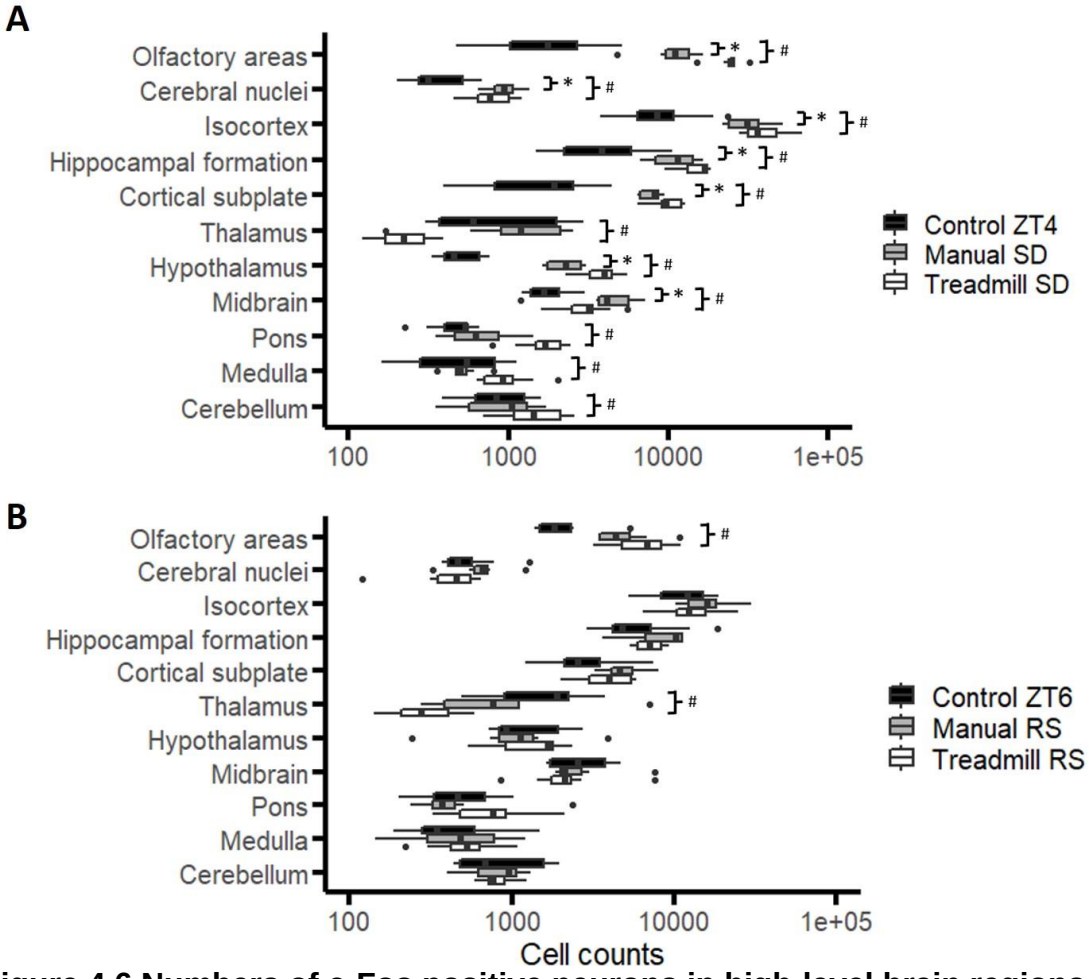

Figure 4.6 Numbers of c-Fos positive neurons in high-level brain regions for SD, RS, and control mice. (A) Numbers of c-Fos positive neurons in control ZT4, manual SD, and treadmill SD groups. Olfactory areas, cerebral nuclei, isocortex, hippocampus (hippocampal formation), cortical subplate, hypothalamus, and midbrain were significantly active in manual SD group compared to control ZT4 group. 10 out of 11 regions (except for thalamus) were significantly active in treadmill SD group compared to control ZT4 group. Thalamus showed significantly lower activity in treadmill SD group compared to control ZT4 group. (B) Numbers of c-Fos positive neurons in control ZT6, manual RS, and treadmill RS groups. No region showed significant difference between manual RS group and control ZT6 group. Olfactory areas was significantly active in treadmill RS group compared to control ZT6 group, and thalamus showed significantly lower activity in treadmill RS group compared to control ZT6 group. *FDR adjusted p-value (after Student's t-test) <0.05 between manual SD/RS and control ZT4/ZT6 groups, #FDR adjusted p-value (after Student's t-test) <0.05 between treadmill SD/RS and control ZT4/ZT6 groups, FDR: False Discovery Rate for multiple testing correction. n=8-10 per group.

Figure 4.7 The connectivity of high-level brain regions for SD, RS, and control mice. The subtraction heatmaps of Pearson correlation coefficient between difference regions between (A) manual SD and control ZT4 groups, (B) treadmill SD and control ZT4 groups, (C) manual RS and control ZT6 groups, (D) treadmill RS and control ZT6 groups. The Pearson correlation coefficients between cortical subplate and thalamus, between midbrain and pons, as well as between thalamus and cerebral nuclei changed significantly in both manual SD and treadmill SD groups compared to control ZT4 group. The Pearson correlation coefficient also changed significantly between cortical subplate and hippocampus in both manual RS and treadmill RS groups compared to control ZT6 group. Magenta squares mean the p-values between control ZT4 and manual SD, or between control ZT4 and treadmill SD are lower than 0.05 (solid line), or 0.001 (dashed line). Brown squares mean the p-values between control ZT6 and manual RS, or between control ZT6 and treadmill RS are lower than 0.05 (solid line) after statistical test by cocor (A Comprehensive Solution for the Statistical Comparison of Correlations, 2015)[138]. n=8-10 per group.

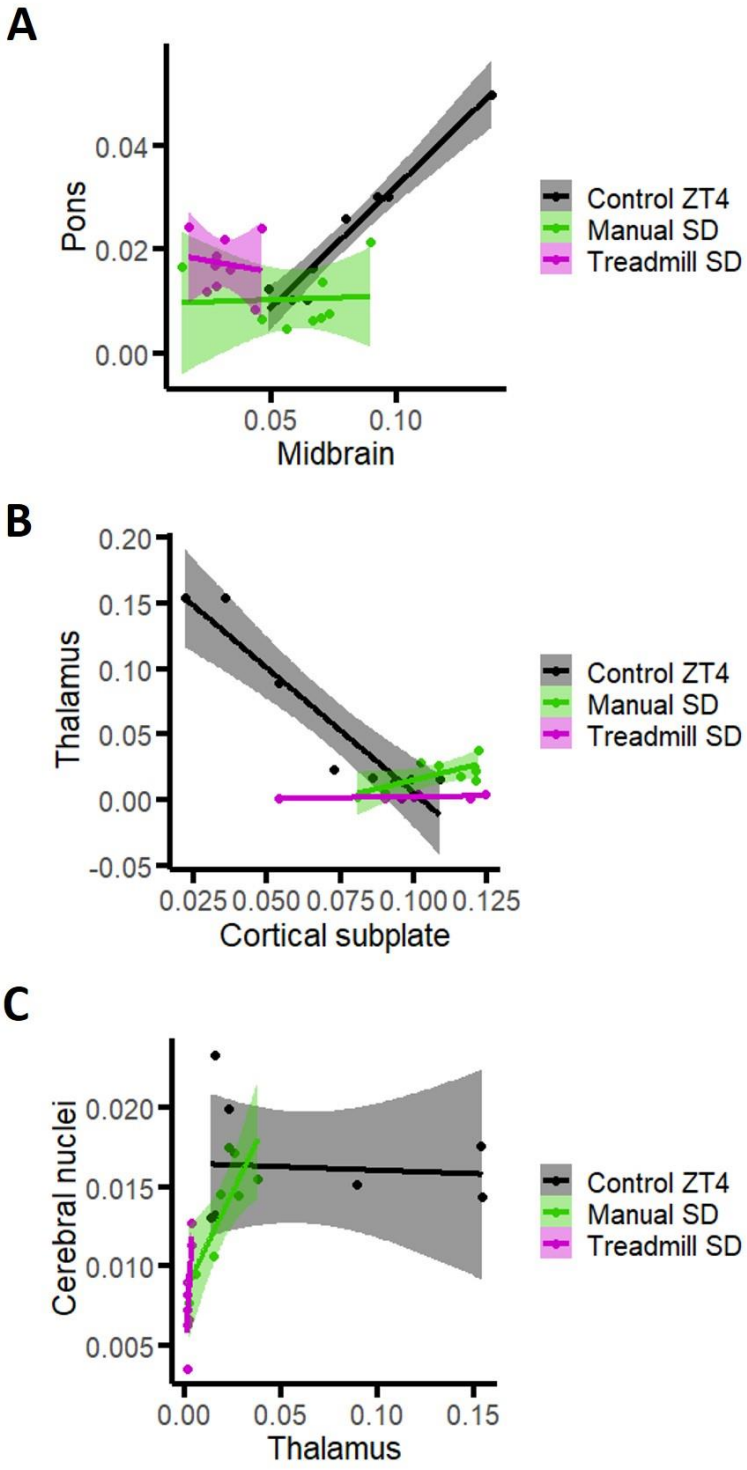

Figure 4.8 Linear regression between different pairs of brain regions. The linear regression between (A) midbrain and pons, (B) cortical subplate and thalamus, (C) thalamus and cerebral nuclei in control ZT4, manual SD, and treadmill SD groups. Line: linear regression. n=8-10 per group.

Visualization of the cell detection results from ClearMap

ClearMap provided us the numbers of c-Fos positive neurons in different brain regions, and allowed us to examine the neuronal activity in different brain regions under different conditions. However, these were all numbers without any images. Therefore, it would be nice if the brain activity could be visualized, and allowed us to have a glimpse of the results from ClearMap.

Luckily, ClearMap provided 2 ways to do this. The first one was called mean neuronal activity heatmaps. It averaged the numbers of c-Fos positive neurons from samples in the same group, and presented it as heatmap. In the previous paragraphs, we found out amygdala areas and cortical subplate were more active in SD groups compared to control ZT4 group (**Fig. 4.4 and 4.6**). Therefore, we were more interested in these two regions, and aimed to visualize these two regions. Amygdala areas, cortical subplate, and olfactory areas were labelled in the mean activity heatmaps from one of the coronal sections of the brain (**Fig. 4.9 A and B**). The neuronal activity was way stronger in manual SD and treadmill SD groups compared to control ZT4 group in both amygdala areas and cortical subplate (**Fig. 4.9 A**). On the contrary, manual and treadmill RS groups only showed subtly stronger activity in amygdala areas compared to control ZT6 group (**Fig. 4.9 B**).

The second way that ClearMap provided to visualize the results was called voxel p-value heatmaps. It compared the intensity (grey value) of voxel between two groups, and ran Student's t-test on every voxel throughout the entire brain (**Fig. 4.9 C and D**). The green channel means the voxel intensity in SD or RS groups was significantly stronger compared to control ZT4 or ZT6 groups (p-value < 0.05). The magenta channel represents the opposite, voxel intensity in SD or RS groups was significantly weaker compared to control ZT4 or ZT6 (p-value lower than 0.05). The results were similar to the mean neuronal activity heatmaps from **Fig. 4.9 A and B**. The green channel was dominant in amygdala areas and cortical subplate in the heatmaps between manual SD and control ZT4 groups, as well as between treadmill SD and control ZT4 groups (**Fig. 4.9 C**). This suggested that the neuronal activity was stronger in SD groups compared to control ZT4 group. On the contrary, the green channel was not dominant in amygdala areas in the heatmaps between manual RS and control ZT6 groups, as well as between treadmill RS and control ZT6 groups (**Fig. 4.9 D**). This suggested that the activity difference between RS groups and ZT6 group was subtle in amygdala areas.

These heatmaps visualized the neuronal activity on readable coronal planes (of the brain), and allowed us to have a glimpse of the results from ClearMap.

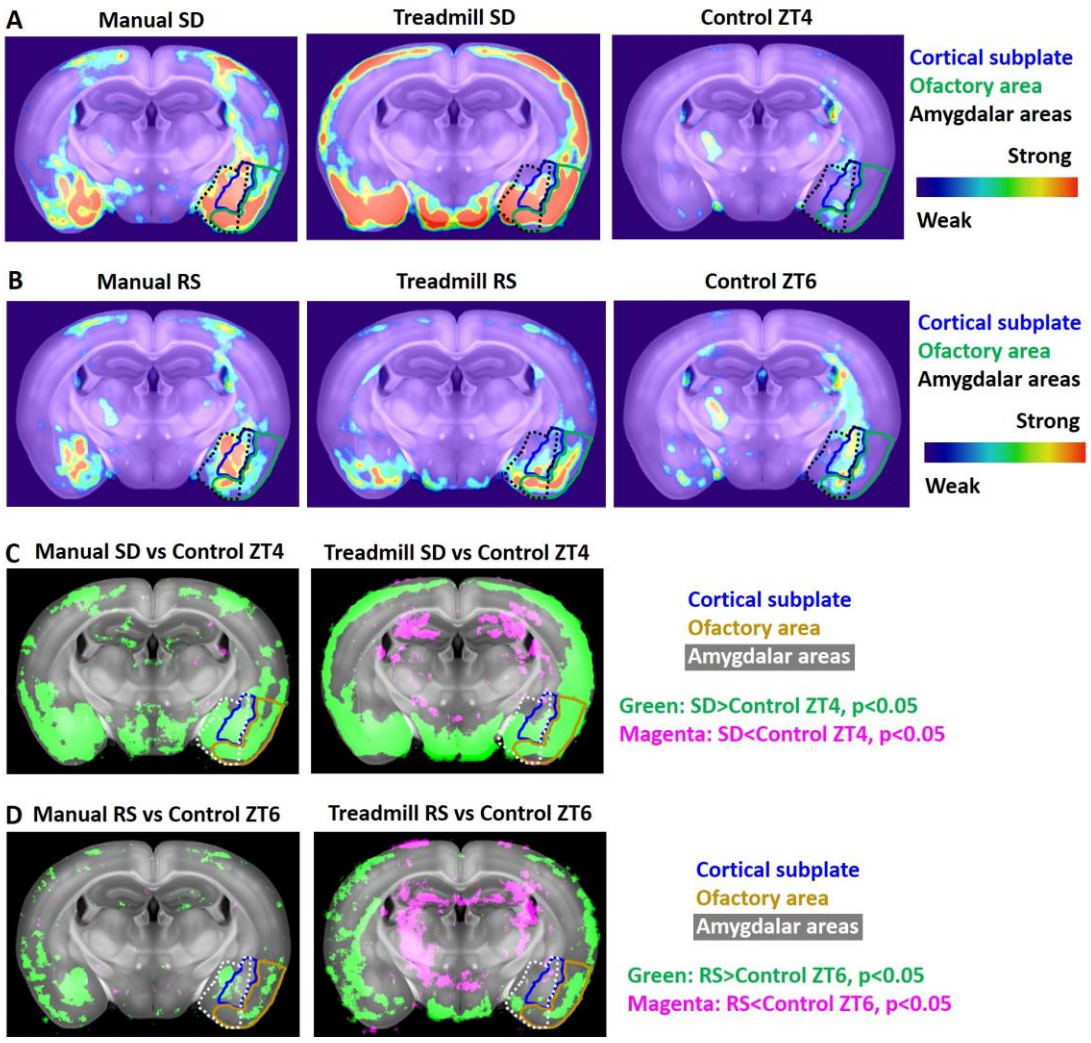

Figure 4.9 Visualization of the neuronal activity and the voxel p-value heatmaps. (A) Mean neuronal activity heatmaps in manual SD, treadmill SD, and control ZT4 groups. The neuronal activity was way stronger in manual SD and treadmill SD groups compared to control ZT4 group in both amygdala areas and cortical subplate. (B) Mean neuronal activity heatmaps in manual RS, treadmill RS, and control ZT6 groups. Manual and treadmill RS groups only showed subtly stronger activity in amygdala areas compared to control ZT6 group. (C) Voxel p-value heatmaps between SD and control ZT4 groups. Green channel means the intensity (grey value) of voxel in SD groups was significantly higher than the intensity in control ZT4 group, and the magenta channel means the intensity (grey value) of voxel in SD groups was significantly lower than the intensity in control ZT4 group (p-value < 0.05). The green channel was dominant in amygdala areas and cortical subplate in the heatmaps between manual SD and control ZT4 groups, as well as between treadmill SD and control ZT4 groups. (D) Voxel p-value heatmaps between RS and control ZT6 groups. Green channel means the intensity (grey value) of voxel in RS groups was significantly higher than the intensity in control ZT6 group, and the magenta channel means the intensity (grey value) of voxel in RS groups was significantly lower than the intensity in control ZT6 group (p-value < 0.05). The green channel was not dominant in amygdala areas in the heatmaps between manual RS and control ZT6 groups, as well as between treadmill RS and control ZT6 groups. Statistics: Student's t-test based on the

intensity (grey value) on each voxel. n=8-10 per group.

Further exploring by PCA

In the last few paragraphs, we used conventional statistics to look for the brain regions that showed different activity between treadmill SD/RS, manual SD/RS, and control ZT4/ZT6 groups. However, we wanted to see if PCA (principal component analysis) could further sort out the brain regions that show differences among treadmill SD/RS, manual SD/RS, and control ZT4/ZT6 groups. This result could be a supplement to our previous results from conventional statistics.

PCA is a dimensional reduction method that orthogonally projects data points onto several principal components in order to have lower-dimensional data but at the same time preserve the original variation as much as possible. It is mostly used to reduce the dimensions of the data and facilitate the following analysis or comparison. Here we used PCA to orthogonally transform the activity of brains regions (numbers of c-Fos positive neurons) to several principal components, which became the new variables of the data and were able to show the regions that caused more differences among different groups in a mathematical way.

In the SD and control ZT4 groups, PC1 (Dimension 1, or Dim1) showed a clear difference between treadmill SD (around -10), manual SD (around 0), and control ZT4 groups (around 11). Especially between treadmill SD and control ZT4 groups since there was no overlap at all. This dimension (PC1) accounted for 26.7% of the variances in the original data, which was more than 1/4 of the contribution (**Fig. 4.10 A**). PC2 (Dimension 2, or Dim2) showed difference between manual SD (around -7) and control ZT4 group (around 4), as well as between manual SD and treadmill SD group (around 4), and it accounted for 14.2% of the variances in the original data (**Fig. 4.10 A**).

I then plotted the 10 brain regions that represented the most on PC1 and PC2 (regions with the 10 highest cos2 on PC1 and PC2), and showed their correlation to PC1 and PC2. Medial vestibular nucleus and lateral vestibular nucleus were positively correlated to PC1, so these regions were more active in control ZT4 group, less active in manual SD group, and the least active in treadmill SD group. On the contrary, piriform area, postpiriform transition area, and entorhinal area were strongly and negatively correlated to PC1, and were more active in treadmill SD group, less active in manual SD group, and the least active in control ZT4 group (**Fig. 4.10 B**). On the other hand, pons showed the strongest positive correlation to PC2, suggesting that pons was more active in control ZT4 and SD Treadmill groups compared to manual SD group. (**Fig. 4.10 B**). However, PC3 (Dimension 3, or Dim3) and PC4 (Dimension 4, or Dim4) did not show too much differences among control ZT4 and the two SD groups (**Fig. 4.10 C and D**).

In the RS and control ZT6 groups, PC1 showed a clear difference between treadmill RS (around -9) and the other 2 groups: manual RS (around 4) and control ZT6 groups (around 8). There was a slight difference between manual RS and control ZT6 groups but very subtle. This dimension (PC1) accounted for 18% of the variances in the original data, which was a bit less compared to

the PC1 from the SD/control ZT4 groups (**Fig. 4.11 A**). PC4 showed differences between manual RS (around -6) and the other 2 groups: treadmill RS (around 2) and control ZT6 groups (around 4). However, it only accounted for 6.7% of the variances in the original data (**Fig. 4.11 C**).

I then plotted the 10 brain regions that represented the most on PC1 and PC2, as well as the 7 brain regions that represented the most on PC3 and PC4. Field CA2, thalamus, zona incerta, and pontine reticular nucleus were strongly and positively correlated to PC1, so these regions were more active in control ZT6 and manual RS groups, less active in treadmill RS group. On the contrary, postpiriform transition area, perirhinal area, and entorhinal area were strongly and negatively correlated to PC1, so these regions were more active in treadmill RS groups, less active in manual RS and control ZT6 groups (**Fig. 4.11 B**). On the other hand, medial preoptic nucleus showed the strongest positive correlation to PC4, suggesting that it was more active in control ZT6 and treadmill RS groups compared to manual RS group. On the contrary, several amygdala nuclei (central amygdalar nucleus, intercalated amygdalar nucleus, basomedial amygdalar nucleus) and bed nuclei of the stria terminalis showed strongest negative correlation to PC4, suggesting that these regions were more active in manual RS group compared to treadmill RS and control ZT6 groups (**Fig. 4.11 D**). However, PC2 and PC3 did not show too much differences among control ZT6, and the two RS groups (**Fig. 4.11 A and C**).

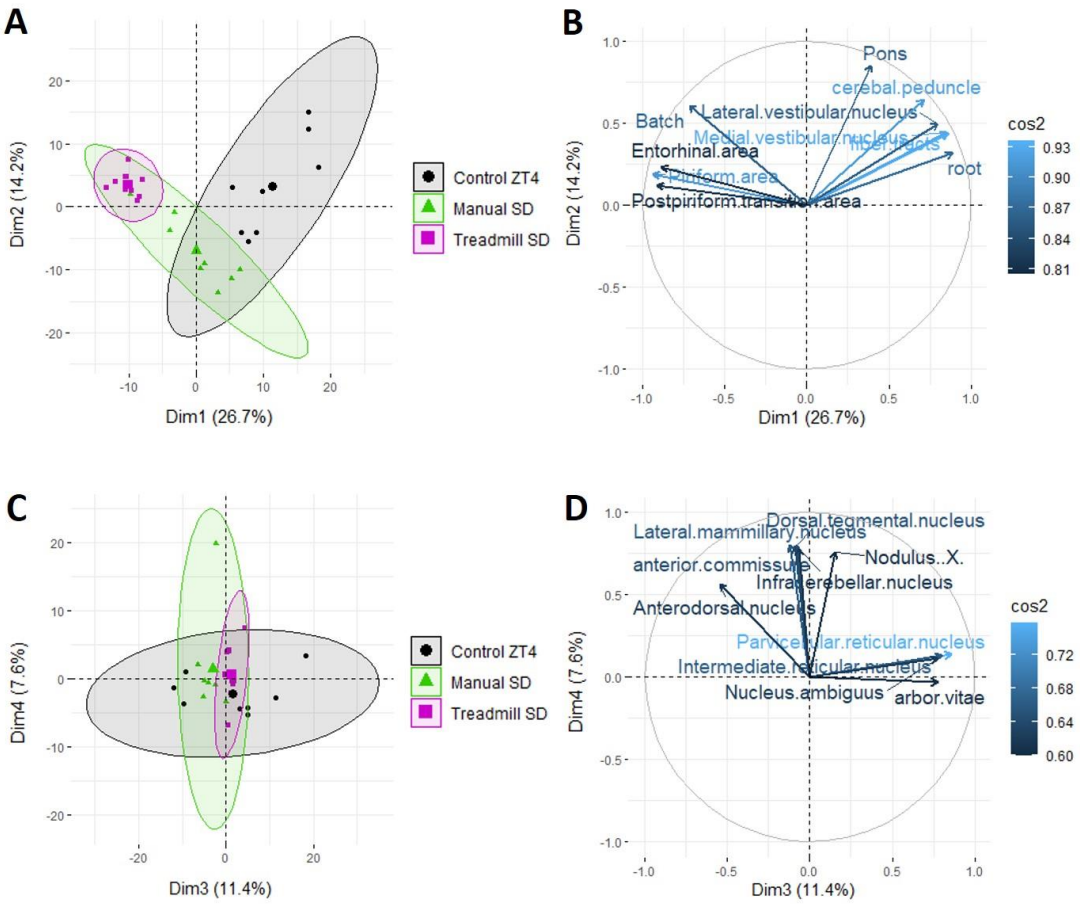

Figure 4.10 PCA for the neuronal activity in SD and control ZT4 groups. (A) PC1 (Dim1) and PC2 (Dim2) for manual SD, treadmill SD, and control ZT4 groups. PC1 showed difference between control ZT4, manual SD, and treadmill SD groups. PC2 showed difference between manual SD and the other 2 groups. (B) The main regions that accounted for PC1 and PC2. (C) PC3 (Dim3) and PC4 (Dim4) for manual SD, treadmill SD, and control ZT4 groups. No strong differences among control ZT4, and the two SD groups. (D) The main regions that accounted for PC3 and PC4. Cos2: The quality of representation of the variables on the principal component. n=8-10 per group.

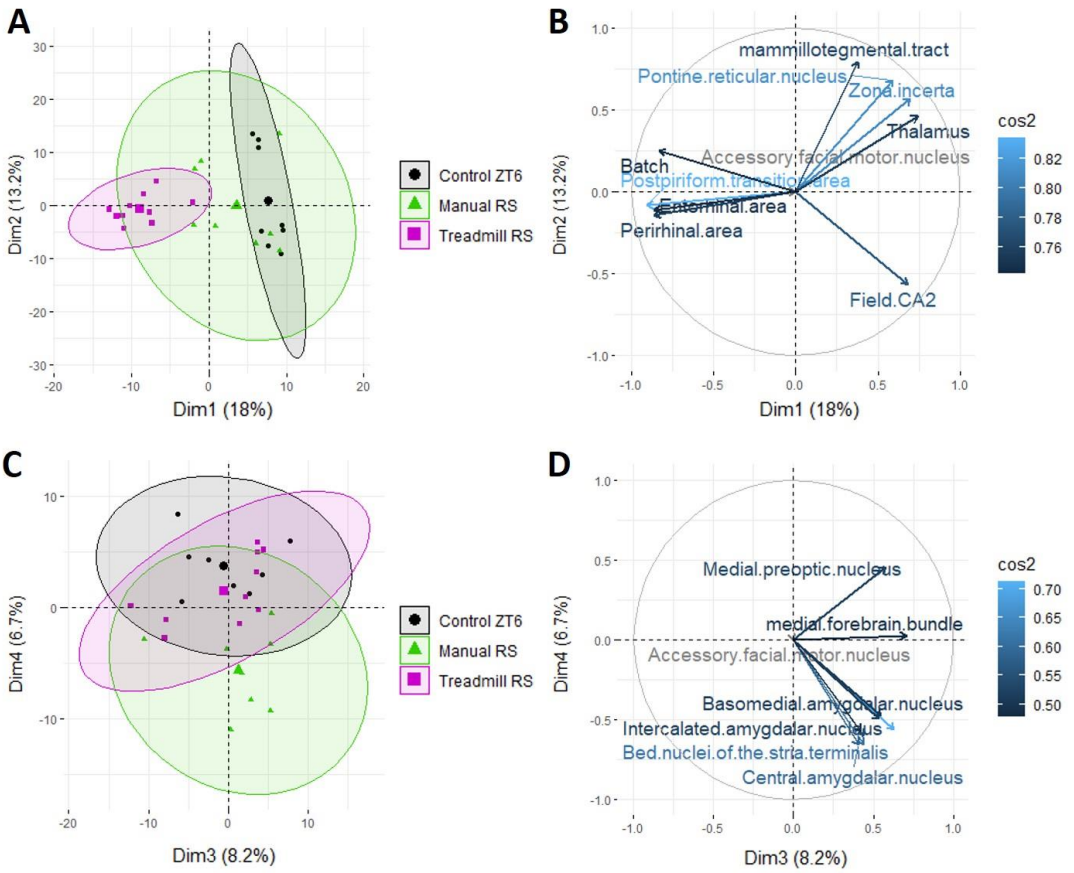

Figure 4.11 PCA for the neuronal activity in RS and control ZT6 groups. (A) PC1 (Dim1) and PC2 (Dim2) for manual RS, treadmill RS, and control ZT6 groups. PC1 showed difference between treadmill RS and the other 2 groups. (B) The main regions that accounted for PC1 and PC2. (C) PC3 (Dim3) and PC4 (Dim4) for manual RS, treadmill RS, and control ZT6 groups. PC4 showed subtle difference between manual RS and the other 2 groups. (D) The main regions that accounted for PC3 and PC4. Cos2: The quality of representation of the variables on the principal component. n=8-10 per group.

Immunohistochemistry validation of the results from tissue clearing

Whole brain mapping is a powerful tool that could automatically detect cells throughout the whole brain and annotate the brain regions. However, the gold standard of immunohistochemistry cell counting is based on traditional tissue sectioning and manual cell counting. Therefore, we did conventional immunohistochemistry validation to support our data (cell counts from tissue clearing and ClearMap). Since the most interesting region that we found was amygdala regions (showed strong activity after SD), we decided to validate the cell counts in amygdala regions.

We collaborated with Dr. Melissa Chee and Nikita Koziel Ly (Carleton University, Canada) to do the immunohistochemistry parcellation. We prepared and stained the tissues, they did the parcellation and manual cell counting. The flowchart of parcellation and an example of the tissue were shown in **Fig. 4.12 A**.

From the results of immunohistochemistry parcellation, 6 amygdala regions showed significantly higher numbers of c-Fos positive neurons in manual SD group compared to control group, these regions were:

1. Basolateral amygdalar nucleus (BLA) and basomedial amygdalar nucleus (BMA) in cortical subplate (**Fig. 4.12 B**).

2. Anterior amygdalar area (AAA), central amygdalar nucleus (CEA), intercalated amygdalar nucleus (IA), and medial amygdalar nucleus (MEA) in striatum-like amygdalar nuclei (**Fig. 4.12 C**).

The results were similar to the tissue clearing data (**Fig.4.4 A**), that BLA, BMA, AAA, CEA, IA, and MEA were more active in manual SD group compared to control group, and lateral amygdalar nucleus (LA) did not show significant difference between manual SD and control group. Therefore, we are confident to say that amygdala neurons (especially BLA and BMA) are significantly active in high sleep-drive condition (after sleep deprivation).

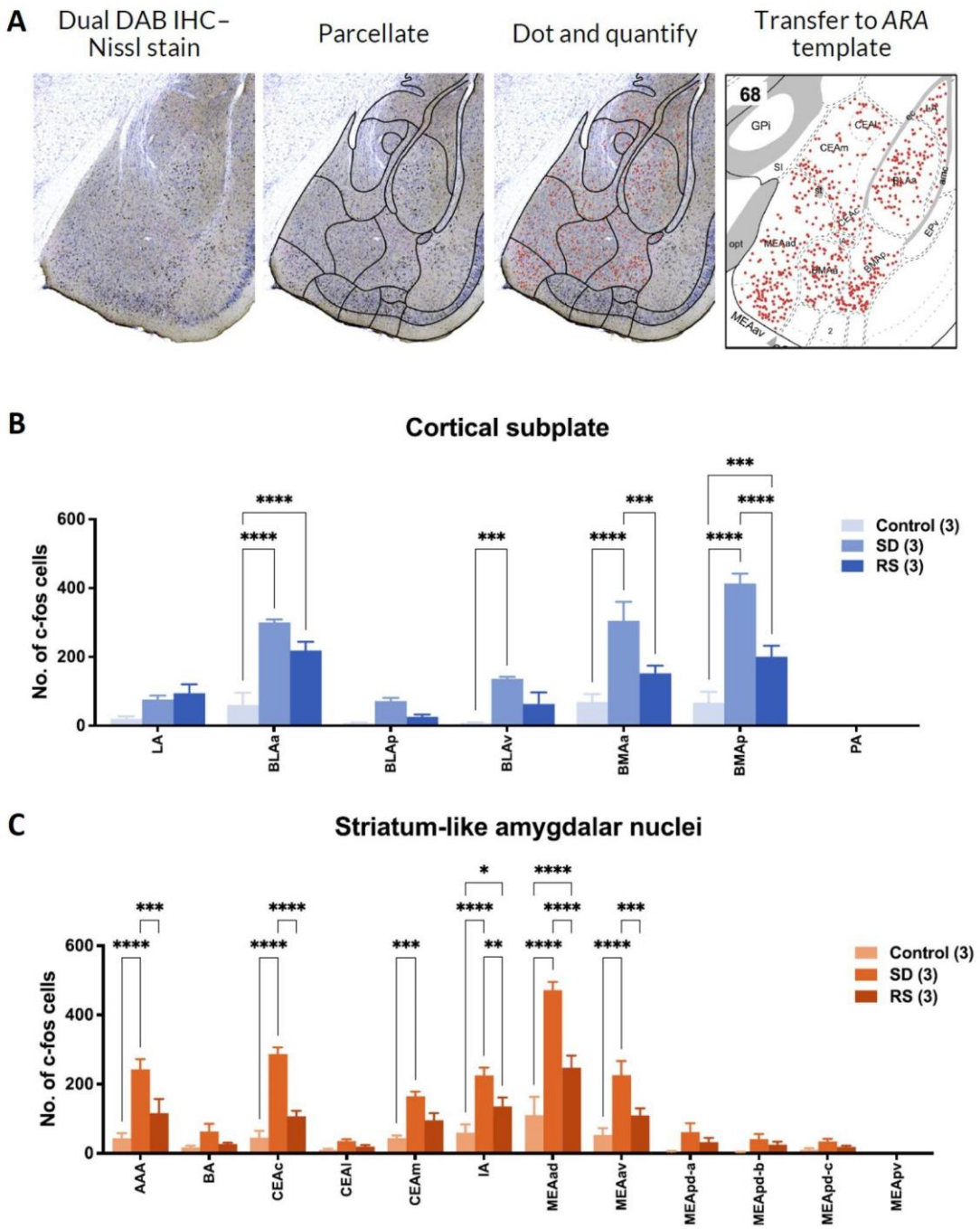

Figure 4.12 immunohistochemistry parcellation in amygdala regions ***(figure was made by Nikita Koziel Ly and Dr. Melissa Chee).*** (A) The steps of parcellation with manual cell counting. (B) The numbers of c-Fos positive cells in amygdala regions in cortical subplate. Basolateral amygdalar nucleus (BLA) and basomedial amygdalar nucleus (BMA) showed significantly higher numbers of c-Fos positive neurons in manual SD group compared to control group. (C) The numbers of c-Fos positive cells in amygdala regions in striatum-like amygdalar nuclei. Anterior amygdalar area (AAA), central amygdalar nucleus (CEA), intercalated amygdalar nucleus (IA), and medial amygdalar nucleus (MEA) showed significantly higher numbers of c-Fos positive neurons in manual SD group compared to control group. *p-value < 0.05. SD: manual SD, RS: manual RS. Control: control ZT4. LA: Lateral amygdalar nucleus. BLAa: Basolateral amygdalar nucleus, anterior part.

BLAp: Basolateral amygdalar nucleus, posterior part. BLAv: Basolateral amygdalar nucleus, ventral part. BMAa: Basomedial amygdalar nucleus, anterior part. BMAp: Basomedial amygdalar nucleus, posterior part. PA: Posterior amygdalar nucleus. AAA: Anterior amygdalar area. BA: Bed nucleus of the accessory olfactory tract. CEAc: Central amygdalar nucleus, capsular part. CEAl: Central amygdalar nucleus, lateral part. CEAm: Central amygdalar nucleus, medial part. IA: Intercalated amygdalar nucleus. MEAad: Medial amygdalar nucleus, anterodorsal part. MEAav: Medial amygdalar nucleus, anteroventral part. MEApd-a: Medial amygdalar nucleus, posterodorsal part, sublayer a. MEApd-b: Medial amygdalar nucleus, posterodorsal part, sublayer b. MEApd-c: Medial amygdalar nucleus, posterodorsal part, sublayer c. MEApv: Medial amygdalar nucleus, posteroventral part. n=3 per group.

#Data in the figure was analysed by Nikita Koziel Ly and Dr. Melissa Chee for the project

Discussion

In this study, we found out that amygdala regions were significantly active after sleep deprivation (**Fig. 4.4**), suggesting they were active when the sleep drive is high. Amygdala is well known for its function for learning, emotion, stress, memory, and anxiety[159–162]. Recently some studies suggested that amygdala regions are also involved in sleep. In 2019, Ma et al. identified GABAergic neurons in central amygdala nucleus (CEA) and glutamatergic neurons in the posterior thalamus promoted NREM sleep[163]. In 2022, Wellman et al. suggested that optogenetic activation of CEA neurons projecting to reticularis pontis oralis enhanced REM sleep but did not alter NREM sleep[164]. In 2022, Hasegawa et al. identified that REM sleep was initiated by basolateral amygdala nucleus (BLA) dopamine signaling[165]. In 2021, Machida et al. suggested that BLA regulated EEG theta-activity during REM sleep[166]. Additionally, in 2022 Matei et al. observed global dissociation of the posterior amygdala from the rest of the brain during REM sleep, suggesting posterior amygdala may be involved in REM sleep regulation[167]. Therefore, previous studies in general showed that CEA and BLA are involved in mediation of REM sleep and NREM sleep.

In our study, we found out that CEA was significantly active after manual sleep deprivation (**Fig. 4.4**), which could suggest that CEA tried to promote NREM sleep when sleep drive was high. This would match the results from Ma et al. However, we didn't have a functional study to identify its functionality. Interestingly, CEA was not significantly active after treadmill sleep deprivation. This might suggest that the high locomotion or stress caused by treadmill changed the mediation mechanism of CEA. In our study, we also found out the BLA and basomedial amygdalar nucleus (BMA) were significantly active after both treadmill and manual sleep deprivation (**Fig. 4.3 and 4.4**). The results from Hasegawa et al. suggested that BLA triggers REM sleep. However, this study didn't involve sleep deprivation, and we would like to know the functions of BLA/BMA when the sleep drive is high. Are BLA/BMA trying to promote sleep when the sleep drive is high? Or are BLA/BMA trying to maintain/keep the mice awake when the sleep drive is high?

In order to answer this question, we did *in vivo* functional study on mice. We used Chemogenetics (hM3Gq and KORD[168]) to either stimulate or inhibit BLA/BMA, and recorded sleep behavior by EEG and piezo. This study is still being analyzed and therefore not yet completed. However, we aimed to see if BLA/BMA play a role in sleep homeostasis especially when the sleep drive is high. Apart from the *in vivo* functional study, we also did single nucleus RNA sequencing. The results from tissue clearing and ClearMap were based on c-Fos signals. C-Fos is a marker for active neurons, so it shows all active neurons, but won't tell any information about the cell clusters.Therefore, with collaboration with Dr. Celia P. Martinez-Jimenez, we did single nucleus RNA sequencing and aimed to find out the cell clusters that were active after sleep deprivation. This study is still being analyzed and therefore not yet completed.

By comparing the Pearson correlation coefficients between different regions, we noticed that the connectivity between midbrain and pons, as well as between cortical subplate and thalamus changed significantly after both

manual and treadmill sleep deprivation (**Fig. 4.7 and 4.8**). The connectivity between midbrain and pons is interesting because they both have wake-promoting regions (dorsal raphe nuclei, ventral tegmental area, and PPT are located in midbrain, while locus coeruleus, LDT, and parabrachial nucleus are located in pons). In the undisturbed control group, midbrain and pons showed strong positive correlation, but in both manual and treadmill SD groups, it showed only weak correlation. This could suggest that the original strong positive correlation between midbrain and pons was changed to weak correlation by high sleep drive and their connectivity was altered.

Similarly, the significant change between cortical subplate and thalamus is also interesting since BLA and BMA are part of cortical subplate. Besides, thalamus is considered to participate in wake-promoting pathways and is crucial in maintenance of consciousness. The circuit between BLA/BMA and thalamus in sleep is unclear, but one study showed that a thalamo-BLA circuit underlied the extinction of remote fear memories[169]. In the undisturbed control group, cortical subplate and thalamus showed strong negative correlation, but in both manual and treadmill SD groups, it showed positive correlation. This could suggest that the original strong negative correlation between thalamus and cortical subplate was changed to positive correlation by high sleep drive and their connectivity was altered.

For conclusion, our current results showed that BLA/BMA were active after SD, and provided target brain regions for the functionality study. The further studies (*in vivo* functional study and single nucleus RNA sequencing) might give us more information about the roles BLA/BMA play in sleep homeostasis. The connectivity between midbrain and pons, as well as between cortical subplate and thalamus altered strongly by sleep deprivation, which could imply potential projection routes that were involved in sleep homeostasis.

(The studies in this chapter were supported by the ERC under the European Union's Horizon 2020 Research and Innovation Program Grant Agreement No. 715933 to Dr. Rhîannan H Williams.)

Chapter 5
Astrocyte–neuron interactions in sleep homeostasis

Introduction

Astrocytes are characteristic star-shaped glial cells in the brain and spinal cord. They perform many functions, including provision of nutrients to the nervous tissue, maintenance of extracellular ion balance, and regulation of cerebral blood flow. Astrocytes have also been suggested to involve in modulating sleep. Recent studies showed that cortical astrocytic Ca^{2+} signals reduced during sleep compared to wakefulness[170], and reduced cortical astrocytic Ca^{2+} reduces sleep drive after sleep loss[171].

On the other hand, the cortical nNOS/NK1R neurons (nNOS neurons) have also been suggested to play a role in modulating sleep. Previous studies showed that cortical nNOS neurons were more active in RS[101], and nNOS knockout mice showed lower sleep percent time in RS and lower delta power in the first 90 minutes of RS[102].

For both astrocytes and nNOS neurons, adenosine was suggested to be involved in the sleep modulating process. Astrocytes that lost the ability of exocytosis, therefore could not release ATP (precursor of adenosine), showed lower sleep percent time and shorter NREM sleep bout in RS[172]. On the other hand, mice lacking adenosine A_{2a} receptor ($A_{2a}R$) have decreased number and activation of nNOS neurons and delayed RS[173,174]. The fact that both cortical astrocytes and nNOS neurons are related to sleep and adenosine made us curious about their interaction in the sleep homeostasis. Since the previous study of nNOS neurons and adenosine A_{2a} receptor was based on cingulate cortex, we decided to further focus on this region[173,174].

Therefore, we wanted to examine the proximity (anatomical pattern) between astrocytes and nNOS neurons in cingulate cortex in sleep homeostasis, as well as the numbers of astrocytes in the cortex in sleep homeostasis. Apart from that, we also wanted to examine the direct role that astrocytes play in sleep homeostasis. Chemogenetics is an *in vivo* technique that can manipulate the activity of specific brain regions.This is done by using specific drugs to exclusively activate specific receptors. The receptors in Chemogenetics are called DREADDS (Designer Receptors Exclusively Activated by Designer Drugs). The most commonly published ones are hM3Gq which activates cells by a Gαq signaling pathway, and hM4Gi which inhibits cells by a Gαi pathway. Both of them can be activated by an exogenous ligand clozapine-N-oxide (CNO)[48].

Hence, we wanted to use chemogenetics (DREADDS with hM3Gq and CNO) to selectively activate astrocytes in cingulate cortex and examine its function on sleep by piezo sleep recording.

Aims and objectives

We aimed to examine the proximity between astrocytes and nNOS neurons in cingulate cortex in sleep homeostasis. We also aimed to manipulate astrocytes and observe the causal relationship between astrocytes and sleep homeostasis. The detailed aims included:

- Use immunohistochemistry to label both astrocytes and nNOS neurons in cingulate cortex, then analyze the proximity (anatomical pattern) between them.
- Quantify the numbers of astrocytes in the cortex in sleep homeostasis.
- Use chemogenetic to activate astrocytes in cingulate cortex and examine how the activity of astrocytes changes the sleep states with or without sleep deprivation.

Results

Proximity analysis of cortical nNOS neurons and astrocytes

In this study, Aldh1l1-creERT2:Ai14 mice were used to have endogenous fluorescence from astrocytes. *Aldh1l1* is the gene for astrocyte-specific enzyme ALDH1L1. It is a marker for astrocytes and was used for specific astrocytes targeting[175]. Ai14 is a Cre-dependent reporter with a *loxP*-flanked STOP cassette stopping the transcription of a CAG promoter. When the STOP cassette is removed by Cre, it can drive the following gene and the cells express red fluorescent protein tdTomato[176]. Therefore, in this study, we injected tamoxifen (100mg/kg, i.p. injection) to activate $CreER^{T2}$, then the $CreER^{T2}$ in astrocytes activated the expression of red fluorescent proteins (Ai14), and provided endogenous red fluorescence specifically in astrocytes. Afterwards, mice were sleep deprived for 4 hours from ZT0 to ZT4. The mice in the SD group were sacrificed after SD and the brains were collected. Mice in the RS group had 2 hours recovery sleep after SD, and were sacrificed at ZT6. Two undisturbed control groups were designed in the study with different sacrificed time to compare with either SD or RS group. Then we labelled both astrocytes and nNOS neurons by immunohistochemistry and did the proximity analysis (**Fig. 5.1 A**).

Since we were more interested in the nNOS neurons in cingulate cortex, we decided to investigate the nNOS neurons in cingulate cortex. After putting three concentric circles (diameter: 300μm, 600μm, 900μm) on the nNOS neurons (with the center of the circle), I calculated astrocytes in the upper half of these circles manually. The circle with diameter 300μm was defined as small circle, the circle with diameter 600μm was defined as middle circle, and the circle with diameter 900μm was defined as large circle (**Fig. 5.1 B**).

The nNOS neurons were defined and chosen based on their typical neuronal shape and projections (**Fig. 5.2 A)**, and the selected nNOS neurons were evenly distributed in cingulate cortex among all four groups (SD, RS, control ZT4, and control ZT6) (**Fig. 5.2 B)**. The astrocytes were also defined and chosen based on their typical astroglial shape with projections (**Fig. 5.2 C)**.

We found out the SD group showed significantly fewer astrocytes compared to control ZT4 group only in the middle circle (27.51 ± 2.29 in SD group, 36.55 ± 3.30 in control ZT4 group, $p = 0.04$) (**Fig. 5.3 B)**, but not in the small circle (8.79 ± 1.11 in SD group, 10.94 ± 1.15 in control ZT4 group, $p = 0.20$) and large circle (56.91 ± 5.12 in SD group, 72.86 ± 6.47 in control ZT4 group, $p = 0.08$) (**Fig. 5.3 A and C)**, even though they both showed trend toward reduction of astrocytes in SD group compared to control ZT4 group. This suggested that the anatomical pattern between nNOS neurons and astrocytes might have changed in the middle layer of the circle (the area between diameter 300-600 μm in the circle). The number of astrocytes was significantly lower in this layer (middle layer) in SD group compared to control ZT4 group (19.36 ± 1.66 in SD group, 25.61 ± 2.19 in control ZT4 group, $p = 0.04$) (**Fig. 5.3 D)**. This implied that there could be a different interaction between nNOS neurons and astrocytes in the middle layer of the circle when the sleep drive is high (SD group). However, more studies will be required to confirm this.

On the other hand, RS group showed significantly fewer astrocytes compared to control ZT6 group in all small (7.73 ± 0.90 in RS group, 11.73 ± 1.33 in control ZT6 group, p = 0.03), middle (25.28 ± 3.22 in RS group, 39.18 ± 4.45 in control ZT6 group, p = 0.03), and large circles (49.35 ± 1.66 in RS group, 82.26 ± 9.03 in control ZT6 group, p = 0.01), as well as the middle layer (17.54 ± 2.44 in RS group, 27.44 ± 3.25 in control ZT6 group, p = 0.03) (**Fig. 5.3 A-D)**. This suggested that there was reduction of astrocytes in cingulate cortex in RS, but might not be related to nNOS neurons since the reduction happened in all three circles with different diameters and distances.

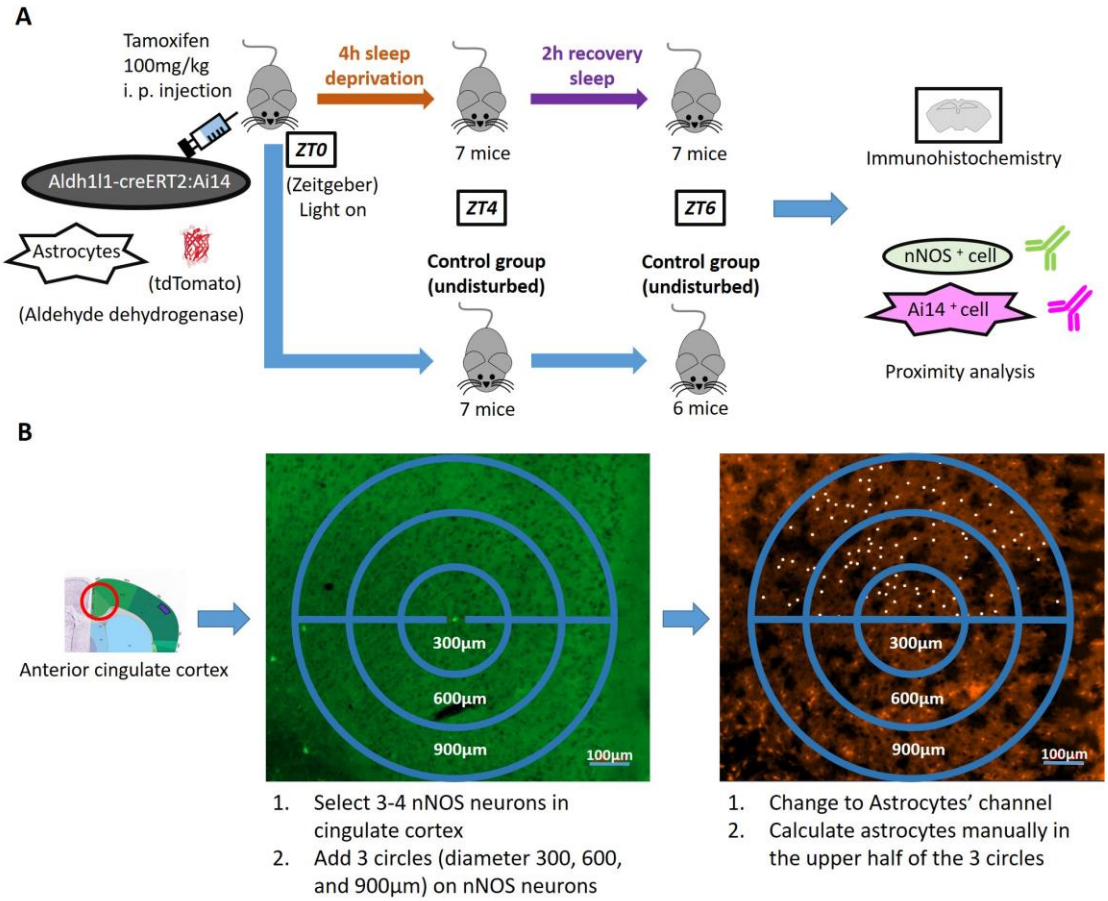

Figure 5.1 Experimental design and analysis steps for the proximity analysis between nNOS neurons and astrocytes. (A) The flowchart of the experimental design. (B) The steps of proximity analysis between nNOS neurons and astrocytes.

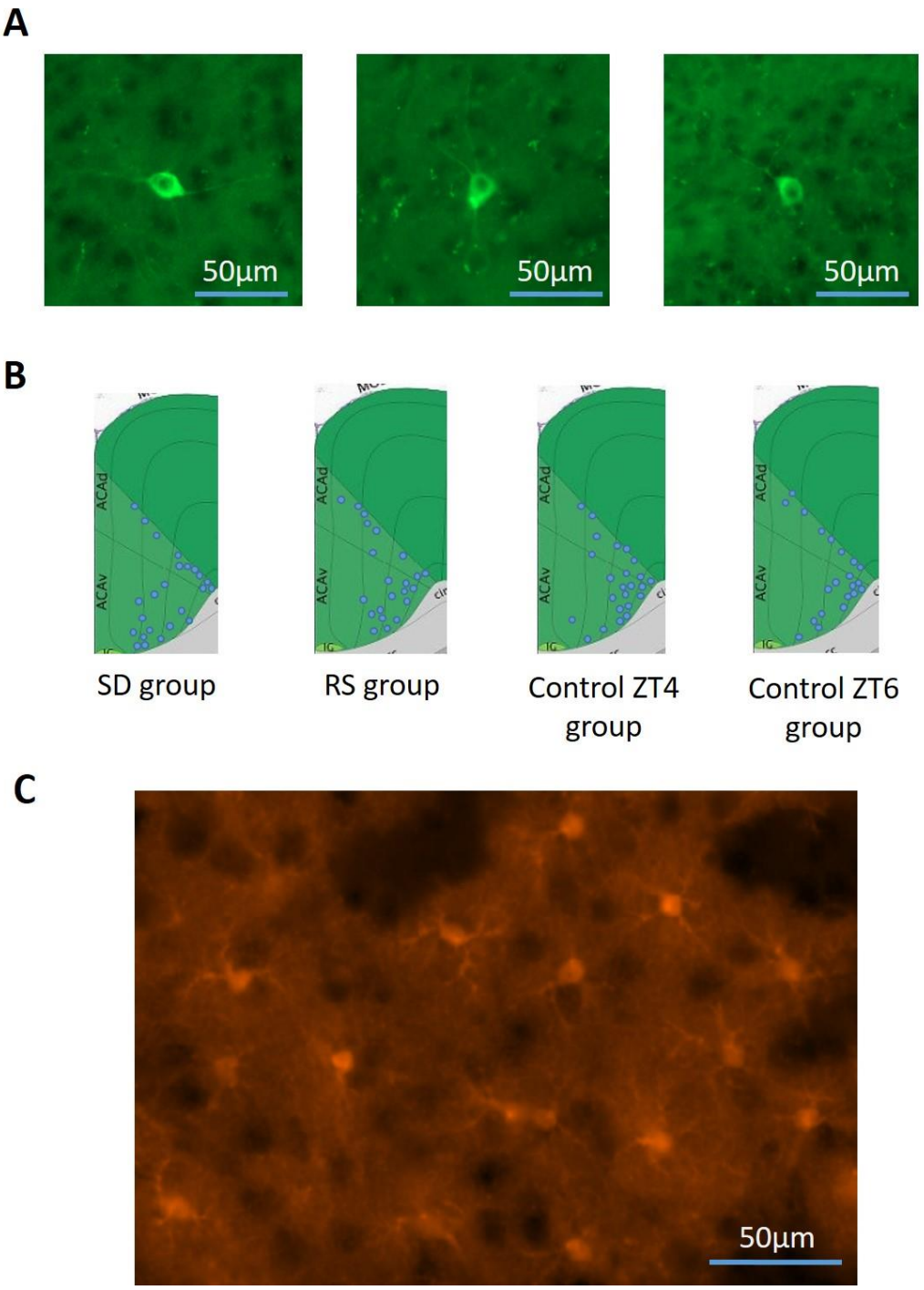

Figure 5.2 Example of nNOS neurons and astrocytes. (A) 3 examples of nNOS neurons from different mice. (B) The distribution of the chosen nNOS neurons in cingulate cortex. The selected nNOS neurons were evenly distributed in cingulate cortex among all four groups (SD, RS, control ZT4, and control ZT6). Blue dots: the chosen nNOS neurons. (C) Example of astrocytes from one mouse.

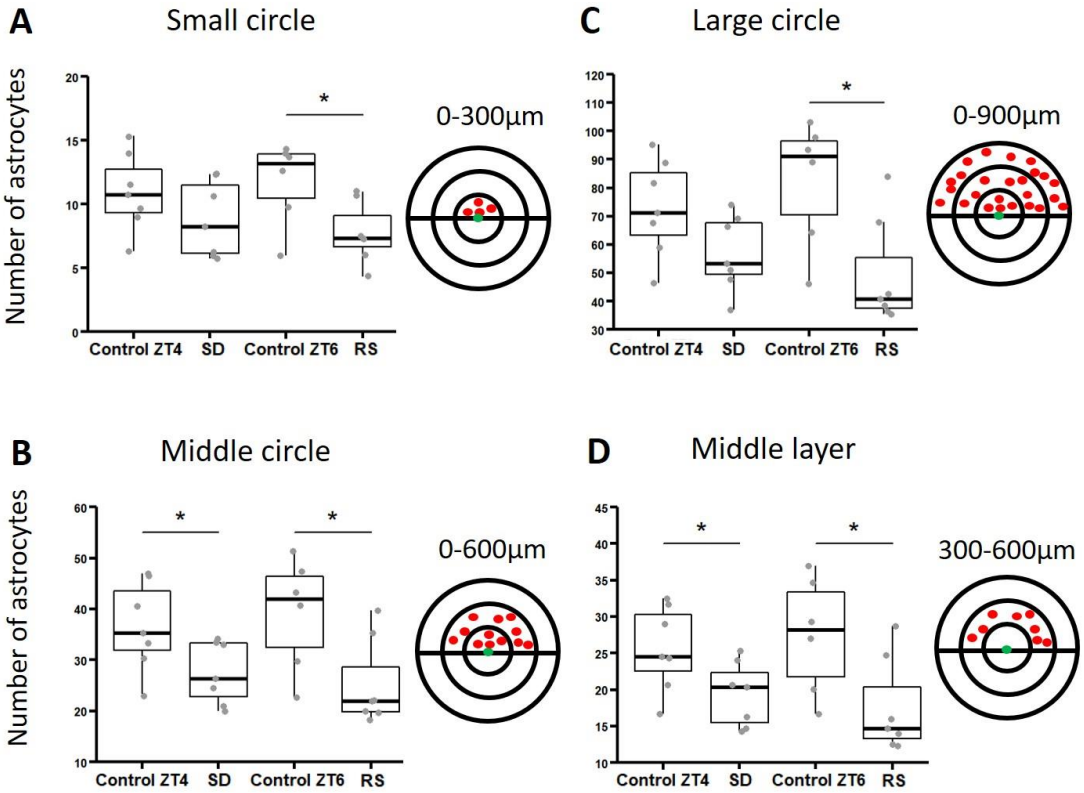

Figure 5.3 Numbers of astrocytes in 3 different diameters of circles and the middle layer. (A) Number of astrocytes in the small circle (diameter 0-300µm). (B) Number of astrocytes in the middle circle (diameter 0-600µm). (C) Number of astrocytes in the large circle (diameter 0-900µm). (D) Number of astrocytes in the middle layer (the area between diameter 300-600 µm in the circle). SD group showed significantly fewer astrocytes compared to control ZT4 group in the middle circle and middle layer, but not in the small circle and large circle. RS group showed significantly fewer astrocytes compared to control ZT6 group in all small, middle, and large circles, as well as the middle layer. *p-value < 0.05, Student's t-test. n=6-7 per group.

Quantification of astrocytes in sleep homeostasis in cortex

We were also interested in how the number of astrocytes changed after SD in cortex (independent to nNOS neurons), since we did see significant changes of the numbers of astrocytes in cingulate cortex in the previous proximity study. However, the ROIs (regions of interest) from the proximity study were based on the locations of nNOS neurons, so it would not be objective if we only wanted to examine the numbers of astrocytes in the cortex. Therefore, we did quantification of astrocytes based on another method. This method was originally developed by LaGrow et al.[139] They used this method to detect c-Fos positive cells automatically in the mouse brain. The method was modified and optimized in our lab to specifically detect astrocytes in cingulate/motor cortex. It first selects patches in cingulate/motor cortex, then automatically detects astrocytes (**Fig. 5.4 A and B)**. Mikołaj Miękus, a master's student at TUM and did his project at our lab, did this part of the study.

The algorithms for patch selection (**Fig. 5.4 A)** and automatic cell detection (**Fig. 5.4 B)** were tested in 8 testing samples, and the median of the precision, recall, and F1 score were 0.709, 0.925, and 0.785, respectively (**Fig. 5.4 C)**. The median of F1 score was similar to the F1 scores from the original publication (of the method) which were around 0.8[139]. **Fig. 5.4 B** also showed an example of manual cell counting (44 cells) versus automatic cell counting (48 cells) in one patch.

The results showed that there was no significant difference between 4 groups (control ZT4: 42.21 ± 4.03, control ZT6: 50 ± 3.60, SD: 35.79 ± 3.81, and RS: 37.20 ± 2.86). However, after combining control ZT4 and control ZT6 groups to "not disturbed" group, and combining SD and RS groups to "sleep loss" group, there was significant difference between these two groups (36.50 ± 2.31 in sleep loss group, 45.71 ± 2.82 in not disturbed group, $p = 0.01$) (**Fig. 5.4 D)**. This suggested that sleep loss was causing reduction of the number of astrocytes in cingulate/motor cortex even though there was no significant difference in the original SD and RS groups. However, both SD and RS groups did show trend of astrocytes reduction compared to their control groups (especially the RS group), and the trend of reduction was similar to the previous proximity study.

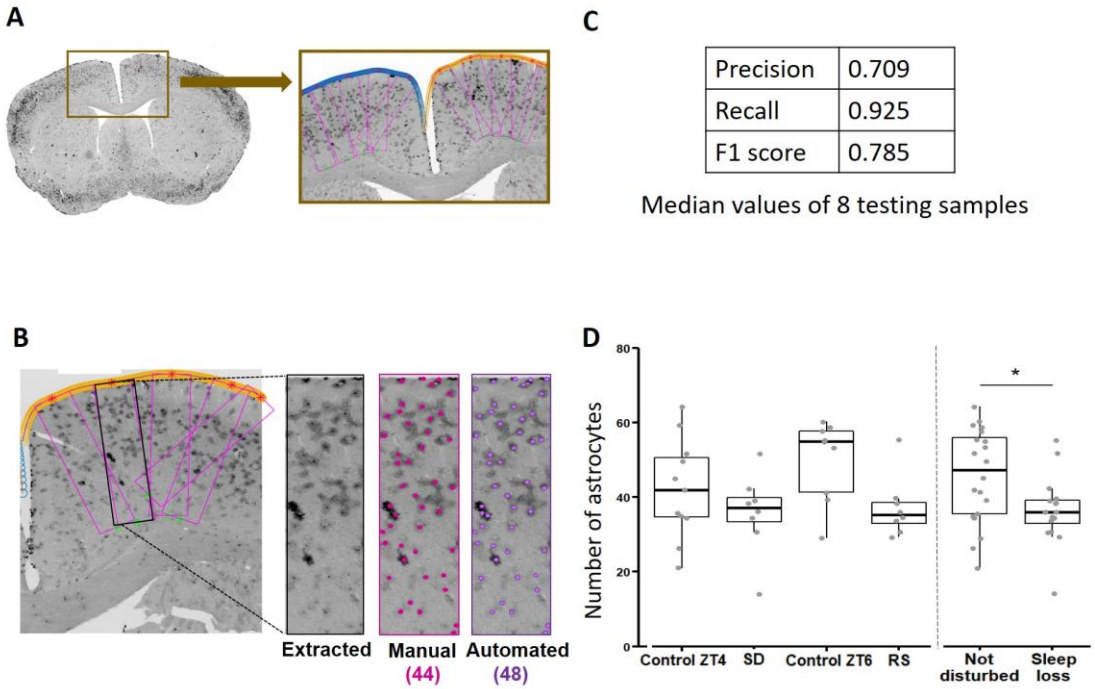

Figure 5.4 Quantification of astrocytes in sleep homeostasis in cortex *(figure was co-made with Mikołaj Miękus and Dr. Rhîannan H Williams)*. (A) Example of patches selected by the algorithm. Magenta square: selected patches. (B) Example of cell counting by algorithm (automated, 48 cells) and by human expert (manual, 44 cells) in one patch. (C) The median of the precision, recall, and F1 score for the modified algorithm based on 8 testing samples. The median of the precision, recall, and F1 score were 0.709, 0.925, and 0.785, respectively (D) Number of astrocytes in the patches. There was no significant difference between control ZT4, control ZT6, SD, and RS groups. However, there was significant difference between “Not disturbed” group and “Sleep loss” group. *p-value < 0.05, Student's t-test. n=8-11 per group.

#Data in figure 5.4 (D) was analysed by Mikołaj Miękus for the project

Chemogenetic stimulation of astrocytes in cingulate/motor cortex

In this study, we wanted to activate astrocytes and see how it changes the sleep behavior. pAAV-GFAP-hM3D(Gq)-mCherry was injected into cingulate cortex/motor cortex bilaterally on a stereotaxic apparatus with head fixed (virus injection group). The tissues of mice were checked by immunohistology to confirm the stereotaxic injection hit the cingulate/motor cortex (**Fig. 5.5 B)**.

After the mice were recovered from surgery, they were placed into piezo cages and the piezo sleep signal was recorded. There were 4 conditions for the study, and for each condition, mice were placed in the piezo cage for 4 days. The first day was considered habituation day so the data was not used. The second day was the "Treatment day" where the injection and SD were done. The third and fourth day were the baseline for the treatment day. On the treatment day, mice were either injected by CNO to activate astrocytes, or vehicle (Veh, 100% saline) as a control. Mice were also either sleep deprived for 4 hours to increase their sleep drive, or left undisturbed to have normal sleep drive. Therefore, there were 4 conditions in the experiment (CNO with SD, CNO undisturbed, Vehicle with SD, Vehicle undisturbed) (**Fig. 5.5 A)**. In the SD groups, mice were sleep deprived from ZT0 to ZT4, which was the first 4 hours of their rest period (light period). The CNO/vehicle was administered at ZT4. This was the time when the SD reached 4 hours and the mice in SD group should have the highest sleep drive. Apart from the virus injection group that mentioned above, we also did the same behaviour experiment on the non-viral injection group which did not have the virus injection (pAAV-GFAP-hM3D(Gq)-mCherry), but went through the same piezo recording, SD, and CNO/Veh injection like the virus injection group.

We then compared the sleep percent time in 4 different conditions on the CNO/vehicle treatment day based on 30-minutes temporal resolution. The CNO/vehicle was administered at ZT4, so we were more interested in the changes that happened few hours after ZT4 (ZT4 to ZT8). First, we looked at the virus injection group, and in the undisturbed condition, CNO group showed trend toward increased sleep percent time from ZT6 to ZT7 compared to vehicle group (Sleep percent time: 79.70 ± 4.52% in CNO group, 48.79 ± 14.22% in vechicle group, $p = 0.12$) **(Fig. 5.6 A)**, even though it didn't reach significant difference. In the conditions while SD was intervened from ZT0 to ZT4, CNO group showed trend toward increased sleep percent time from ZT5 to ZT6 compared to vehicle group (85.18 ± 1.50% in CNO group, 66.63 ± 9.81% in vechicle group, $p = 0.15$) **(Fig. 5.6 B)**, even though it didn't reach significant difference either. Therefore, we didn't see any significant changes between CNO and vehicle groups within 4 hours after the injection for both SD and undisturbed conditions. Nevertheless, we observed some significant differences before ZT4 (ZT1-ZT1.5 in undisturbed condition, 22.58 ± 9.91% in CNO group, 58.69 ± 12.35% in vechicle group, $p = 0.004$) and after ZT8 including ZT9.5-ZT10 in undisturbed condition (49.08 ± 6.85% in CNO group, 69.88 ± 8.75% in vechicle group, $p = 0.001$) **(Fig. 5.6 A)**, ZT8-ZT8.5 in SD condition (86.44 ± 7.33% in CNO group, 14.89 ± 6.63% in vechicle group, $p = 0.03$), and ZT11.5-ZT12 in SD condition (77.88 ± 7.99% in CNO group, 52.26 ± 6.01% in vechicle group, $p = 0.01$) **(Fig. 5.6 B)**.

For the non-viral injection group, no significant difference was observed at any time point in the undisturbed condition (**Fig. 5.7 A**). This is the same for the condition while SD was intervened from ZT0 to ZT4, no significant difference was observed at any time point (**Fig. 5.7 B**). However, CNO group showed trend toward increased sleep percent time from ZT5 to ZT6 compared to vehicle group (85.18 ± 1.50% in CNO group, 66.63 ± 9.81% in vechicle group, p = 0.125) **(Fig. 5.7 B)**. This is similar to the trend in the virus injection group **(Fig. 5.6 B)**, suggesting that the trend of increased sleep percent time from ZT5 to ZT6 after SD might be caused by non-specific activation of CNO, rather than cortical astrocytes.

Since we noticed the baselines from each piezo recording were not always the same, we subtracted the sleep percent time between the treatment day and the baseline day, and compared the baseline-subtracted sleep percent time between CNO and vehicle groups. For the virus injection group, the results showed that the sleep percent time increased significantly between ZT4 to ZT8 in CNO group compared to vehicle group when the mice were not disturbed (Baseline-subtracted sleep percent time: 3.27 ± 2.47% in CNO group, -6.31 ± 2.09% in vehicle group, p = 0.03) **(Fig. 5.8 A)**. However, there was no significant difference between CNO and vehicle groups after 4 hours SD (2.79 ± 4.71% in CNO group, -2.79 ± 4.96% in vehicle group, p = 0.24) **(Fig. 5.8 B)**. This suggested that the active astrocytes in cingulate/motor cortex could modify sleep state by promoting sleep. However, when the sleep drive was high, they lost the ability to modify sleep states. It is likely that other mechanisms overpowered astrocytic mechanisms and took over the modifying role.

For the non-viral injection group, no significant difference was observed at any time point in the undisturbed condition (Baseline-subtracted sleep percent time between ZT4-ZT8: -1.94 ± 3.61% in CNO group, -1.84 ± 1.87% in vehicle group, p = 1) (**Fig. 5.9 A**). This suggested that the sleep promotion of CNO in the virus injection group (while the mice were not disturbed) **(Fig. 5.8 A)** was more likely caused by cortical astrocytes, rather than non-specific activation of CNO. As for the condition while SD was intervened, no significant difference was observed at any time point (Baseline-subtracted sleep percent time between ZT4-ZT8: 10.2 ± 4.45% in CNO group, 6.29 ± 4.09% in vehicle group, p = 0.31) (**Fig. 5.9 B**).

Apart from the sleep time, the sleep architecture is also an important parameter for sleep behavior. Therefore, we also examined the mean bout duration during sleep for 24 hours based on 1-hour temporal resolution for the virus injection group. The results showed that there was no significant difference between CNO and vehicle groups when the mice were not disturbed. However CNO group showed subtle trend toward increased sleep mean bout duration from ZT6 to ZT7 (2 hours after CNO/vehicle injection) compared to the vehicle group (14.16 ± 2.54 minutes in CNO group, 8.89 ± 4.60 minutes in vehicle group, p = 0.16) **(Fig. 5.10 A)**. Similarly, there was no significant difference between CNO and vehicle groups after 4 hours SD, but CNO group showed trend toward increased sleep mean bout duration in from

ZT8 to ZT9 (4 hours after CNO/vehicle injection) compared to the vehicle group (21.06 ± 5.47 minutes in CNO group, 6.05 ± 0.95 minutes in vehicle group, p = 0.14) **(Fig. 5.10 B)**. This (sleep bout duration) could be the reason for the trend toward increased sleep percent time from ZT6 to ZT7 after CNO injection in undisturbed group **(Fig. 5.6 A)**, and the significant increase of sleep percent time from ZT8 to ZT8.5 after CNO injection in SD group **(Fig. 5.6 B)**. However, more studies on sleep architecture are required to prove this.

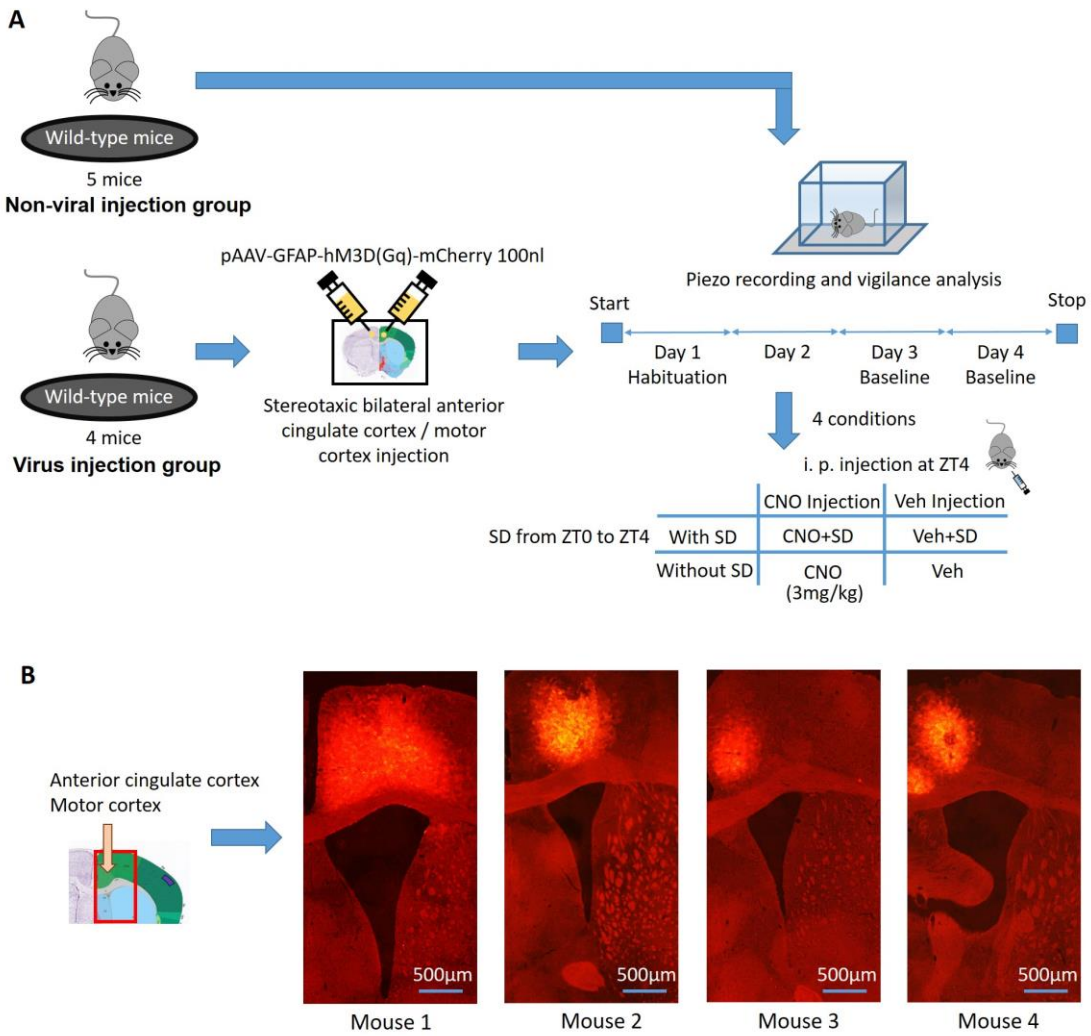

Figure 5.5 Experimental design for the chemogenetic stimulation of astrocytes and the injection site check. (A) The flowchart of the experimental design. SD: Sleep deprivation, CNO: clozapine N-oxide, Veh: Vehicle. (B) The immunohistological images of the stereotaxic injection site in cingulate/motor cortex for 4 mice. Red channel: hM3Dq-mCherry.

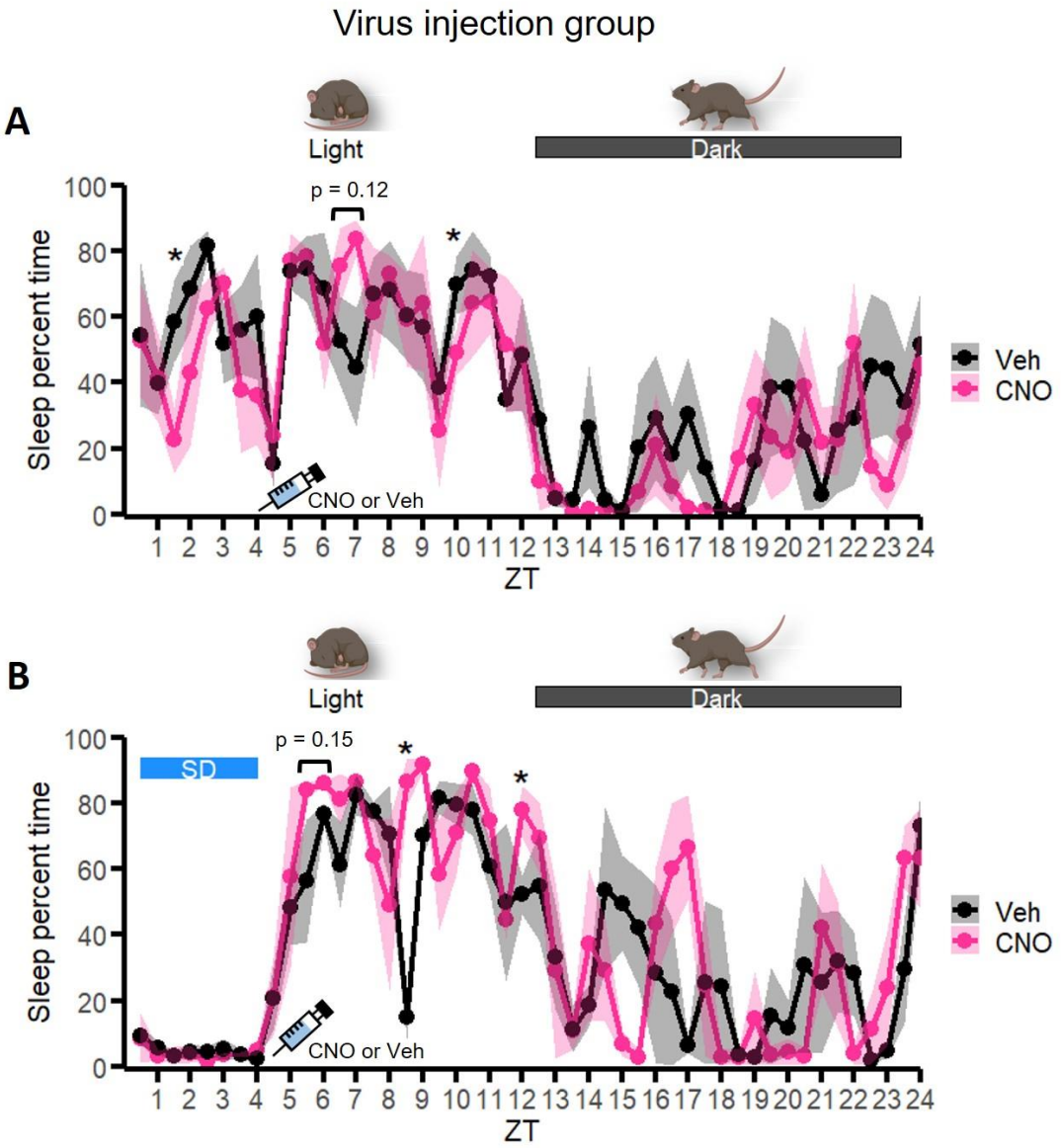

Figure 5.6 Sleep percent time in 4 conditions for 24 hours (virus injection group). (A) Sleep percent time of CNO and vehicle (Veh) groups without SD (undisturbed). CNO group showed trend toward increased sleep percent time from ZT6 to ZT7 compared to vehicle group. ZT1-ZT1.5 and ZT9.5-ZT10 also showed significant difference. (B) Sleep percent time of CNO and vehicle (Veh) groups with SD. CNO group showed trend toward increased sleep percent time from ZT5 to ZT6 compared to vehicle group. ZT8-ZT8.5 and ZT11.5-ZT12 also showed significant difference. Time bin: 30 minutes. Line: Mean ± SEM. *p-value < 0.05, Wilcoxon signed-rank test. n=3-4.

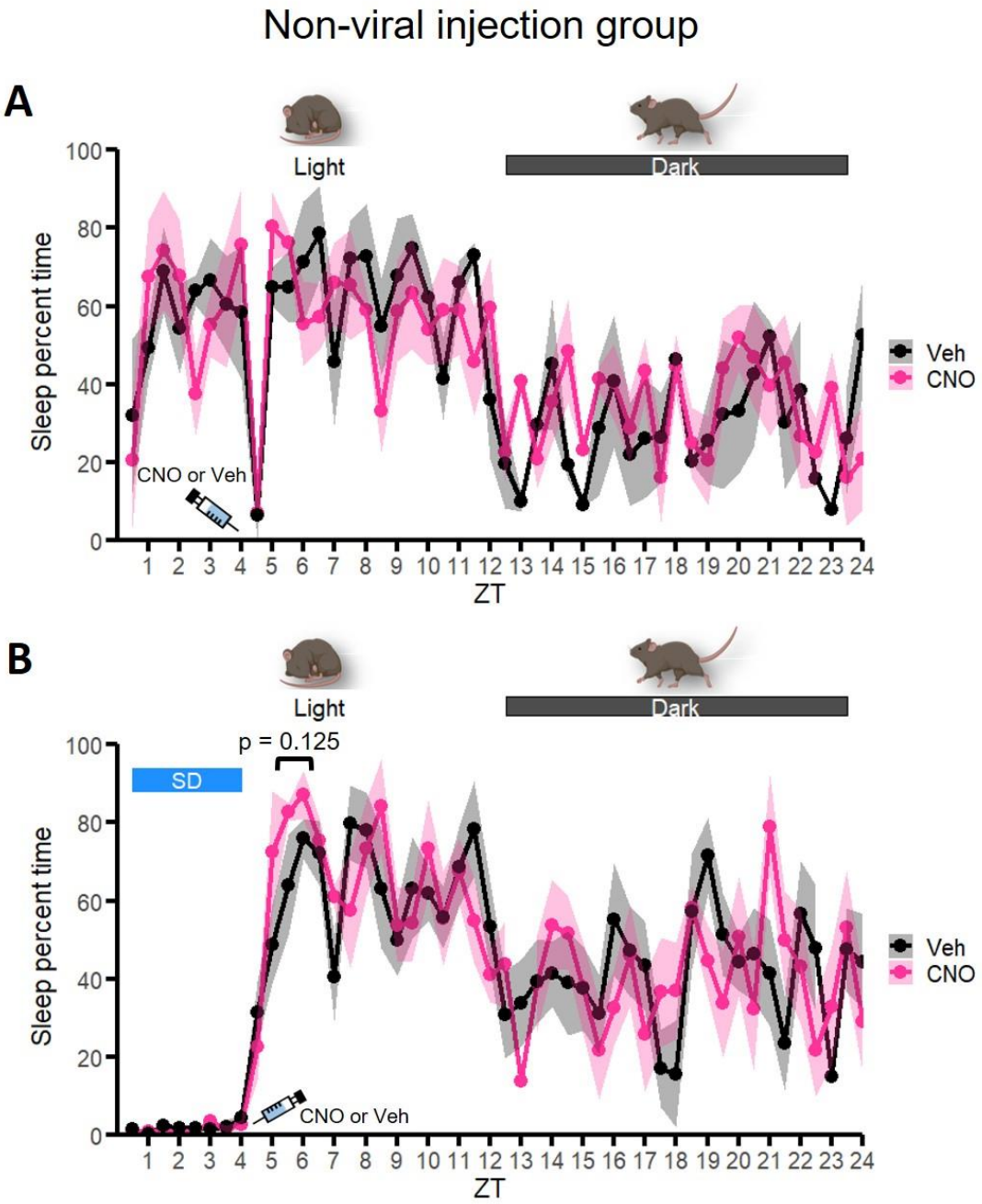

Figure 5.7 Sleep percent time in 4 conditions for 24 hours (non-viral injection group). (A) Sleep percent time of CNO and vehicle (Veh) groups without SD (undisturbed). No significant difference was observed. (B) Sleep percent time of CNO and vehicle (Veh) groups with SD. CNO group showed trend toward increased sleep percent time from ZT5 to ZT6 compared to vehicle group. Time bin: 30 minutes. Line: Mean ± SEM. Statistics: Wilcoxon signed-rank test. n=5.

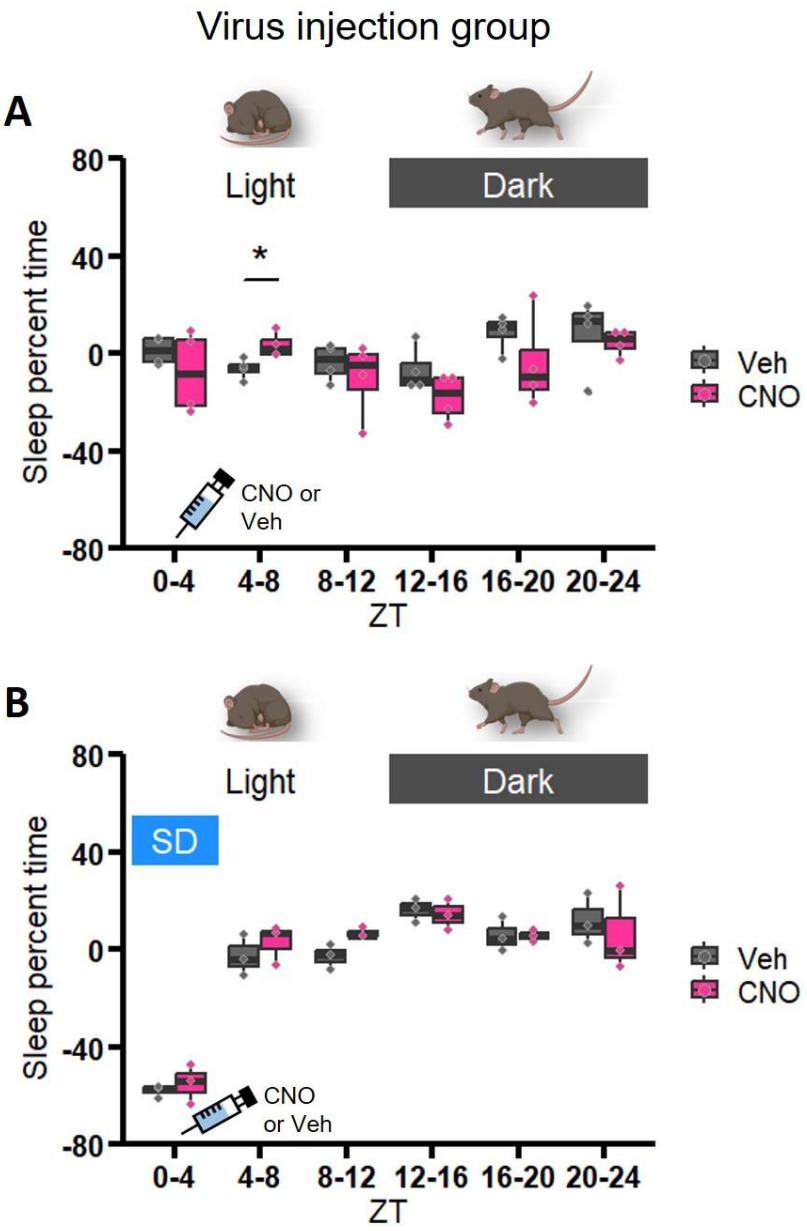

Figure 5.8 Baseline-subtracted sleep percent time in 4 conditions for 24 hours (virus injection group). (A) Baseline-subtracted sleep percent time of CNO and vehicle (Veh) groups without SD (undisturbed). Sleep percent time increased significantly between ZT4 to ZT8. (B) Baseline-subtracted sleep percent time of CNO and vehicle (Veh) groups with SD. No significant difference was observed. Time bin: 4 hours. *p-value < 0.05, Wilcoxon signed-rank test. n=3-4.

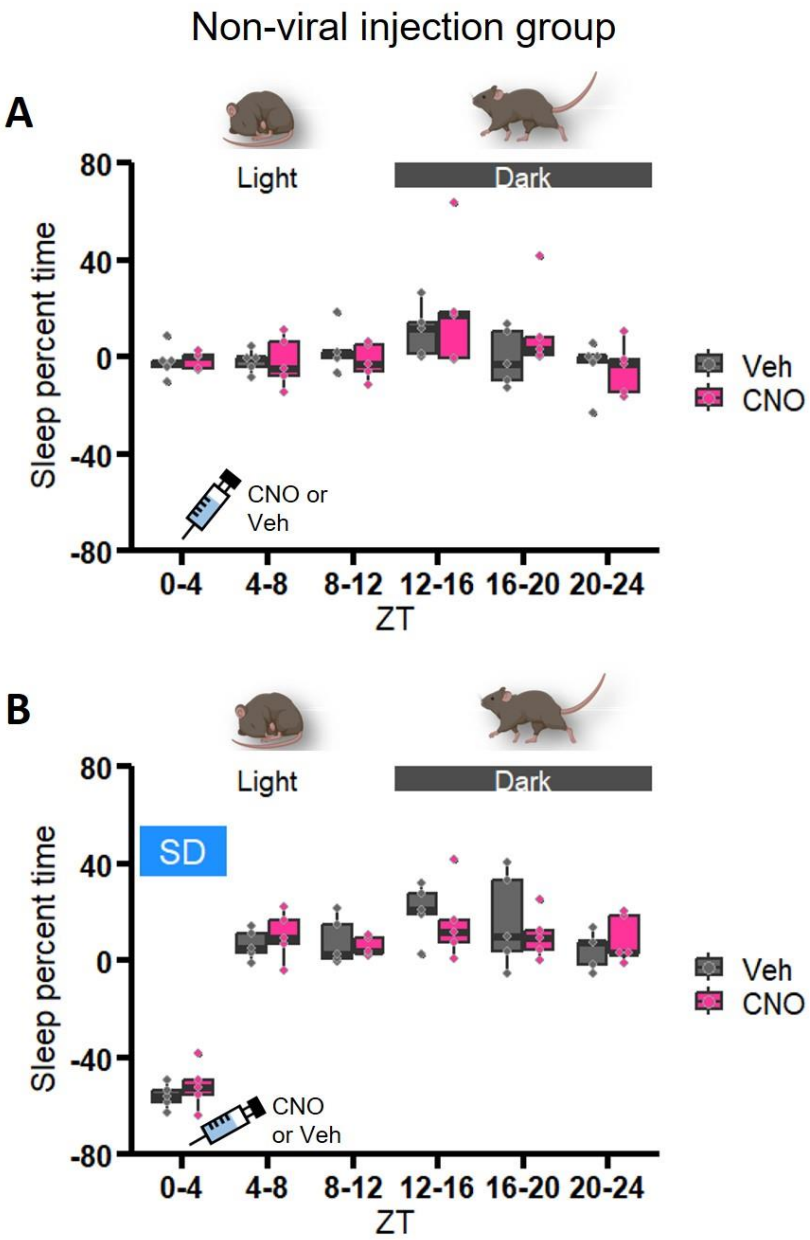

Figure 5.9 Baseline-subtracted sleep percent time in 4 conditions for 24 hours (non-viral injection group). (A) Baseline-subtracted sleep percent time of CNO and vehicle (Veh) groups without SD (undisturbed). No significant difference was observed. (B) Baseline-subtracted sleep percent time of CNO and vehicle (Veh) groups with SD. No significant difference was observed. Time bin: 4 hours. Statistics: Wilcoxon signed-rank test. n=5.

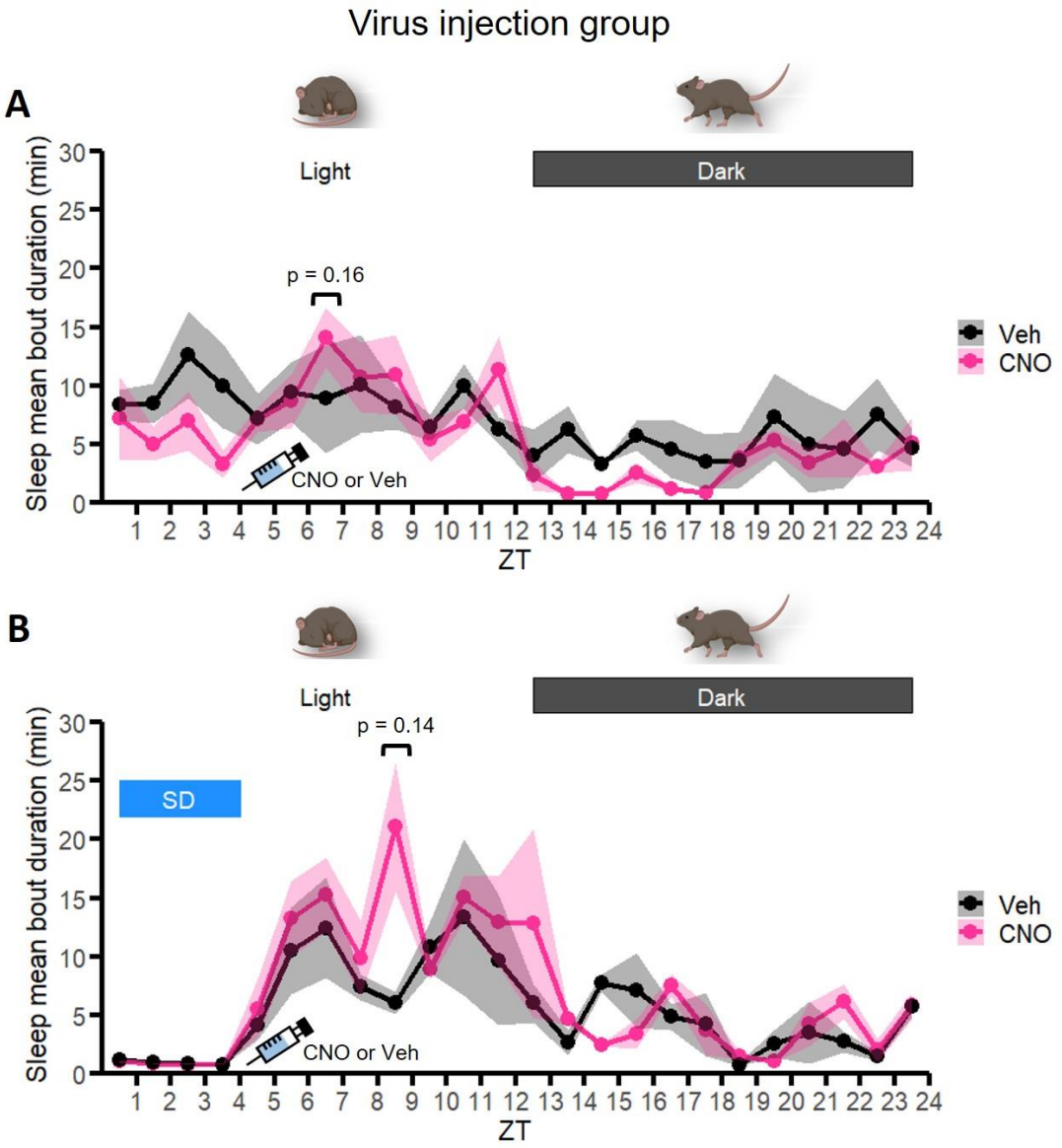

Figure 5.10 Sleep mean bout duration in 4 conditions for 24 hours (virus injection group). (A) Sleep mean bout duration of CNO and vehicle (Veh) groups without SD (undisturbed). CNO group showed subtle trend toward increased sleep percent time from ZT6 to ZT7 compared to vehicle group. (B) Sleep mean bout duration of CNO and vehicle (Veh) groups with SD. CNO group showed trend toward increased sleep percent time from ZT8 to ZT9 compared to vehicle group. Time bin: 1 hour. Line: Mean ± SEM. Statistics: Wilcoxon signed-rank test. n=3-4.

Discussion

The proximity analysis between nNOS neurons and astrocytes suggested the number of astrocytes reduced significantly after SD only between distance in 300-600μm (middle layer) from nNOS neurons (**Fig. 5.3)**. Originally we expected to see changes of astrocytes (either more or less) in the small circle (0-300μm), as a result of nNOS-astrocyte interaction in the proximity. Instead, we saw changes in the middle layer. This suggested that if nNOS neurons and astrocytes did have interaction after SD, nNOS neurons were more likely to affect the astrocytes in the middle layer. However, our study was only based on anatomical apposition which cannot prove their function. Hence, a functional study will be required to investigate their interaction. The situation after RS was different. All three circles showed significantly fewer astrocytes after RS (**Fig. 5.3)**. This could suggest that if nNOS neurons and astrocytes had interaction after RS, nNOS neurons were able to affect the astrocytes in a long distance (up to 900μm). Or, the reduction of astrocytes had nothing to do with nNOS neurons, and just reduced in the whole cingulate cortex. This would need a separate study to quantify the astrocytes independently without nNOS neurons.

The second part of the study actually answered this question. Mikołaj Miękus did a quantification of astrocytes in cingulate/motor cortex by selecting 3 patches in cingulate/motor cortex in each mouse. Even though there was no significant difference between SD, RS, and control groups, the sleep loss group showed significantly lower number of astrocytes compared to undisturbed group (**Fig. 5.4)**. This suggested that sleep loss caused reduction of astrocytes in the entire cingulate/motor cortex, and might be independent to nNOS neurons. We suspected that astrocytes were either moving away or dying in high sleep-drive condition. However, we don't know the reason of astrocytes reduction and more studies would be required to answer this. Apart from the number of astrocytes, the morphology of astrocytes could also change after sleep loss and could suggest their interactions to neurons. Therefore, studies on morphology would be beneficial.

In the third part of the study, we found out that the selective activation of astrocytes by chemogenetics in cingulate/motor cortex promoted sleep in the next 4 hours (**Fig. 5.8)**. However, when the activation of astrocytes was followed by sleep deprivation, the activated astrocytes did not change the sleep states. We suspected that the astrocytes in cingulate/motor cortex might already be activated by the high sleep drive, so supplemental activation of astrocytes did not make any difference. Or, the sleep-mediating role of astrocytes in usual condition was taken over by other mechanisms/cells, so even though astrocytes were activated after chemogenetic stimulation, they were no longer mediating the sleep state. However, these were only assumptions, and will require further studies to examine the reasons.

If we compare our results to other recent publications about astrocytes and sleep, the conclusions are not always the same. Bojarskaite et al. did calcium imaging on astrocytes in barrel cortex, and found out that astrocytic Ca^{2+} signals were reduced during sleep compared to wakefulness[170]. This suggested astrocytes were more active in wakefulness compared to sleep.

They also found out that astrocytic Ca^{2+} signals increased before the transitions from SWS (slow-wave sleep) to wakefulness. This suggested astrocytes may play a role in modulating sleep-to-wake transitions[170]. This result is a bit different compared to our results, where activation of astrocytes promoted sleep. One possible reason to explain this is the differences of virus injection regions. They injected virus in barrel cortex, and we injected virus in cingulate/motor cortex. Hence, this suggested that astrocytes in different cortex regions could play different roles in modulating sleep and wake.

Ingiosi et al. also did calcium imaging to record astrocytic Ca^{2+} signals but they focused on frontal cortex. They found out that astrocytic Ca^{2+} signals in frontal cortex were strongest in wakefulness, second strongest in NREM sleep, and weak in REM sleep[171]. This is similar to the results from Bojarskaite et al. They also found out that astrocytic Ca^{2+} signals increased when the sleep drive increased, and reduced astrocytic Ca^{2+} signals reduced sleep drive after sleep loss[171]. This suggested astrocytes may be important to mediate the sleep drive after sleep loss. This conclusion is complementary to our first assumption about why chemogenetic activation of astrocytes did not change the sleep state after sleep deprivation. According to this study, the activity of astrocytes increased when sleep drive increased. Hence, astrocytes were already active after 4 hours sleep deprivation before we tried to stimulate them by chemogenetics, so the supplemental activation of astrocytes was not effective enough to change the sleep state.

Vaidyanathan et al. did chemogenetics and calcium imaging combined study on astrocytes in visual cortex, and found out that astrocytic Gi-coupled GPCR signaling increased sleep depth, while astrocytic Gq-coupled GPCR signaling increased sleep duration[177]. This is complementary to our results, where activation of astrocytes promoted sleep. This suggested that astrocytes in different regions of cortex could also play similar roles in modulating sleep and wake.

(The studies in this chapter were supported by the ERC under the European Union's Horizon 2020 Research and Innovation Program Grant Agreement No. 715933 to Dr. Rhîannan H Williams.)

Chapter 6
Phenotypic assessment and neural activity mapping of *MEIS1* point mutation mice

Introduction

Restless legs syndrome (RLS) is a long-term sensorimotor disorder that causes a strong urge to move legs. Patients have uncomfortable and unpleasant sensations in their legs, and it is eased after moving them. The feelings generally worsen in the evening or night when patients start to rest and during the rest period. Hence, it normally causes disturbance in sleep, and may develop daytime sleepiness, low energy, and depressed mood[178]. Females have a higher prevalence than males, and it increases progressively by age[179]. The prevalence is estimated at 2.5-15% of the U.S. general population[180].

The cause of RLS is normally considered primary or idiopathic. However, RLS has a strong genetic component and it is considered inherited. Several gene variants have been associated with RLS. These include *MEIS1*, *BTBD9*, *MAP2K5*, and *PTPRD*[181–183]. Other possible causes include low levels of iron in the brain and dysfunction of basal ganglia/substantia nigra which control muscle movement by using dopamine as neurotransmitter, and project to the striatum, an area that is also important for movement control[178,184]. Treatments for RLS include lifestyle changes and medication. Changes of lifestyle include limiting the intake of alcohol, nicotine, and caffeine, as well as improving sleep habits. Medications used include dopamine precursor such as levodopa, DOPA decarboxylase (DDC) inhibitors such as carbidopa, and dopamine agonist such as pramipexole, ropinirole, and rotigotine[185].

Even though previous studies have suggested some causes for RLS, the full development of RLS is still unclear. Hence, a disease mouse model of RLS would be helpful for further studies.

MEIS1 is a homeobox transcription factor which belongs to the TALE (three amino acid loop extension) family of homeodomain proteins, and it is critical for some developments such as neurodevelopment and the development of proximodistal limb axis[186]. Genetic variations in *MEIS1* have been associated with RLS patients[183,187]. One of the nonsynonymous coding variants, p.Arg272His, was found to be 7 times more frequent to have variant in RLS patients compared to controls[140].

Hence, The Institute of Neurogenomics, The Institute of Developmental Genetics, and the German Mouse Clinic at the Helmholtz Zentrum Muenchen developed a disease mouse model of RLS based on point mutation at p.Arg272His (G815A), and it is called Meis1$^{R272H/R272H}$ (*MEIS1* point mutation) mice. We then wanted to evaluate if we can see changes of locomotor activity, calorimetry, sensory responses, and sleep pattern in Meis1$^{R272H/R272H}$ mice that are similar to the RLS patients, and further examined the possible regions that might cause this by using whole brain activity mapping.

Aims and objectives

We aimed to evaluate the RLS mouse model (Meis1$^{R272H/R272H}$ mice) by using different behavioural tests. We also wanted to do whole brain activity mapping to examine the brain regions that might contribute to the changes of behavior and sleep pattern in Meis1$^{R272H/R272H}$ mice. The detailed aims included:

- Evaluate if the RLS mouse model (Meis1$^{R272H/R272H}$ mice) shows behavior patterns that are similar to human RLS patients by examining locomotor activity, calorimetry, sensory responses, and sleep behavior of Meis1$^{R272H/R272H}$ mice.
- Use tissue clearing (iDISCO+) to do whole brain imaging, then use ClearMap to detect active neurons and annotate them to different brain regions. Afterwards, observe the regions that show differences between wildtype and Meis1$^{R272H/R272H}$ mice, and regions that show diurnal differences in Meis1$^{R272H/R272H}$ mice.
- Collapse all brain regions into 11 high-level brain regions, and examine the changes of connectivity between Meis1$^{R272H/R272H}$ and wildtype mice, as well as the diurnal changes of connectivity in Meis1$^{R272H/R272H}$ mice.

Results

Study A: Locomotor, calorimetry, and sensory assessment of Meis1$^{R272H/R272H}$ mice

In order to evaluate Meis1$^{R272H/R272H}$ mice as a potential model for RLS, we first assessed their locomotor, calorimetry, and sensory function. The phenotypic screens included wheel-running, Indirect calorimetry (RER; VCO_2/VO_2 and distance travelled), open field test, hot-plate response test, and rotarod (**Fig. 6.1**).

Young Meis1$^{R272H/R272H}$ mice showed lower activity in dark period (Revolutions: 1508 ± 167 rev/h for Meis1$^{R272H/R272H}$ mice, 2058 ± 288 rev/h for wildtype mice, p-value = 0.04), and showed subtle trend toward lower activity in light period (60 ± 7 rev/h for Meis1$^{R272H/R272H}$ mice, 70 ± 9 rev/h for wildtype mice) and 24h (784 ± 85 rev/h for Meis1$^{R272H/R272H}$ mice, 1064 ± 147 rev/h for wildtype mice) compared to wildtype mice. Aged Meis1$^{R272H/R272H}$ mice showed very subtle trend toward higher activity in dark period (978.4 ± 190.6 rev/h for Meis1$^{R272H/R272H}$ mice, 688.4 ± 194.3 rev/h for wildtype mice), light period (48.7 ± 9.6 rev/h for Meis1$^{R272H/R272H}$ mice, 22.5 ± 6.9 rev/h for wildtype mice), and 24h (513.6 ± 99.5 rev/h for Meis1$^{R272H/R272H}$ mice, 355.4 ± 100.4 rev/h for wildtype mice) compared to wildtype mice. Overall, Meis1$^{R272H/R272H}$ mice did not show significantly higher wheel-running activity at either age (**Fig. 6.2 A and B**).

In the 21h indirect calorimetry, Meis1$^{R272H/R272H}$ mice showed subtle trend toward higher RER (VCO_2/VO_2) in both light period (0.85 ± 0.01 for Meis1$^{R272H/R272H}$ mice, 0.82 ± 0.01 for wildtype mice) and dark period (0.87 ± 0.02 for Meis1$^{R272H/R272H}$ mice, 0.84 ± 0.01 for wildtype mice) compared to wildtype mice (**Fig. 6.2 C and D**). The activity monitoring in the calorimetry system (distance travelled) did not show any differences between genotypes (**Fig. 6.2 E and F**).

In the open field test, Meis1$^{R272H/R272H}$ mice showed trend toward higher travelled distance in the 20 min period assessed compared to wildtype mice (20.30m for Meis1$^{R272H/R272H}$ mice, 18.14m for wildtype mice, p-value = 0.12). Meis1$^{R272H/R272H}$ mice also showed trend toward higher time spent in the centre at 10 min, but overall did not differ significantly from wildtype mice (**Fig. 6.2 G**).

In the hot-plate response test, Meis1$^{R272H/R272H}$ mice showed trend toward longer reaction time across two trials compared to wildtype mice (18 ± 2.1s, for Meis1$^{R272H/R272H}$ mice, 16.5 ± 2.2s for wildtype mice, p-value = 0.18) (**Fig. 6.2 H**). In the rotorod, Meis1$^{R272H/R272H}$ mice fell off (from the rotorod) on 75.6% of trials, and wildtype mice fell off on 64% of trials (p-value = 0.33). The result suggested that Meis1$^{R272H/R272H}$ mice showed trend toward higher falling rate compared to wildtype mice, even though there was no significant difference between genotypes (**Fig. 6.2 I**).

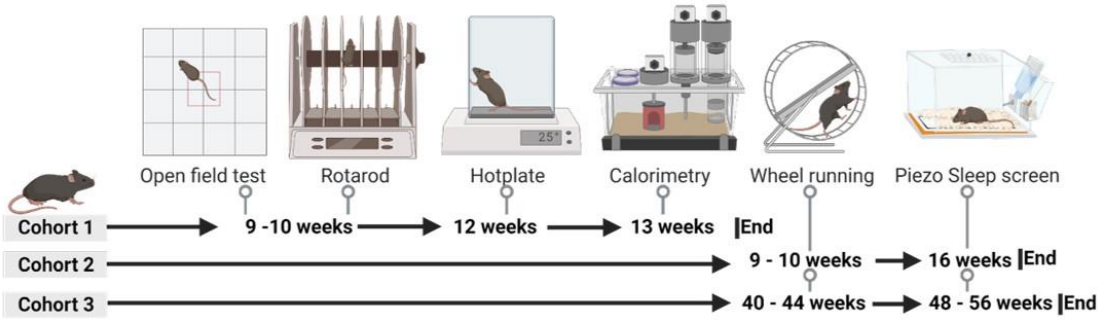

Figure 6.1 Experimental flowchart for phenotypic assessment *(figure was made by Dr. Rhîannan H Williams)*. The flowchart and timeline for locomotor, calorimetry, sensory, and sleep assessment with 3 different cohorts.

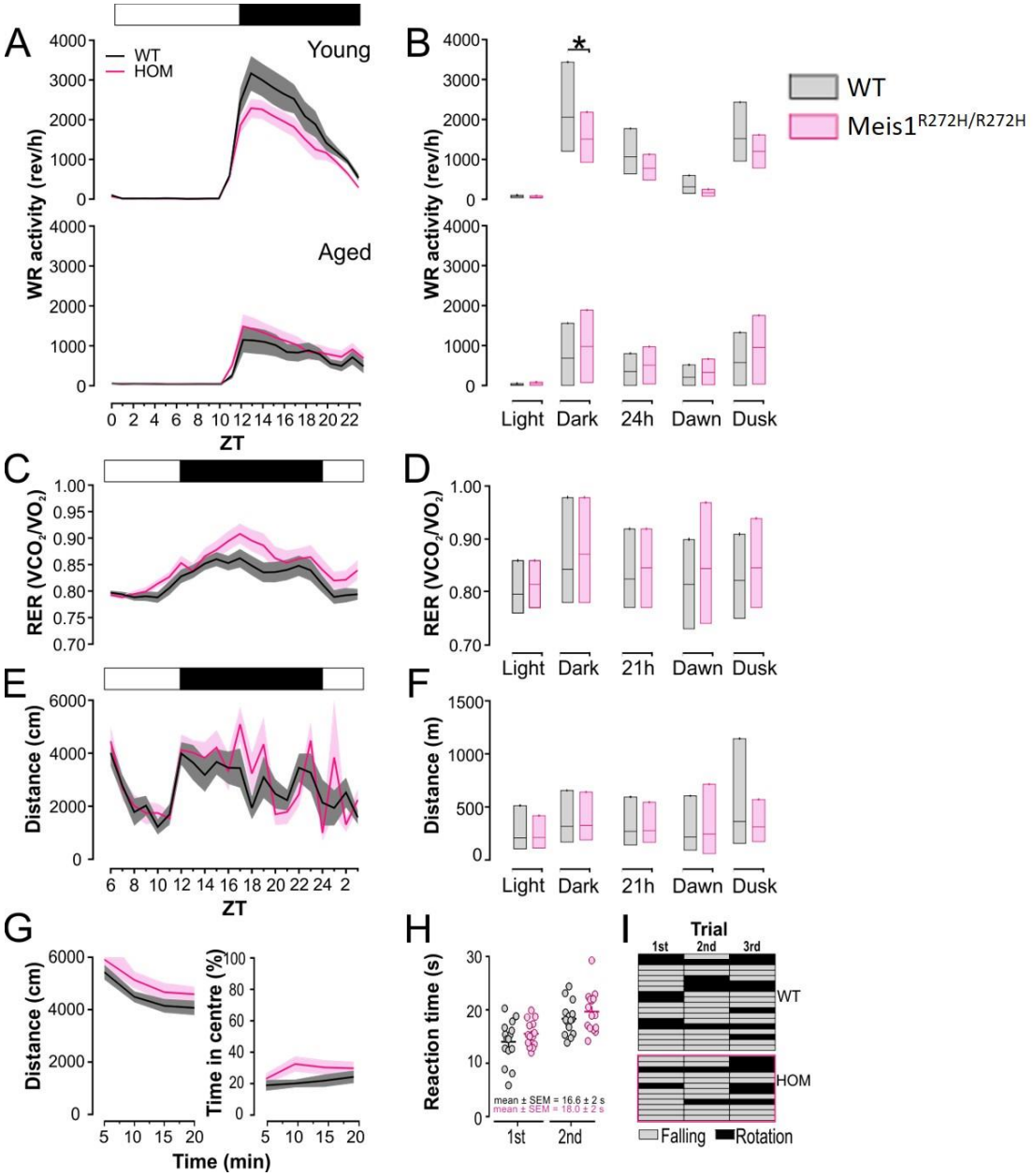

Figure 6.2 Locomotor, calorimetry, and sensory assessment for Meis1$^{R272H/R272H}$ and wildtype mice *(figure was co-made with Dr. Rhîannan H Williams)*.

(A-B) Wheel-running activity in light period, dark period, 24h, and at dawn (ZT23-1) and dusk (ZT11-13). Young Meis1$^{R272H/R272H}$ mice showed lower activity (1508 ± 167 rev/h) in dark period compared to wildtype mice (2058 ± 288 rev/h, *p-value = 0.04: 2 way RM-ANOVA). (C-D) RER (VCO_2/VO_2) in 21h indirect calorimetry. Meis1$^{R272H/R272H}$ mice showed trend toward higher RER (VCO_2/VO_2) in both light period and dark period, but did not reach significant difference. (E-F) The locomotor activity measured in the calorimetry system (distance travelled). There was no difference between genotypes. (G) The locomotor activity measured in open field test. Meis1$^{R272H/R272H}$ mice showed trend toward higher travelled distance and higher time spent in the centre compared to wildtype mice, but did not reach significant difference. (H) The hotplate sensory response was measured by reaction time for heat. Meis1$^{R272H/R272H}$ mice showed trend toward longer reaction time across two

trials compared to wildtype mice, but did not reach significant difference. (I) The proportion of falling and remaining on rotorod (rotation) in the duration of rotarod test. Meis1$^{R272H/R272H}$ mice fell off (from the rotorod) on 75.6% of trials, and wildtype mice fell off on 64% of trials. Meis1$^{R272H/R272H}$ mice showed trend toward higher falling rate compared to wildtype mice, but did not reach significant difference. Line: Mean ± SEM. n=7-15 per genotype.

Sleep behavior of Meis1$^{R272H/R272H}$ mice

RLS patients have uncomfortable and unpleasant sensations in legs, and it gets worse in the evening or at night when patients start to rest. Hence, it normally causes disturbance in sleep. Hence, we put both wildtype and Meis1$^{R272H/R272H}$ mice in piezo cages to record their sleep behavior.

The wake activity in 24h was 65.6 ± 4.9 % in young Meis1$^{R272H/R272H}$ mice, 63.3 ± 3.9 % in aged Meis1$^{R272H/R272H}$ mice, 62 ± 4.7% in young wildtype mice, and 60.5 ± 3.7 % in aged wildtype mice. However, in both young and aged Meis1$^{R272H/R272H}$ mice, the wake activity did not show differences in light period, dark period, and 24h compared to wildtype mice (**Fig. 6.3 A and B**).

We then assessed the wake activity at dawn (ZT23-1) and dusk (ZT11-13), since the uncomfortable and unpleasant sensations in legs that cause RLS patients' sleep disturbance generally worsen when patients start to rest (dusk for humans and dawn for mice). Young Meis1$^{R272H/R272H}$ mice showed trend toward higher wake activity at dawn compared to wildtype mice (91.3 ± 3.8% for Meis1$^{R272H/R272H}$ mice, 81.8 ± 3.8% for wildtype mice), while aged Meis1$^{R272H/R272H}$ mice showed significantly higher wake activity at dawn compared to wildtype mice (83.6 ± 2.9% for Meis1$^{R272H/R272H}$ mice, 72.43 ± 4.0% for wildtype mice, p-value = 0.029) . For dusk, there was no significant difference between genotypes in both young and aged groups (**Fig. 6.3 B**).

Breathing rate in sleep for Meis1$^{R272H/R272H}$ mice

The algorithms used in piezo system to determine vigilance states were based on breathing and gross locomotor activity. Therefore, it also provided the breathing rate in sleep. Breathing in sleep is intriguing because some studies suggested the connection between RLS and sleep apnea. A meta-analysis in 2022 showed that RLS had a significant increase in apnea-hypopnea index (an index used to indicate the severity of sleep apnea)[188]. Another study done by the International Restless Legs Syndrome Study Group showed that clinically significant RLS occurred in 8.3% of OSA (obstructive sleep apnea) patients compared with 2.5% in the control group[189]. We were not able to look at sleep apnea, but we were able to look at the breathing rate in sleep.

The breathing rate during sleep across 24h was 3.13 ± 0.08 Hz in young Meis1$^{R272H/R272H}$ mice, 3.04 ± 0.08 Hz in aged Meis1$^{R272H/R272H}$ mice, 3.00 ± 0.08 Hz in young wildtype mice, and 3.05 ± 0.06 Hz in aged wildtype mice. However, the results showed that there was no significant difference between Meis1$^{R272H/R272H}$ mice and wildtype mice at any time period examined between genotypes (**Fig. 6.3 C and D**).

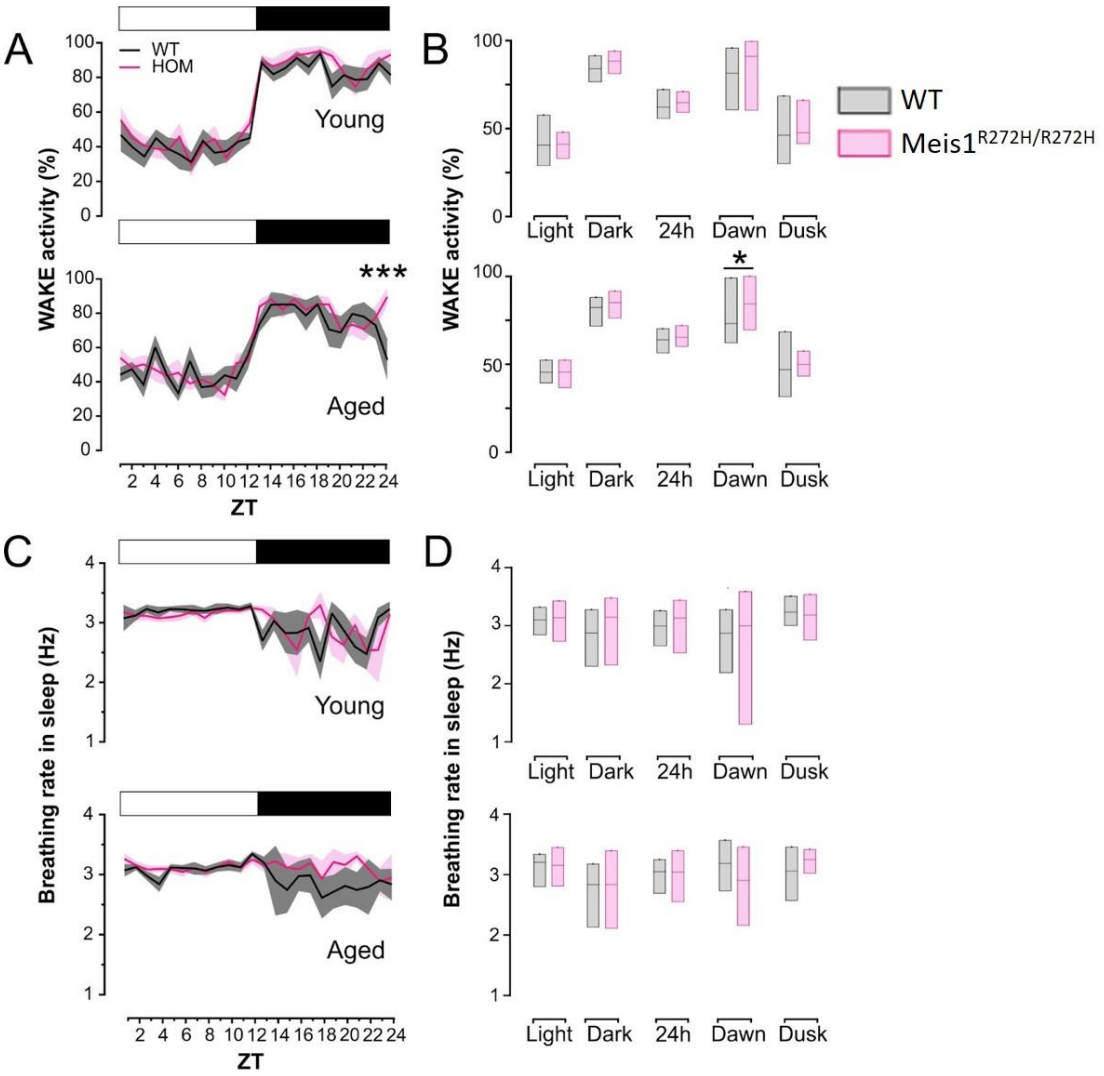

Figure 6.3 Wake activity and breathing rate in sleep for Meis1$^{R272H/R272H}$ and wildtype mice *(figure was co-made with Dr. Rhîannan H Williams)*. (A-B) The wake activity in light period, dark period, 24h, and at dawn (ZT23-1) and dusk (ZT11-13). Young Meis1$^{R272H/R272H}$ mice showed trend toward higher wake activity at dawn compared to wildtype mice, while aged Meis1$^{R272H/R272H}$ mice (83.6 ± 2.9%) showed significantly higher wake activity at dawn compared to wildtype mice (72.43 ± 4.0%, *p-value = 0.029, 2 way RM-ANOVA). (C-D) The breathing rate in light period, dark period, 24h, and at dawn (ZT23-1) and dusk (ZT11-13). There was no significant difference between Meis1$^{R272H/R272H}$ mice and wildtype mice at any time period examined between genotypes. Line: Mean ± SEM. n=7-11 per genotype.

Integration of phenotypic signatures for Meis1$^{R272H/R272H}$ mice

In order to examine the commonality between phenotypic responses in locomotor and sensorimotor tests, we computed Pearson correlation coefficients between traits and genotypes. Most of the examined parameters did not show significant differences between genotypes. However, the correlation between hot-plate reaction time and distance travelled (in the calorimetry chamber) was negative in wildtype mice ($r = -0.51$, $p = 0.04$), and was absent in Meis1$^{R272H/R272H}$ mice ($r = -0.01$, $p = 0.94$) (**Fig. 6.4 A**).

We also computed PCA to examine the integrated phenotypic data (**Fig. 6.4 B**). In PCA dimension 1 (accounted for 37.9% of the variance), the loadings between Meis1$^{R272H/R272H}$ mice and wildtype mice were significantly different (0.55 ± 0.11 for Meis1$^{R272H/R272H}$ mice, -0.55 ± 0.07 for wildtype mice, p-value = 0.045) (**Fig. 6.4 C**). In PCA dimension 3 (accounted for 17.4% of the variance), the loadings between Meis1$^{R272H/R272H}$ mice and wildtype mice showed subtle difference, but did not reach significant difference (0.25 ± 0.06 for Meis1$^{R272H/R272H}$ mice, -0.25 ± 0.06 for wildtype mice, p-value = 0.17) (**Fig. 6.4 B**). Therefore, integrating phenotypes reveals an overall phenotypic shift between Meis1$^{R272H/R272H}$ mice and wildtype mice.

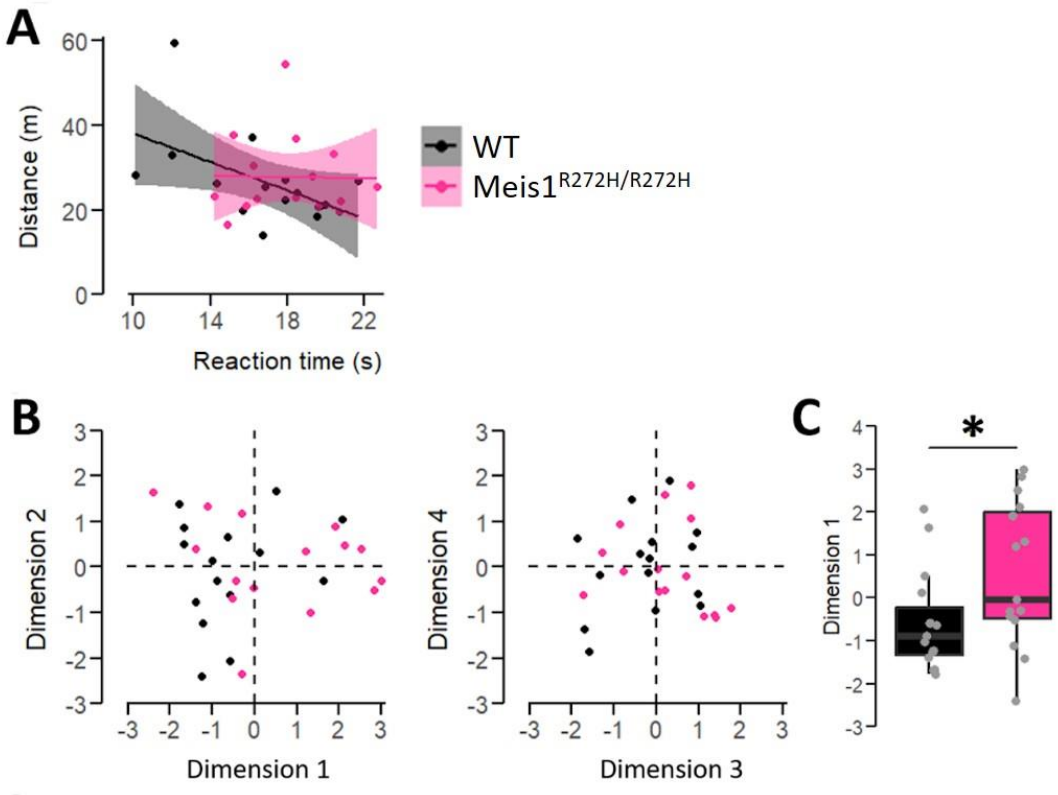

Figure 6.4 Integration of phenotypic signatures for Meis1$^{R272H/R272H}$ and wildtype mice.
(A) The regression correlation between hot-plate reaction time and distance travelled (in the calorimetry chamber). Wildtype mice showed negative correlation (r = -0.51, p = 0.04), while Meis1$^{R272H/R272H}$ mice showed almost 0 correlation (r = -0.01, p = 0.94). (B-C) PCA based on main phenotypic signatures. PCA dimension 1 showed significant difference between Meis1$^{R272H/R272H}$ mice (0.55 ± 0.11) and wildtype mice (-0.55 ± 0.07, p-value = 0.045). *p-value < 0.05, Student's t-test. n=15 per genotype.

Study B: Assessment of sleep behavior of Meis1$^{R272H/R272H}$ mice by EEG and piezo

The results of the sleep behavior study from the phenotypic assessment was fruitful. It suggested that aged Meis1$^{R272H/R272H}$ mice had higher wake activity at dawn compared to wildtype mice. However, the gold standard to examine sleep behavior is the vigilance analysis from EEG/EMG recording. Therefore, we decided to run another cohort and record sleep by both piezo and EEG/EMG.

Hence, we put both wildtype and Meis1$^{R272H/R272H}$ mice in piezo cages to record their sleep behavior for 4 days, as well as one day recording of EEG. We recorded their sleep behavior when they were around 8-9 months old (defined as young adult), and the second time when they were 12-14 months old (defined as aged adult) (**Fig. 6.5**).

The first day of piezo recording was considered habituation, and was not used for analysis. We then averaged the sleep percent time from day 2 to day 4, and made an averaged sleep percent time for 24 hours based on 1-hour temporal resolution. The results showed that young adult Meis1$^{R272H/R272H}$ mice slept significantly less in ZT23-24 compared to wildtype mice (Sleep percent time: 7.86 ± 2.43% for Meis1$^{R272H/R272H}$ mice, 28.20 ± 6.59% for wildtype mice, p = 0.03) (**Fig. 6.6 A**). On the other hand, aged adult Meis1$^{R272H/R272H}$ mice slept significantly less in ZT0-1 (24.66 ± 3.82% for Meis1$^{R272H/R272H}$ mice, 41.11 ± 1.92% for wildtype mice, p = 0.01), ZT11-12 (42.24 ± 3.68% for Meis1$^{R272H/R272H}$ mice, 55.45 ± 2.20% for wildtype mice, p = 0.02), and ZT22-23 (13.95 ± 4.36% for Meis1$^{R272H/R272H}$ mice, 33.69 ± 5.88% for wildtype mice, p = 0.03) compared to wildtype mice (**Fig. 6.6 B**). These results suggested that the differences were more significant at the transition time between light and dark periods (dawn and dusk).

We then examined the sleep percent time in light period (ZT0-12), dark period (ZT12-24), and across 24h. We also examined dawn (ZT23-1) and dusk (ZT11-13) since we saw differences in the last figure.
We noticed that young adult Meis1$^{R272H/R272H}$ mice slept significantly less compared to wildtype mice in dark period (Sleep percent time: 26.69 ± 0.76% for Meis1$^{R272H/R272H}$ mice, 30.80 ± 1.19% for wildtype mice, p = 0.02), but showed no difference in light period (57.89 ± 1.53% for Meis1$^{R272H/R272H}$ mice, 58.33 ± 0.36% for wildtype mice, p = 0.79), as well as in entire 24 hours (42.29 ± 1.04% for Meis1$^{R272H/R272H}$ mice, 44.56 ± 0.61% for wildtype mice, p = 0.11) (**Fig. 6.7 A**). The aged adult Meis1$^{R272H/R272H}$ mice showed no difference in dark period (23.70 ± 2.65% for Meis1$^{R272H/R272H}$ mice, 24.12 ± 2.62% for wildtype mice, p = 0.91), light period (53.40 ± 2.27% for Meis1$^{R272H/R272H}$ mice, 58.94 ± 1.20% for wildtype mice, p = 0.08), as well as entire 24 hours (38.55 ± 2.03% for Meis1$^{R272H/R272H}$ mice, 41.53 ± 0.96% for wildtype mice, p = 0.25) compared to wildtype mice, even though Meis1$^{R272H/R272H}$ mice showed trend toward lower sleep percent time in light period compared to wildtype mice (**Fig. 6.7 B**).

For dawn and dusk, the results showed that young adult Meis1$^{R272H/R272H}$ mice

slept significantly less at dawn compared to the wildtype mice (Sleep percent time: 38.21 ± 5.25% for Meis1$^{R272H/R272H}$ mice, 51.68 ± 2.91% for wildtype mice, p = 0.04) (**Fig. 6.7 C)**. This is the same for aged adult Meis1$^{R272H/R272H}$ mice, which also slept significantly less at dawn compared to the wildtype mice (14.86 ± 1.71% for Meis1$^{R272H/R272H}$ mice, 32.58 ± 5.19% for wildtype mice, p = 0.03) (**Fig. 6.7 D)**. However, there was no significant difference between Meis1$^{R272H/R272H}$ and wildtype mice at dusk for both young adult mice (34.96 ± 1.95% for Meis1$^{R272H/R272H}$ mice, 30.68 ± 2.18% for wildtype mice, p = 0.18), and aged adult mice (28.94 ± 2.33% for Meis1$^{R272H/R272H}$ mice, 33.45 ± 0.48% for wildtype mice, p = 0.14) (**Fig. 6.7 C and D**).

In this cohort, we also recorded EEG/EMG for 24 hours (1 day) (**Fig. 6.8 A and B**). The EEG results showed that both young and aged adult Meis1$^{R272H/R272H}$ mice slept significantly less (higher wake percent time) at dawn compared to wildtype mice (p-value < 0.05). However, there was no significant difference between Meis1$^{R272H/R272H}$ and wildtype mice at dusk (**Fig. 6.8 C and D**). This result was the same as the piezo recording (**Fig. 6.7**). Both recordings showed significant differences between Meis1$^{R272H/R272H}$ and wildtype mice at dawn, and no significant difference at dusk.

These results suggested that both young and aged adult Meis1$^{R272H/R272H}$ mice had stronger sleep disturbance at dawn (ZT23-ZT1) compared to wildtype mice, which matched the symptom from human RLS patients. Besides, aged adult Meis1$^{R272H/R272H}$ mice showed trend toward lower sleep percent time in light period compared to wildtype mice. Hence, Meis1$^{R272H/R272H}$ mice showed similar sleep disturbance as the RLS human patients. This supported Meis1$^{R272H/R272H}$ mice to be a possible disease mouse model to study RLS.

The results from this cohort were not exactly the same to the cohort from phenotypic assessment (**Fig. 6.3 A and B**), but they did show similar features. The aged adult Meis1$^{R272H/R272H}$ mice from both cohorts showed lower sleep percent time (higher wake activity) at dawn compared to the wildtype mice. The young adult Meis1$^{R272H/R272H}$ mice from phenotypic assessment did not show significantly higher wake activity compared to the wildtype mice, but it showed trend toward higher wake activity. The differences might be caused by different recording cages, environments, and the personnels that performed the recordings. However, Meis1$^{R272H/R272H}$ mice from both cohorts showed higher wake activity at dawn compared to the wildtype mice. This further supports the results of the hyperactivity of Meis1$^{R272H/R272H}$ mice at dawn.

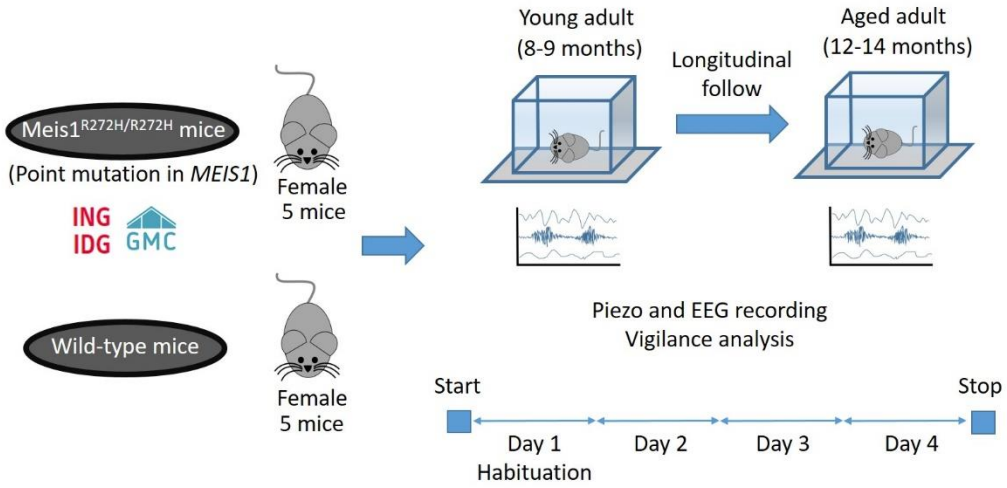

Figure 6.5 Experimental design for the sleep behavior study. The flowchart of the experiment for sleep behavior study.

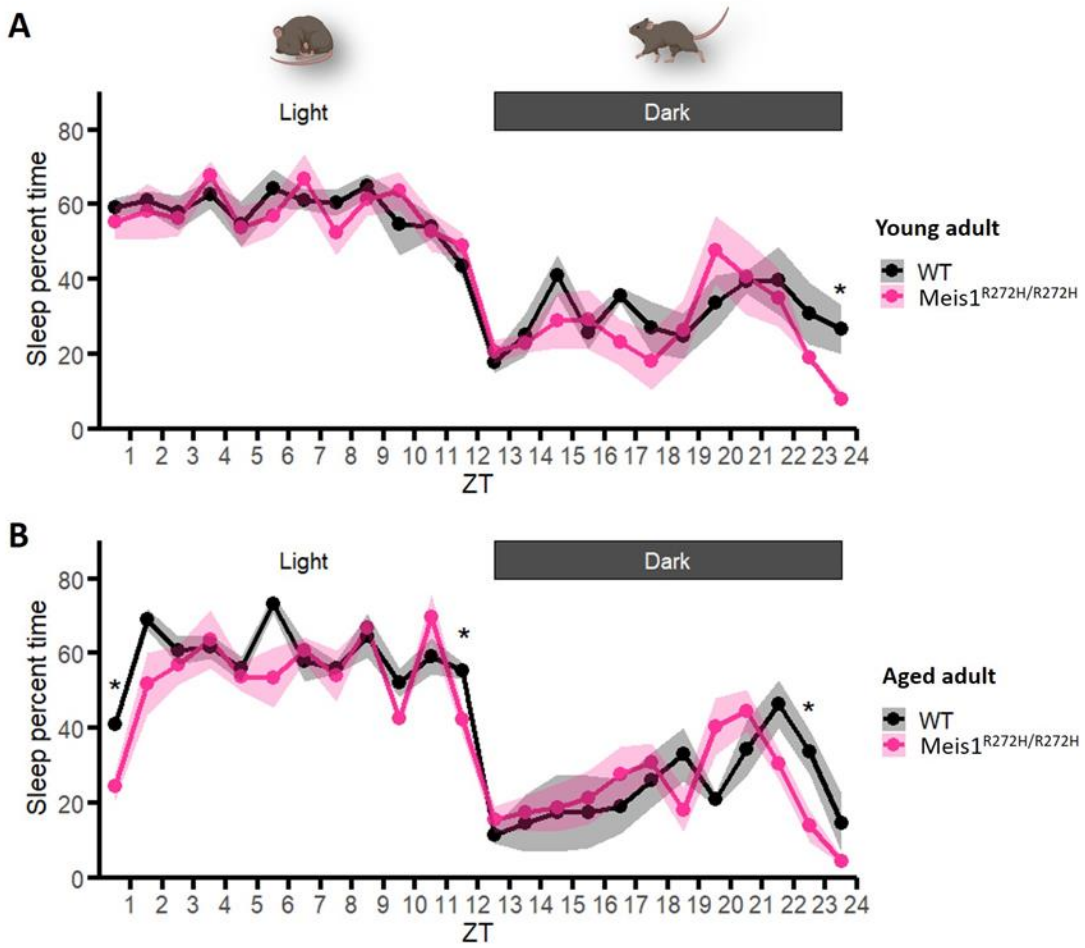

Figure 6.6 Averaged sleep percent time from day two to day four. (A) Averaged sleep percent time in young adult Meis1$^{R272H/R272H}$ and wildtype mice from day 2 to 4. Meis1$^{R272H/R272H}$ mice slept significantly less in ZT23-24 compared to wildtype mice. (B) Averaged sleep percent time in aged adult Meis1$^{R272H/R272H}$ and wildtype mice from day 2 to 4. Meis1$^{R272H/R272H}$ mice slept significantly less in ZT0-1, ZT11-12, and ZT22-23 compared to wildtype mice. Time bin: 1 hour. Line: Mean ± SEM. *p-value < 0.05, Student's t-test. n=4-5 per genotype.

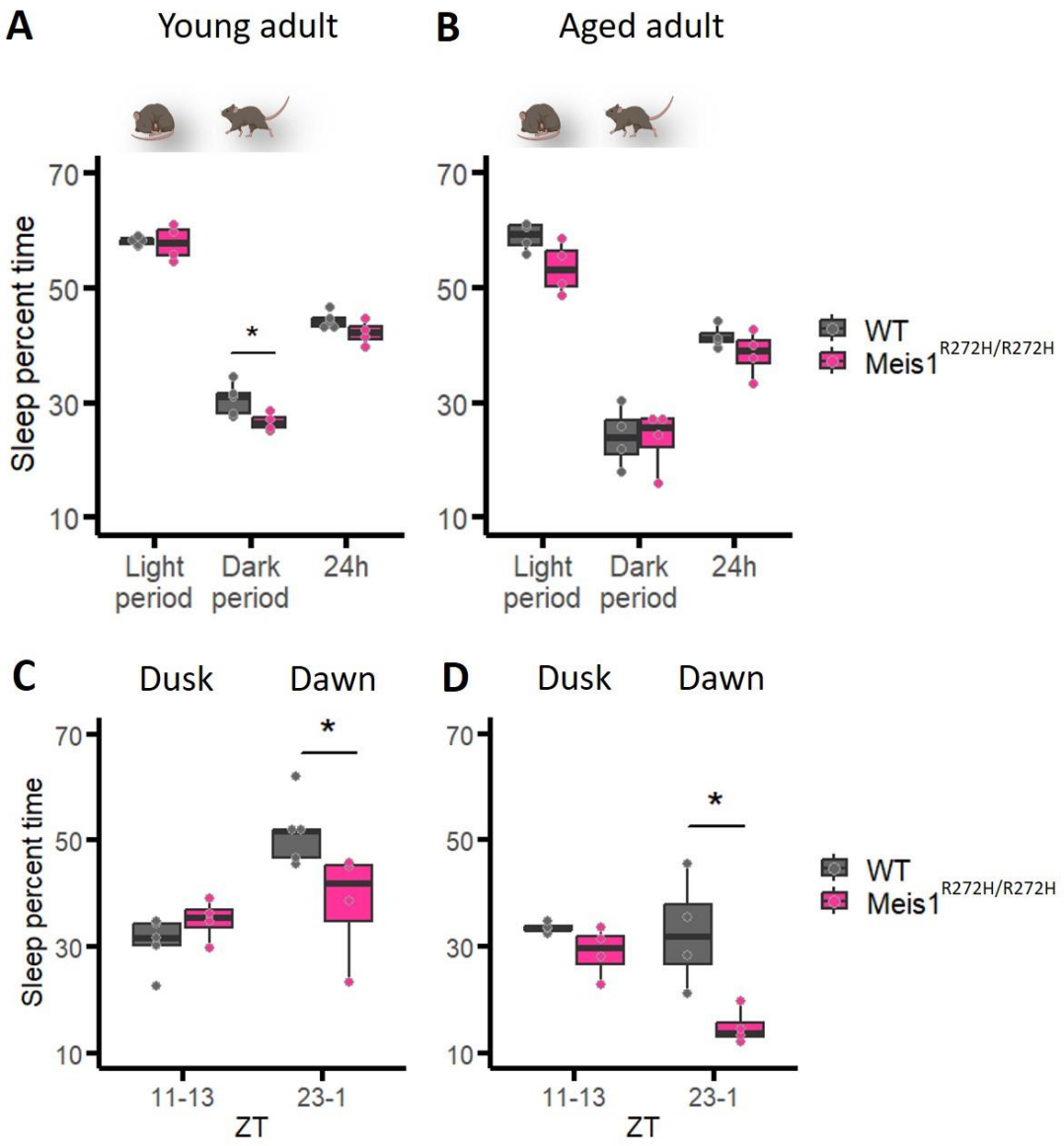

Figure 6.7 Sleep percent time in dark period, light period, 24 hours, as well as at dawn and dusk for Meis1$^{R272H/R272H}$ and wildtype mice. (A) Sleep percent time in light and dark periods in young adult Meis1$^{R272H/R272H}$ and wildtype mice. Meis1$^{R272H/R272H}$ mice slept significantly less compared to wildtype mice in dark period, but showed no difference in light period. (B) Sleep percent time in light and dark periods in aged adult Meis1$^{R272H/R272H}$ and wildtype mice. Meis1$^{R272H/R272H}$ mice showed no difference in both light and dark periods compared to wildtype mice, even though Meis1$^{R272H/R272H}$ mice showed trend toward lower sleep percent time in light period compared to wildtype mice. (C) Sleep percent time at dawn (ZT23-ZT1) and dusk (ZT11-ZT13) in young adult Meis1$^{R272H/R272H}$ and wildtype mice. (D) Sleep percent time at dawn (ZT23-ZT1) and dusk (ZT11-ZT13) in aged adult Meis1$^{R272H/R272H}$ and wildtype mice. Both young and aged adult Meis1$^{R272H/R272H}$ mice slept significantly less at dawn compared to the wildtype mice. However, there was no significant difference between Meis1$^{R272H/R272H}$ and wildtype mice at dusk. *p-value < 0.05, Student's t-test. n=4-5 per genotype.

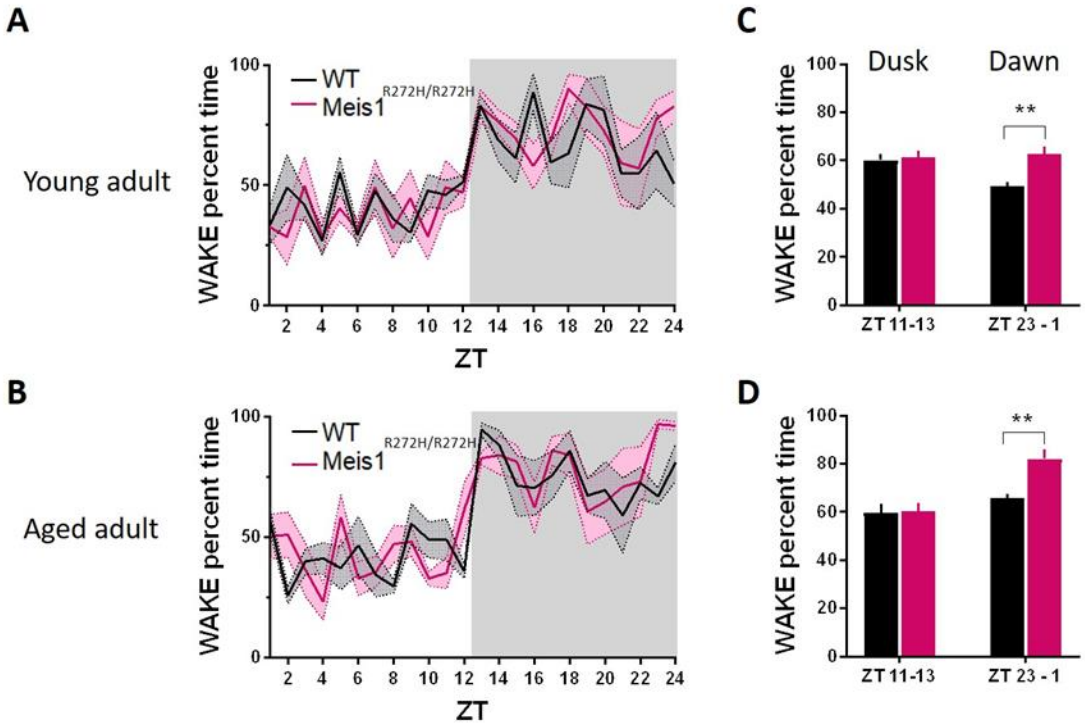

Figure 6.8 Wake percent time recorded by EEG for Meis1$^{R272H/R272H}$ and wildtype mice *(figure was made by Dr. Rhîannan H Williams)*. (A) Wake percent time in young adult Meis1$^{R272H/R272H}$ and wildtype mice in 24 hours EEG recording. (B) Wake percent time in aged adult Meis1$^{R272H/R272H}$ and wildtype mice in 24 hours EEG recording. Line: Mean ± SEM. (C) Wake percent time at dawn (ZT23-ZT1) and dusk (ZT11-ZT13) in young adult Meis1$^{R272H/R272H}$ and wildtype mice. (D) Wake percent time at dawn (ZT23-ZT1) and dusk (ZT11-ZT13) in aged adult Meis1$^{R272H/R272H}$ and wildtype mice. Both young and aged adult Meis1$^{R272H/R272H}$ mice showed significantly longer wake percent time at dawn compared to the wildtype mice. However, there was no significant difference between Meis1$^{R272H/R272H}$ and wildtype mice at dusk. **p-value < 0.05. n=4-5 per genotype.

#Data in the figure was prepared and analysed by Dr. Rhîannan H Williams for the project

Assessment of breathing rate of Meis1$^{R272H/R272H}$ mice by piezo

Same as the sleep percent time, the breathing rates in sleep from day 2 to day 4 were averaged to make a 24-hours breathing rate figure based on 1-hour temporal resolution. The results showed that there was no significant difference between the young adult Meis1$^{R272H/R272H}$ mice and wildtype mice at any time point (**Fig. 6.9 A**). However, aged adult Meis1$^{R272H/R272H}$ mice showed significantly lower breathing rate during sleep in ZT8-9 (2.57 ± 0.13 Hz for Meis1$^{R272H/R272H}$ mice, 2.92 ± 0.03 Hz for wildtype mice, p = 0.02), and ZT21-22 (2.53 ± 0.08 Hz for Meis1$^{R272H/R272H}$ mice, 3.01 ± 0.08 Hz for wildtype mice, p = 0.02) compared to wildtype mice (**Fig. 6.9 B**).

We then examined the breathing rate during sleep in light period, dark period, entire 24 hours, as well as at dawn and dusk. The results showed that there was no significant difference between the young adult Meis1$^{R272H/R272H}$ mice and wildtype mice at any time period. However, young adult Meis1$^{R272H/R272H}$ mice showed subtle trend toward lower breathing rate in dark period compared to wildtype mice (2.61 ± 0.07 Hz for Meis1$^{R272H/R272H}$ mice, 2.80 ± 0.7 Hz for wildtype mice, p = 0.2) (**Fig. 6.10 A**). Similarly, aged adult Meis1$^{R272H/R272H}$ mice also did not show significant difference at any time period compared to wildtype mice. However, aged adult Meis1$^{R272H/R272H}$ mice showed trend toward lower breathing rate in all periods compared to wildtype mice. Across 24 hours aged adult Meis1$^{R272H/R272H}$ mice had a breathing rate of 2.59 ± 0.13 Hz, and wildtype mice, 2.96 ± 0.08 Hz (p = 0.11) (**Fig. 6.10 B**). These results suggested that aged adult Meis1$^{R272H/R272H}$ mice had a trend toward lower breathing rate in sleep compared to wildtype mice. However, more studies on breathing rate are required to prove the real changes.

The results from this cohort were also not exactly the same to the cohort from phenotypic assessment (**Fig. 6.3 C and D**). The young adult Meis1$^{R272H/R272H}$ mice from both cohorts did not show different breathing rate compared to wildtype mice. This was the same for aged adult Meis1$^{R272H/R272H}$ mice from the phenotypic assessment. However, the aged adult Meis1$^{R272H/R272H}$ mice showed trend toward lower breathing rate compared to wildtype mice. So far we could not explain the reasons that caused the differences. But it could be caused by different recording cages, environments, and the personnels that performed the recordings.

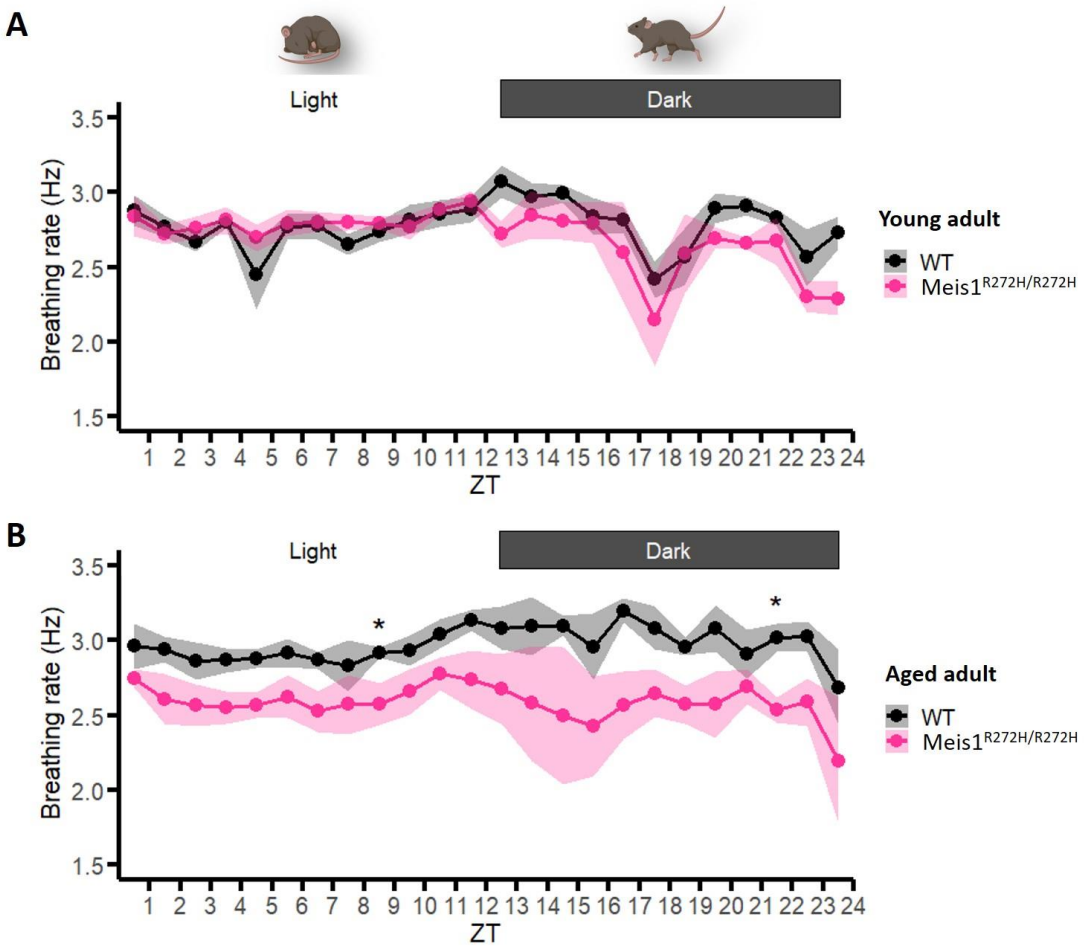

Figure 6.9 Averaged breathing rate in sleep from day two to day four. (A) Averaged breathing rate in sleep during baseline recording (no intervention) in young adult Meis1$^{R272H/R272H}$ and wildtype mice from day 2 to 4 . No significant difference at any time point. (B) Averaged breathing rate during sleep in aged adult Meis1$^{R272H/R272H}$ and wildtype mice from day 2 to 4. Meis1$^{R272H/R272H}$ mice showed lower breathing rate during sleep in ZT8-9 and ZT21-22 compared to wildtype mice. Time bin: 1 hour. Line: Mean ± SEM. *p-value < 0.05, Wilcoxon rank sum test (Mann Whitney U test). n=4-5 per genotype.

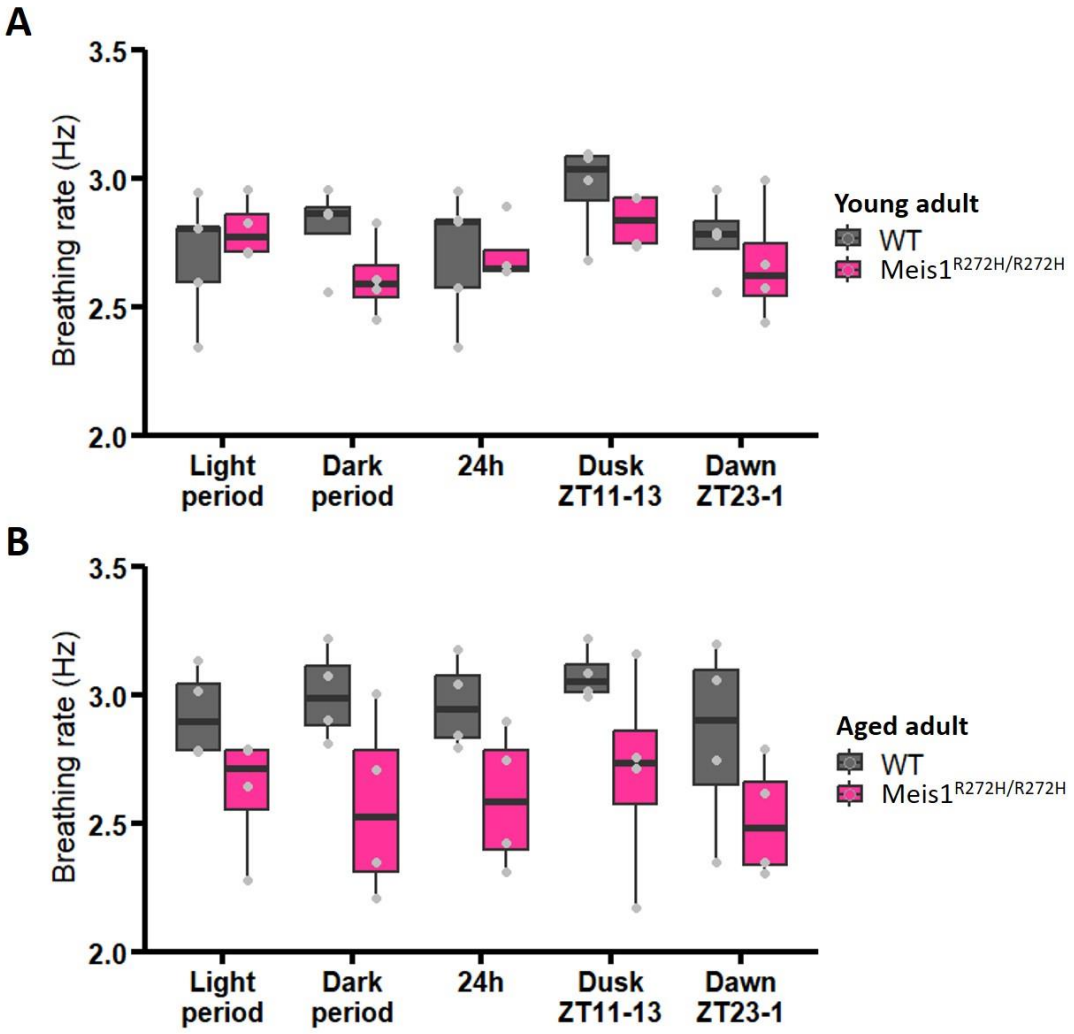

Figure 6.10 Breathing rate during sleep in dark period, light period, 24h, as well as at dawn and dusk for Meis1$^{R272H/R272H}$ and wildtype mice. (A) Breathing rate during sleep in 5 time periods in young adult Meis1$^{R272H/R272H}$ and wildtype mice. There was no significant difference at any time period, but Meis1$^{R272H/R272H}$ mice showed subtle trend toward lower breathing rate in dark period compared to wildtype mice. (B) Breathing rate during sleep in 5 time periods in aged adult Meis1$^{R272H/R272H}$ and wildtype mice. There was no significant difference at any time period, but Meis1$^{R272H/R272H}$ mice showed subtle trend toward lower breathing rate in all time periods compared to wildtype mice. Statistics: Wilcoxon rank sum test (Mann Whitney U test). n=4-5 per genotype.

Calculate and annotate active neurons by ClearMap

In order to examine the brain regions that contributed to the hyperactivity of Meis1$^{R272H/R272H}$ at dawn, brain tissues from Meis1$^{R272H/R272H}$ and wildtype mice were taken out at either ZT0 (dawn) or ZT12 (dusk). iDISCO+ was then performed to clear the tissues, as well as immunolabeling c-Fos positive neurons. Afterwards, samples were imaged by light sheet microscopy and ClearMap was run for automatic cell detection and annotation (**Fig. 6.11 A**).

The same analysis method from chapter 3 “Sleep deprivation methodology” was used in this study, including the decision making of intensity threshold for cell detection. Similar to chapter 3, after the threshold optimization steps were finalized, ClearMap was run based on the chosen thresholds, and I compared the results between ClearMap automatic cell detection and human manual cell counting at small areas in the cortex. The median of Precision, Recall, and F1 score for our 22 samples were 89%, 66%, and 75%, respectively (**Fig. 6.11 B**).

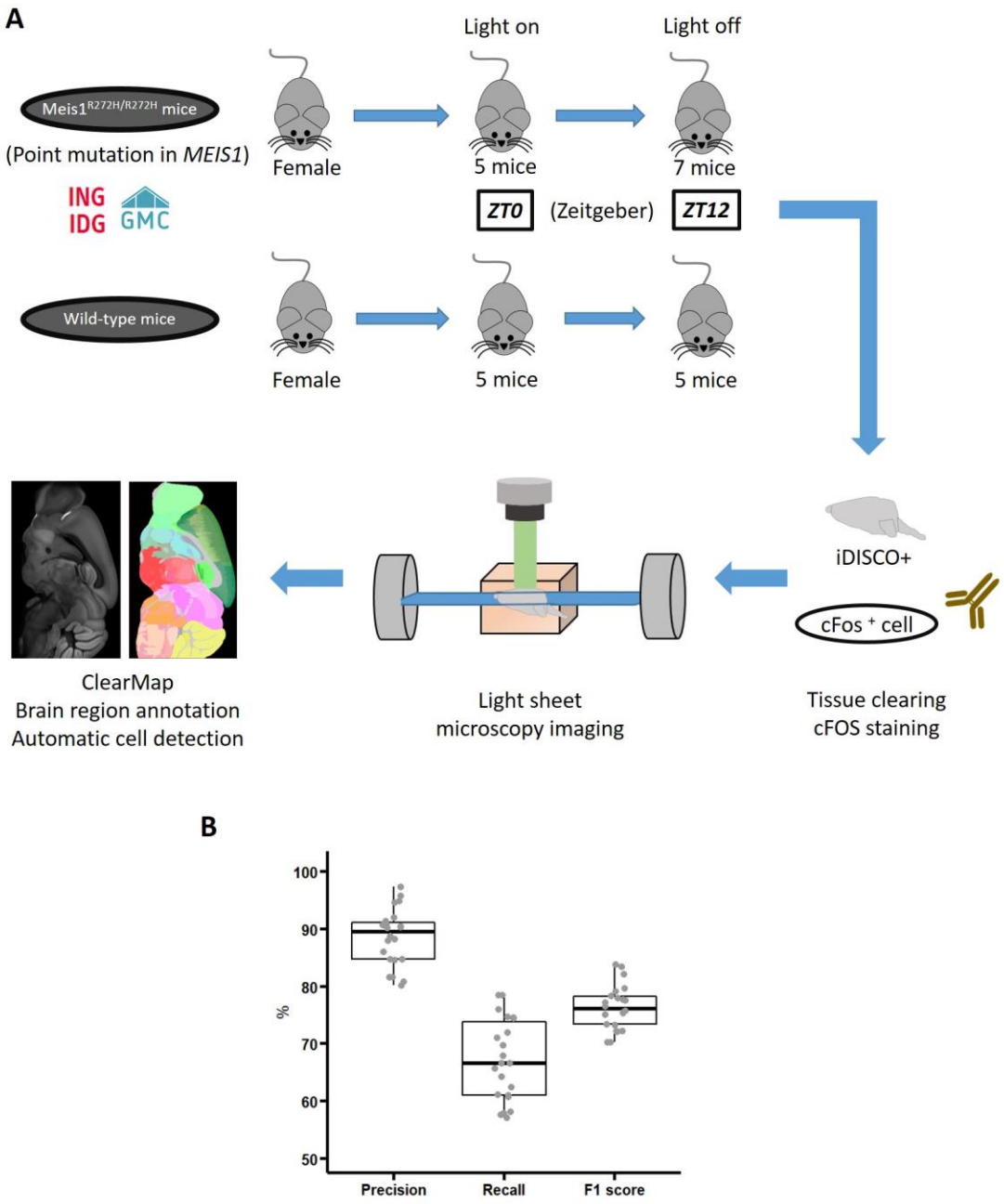

Figure 6.11 Experimental design for iDISCO+ and comparison between automatic and manual cell counts. (A) The flowchart of experimental design. (B) The median of Precision, Recall, and F1 score were 89%, 66%, and 75%, respectively, between the automatic and manual cell counts in the chosen areas. n=22.

Whole brain mapping suggests some brains regions that might contribute to hyperactivity in Meis1$^{R272H/R272H}$ mice

After using ClearMap for whole brain mapping and automatic cell detection, we got the cell counts for over 250 regions (**Supplementary table 2 in Appendices**). In order to have an overview for the cell counts from all brain regions across all 4 groups, the original cell counts were scaled to the percentage of active cells in the whole brain (cell count in one region/cell count in the whole brain), and the brain regions were arranged based on 9 high-level brain regions (**Fig. 6.12**).

Then volcano plots were made to find out the regions that showed low p-value and high fold change between Meis1$^{R272H/R272H}$ and wildtype mice at ZT0 and ZT12. The differences between Meis1$^{R272H/R272H}$ and wildtype mice were subtle at ZT0 (**Fig. 6.13 A**), and more obvious at ZT12 (more regions with lower p-value) (**Fig. 6.13 B**). Zona incerta and pallidum showed low p-value and high fold change (more active in Meis1$^{R272H/R272H}$ compared to wildtype mice) at ZT12 (-log10(p-value) > 2.3 and log2(fold change) > 1)). This result is intriguing because zona incerta is involved in arousal, attention, and locomotion[190], and pallidum is involved in the regulation of voluntary movement and movement planning[205,206]. The higher activity of these two regions could potentially lead to different phenotypes, even though there was no significant difference for sleep/wake percent time between Meis1$^{R272H/R272H}$ and wildtype mice at dusk (results from piezo and EEG recordings) (**Fig. 6.7 and 6.8**).

Since the differences between Meis1$^{R272H/R272H}$ and wildtype mice at ZT0 were subtle, we decided to examine the diurnal differences (dawn vs dusk, or ZT0 vs ZT12) in Meis1$^{R272H/R272H}$ and wildtype mice. Pedunculopontine nucleus and 4 preoptic areas (anteroventral preoptic nucleus, medial preoptic area, anterodorsal preoptic nucleus, ventrolateral preoptic nucleus) showed low p-value and high fold change (more active at ZT12 compared to ZT0) between Meis1$^{R272H/R272H}$ ZT0 and Meis1$^{R272H/R272H}$ ZT12 groups (-log10(p-value) > 1.8 and log2(fold change) > 1.6)) (**Fig. 6.13 C**). On the contrary, uvula (IX) of cerebellum showed low p-value, but it was more active at ZT0 compared to ZT12 (-log10(p-value) > 2.8 and log2(fold change) < -1.3)) (**Fig. 6.13 C**). We were especially interested in pedunculopontine nucleus (PPN) and ventrolateral preoptic nucleus (VLPO), since PPN is involved in posture and gait control and VLPO is a NREM sleep-promoting region[82,91,92]. These two regions could potentially contribute to the hyperactivity of Meis1$^{R272H/R272H}$ mice at dawn (results from piezo and EEG recordings) (**Fig. 6.7 and 6.8**).

In the wildtype mice, the diurnal differences were subtle (fewer regions with lower p-value). However, rostral linear nucleus raphe showed low p-value and high fold change (more active at ZT0 compared to ZT12) between wildtype ZT0 and wildtype ZT12 groups (-log10(p-value) > 2.3 and log2(fold change) < -3.1)) (**Fig. 6.13 D**), even though this region is less relevant to sleep and vigilance. The regions mentioned in this paragraph and the last two paragraphs were selected based on their distribution in the volcano plots, where they showed low p-value compared to other brain regions, but not

based on specific thresholds.

We then wanted to examine if the regions that showed low p-value and high fold change in the volcano plots showed significant differences. However, none of the regions that were labelled in **Fig. 6.13** (1. Pedunculopontine nucleus, 2.Anteroventral preoptic nucleus, 3. Medial preoptic area, 4. Anterodorsal preoptic nucleus, 5.Ventrolateral preoptic nucleus, 6. Rostral linear nucleus raphe, 7. Zona incerta, 8. Uvula (IX) of cerebellum, 9. Pallidum) showed significant difference between Meis1$^{R272H/R272H}$ and wildtype mice, as well as between ZT0 and ZT12 groups. (Two-way ANOVA with multiple testing correction) (**Fig. 6.14 A and B**). In fact, no brain region (in the entire brain) showed significant difference between Meis1$^{R272H/R272H}$ and wildtype mice, as well as between ZT0 and ZT12 groups. This suggested that there were trend of changes in some regions (for example, PPN and VLPO between Meis1$^{R272H/R272H}$ ZT0 and ZT12 groups), but the differences were not strong enough to reach significant differences after multiple testing correction.

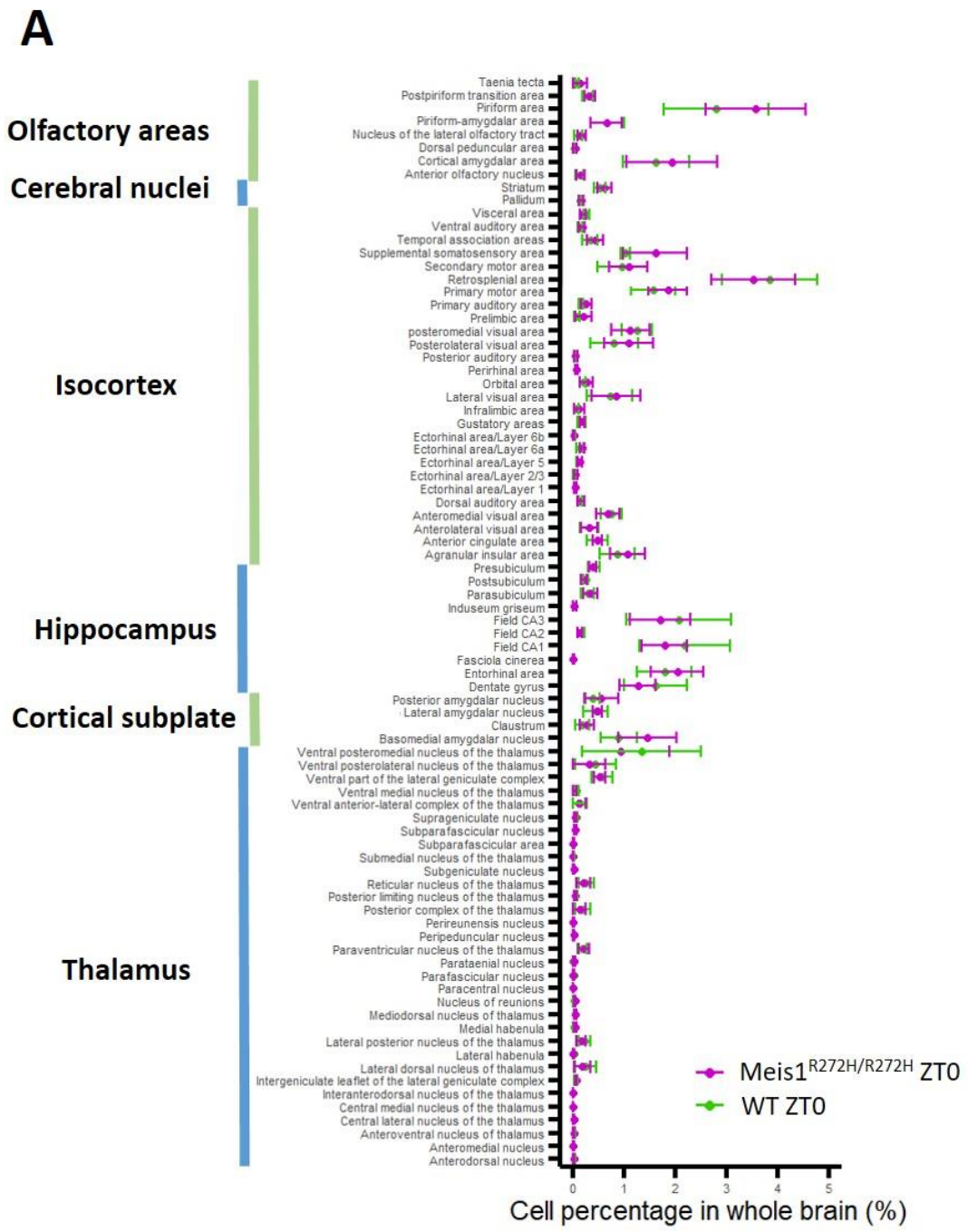

Figure 6.12 (A) Cell percentage of c-Fos positive neurons in olfactory areas, cerebral nuclei, isocortex, hippocampus, cortical subplate, and thalamus in Meis1$^{R272H/R272H}$ and wildtype mice at ZT0. Line: Mean ± SEM. n=5-7 per group.

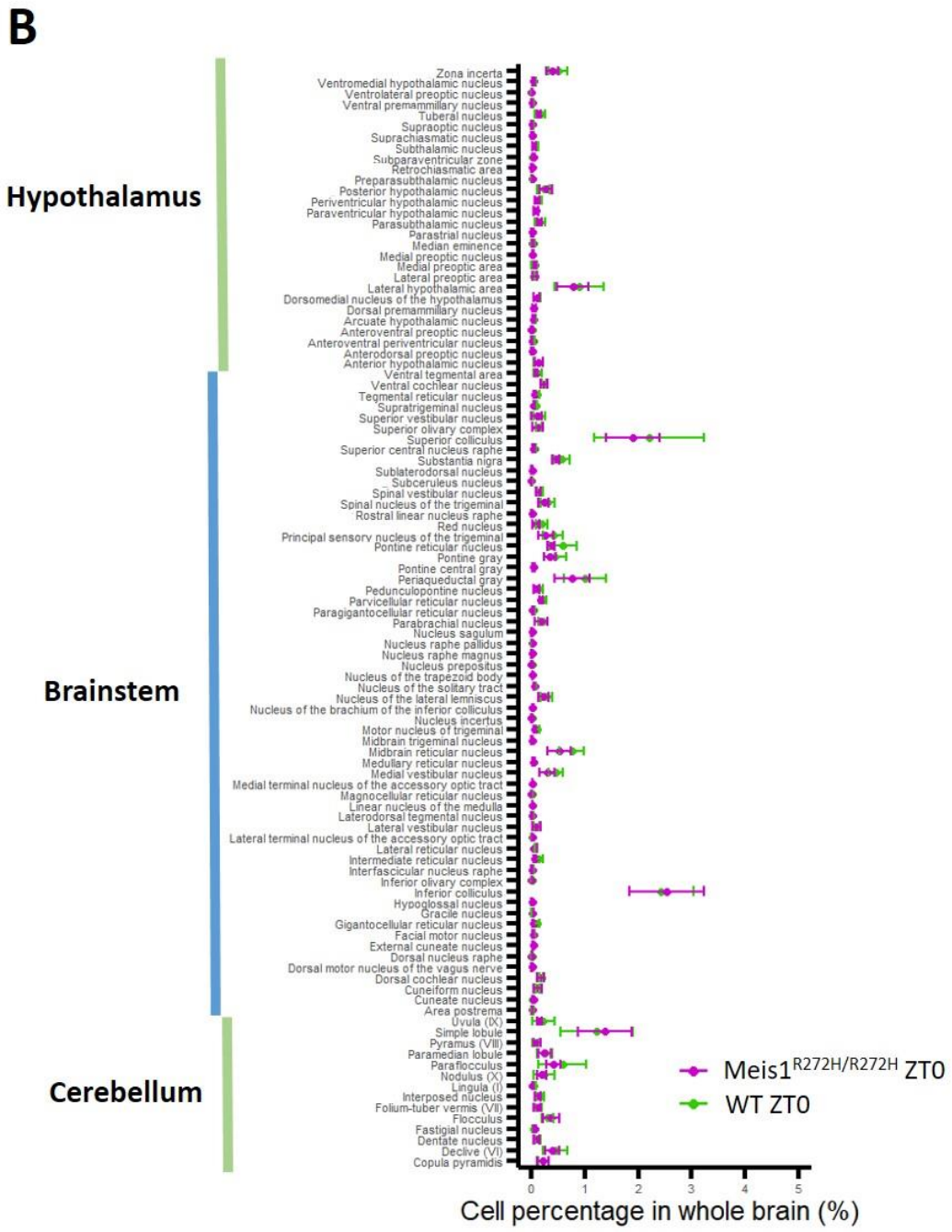

Figure 6.12 (B) Cell percentage of c-Fos positive neurons in hypothalamus, brainstem, and cerebellum in Meis1$^{R272H/R272H}$ and wildtype mice at ZT0. Line: Mean ± SEM. n=5-7 per group.

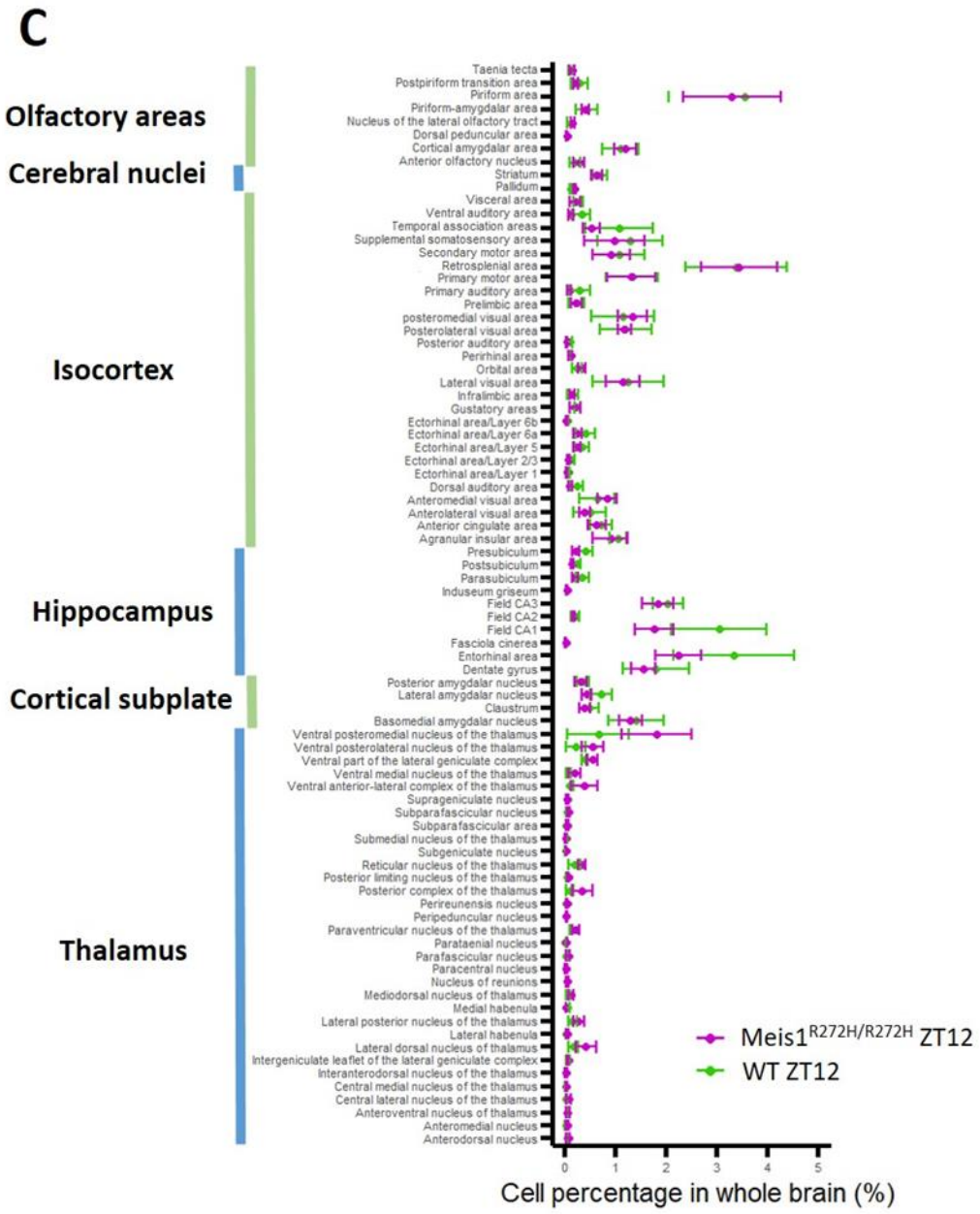

Figure 6.12 (C) Cell percentage of c-Fos positive neurons in olfactory areas, cerebral nuclei, isocortex, hippocampus, cortical subplate, and thalamus in Meis1$^{R272H/R272H}$ and wildtype mice at ZT12. Line: Mean ± SEM. n=5-7 per group.

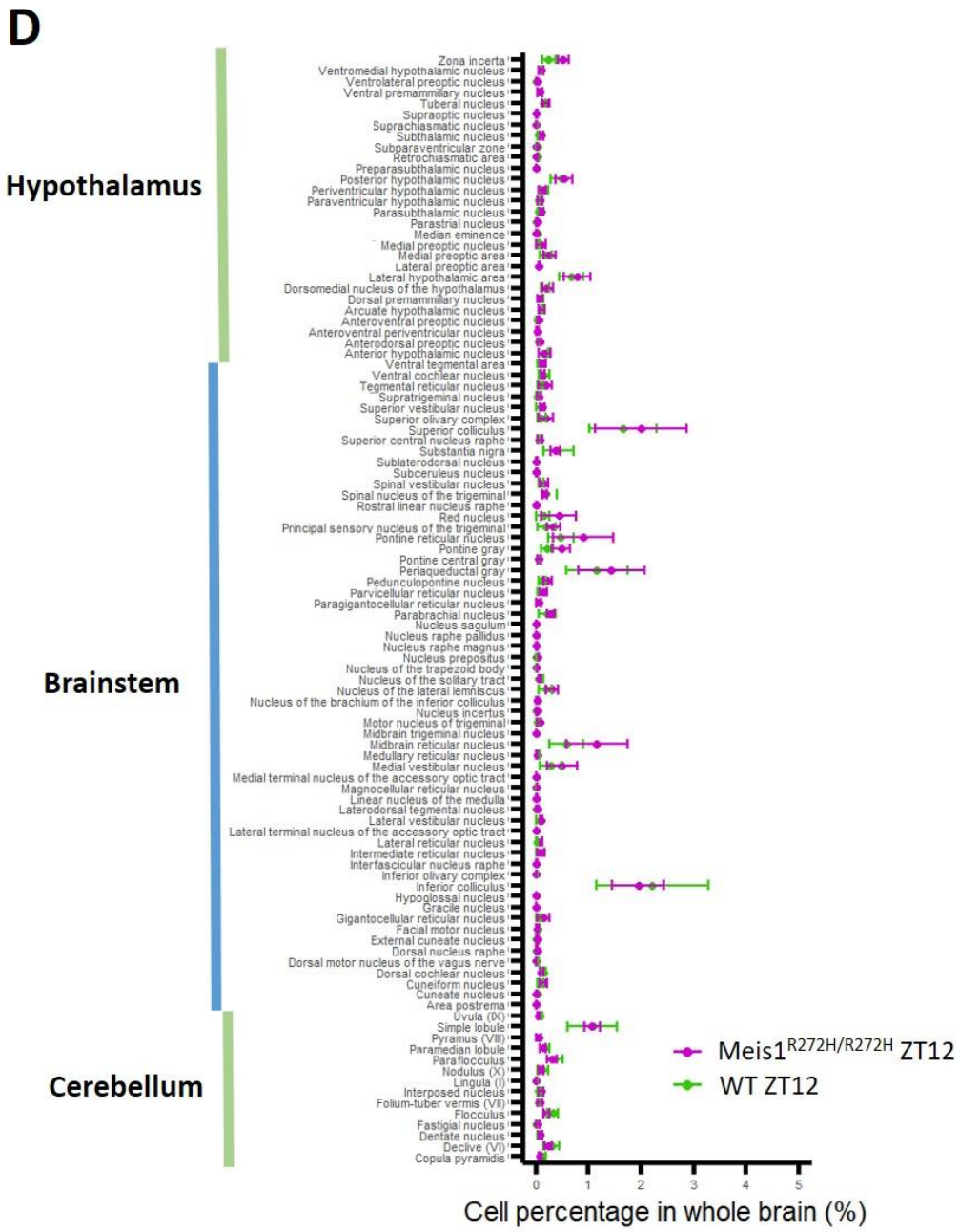

Figure 6.12 (D) Cell percentage of c-Fos positive neurons in hypothalamus, brainstem, and cerebellum in Meis1$^{R272H/R272H}$ and wildtype mice at ZT12. Line: Mean ± SEM. n=5-7 per group.

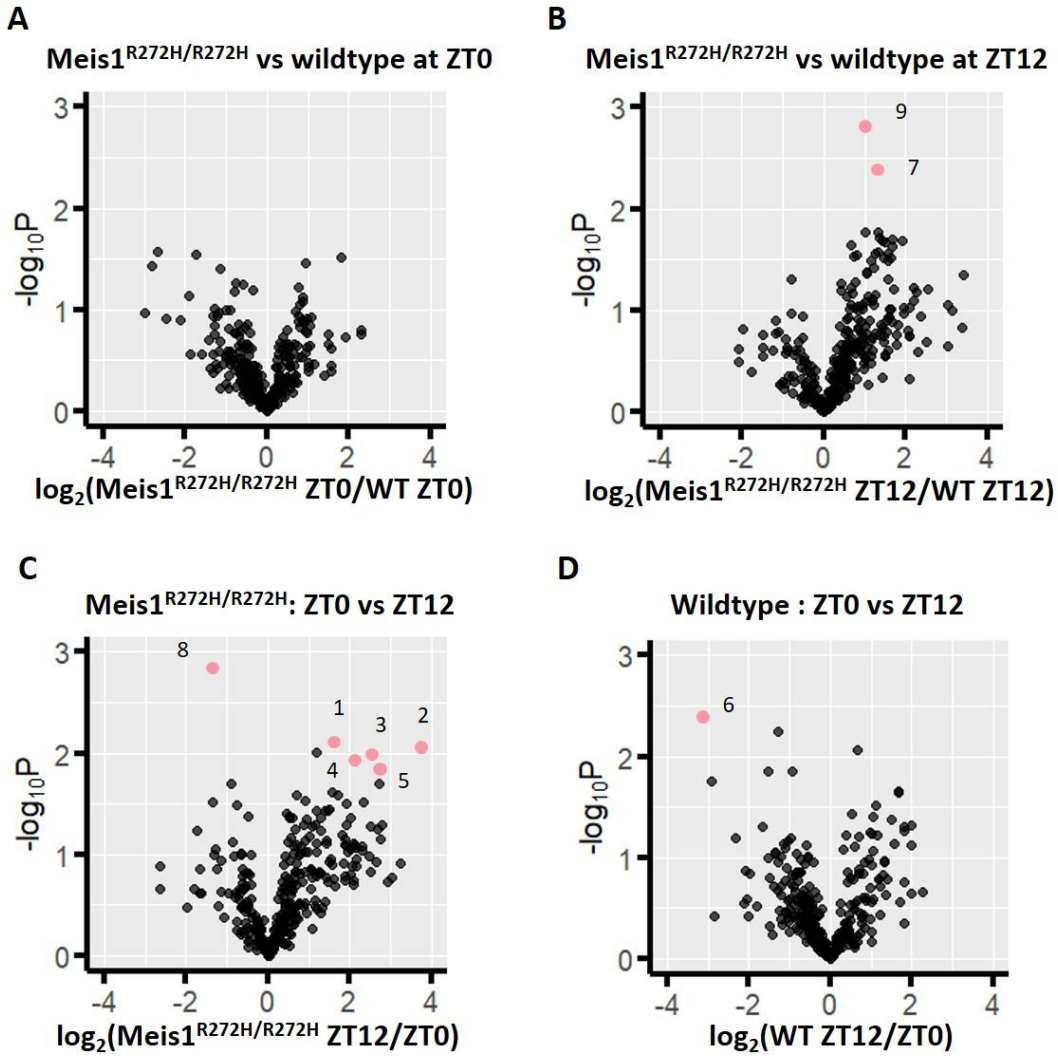

1	Pedunculopontine nucleus
2	Anteroventral preoptic nucleus
3	Medial preoptic area
4	Anterodorsal preoptic nucleus
5	Ventrolateral preoptic nucleus
6	Rostral linear nucleus raphe
7	Zona incerta
8	Uvula (IX) of cerebellum
9	Pallidum

Figure 6.13 Volcano plot of c-Fos positive neurons for Meis1$^{R272H/R272H}$ and wildtype mice. (A) Volcano plot between Meis1$^{R272H/R272H}$ and wildtype mice at ZT0. (B) Volcano plot between Meis1$^{R272H/R272H}$ and wildtype mice at ZT12. Zona incerta and pallidum showed low p-value and high fold change (more active in Meis1$^{R272H/R272H}$ compared to wildtype mice). (C) Volcano plot between Meis1$^{R272H/R272H}$ ZT0 and Meis1$^{R272H/R272H}$ ZT12 groups. Pedunculopontine nucleus and 4 preoptic areas (anteroventral preoptic nucleus, medial preoptic area, anterodorsal preoptic nucleus, ventrolateral preoptic nucleus) showed low p-value and high fold change (more active at ZT12 compared to ZT0). Uvula (IX) of cerebellum also showed low p-value

and high fold change (more active at ZT0 compared to ZT12). (D) Volcano plot between wildtype ZT0 and wildtype ZT12 groups. Rostral linear nucleus raphe showed low p-value and high fold change (more active at ZT0 compared to ZT12). p-values were calculated by Student's t-test. n=5-7 per group.

Regions: 1. Pedunculopontine nucleus, 2.Anteroventral preoptic nucleus, 3. Medial preoptic area, 4. Anterodorsal preoptic nucleus, 5.Ventrolateral preoptic nucleus, 6. Rostral linear nucleus raphe, 7. Zona incerta, 8. Uvula (IX) of cerebellum, 9. Pallidum.

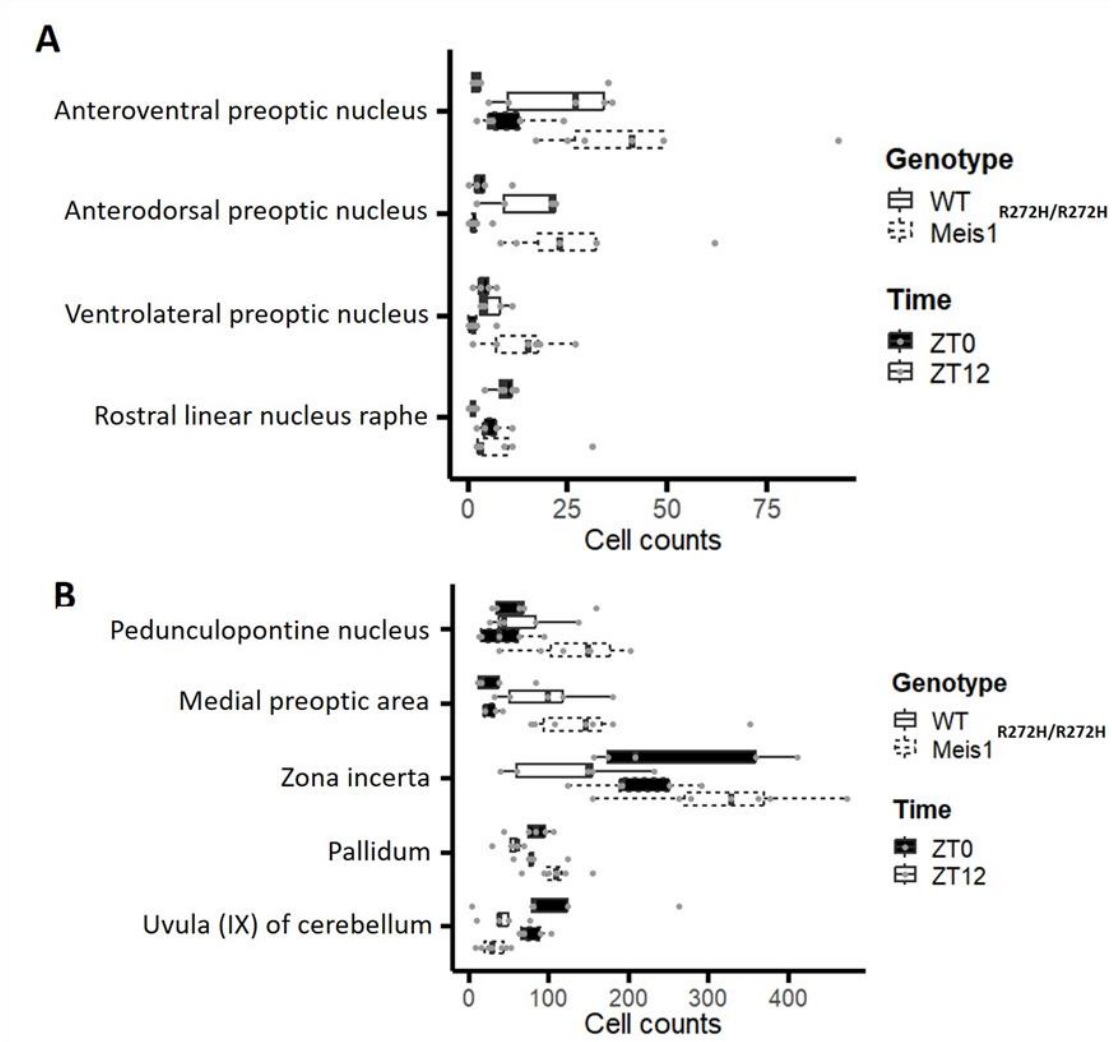

Figure 6.14 Numbers of c-Fos positive neurons in regions that were labelled in Fig. 6.8. (A) Cell counts of active neurons in anteroventral preoptic nucleus, anterodorsal preoptic nucleus, ventrolateral preoptic nucleus, and rostral linear nucleus raphe. (B) Cell counts of active neurons in pedunculopontine, medial preoptic area, zona incerta, pallidum, and uvula (IX) of cerebellum. No significant difference was found. No brain region showed significant difference between Meis1$^{R272H/R272H}$ and wildtype mice, as well as between ZT0 and ZT12 groups, even though some regions showed trend of differences. Statistics: Two-way ANOVA with multiple testing correction. Multiple testing correction: FDR (False Discovery Rate). n=5-7 per group.

Examine the neuronal activity in RLS and locomotion related brain regions

RLS is a neurological disorder, and has been associated with dopamine deficiency in some brain regions such as substantia nigra and striatum[191]. Both of them may have dysfunction in RLS patients. Therefore, we wanted to examine the activity of these brain regions in Meis1$^{R272H/R272H}$ mice. Furthermore, we wanted to examine the activity of locomotion related brain regions (primary motor and secondary motor areas) in Meis1$^{R272H/R272H}$ mice, since RLS patients have a strong urge to move their legs.

However, none of these regions showed significant difference between Meis1$^{R272H/R272H}$ and wildtype mice, as well as between ZT0 and ZT12 groups (**Fig. 6.15**). This suggested that the dopamine deficiency in substantia nigra and striatum might not reflect directly on neuronal activity. On the other hand, even though there was no significant difference in primary motor area, Meis1$^{R272H/R272H}$ mice still showed subtle trend toward higher number of active neurons in primary motor area compared to wildtype mice at ZT0, reflecting the hyperactivity of Meis1$^{R272H/R272H}$ mice at dawn (results from piezo and EEG recordings).

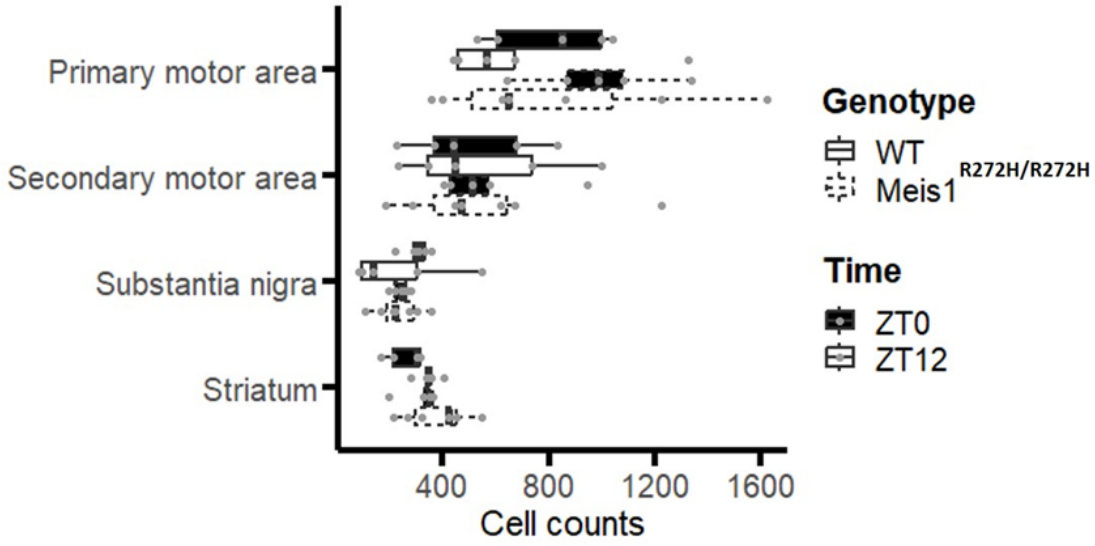

Figure 6.15 Numbers of c-Fos positive neurons in RLS and locomotion related brain regions. Cell counts of active neurons in primary motor area, secondary motor area, substantia nigra, and striatum. No region showed significant difference between Meis1$^{R272H/R272H}$ and wildtype mice, as well as between ZT0 and ZT12 groups. However, Meis1$^{R272H/R272H}$ mice showed subtle trend toward higher number of active neurons in primary motor area compared to wildtype mice at ZT0. Statistics: Two-way ANOVA with multiple testing correction. Multiple testing correction: FDR (False Discovery Rate). n=5-7 per group.

Examine the neuronal activity and connectivity in high-level brain regions

Apart from the changes of neural activity in small brain regions, we also wanted to see the activity changes in high-level brain regions and their connectivity in Meis1$^{R272H/R272H}$ and wildtype mice. Brain regions were collapsed into 11 high-level brain regions (olfactory areas, cerebral nuclei, isocortex, hippocampus, cortical subplate, thalamus, hypothalamus, midbrain, pons, medulla, and cerebellum) as described in chapter 3. Sleep deprivation methodology. However, no region showed significant difference between Meis1$^{R272H/R272H}$ and wildtype mice, as well as between ZT0 and ZT12 groups (Two-way ANOVA with multiple testing correction) (**Fig. 6.16**).

Next, we examined the connectivity between the high-level brain regions. The cell counts were first scaled and the Pearson correlation coefficients were computed in all 11 brain regions. Then the heatmaps were plotted to show the Pearson correlation coefficient. The heatmaps from Meis1$^{R272H/R272H}$ ZT0 and wildtype ZT0 groups, from Meis1$^{R272H/R272H}$ ZT12 and wildtype ZT12 groups, from Meis1$^{R272H/R272H}$ ZT0 and Meis1$^{R272H/R272H}$ ZT12 groups, as well as from wildtype ZT0 and wildtype ZT12 groups were subtracted to show the differences (**Fig. 6.17**).

The Pearson correlation coefficient between midbrain and hypothalamus ($r = -0.44$ in Meis1$^{R272H/R272H}$ mice, $r = 0.92$ in wildtype mice, $p = 0.03$), and between thalamus and olfactory areas ($r = -0.96$ in Meis1$^{R272H/R272H}$ mice, $r = -0.03$ in wildtype mice, $p = 0.04$) showed significant difference in the comparison between Meis1$^{R272H/R272H}$ and wildtype mice at ZT0 (**Fig. 6.17 A**). This change of connectivity (between midbrain and hypothalamus, and between thalamus and olfactory areas) could contribute to the hyperactivity of Meis1$^{R272H/R272H}$ mice at dawn (results from piezo and EEG recordings). However, there was no significant difference between Meis1$^{R272H/R272H}$ and wildtype mice at ZT12 (**Fig. 6.17 B**). In **Fig. 6.17 A and B**, yellow means the correlation is more positive in Meis1$^{R272H/R272H}$ mice compared to wildtype mice. On the contrary, blue means the correlation is more positive in wildtype mice compared to Meis1$^{R272H/R272H}$ mice.

Since we only observed two correlations that showed difference, we then further examined the diurnal changes of connectivity in Meis1$^{R272H/R272H}$ and wildtype mice. The Pearson correlation coefficients between thalamus and hippocampus ($r = 0.66$ at ZT0, $r = -0.74$ at ZT12, $p = 0.04$), hippocampus and isocortex ($r = -0.62$ at ZT0, $r = 0.90$ at ZT12, $p = 0.01$), as well as midbrain and isocortex ($r = -0.10$ at ZT0, $r = -0.95$ at ZT12, $p = 0.03$) showed significant difference between Meis1$^{R272H/R272H}$ ZT0 and Meis1$^{R272H/R272H}$ ZT12 groups (**Fig. 6.17 C**). On the other hand, there was no significant difference between WT ZT0 and WT ZT12 groups (**Fig. 6.17 D**). In **Fig. 6.17 C and D**, yellow means the correlation is more positive at ZT0 compared to ZT12. On the contrary, blue means the correlation is more positive at ZT12 compared to at ZT0. These results suggested that the diurnal changes of connectivity were stronger in Meis1$^{R272H/R272H}$ mice compared to wildtype mice. Furthermore, the regions that showed strong diurnal changes in Meis1$^{R272H/R272H}$ mice could

contribute to the hyperactivity of Meis1$^{R272H/R272H}$ mice at dawn (results from piezo and EEG recordings).

In order to have a better look at the correlation in each genotype and the distribution of the data, linear regression between two regions was computed and plotted. Only the regions that showed significantly different correlation between Meis1$^{R272H/R272H}$ and wildtype mice, or between ZT0 and ZT12 were shown (mentioned above). The correlation between midbrain and hypothalamus was negative in Meis1$^{R272H/R272H}$ mice ($r = -0.44$, $p = 0.45$), and was strongly positive in wildtype mice ($r = 0.92$, $p = 0.02$) at ZT0 (**Fig. 6.18 A**). On the other hand, the correlation between thalamus and olfactory areas was strongly negative in Meis1$^{R272H/R272H}$ mice ($r = -0.96$, $p = 0.007$), but was absent in wildtype mice ($r = -0.03$, $p = 0.95$) at ZT0 (**Fig. 6.18 B**). For Meis1$^{R272H/R272H}$ mice, the correlation between thalamus and hippocampus was positive at ZT0 ($r = 0.66$, $p = 0.22$), and was negative at ZT12 ($r = -0.74$, $p = 0.055$) (**Fig. 6.18 C**). On the contrary, the correlation between hippocampus and isocortex was negative at ZT0 ($r = -0.62$, $p = 0.26$), and was strongly positive at ZT12 ($r = 0.90$, $p = 0.005$) (**Fig. 6.18 D**). Last but not least, the correlation between midbrain and isocortex was absent at ZT0 ($r = -0.10$, $p = 0.87$), and was strongly negative at ZT12 ($r = -0.95$, $p < 0.001$) (**Fig. 6.18 E**).

The linear regression was mainly to examine the correlation in each genotype and the distribution of the data, and further support the changes of connectivity in the heatmaps above.

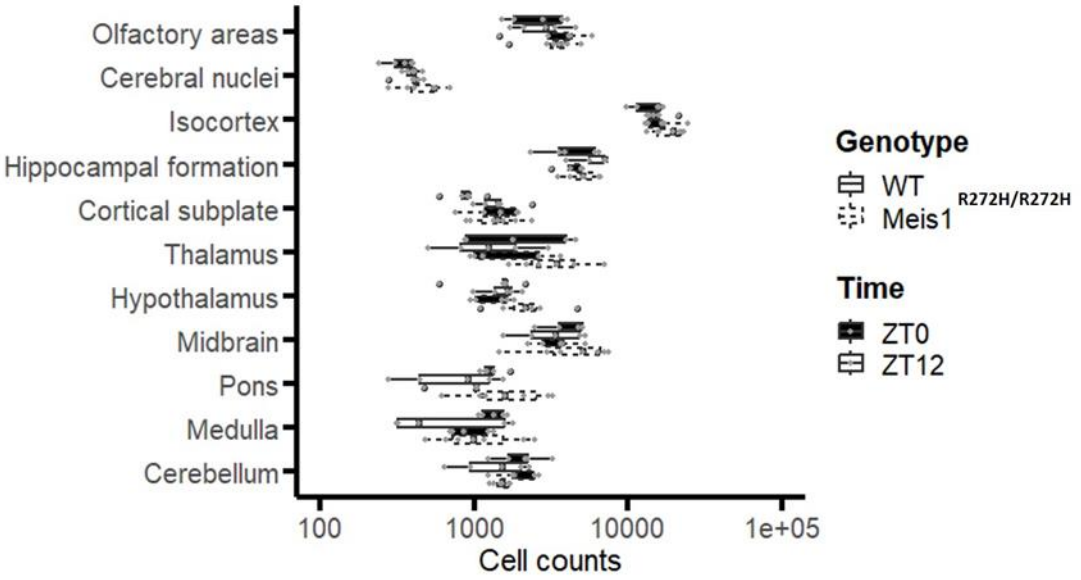

Figure 6.16 Numbers of c-Fos positive neurons in high-level brain regions for Meis1$^{R272H/R272H}$ and wildtype mice. Numbers of c-Fos positive neurons in 11 high-level brain regions. No region showed significant difference between Meis1$^{R272H/R272H}$ and wildtype mice, as well as between ZT0 and ZT12 groups. Statistics: Two-way ANOVA with multiple testing correction. Multiple testing correction: FDR (False Discovery Rate). n=5-7 per group.

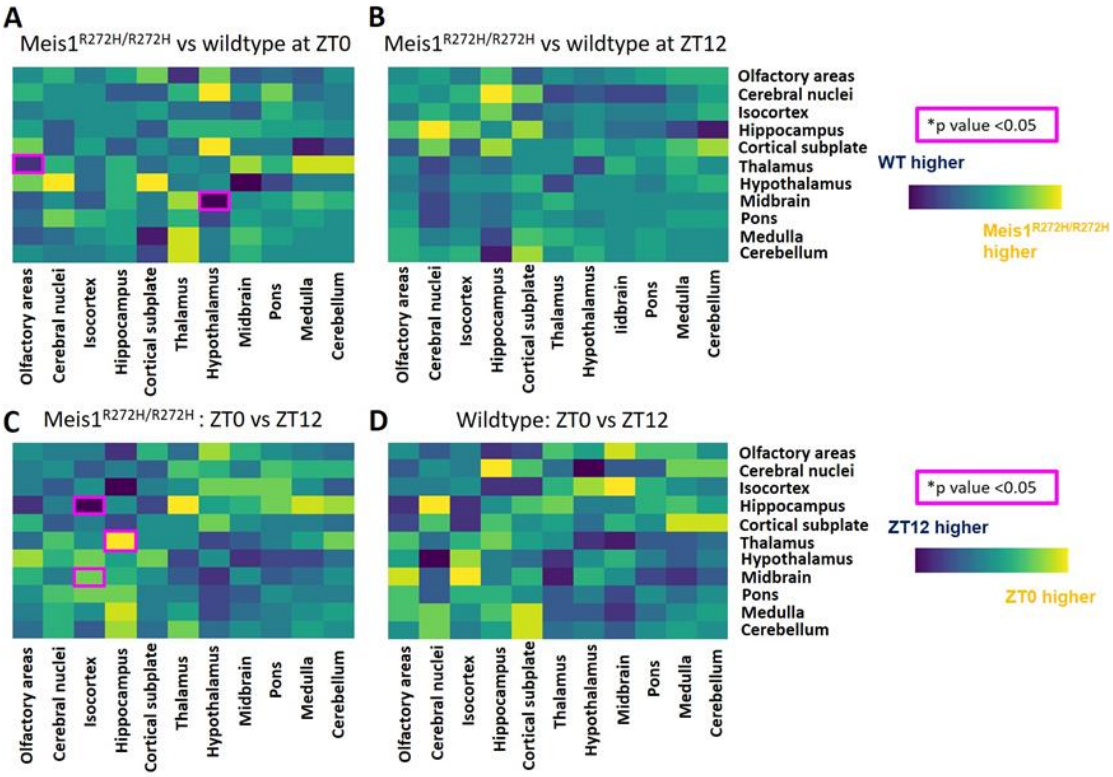

Figure 6.17 The connectivity of high-level brain regions for Meis1$^{R272H/R272H}$ and wildtype mice. The subtraction heatmaps of Pearson correlation coefficient between difference regions between (A) Meis1$^{R272H/R272H}$ and wildtype mice at ZT0, (B) Meis1$^{R272H/R272H}$ and wildtype mice at ZT12, (C) ZT0 and ZT12 in Meis1$^{R272H/R272H}$ mice, (D) ZT0 and ZT12 in wildtype mice. The Pearson correlation coefficient between midbrain and hypothalamus, and between olfactory areas and thalamus showed significant difference in the comparison between Meis1$^{R272H/R272H}$ and wildtype mice at ZT0. The Pearson correlation coefficients between midbrain and isocortex, thalamus and hippocampus, as well as hippocampus and isocortex also showed significant difference between Meis1$^{R272H/R272H}$ ZT0 and Meis1$^{R272H/R272H}$ ZT12 groups. Magenta squares mean p-values between Meis1$^{R272H/R272H}$ and wildtype mice, or between ZT0 and ZT12 groups are lower than 0.05 after statistical test by cocor (A Comprehensive Solution for the Statistical Comparison of Correlations, 2015)[138]. n=5-7 per group.

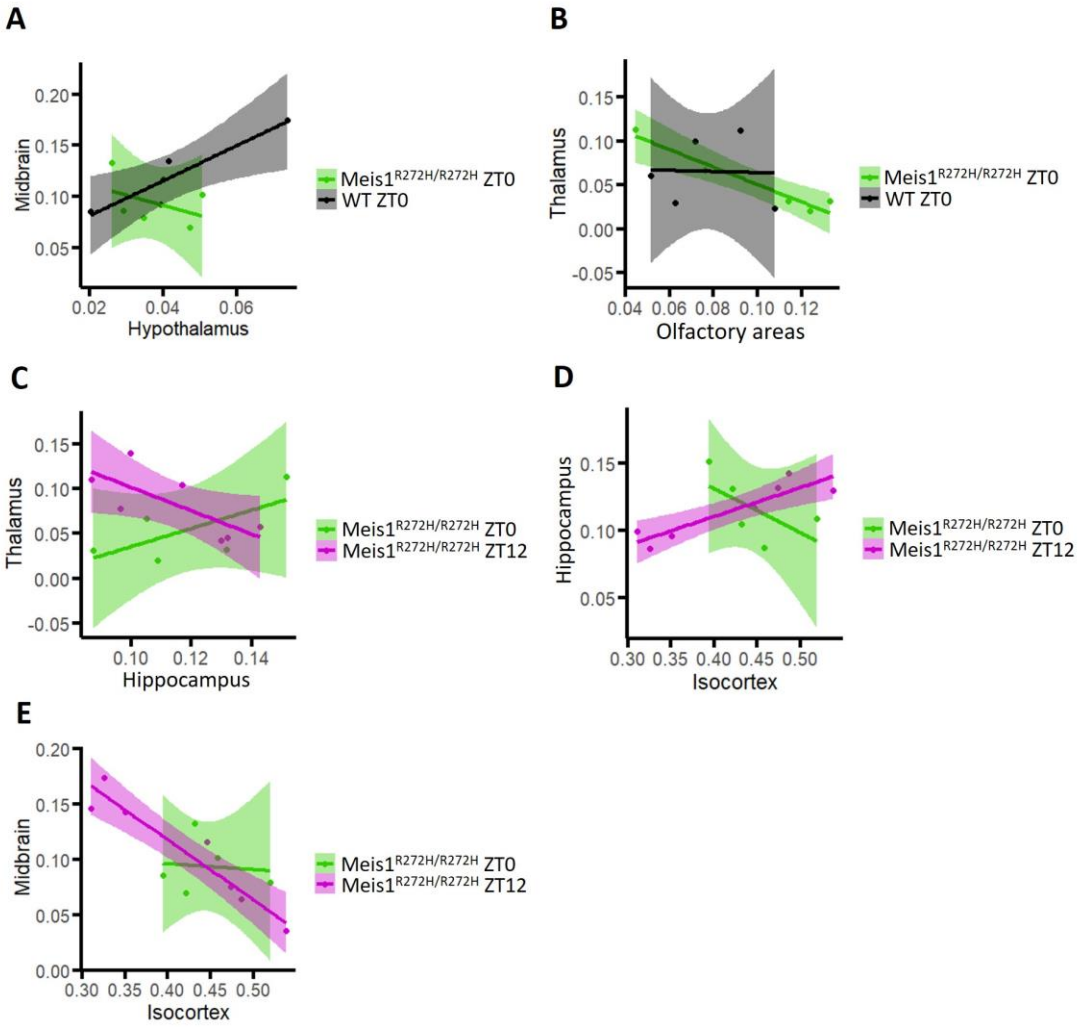

Figure 6.18 Linear regression between different pairs of brain regions. (A) The linear regression between midbrain and hypothalamus, (B) and between thalamus and olfactory areas between Meis1$^{R272H/R272H}$ and wildtype mice at ZT0. (C) The linear regression between thalamus and hippocampus, (D) hippocampus and isocortex, (E) as well as midbrain and isocortex between Meis1$^{R272H/R272H}$ ZT0 and ZT12 groups. n=5-7 per group.

Discussion

The Meis1$^{R272H/R272H}$ mice were aimed to be a disease mouse model for RLS to facilitate the studies on RLS. According to the "Consensus Guidelines on Rodent Models of Restless Legs Syndrome" published in 2021, the RLS rodent models are expected (recommended) to have decreased total sleep time during the light period (rest period) as based on the sleep disturbance observed on RLS patients[192]. In our study, Meis1$^{R272H/R272H}$ mice did not show significant reduction of sleep percent time in light period compared to wildtype mice. However, the aged adult Meis1$^{R272H/R272H}$ mice showed trend toward lower sleep percent time in light period compared to wildtype mice (**Fig. 6.7 B**). Furthermore, the young adult Meis1$^{R272H/R272H}$ mice showed significant reduction of sleep percent time in dark period compared to wildtype mice, which suggested they did have sleep disturbance. The guidelines also suggested the RLS rodent models are expected (recommended) to have increased latency to sustained rest. This normally happens at the beginning of the rest period, which means the dawn for mice. Meis1$^{R272H/R272H}$ mice showed significantly shorter sleep percent time (longer wake percent time) at dawn compared to wildtype mice, suggesting they had longer latency to sleep at the beginning of the rest period (**Fig. 6.3 A-B, 6.7 C-D, and 6.8 C-D**).

The locomotor assay suggested that Meis1$^{R272H/R272H}$ mice showed trend toward higher travelled distance in the open field locomotor assay (**Fig. 6.2 G**), which was similar to one of the guidelines for RLS: increase in total activity (movements/distance traveled) in the home cage. Furthermore, Meis1$^{R272H/R272H}$ mice showed trend of increased RER, and we could infer that Meis1$^{R272H/R272H}$ mice have a trend of higher activity/exercise level since RER increased when activity level increased[193].

In the sensory assay, Meis1$^{R272H/R272H}$ mice showed trend toward increased susceptibility to fall and longer reaction time to heat (**Fig. 6.2 H and I**), suggesting subtle impairment in sensory function. These trends are similar to RLS patents, since one study showed that RLS is a risk factor for falling in elderly (OR = 3.1, p = 0.049)[194], and another study suggested that high percentage of RLS patients had impairment of temperature perception (in 72% of the secondary RLS patients and in 55% of idiopathic RLS patients)[195].

If we compare Meis1$^{R272H/R272H}$ mice to other RLS mouse models, similar trends were observed. In 2017, a Meis1 haploinsufficient mouse model, heterozygous Meis1^{tm1Mtor} mice (created in 2005[196]), was tested to examine RLS-like phenotypes[197]. Meis1^{tm1Mtor} mice showed hyperactivity in distance traveled[197]. This is similar to Meis1$^{R272H/R272H}$ mice which showed trend toward increased activity in the open field test. However, Meis1^{tm1Mtor} mice did not show changes on time–course of wake, NREM sleep, and REM sleep[198], unlike Meis1$^{R272H/R272H}$ mice which showed changes in sleep percent time at dawn. In 2020, another RLS mouse model was developed by breeding the *Meis1fl/fl* mice and Emx1-*Cre* mice to generate double-heterozygous Emx1-*Cre/+;Meis1fl/+* mice (*Meis1* KO mice)[199]. The *Meis1* KO mice showed increased activity for wheel-running and significantly farther distance traveled in an open field arena. *Meis1* KO mice were also more likely to wake during the light period[199]. Meis1$^{R272H/R272H}$ mice had similar features, which showed

trend toward increased activity in the open field test, and showed trend toward decreased sleep percent time in the light period.

Additionally, *Btbd9* mutant mice, which was developed based on iron deficiency, also showed higher distance traveled and longer wake time in rest period[200]. These features are similar to Meis1$^{R272H/R272H}$ mice too. Another RLS mouse model, BXD40f mice, which was also developed based on iron deficiency, had repeated peak increases in activity during the last 2 hours of the active period[201]. This result is similar to Meis1$^{R272H/R272H}$ mice, which had higher wake activity at dawn. These examinations suggested that Meis1$^{R272H/R272H}$ mice showed some RLS-like phenotypes that were observed at other RLS mouse models, and could further support Meis1$^{R272H/R272H}$ mice to be a possible RLS mouse model.

From the whole brain mapping we noticed pedunculopontine nucleus (PPN) and ventrolateral preoptic nucleus (VLPO) showed trend toward lower activity at ZT0 compared to ZT12 in Meis1$^{R272H/R272H}$ mice (**Fig. 6.11**). Since PPN is involved in posture and gait control, and VLPO is a NREM sleep-promoting region, the low activity of these regions at ZT0 could contribute to the hyperactivity of Meis1$^{R272H/R272H}$ mice at dawn (ZT0)[82,91,92]. Therefore, examination of these two regions may shed light on what causes hyperactivity in Meis1$^{R272H/R272H}$ mice.

The whole brain mapping also suggested that the connectivity between midbrain and hypothalamus was different between Meis1$^{R272H/R272H}$ and wildtype mice at ZT0, where Meis1$^{R272H/R272H}$ mice showed negative correlation and wildtype mice showed strong positive correlation (**Fig. 6.15 and 6.16**). This is interesting because substantia nigra is located in the ventral midbrain and it shows low levels of iron in some RLS patients. Furthermore, BTBD9 (one of the genes that was associated with RLS) was identified as a candidate gene for iron regulation in the midbrain in mice[184]. In the meanwhile, A11 dopaminergic system in the hypothalamus is considered the primary source of descending dopaminergic input into the spinal cord, and is potentially involved in the development of RLS symptoms[202,203]. Hence, examination of these two regions could be beneficial to understand the hyperactivity of Meis1$^{R272H/R272H}$ mice at dawn (ZT0).

(The studies in this chapter were supported by the ERC under the European Union's Horizon 2020 Research and Innovation Program Grant Agreement No. 715933 to Dr. Rhîannan H Williams, and internal funding (Helmholtz Munich) to Prof. Dr. Juliane Winkelmann.)

Chapter 7
Summary and Conclusion

The aims of this study were to partially unravel the brain regions and neural/astrocytic circuitry involved in sleep homeostasis, and provide targets and platforms for future sleep studies. Therefore, the study was developed in different aspects:

First, in order to make sure our sleep recording methods and sleep deprivation (SD) methods were complied with other sleep studies, we compared sleep recording between EEG/EMG (gold standard) and piezo, and compared SD between manual and treadmill for 4 and 6 hours. Then we compared the whole brain neuronal activity and connectivity between manual and treadmill SD. This would suggest the sleep recording methods and SD methods that were able to be used in the following studies. We noticed the sleep percent time did not show significant difference between EEG/EMG and piezo, suggesting piezo is an acceptable alternative for sleep recording. The sleep percent time in the recovery period after different SD methods and durations also did not show significant difference, suggesting the sleep drives caused by different SD methods and durations did not show difference, and can be used in further studies. However, whole brain mapping suggested that manual and treadmill SD may result in different activities in certain brain regions such as tuberomammillary nucleus (TMN). The connectivity between olfactory areas and three brain regions (cerebral nuclei, isocortex, and cortical subplate) also showed significant difference, suggesting even though different SD methods didn't show differences at sleep drive, they might show different brain activities and connectivities.

Second, after the sleep recording methods and SD methods were verified, we did whole brain neuronal activity mapping and connectivity analysis to reveal the brain regions that showed strong activity after SD while the sleep drive was high. The aims were to unravel the brain regions and possible circuitry involved in sleep homeostasis, and suggest candidate brain regions for *in vivo* functional study. We noticed amygdala regions, especially basolateral amygdalar nucleus (BLA) and basomedial amygdalar nucleus (BMA) were significantly active after SD, suggesting BLA/BMA might involve in sleep homeostasis and could be the brain region to study functionality on. The connectivity between thalamus and cortical subplate, as well as between pons and midbrain changed significantly after SD, suggesting possible circuitries that might involve in sleep homeostasis, and could be the target circuits to do further study on.

Third, apart from investigating neurons, we also investigated astrocytes since astrocytes were suggested to involve in modulating sleep. The proximity between cortical astrocytes and nNOS neurons, as well as the functionality of cortical astrocytes were verified. This would suggest the anatomical pattern and functionality of cortical astrocytes in sleep homeostasis. We noticed astrocytes' number reduced significantly between the distance in 300-600μm from nNOS neurons after SD, suggesting the interaction between astrocytes

and nNOS neurons might change in this range. Furthermore, the sleep loss (SD+RS) group showed significantly lower number of astrocytes compared to undisturbed group in cingulate/motor cortex, suggesting high sleep drive led to reduction of astrocytes in this region. In the *in vivo* chemogenetic study, we noticed the activation of astrocytes in cingulate/motor cortex can promote sleep when mice were not disturbed by SD. However, after 4h of SD, the activation of astrocytes didn't seem to promote sleep. The reason for this is elusive, but we suspect that the astrocytes in cingulate/motor cortex might already be activated by SD due to the high sleep drive, so additional activation of astrocytes by chemogenetics didn't further impact the sleep state.

Last but not least, we examined a disease mouse model (Meis1$^{R272H/R272H}$ mice) for restless legs syndrome (RLS). The phenotypic assessment of Meis1$^{R272H/R272H}$ mice were performed, and the whole brain neuronal activity and connectivity were analyzed. This would suggest if the Meis1$^{R272H/R272H}$ mice showed RLS-like sleep phenotypes, and the possible regions causing hyperactivity. We noticed Meis1$^{R272H/R272H}$ mice showed trend toward higher travelled distance in open field test, and showed trend toward increased susceptibility to fall and longer reaction time to heat. These suggested trends of hyperactivity and impairment of sensory function, and showed RLS-like locomotor and sensory phenotypes. Besides, Meis1$^{R272H/R272H}$ mice slept significantly less during the dawn transition period, and showed trend toward lower sleep percent time in the light period, suggesting Meis1$^{R272H/R272H}$ mice showed RLS-like sleep phenotypes. These results suggested that Meis1$^{R272H/R272H}$ mice showed RLS-like phenotypes, and supported them to be a RLS mouse model. Whole brain mapping of Meis1$^{R272H/R272H}$ mice suggested pedunculopontine nucleus (PPN) and ventrolateral preoptic nucleus (VLPO) showed trend toward lower activity at dawn, and the connectivity between midbrain and hypothalamus was significantly different at dawn. These suggested the potential brain regions and circuitry that could cause hyperactivity for Meis1$^{R272H/R272H}$ mice at dawn. This part of the study did not directly answer the brain regions and circuitry involved in sleep homeostasis. However, it provided a possible RLS disease mouse model and answered the possible brain regions and circuitry that may cause the hyperactivity in RLS.

In summary, we found no difference between EEG/EMG and piezoelectric sleep recordings, and no difference in SD efficiency between different SD methods and durations. We have shown that the BLA and BMA are active when sleep drive is high, and that connectivity between the thalamus and subcortical plate and between the pons and midbrain are altered after SD. We have shown that cortical astrocytes promot sleep when mice are undisturbed, but show no difference after SD. We also found that the number of cortical astrocytes was reduced after sleep deprivation, specifically those located 300–600 μm away from nNOS neurons after SD. We have shown a RLS disease mouse model (Meis1$^{R272H/R272H}$ mice) which showed a trend of hyperactivity and impairment of sensory function, and sleep less significantly at dawn resembling the RLS-like phenotypes. We also showed the possible brain regions and circuitry that may contribute to dawn hyperactivity in

Meis1$^{R272H/R272H}$ mice.

However, there is still a lot to do in order to unravel the brain regions and circuitry involved in sleep homeostasis and RLS. The brain regions and circuitries pointed out from this study could be candidates or targets for future functional studies to prove their real functionalities in sleep homeostasis, and the RLS disease mouse model (Meis1$^{R272H/R272H}$ mice) could become a platform for future RLS studies for mechanisms or therapeutic targets. We believe the studies for sleep homeostasis and RLS will continue until all the mysteries are revealed.

References

1. Rechtschaffen A, Bergmann BM, Everson CA, Kushida CA, Gilliland MA. Sleep deprivation in the rat: X. Integration and discussion of the findings. *Sleep*. 1989;12(1):68-87.

2. Everson CA. Sustained sleep deprivation impairs host defense. *Am J Physiol*. 1993;265(5 Pt 2):R1148-1154. doi:10.1152/ajpregu.1993.265.5.R1148

3. Bonnet MH. Chapter 5 - Acute Sleep Deprivation. In: Kryger MH, Roth T, Dement WC, eds. *Principles and Practice of Sleep Medicine (Fourth Edition)*. Philadelphia: W.B. Saunders; 2005:51-66. doi:10.1016/B0-72-160797-7/50012-4

4. Dinges DF, Rogers NL, Baynard MD. Chapter 6 - Chronic Sleep Deprivation. In: Kryger MH, Roth T, Dement WC, eds. *Principles and Practice of Sleep Medicine (Fourth Edition)*. Philadelphia: W.B. Saunders; 2005:67-76. doi:10.1016/B0-72-160797-7/50013-6

5. Kripke DF, Simons RN, Garfinkel L, Hammond EC. Short and long sleep and sleeping pills. Is increased mortality associated? *Arch Gen Psychiatry*. 1979;36(1):103-116. doi:10.1001/archpsyc.1979.01780010109014

6. Kripke DF, Garfinkel L, Wingard DL, Klauber MR, Marler MR. Mortality associated with sleep duration and insomnia. *Arch Gen Psychiatry*. 2002;59(2):131-136. doi:10.1001/archpsyc.59.2.131

7. Dement WC. The study of human sleep: a historical perspective. *Thorax*. 1998;53 Suppl 3(Suppl 3):S2-7.

8. Loomis AL, Harvey EN, Hobart GA. Cerebral States During Sleep, as Studied by Human Brain Potentials. *J Exp Psychol*. 1937;21(2):127. doi:10.1037/h0057431

9. Aserinsky E, Kleitman N. Regularly occurring periods of eye motility, and concomitant phenomena, during sleep. *Science*. 1953;118(3062):273-274. doi:10.1126/science.118.3062.273

10. Dement W, Kleitman N. Cyclic variations in EEG during sleep and their relation to eye movements, body motility, and dreaming. *Electroencephalogr Clin Neurophysiol*. 1957;9(4):673-690. doi:10.1016/0013-4694(57)90088-3

11. Dement W, Wolpert EA. The relation of eye movements, body motility, and external stimuli to dream content. *J Exp Psychol*. 1958;55(6):543-553. doi:10.1037/h0040031

12. Schulz H, Salzarulo P. The Development of Sleep Medicine: A Historical Sketch. *J Clin Sleep Med JCSM Off Publ Am Acad Sleep Med*. 2016;12(7):1041-1052. doi:10.5664/jcsm.5946

13. Scheiermann C, Kunisaki Y, Frenette PS. Circadian control of the immune system.

Nat Rev Immunol. 2013;13(3):190-198. doi:10.1038/nri3386

14. Bass J. Circadian topology of metabolism. *Nature*. 2012;491(7424):348-356. doi:10.1038/nature11704

15. Wurtman RJ, Axelrod J, Phillips LS. MELATONIN SYNTHESIS IN THE PINEAL GLAND: CONTROL BY LIGHT. *Science*. 1963;142(3595):1071-1073. doi:10.1126/science.142.3595.1071

16. Moore RY, Heller A, Wurtman RJ, Axelrod J. Visual pathway mediating pineal response to environmental light. *Science*. 1967;155(3759):220-223. doi:10.1126/science.155.3759.220

17. Moore RY, Lenn NJ. A retinohypothalamic projection in the rat. *J Comp Neurol*. 1972;146(1):1-14. doi:10.1002/cne.901460102

18. Moore RY, Eichler VB. Loss of a circadian adrenal corticosterone rhythm following suprachiasmatic lesions in the rat. *Brain Res*. 1972;42(1):201-206. doi:10.1016/0006-8993(72)90054-6

19. Stephan FK, Zucker I. Circadian rhythms in drinking behavior and locomotor activity of rats are eliminated by hypothalamic lesions. *Proc Natl Acad Sci U S A*. 1972;69(6):1583-1586. doi:10.1073/pnas.69.6.1583

20. Welsh DK, Logothetis DE, Meister M, Reppert SM. Individual neurons dissociated from rat suprachiasmatic nucleus express independently phased circadian firing rhythms. *Neuron*. 1995;14(4):697-706. doi:10.1016/0896-6273(95)90214-7

21. Benington JH. Sleep homeostasis and the function of sleep. *Sleep*. 2000;23(7):959-966.

22. Carskadon MA, Dement WC. Effects of total sleep loss on sleep tendency. *Percept Mot Skills*. 1979;48(2):495-506. doi:10.2466/pms.1979.48.2.495

23. Brendel DH, Reynolds CF, Jennings JR, et al. Sleep stage physiology, mood, and vigilance responses to total sleep deprivation in healthy 80-year-olds and 20-year-olds. *Psychophysiology*. 1990;27(6):677-685. doi:10.1111/j.1469-8986.1990.tb03193.x

24. Feinberg I. Changes in sleep cycle patterns with age. *J Psychiatr Res*. 1974;10(3-4):283-306. doi:10.1016/0022-3956(74)90011-9

25. Borbély AA. A two process model of sleep regulation. *Hum Neurobiol*. 1982;1(3):195-204.

26. Borbély AA, Daan S, Wirz-Justice A, Deboer T. The two-process model of sleep regulation: a reappraisal. *J Sleep Res*. 2016;25(2):131-143. doi:10.1111/jsr.12371

27. Tobler I, Borbély AA, Groos G. The effect of sleep deprivation on sleep in rats with suprachiasmatic lesions. *Neurosci Lett*. 1983;42(1):49-54. doi:10.1016/0304-

3940(83)90420-2

28. Trachsel L, Edgar DM, Seidel WF, Heller HC, Dement WC. Sleep homeostasis in suprachiasmatic nuclei-lesioned rats: effects of sleep deprivation and triazolam administration. *Brain Res*. 1992;589(2):253-261. doi:10.1016/0006-8993(92)91284-l

29. Krueger JM, Clinton JM, Winters BD, et al. Involvement of cytokines in slow wave sleep. *Prog Brain Res*. 2011;193:39-47. doi:10.1016/B978-0-444-53839-0.00003-X

30. Kohlschütter EOH. Messungen der Festigkeit des Schlafes. *Z Fuer Ration Med Dritte Reihe*. 1863;Dritte Reihe, 17:209-253.

31. Howell WH. A CONTRIBUTION TO THE PHYSIOLOGY OF SLEEP, BASED UPON PLETHYSMOGRAPHIC EXPERIMENTS. *J Exp Med*. 1897;2(3):313-345. doi:10.1084/jem.2.3.313

32. Angelo Mosso - La Fatica - Milano, Fratelli Treves Editori, 1891. *Collezionismo Cartaceo*. https://www.segnideltempo.it/prodotto/angelo-mosso-la-fatica-milano-fratelli-treves-editori-1891/. Accessed June 12, 2023.

33. Szymanski JS. Aktivität und Ruhe bei Tieren und Menschen. *Z Fuer Allg Physiol*. 1920;18:105-162.

34. Caton, Richard - The electric currents of the brain. https://echo.mpiwg-berlin.mpg.de/ECHOdocuView?url=/permanent/vlp/lit27690/index.meta&viewMode=auto&pn=1. Accessed June 12, 2023.

35. Berger H. Über das Elektrenkephalogramm des Menschen. *Arch Für Psychiatr Nervenkrankh*. 1929;87(1):527-570. doi:10.1007/BF01797193

36. Schnitzler A, Gross J. Normal and pathological oscillatory communication in the brain. *Nat Rev Neurosci*. 2005;6(4):285-296. doi:10.1038/nrn1650

37. Walker P. Chambers dictionary of science and technology. 1999;Edinburgh: Chambers:312.

38. Jouvet M. The role of monoamines and acetylcholine-containing neurons in the regulation of the sleep-waking cycle. *Ergeb Physiol*. 1972;64:166-307. doi:10.1007/3-540-05462-6_2

39. Webster HH, Jones BE. Neurotoxic lesions of the dorsolateral pontomesencephalic tegmentum-cholinergic cell area in the cat. II. Effects upon sleep-waking states. *Brain Res*. 1988;458(2):285-302. doi:10.1016/0006-8993(88)90471-4

40. Nitz D, Siegel JM. GABA release in posterior hypothalamus across sleep-wake cycle. *Am J Physiol*. 1996;271(6 Pt 2):R1707-1712.

doi:10.1152/ajpregu.1996.271.6.R1707

41. Sauer B, Henderson N. Site-specific DNA recombination in mammalian cells by the Cre recombinase of bacteriophage P1. *Proc Natl Acad Sci U S A*. 1988;85(14):5166-5170. doi:10.1073/pnas.85.14.5166

42. van den Pol AN, Ozduman K, Wollmann G, et al. Viral strategies for studying the brain, including a replication-restricted self-amplifying delta-G vesicular stomatis virus that rapidly expresses transgenes in brain and can generate a multicolor golgi-like expression. *J Comp Neurol*. 2009;516(6):456-481. doi:10.1002/cne.22131

43. Duebel J, Marazova K, Sahel JA. Optogenetics. *Curr Opin Ophthalmol*. 2015;26(3):226-232. doi:10.1097/ICU.0000000000000140

44. Britt JP, McDevitt RA, Bonci A. Use of channelrhodopsin for activation of CNS neurons. *Curr Protoc Neurosci*. 2012;Chapter 2:Unit2.16. doi:10.1002/0471142301.ns0216s58

45. Yizhar O, Fenno LE, Davidson TJ, Mogri M, Deisseroth K. Optogenetics in neural systems. *Neuron*. 2011;71(1):9-34. doi:10.1016/j.neuron.2011.06.004

46. Adamantidis AR, Zhang F, Aravanis AM, Deisseroth K, de Lecea L. Neural substrates of awakening probed with optogenetic control of hypocretin neurons. *Nature*. 2007;450(7168):420-424. doi:10.1038/nature06310

47. Armbruster BN, Li X, Pausch MH, Herlitze S, Roth BL. Evolving the lock to fit the key to create a family of G protein-coupled receptors potently activated by an inert ligand. *Proc Natl Acad Sci U S A*. 2007;104(12):5163-5168. doi:10.1073/pnas.0700293104

48. Roth BL. DREADDs for Neuroscientists. *Neuron*. 2016;89(4):683-694. doi:10.1016/j.neuron.2016.01.040

49. Smith KS, Bucci DJ, Luikart BW, Mahler SV. DREADDS: Use and application in behavioral neuroscience. *Behav Neurosci*. 2016;130(2):137-155. doi:10.1037/bne0000135

50. Sasaki K, Suzuki M, Mieda M, Tsujino N, Roth B, Sakurai T. Pharmacogenetic modulation of orexin neurons alters sleep/wakefulness states in mice. *PloS One*. 2011;6(5):e20360. doi:10.1371/journal.pone.0020360

51. Tian L, Hires SA, Mao T, et al. Imaging neural activity in worms, flies and mice with improved GCaMP calcium indicators. *Nat Methods*. 2009;6(12):875-881. doi:10.1038/nmeth.1398

52. Poskanzer KE, Yuste R. Astrocytes regulate cortical state switching in vivo. *Proc Natl Acad Sci U S A*. 2016;113(19):E2675-2684. doi:10.1073/pnas.1520759113

53. Chen TW, Wardill TJ, Sun Y, et al. Ultrasensitive fluorescent proteins for imaging neuronal activity. *Nature*. 2013;499(7458):295-300. doi:10.1038/nature12354

54. Lütcke H, Murayama M, Hahn T, et al. Optical recording of neuronal activity with a genetically-encoded calcium indicator in anesthetized and freely moving mice. *Front Neural Circuits*. 2010;4:9. doi:10.3389/fncir.2010.00009

55. Ghosh KK, Burns LD, Cocker ED, et al. Miniaturized integration of a fluorescence microscope. *Nat Methods*. 2011;8(10):871-878. doi:10.1038/nmeth.1694

56. Flusberg BA, Nimmerjahn A, Cocker ED, et al. High-speed, miniaturized fluorescence microscopy in freely moving mice. *Nat Methods*. 2008;5(11):935-938. doi:10.1038/nmeth.1256

57. Shiromani PJ, Peever JH. New Neuroscience Tools That Are Identifying the Sleep-Wake Circuit. *Sleep*. 2017;40(4):zsx032. doi:10.1093/sleep/zsx032

58. Cox J, Pinto L, Dan Y. Calcium imaging of sleep-wake related neuronal activity in the dorsal pons. *Nat Commun*. 2016;7:10763. doi:10.1038/ncomms10763

59. Susaki EA, Tainaka K, Perrin D, et al. Whole-brain imaging with single-cell resolution using chemical cocktails and computational analysis. *Cell*. 2014;157(3):726-739. doi:10.1016/j.cell.2014.03.042

60. Tomer R, Ye L, Hsueh B, Deisseroth K. Advanced CLARITY for rapid and high-resolution imaging of intact tissues. *Nat Protoc*. 2014;9(7):1682-1697. doi:10.1038/nprot.2014.123

61. Callaway EM, Luo L. Monosynaptic Circuit Tracing with Glycoprotein-Deleted Rabies Viruses. *J Neurosci Off J Soc Neurosci*. 2015;35(24):8979-8985. doi:10.1523/JNEUROSCI.0409-15.2015

62. Gunaydin LA, Grosenick L, Finkelstein JC, et al. Natural neural projection dynamics underlying social behavior. *Cell*. 2014;157(7):1535-1551. doi:10.1016/j.cell.2014.05.017

63. Nieh EH, Matthews GA, Allsop SA, et al. Decoding neural circuits that control compulsive sucrose seeking. *Cell*. 2015;160(3):528-541. doi:10.1016/j.cell.2015.01.003

64. C. von Economo. Sleep as a problem of localization. *J Nerv Ment*. 1930;(Dis. 71):249-259.

65. Moruzzi G, Magoun HW. Brain stem reticular formation and activation of the EEG. *Electroencephalogr Clin Neurophysiol*. 1949;1(4):455-473.

66. Carter ME, Yizhar O, Chikahisa S, et al. Tuning arousal with optogenetic modulation of locus coeruleus neurons. *Nat Neurosci*. 2010;13(12):1526-1533. doi:10.1038/nn.2682

67. Ito H, Yanase M, Yamashita A, et al. Analysis of sleep disorders under pain using an optogenetic tool: possible involvement of the activation of dorsal raphe nucleus-serotonergic neurons. *Mol Brain*. 2013;6:59. doi:10.1186/1756-6606-6-59

68. Wisor JP, Nishino S, Sora I, Uhl GH, Mignot E, Edgar DM. Dopaminergic role in stimulant-induced wakefulness. *J Neurosci Off J Soc Neurosci*. 2001;21(5):1787-1794. doi:10.1523/JNEUROSCI.21-05-01787.2001

69. Eban-Rothschild A, Rothschild G, Giardino WJ, Jones JR, de Lecea L. VTA dopaminergic neurons regulate ethologically relevant sleep-wake behaviors. *Nat Neurosci*. 2016;19(10):1356-1366. doi:10.1038/nn.4377

70. Parmentier R, Zhao Y, Perier M, et al. Role of histamine H1-receptor on behavioral states and wake maintenance during deficiency of a brain activating system: A study using a knockout mouse model. *Neuropharmacology*. 2016;106:20-34. doi:10.1016/j.neuropharm.2015.12.014

71. Yu X, Zecharia A, Zhang Z, et al. Circadian factor BMAL1 in histaminergic neurons regulates sleep architecture. *Curr Biol CB*. 2014;24(23):2838-2844. doi:10.1016/j.cub.2014.10.019

72. Fujita A, Bonnavion P, Wilson MH, et al. Hypothalamic Tuberomammillary Nucleus Neurons: Electrophysiological Diversity and Essential Role in Arousal Stability. *J Neurosci Off J Soc Neurosci*. 2017;37(39):9574-9592. doi:10.1523/JNEUROSCI.0580-17.2017

73. Scammell TE, Arrigoni E, Lipton JO. Neural Circuitry of Wakefulness and Sleep. *Neuron*. 2017;93(4):747-765. doi:10.1016/j.neuron.2017.01.014

74. Yu X, Ye Z, Houston CM, et al. Wakefulness Is Governed by GABA and Histamine Cotransmission. *Neuron*. 2015;87(1):164-178. doi:10.1016/j.neuron.2015.06.003

75. Shi YF, Han Y, Su YT, Yang JH, Yu YQ. Silencing of Cholinergic Basal Forebrain Neurons Using Archaerhodopsin Prolongs Slow-Wave Sleep in Mice. *PloS One*. 2015;10(7):e0130130. doi:10.1371/journal.pone.0130130

76. Chen L, Yin D, Wang TX, et al. Basal Forebrain Cholinergic Neurons Primarily Contribute to Inhibition of Electroencephalogram Delta Activity, Rather Than Inducing Behavioral Wakefulness in Mice. *Neuropsychopharmacol Off Publ Am Coll Neuropsychopharmacol*. 2016;41(8):2133-2146. doi:10.1038/npp.2016.13

77. Anaclet C, Pedersen NP, Ferrari LL, et al. Basal forebrain control of wakefulness and cortical rhythms. *Nat Commun*. 2015;6:8744. doi:10.1038/ncomms9744

78. Irmak SO, de Lecea L. Basal forebrain cholinergic modulation of sleep transitions. *Sleep*. 2014;37(12):1941-1951. doi:10.5665/sleep.4246

79. Xu M, Chung S, Zhang S, et al. Basal forebrain circuit for sleep-wake control. *Nat*

Neurosci. 2015;18(11):1641-1647. doi:10.1038/nn.4143

80. Wang HL, Morales M. Pedunculopontine and laterodorsal tegmental nuclei contain distinct populations of cholinergic, glutamatergic and GABAergic neurons in the rat. *Eur J Neurosci*. 2009;29(2):340-358. doi:10.1111/j.1460-9568.2008.06576.x

81. Boucetta S, Cissé Y, Mainville L, Morales M, Jones BE. Discharge profiles across the sleep-waking cycle of identified cholinergic, GABAergic, and glutamatergic neurons in the pontomesencephalic tegmentum of the rat. *J Neurosci Off J Soc Neurosci*. 2014;34(13):4708-4727. doi:10.1523/JNEUROSCI.2617-13.2014

82. Kroeger D, Ferrari LL, Petit G, et al. Cholinergic, Glutamatergic, and GABAergic Neurons of the Pedunculopontine Tegmental Nucleus Have Distinct Effects on Sleep/Wake Behavior in Mice. *J Neurosci Off J Soc Neurosci*. 2017;37(5):1352-1366. doi:10.1523/JNEUROSCI.1405-16.2016

83. Furman M, Zhan Q, McCafferty C, et al. Optogenetic stimulation of cholinergic brainstem neurons during focal limbic seizures: Effects on cortical physiology. *Epilepsia*. 2015;56(12):e198-202. doi:10.1111/epi.13220

84. Fischer DB, Boes AD, Demertzi A, et al. A human brain network derived from coma-causing brainstem lesions. *Neurology*. 2016;87(23):2427-2434. doi:10.1212/WNL.0000000000003404

85. Fuller PM, Sherman D, Pedersen NP, Saper CB, Lu J. Reassessment of the structural basis of the ascending arousal system. *J Comp Neurol*. 2011;519(5):933-956. doi:10.1002/cne.22559

86. Kaur S, Pedersen NP, Yokota S, et al. Glutamatergic signaling from the parabrachial nucleus plays a critical role in hypercapnic arousal. *J Neurosci Off J Soc Neurosci*. 2013;33(18):7627-7640. doi:10.1523/JNEUROSCI.0173-13.2013

87. Chemelli RM, Willie JT, Sinton CM, et al. Narcolepsy in orexin knockout mice: molecular genetics of sleep regulation. *Cell*. 1999;98(4):437-451. doi:10.1016/s0092-8674(00)81973-x

88. Branch AF, Navidi W, Tabuchi S, et al. Progressive Loss of the Orexin Neurons Reveals Dual Effects on Wakefulness. *Sleep*. 2016;39(2):369-377. doi:10.5665/sleep.5446

89. Bonnavion P, Jackson AC, Carter ME, de Lecea L. Antagonistic interplay between hypocretin and leptin in the lateral hypothalamus regulates stress responses. *Nat Commun*. 2015;6:6266. doi:10.1038/ncomms7266

90. Yamanaka A, Beuckmann CT, Willie JT, et al. Hypothalamic orexin neurons regulate arousal according to energy balance in mice. *Neuron*. 2003;38(5):701-713. doi:10.1016/s0896-6273(03)00331-3

91. Sherin JE, Elmquist JK, Torrealba F, Saper CB. Innervation of histaminergic tuberomammillary neurons by GABAergic and galaninergic neurons in the ventrolateral preoptic nucleus of the rat. *J Neurosci Off J Soc Neurosci*. 1998;18(12):4705-4721. doi:10.1523/JNEUROSCI.18-12-04705.1998

92. Uschakov A, Gong H, McGinty D, Szymusiak R. Efferent projections from the median preoptic nucleus to sleep- and arousal-regulatory nuclei in the rat brain. *Neuroscience*. 2007;150(1):104-120. doi:10.1016/j.neuroscience.2007.05.055

93. Alam MA, Kumar S, McGinty D, Alam MN, Szymusiak R. Neuronal activity in the preoptic hypothalamus during sleep deprivation and recovery sleep. *J Neurophysiol*. 2014;111(2):287-299. doi:10.1152/jn.00504.2013

94. Gallopin T, Luppi PH, Cauli B, et al. The endogenous somnogen adenosine excites a subset of sleep-promoting neurons via A2A receptors in the ventrolateral preoptic nucleus. *Neuroscience*. 2005;134(4):1377-1390. doi:10.1016/j.neuroscience.2005.05.045

95. Zhang Z, Ferretti V, Güntan İ, et al. Neuronal ensembles sufficient for recovery sleep and the sedative actions of α2 adrenergic agonists. *Nat Neurosci*. 2015;18(4):553-561. doi:10.1038/nn.3957

96. Hassani OK, Lee MG, Henny P, Jones BE. Discharge profiles of identified GABAergic in comparison to cholinergic and putative glutamatergic basal forebrain neurons across the sleep-wake cycle. *J Neurosci Off J Soc Neurosci*. 2009;29(38):11828-11840. doi:10.1523/JNEUROSCI.1259-09.2009

97. Kim T, Thankachan S, McKenna JT, et al. Cortically projecting basal forebrain parvalbumin neurons regulate cortical gamma band oscillations. *Proc Natl Acad Sci U S A*. 2015;112(11):3535-3540. doi:10.1073/pnas.1413625112

98. Manns ID, Alonso A, Jones BE. Discharge properties of juxtacellularly labeled and immunohistochemically identified cholinergic basal forebrain neurons recorded in association with the electroencephalogram in anesthetized rats. *J Neurosci Off J Soc Neurosci*. 2000;20(4):1505-1518. doi:10.1523/JNEUROSCI.20-04-01505.2000

99. Anaclet C, Ferrari L, Arrigoni E, et al. The GABAergic parafacial zone is a medullary slow wave sleep-promoting center. *Nat Neurosci*. 2014;17(9):1217-1224. doi:10.1038/nn.3789

100. Tricoire L, Vitalis T. Neuronal nitric oxide synthase expressing neurons: a journey from birth to neuronal circuits. *Front Neural Circuits*. 2012;6:82. doi:10.3389/fncir.2012.00082

101. Gerashchenko D, Wisor JP, Burns D, et al. Identification of a population of sleep-active cerebral cortex neurons. *Proc Natl Acad Sci U S A*. 2008;105(29):10227-10232. doi:10.1073/pnas.0803125105

102. Morairty SR, Dittrich L, Pasumarthi RK, et al. A role for cortical nNOS/NK1 neurons in coupling homeostatic sleep drive to EEG slow wave activity. *Proc Natl Acad Sci U S A*. 2013;110(50):20272-20277. doi:10.1073/pnas.1314762110

103. Saper CB, Fuller PM, Pedersen NP, Lu J, Scammell TE. Sleep state switching. *Neuron*. 2010;68(6):1023-1042. doi:10.1016/j.neuron.2010.11.032

104. Jouvet M. [Research on the neural structures and responsible mechanisms in different phases of physiological sleep]. *Arch Ital Biol*. 1962;100:125-206.

105. Siegel JM, Nienhuis R, Tomaszewski KS. REM sleep signs rostral to chronic transections at the pontomedullary junction. *Neurosci Lett*. 1984;45(3):241-246. doi:10.1016/0304-3940(84)90233-7

106. Hobson JA, McCarley RW, Wyzinski PW. Sleep cycle oscillation: reciprocal discharge by two brainstem neuronal groups. *Science*. 1975;189(4196):55-58. doi:10.1126/science.1094539

107. Krenzer M, Anaclet C, Vetrivelan R, et al. Brainstem and spinal cord circuitry regulating REM sleep and muscle atonia. *PloS One*. 2011;6(10):e24998. doi:10.1371/journal.pone.0024998

108. Van Dort CJ, Zachs DP, Kenny JD, et al. Optogenetic activation of cholinergic neurons in the PPT or LDT induces REM sleep. *Proc Natl Acad Sci U S A*. 2015;112(2):584-589. doi:10.1073/pnas.1423136112

109. Fuller PM, Saper CB, Lu J. The pontine REM switch: past and present. *J Physiol*. 2007;584(Pt 3):735-741. doi:10.1113/jphysiol.2007.140160

110. Sakai K, Crochet S, Onoe H. Pontine structures and mechanisms involved in the generation of paradoxical (REM) sleep. *Arch Ital Biol*. 2001;139(1-2):93-107.

111. Lu J, Sherman D, Devor M, Saper CB. A putative flip-flop switch for control of REM sleep. *Nature*. 2006;441(7093):589-594. doi:10.1038/nature04767

112. Luppi PH, Clement O, Sapin E, et al. Brainstem mechanisms of paradoxical (REM) sleep generation. *Pflugers Arch*. 2012;463(1):43-52. doi:10.1007/s00424-011-1054-y

113. Crochet S, Sakai K. Effects of microdialysis application of monoamines on the EEG and behavioural states in the cat mesopontine tegmentum. *Eur J Neurosci*. 1999;11(10):3738-3752. doi:10.1046/j.1460-9568.1999.00760.x

114. Luebke JI, Greene RW, Semba K, Kamondi A, McCarley RW, Reiner PB. Serotonin hyperpolarizes cholinergic low-threshold burst neurons in the rat laterodorsal tegmental nucleus in vitro. *Proc Natl Acad Sci U S A*. 1992;89(2):743-747. doi:10.1073/pnas.89.2.743

115. Boissard R, Fort P, Gervasoni D, Barbagli B, Luppi PH. Localization of the

GABAergic and non-GABAergic neurons projecting to the sublaterodorsal nucleus and potentially gating paradoxical sleep onset. *Eur J Neurosci*. 2003;18(6):1627-1639. doi:10.1046/j.1460-9568.2003.02861.x

116. Sapin E, Lapray D, Bérod A, et al. Localization of the brainstem GABAergic neurons controlling paradoxical (REM) sleep. *PloS One*. 2009;4(1):e4272. doi:10.1371/journal.pone.0004272

117. Hayashi Y, Kashiwagi M, Yasuda K, et al. Cells of a common developmental origin regulate REM/non-REM sleep and wakefulness in mice. *Science*. 2015;350(6263):957-961. doi:10.1126/science.aad1023

118. Maloney KJ, Mainville L, Jones BE. c-Fos expression in GABAergic, serotonergic, and other neurons of the pontomedullary reticular formation and raphe after paradoxical sleep deprivation and recovery. *J Neurosci Off J Soc Neurosci*. 2000;20(12):4669-4679. doi:10.1523/JNEUROSCI.20-12-04669.2000

119. Weber F, Chung S, Beier KT, Xu M, Luo L, Dan Y. Control of REM sleep by ventral medulla GABAergic neurons. *Nature*. 2015;526(7573):435-438. doi:10.1038/nature14979

120. Lu J, Bjorkum AA, Xu M, Gaus SE, Shiromani PJ, Saper CB. Selective activation of the extended ventrolateral preoptic nucleus during rapid eye movement sleep. *J Neurosci Off J Soc Neurosci*. 2002;22(11):4568-4576. doi:10.1523/JNEUROSCI.22-11-04568.2002

121. Tsunematsu T, Ueno T, Tabuchi S, et al. Optogenetic manipulation of activity and temporally controlled cell-specific ablation reveal a role for MCH neurons in sleep/wake regulation. *J Neurosci Off J Soc Neurosci*. 2014;34(20):6896-6909. doi:10.1523/JNEUROSCI.5344-13.2014

122. Vetrivelan R, Kong D, Ferrari LL, et al. Melanin-concentrating hormone neurons specifically promote rapid eye movement sleep in mice. *Neuroscience*. 2016;336:102-113. doi:10.1016/j.neuroscience.2016.08.046

123. Dugovic C, Shelton JE, Yun S, Bonaventure P, Shireman BT, Lovenberg TW. Orexin-1 receptor blockade dysregulates REM sleep in the presence of orexin-2 receptor antagonism. *Front Neurosci*. 2014;8:28. doi:10.3389/fnins.2014.00028

124. Hasegawa E, Yanagisawa M, Sakurai T, Mieda M. Orexin neurons suppress narcolepsy via 2 distinct efferent pathways. *J Clin Invest*. 2014;124(2):604-616. doi:10.1172/JCI71017

125. Parpura V, Basarsky TA, Liu F, Jeftinija K, Jeftinija S, Haydon PG. Glutamate-mediated astrocyte-neuron signalling. *Nature*. 1994;369(6483):744-747. doi:10.1038/369744a0

126. García-Marín V, García-López P, Freire M. Cajal's contributions to glia research. *Trends Neurosci*. 2007;30(9):479-487. doi:10.1016/j.tins.2007.06.008

127. Jessen NA, Munk ASF, Lundgaard I, Nedergaard M. The Glymphatic System: A Beginner's Guide. *Neurochem Res*. 2015;40(12):2583-2599. doi:10.1007/s11064-015-1581-6

128. Iliff JJ, Wang M, Liao Y, et al. A paravascular pathway facilitates CSF flow through the brain parenchyma and the clearance of interstitial solutes, including amyloid β. *Sci Transl Med*. 2012;4(147):147ra111. doi:10.1126/scitranslmed.3003748

129. Pelluru D, Konadhode RR, Bhat NR, Shiromani PJ. Optogenetic stimulation of astrocytes in the posterior hypothalamus increases sleep at night in C57BL/6J mice. *Eur J Neurosci*. 2016;43(10):1298-1306. doi:10.1111/ejn.13074

130. Blanco-Centurion C, Xu M, Murillo-Rodriguez E, et al. Adenosine and sleep homeostasis in the Basal forebrain. *J Neurosci Off J Soc Neurosci*. 2006;26(31):8092-8100. doi:10.1523/JNEUROSCI.2181-06.2006

131. Pascual O, Casper KB, Kubera C, et al. Astrocytic purinergic signaling coordinates synaptic networks. *Science*. 2005;310(5745):113-116. doi:10.1126/science.1116916

132. Schmitt LI, Sims RE, Dale N, Haydon PG. Wakefulness affects synaptic and network activity by increasing extracellular astrocyte-derived adenosine. *J Neurosci Off J Soc Neurosci*. 2012;32(13):4417-4425. doi:10.1523/JNEUROSCI.5689-11.2012

133. Radulovacki M, Virus RM, Djuricic-Nedelson M, Green RD. Adenosine analogs and sleep in rats. *J Pharmacol Exp Ther*. 1984;228(2):268-274.

134. Fredholm BB, Bättig K, Holmén J, Nehlig A, Zvartau EE. Actions of caffeine in the brain with special reference to factors that contribute to its widespread use. *Pharmacol Rev*. 1999;51(1):83-133.

135. Mang GM, Nicod J, Emmenegger Y, Donohue KD, O'Hara BF, Franken P. Evaluation of a piezoelectric system as an alternative to electroencephalogram/ electromyogram recordings in mouse sleep studies. *Sleep*. 2014;37(8):1383-1392. doi:10.5665/sleep.3936

136. Renier N, Adams EL, Kirst C, et al. Mapping of Brain Activity by Automated Volume Analysis of Immediate Early Genes. *Cell*. 2016;165(7):1789-1802. doi:10.1016/j.cell.2016.05.007

137. Perens J, Salinas CG, Skytte JL, et al. An Optimized Mouse Brain Atlas for Automated Mapping and Quantification of Neuronal Activity Using iDISCO+ and Light Sheet Fluorescence Microscopy. *Neuroinformatics*. 2021;19(3):433-446. doi:10.1007/s12021-020-09490-8

138. Diedenhofen B, Musch J. cocor: a comprehensive solution for the statistical comparison of correlations. *PloS One*. 2015;10(3):e0121945.

doi:10.1371/journal.pone.0121945

139. LaGrow TJ, Moore MG, Prasad JA, Webber A, Davenport MA, Dyer EL. Sparse Recovery Methods for Cell Detection and Layer Estimation. December 2018:445742. doi:10.1101/445742

140. Schulte EC, Kousi M, Tan PL, et al. Targeted resequencing and systematic in vivo functional testing identifies rare variants in MEIS1 as significant contributors to restless legs syndrome. *Am J Hum Genet*. 2014;95(1):85-95. doi:10.1016/j.ajhg.2014.06.005

141. Rozman J, Klingenspor M, Hrabě de Angelis M. A review of standardized metabolic phenotyping of animal models. *Mamm Genome Off J Int Mamm Genome Soc*. 2014;25(9-10):497-507. doi:10.1007/s00335-014-9532-0

142. Eddy NB, Leimbach D. Synthetic analgesics. II. Dithienylbutenyl- and dithienylbutylamines. *J Pharmacol Exp Ther*. 1953;107(3):385-393.

143. Jones BJ, Roberts DJ. The quantiative measurement of motor inco-ordination in naive mice using an acelerating rotarod. *J Pharm Pharmacol*. 1968;20(4):302-304. doi:10.1111/j.2042-7158.1968.tb09743.x

144. Mang GM, Franken P. Sleep and EEG Phenotyping in Mice. *Curr Protoc Mouse Biol*. 2012;2(1):55-74. doi:10.1002/9780470942390.mo110126

145. Flores AE, Flores JE, Deshpande H, et al. Pattern recognition of sleep in rodents using piezoelectric signals generated by gross body movements. *IEEE Trans Biomed Eng*. 2007;54(2):225-233. doi:10.1109/TBME.2006.886938

146. Zamore Z, Veasey SC. Neural consequences of chronic sleep disruption. *Trends Neurosci*. 2022;45(9):678-691. doi:10.1016/j.tins.2022.05.007

147. Bouganim S, Bergdahl A. Constructing an inexpensive and versatile homemade rodent treadmill. *Lab Anim*. 2017;46(3):67-69. doi:10.1038/laban.1196

148. Murack M, Chandrasegaram R, Smith KB, et al. Chronic sleep disruption induces depression-like behavior in adolescent male and female mice and sensitization of the hypothalamic-pituitary-adrenal axis in adolescent female mice. *Behav Brain Res*. 2021;399:113001. doi:10.1016/j.bbr.2020.113001

149. Surbhi null, Borniger JC, Russart KLG, Zhang N, Magalang UJ, Nelson RJ. miR-155 deletion modulates lipopolysaccharide-induced sleep in female mice. *Chronobiol Int*. 2019;36(2):188-202. doi:10.1080/07420528.2018.1525617

150. Ueda HR, Ertürk A, Chung K, et al. Tissue clearing and its applications in neuroscience. *Nat Rev Neurosci*. 2020;21(2):61-79. doi:10.1038/s41583-019-0250-1

151. Yu T, Zhu J, Li D, Zhu D. Physical and chemical mechanisms of tissue optical clearing. *iScience*. 2021;24(3):102178. doi:10.1016/j.isci.2021.102178

152. Dodt HU, Leischner U, Schierloh A, et al. Ultramicroscopy: three-dimensional visualization of neuronal networks in the whole mouse brain. *Nat Methods*. 2007;4(4):331-336. doi:10.1038/nmeth1036

153. Chiu R, Boyle WJ, Meek J, Smeal T, Hunter T, Karin M. The c-Fos protein interacts with c-Jun/AP-1 to stimulate transcription of AP-1 responsive genes. *Cell*. 1988;54(4):541-552. doi:10.1016/0092-8674(88)90076-1

154. Hu E, Mueller E, Oliviero S, Papaioannou VE, Johnson R, Spiegelman BM. Targeted disruption of the c-fos gene demonstrates c-fos-dependent and -independent pathways for gene expression stimulated by growth factors or oncogenes. *EMBO J*. 1994;13(13):3094-3103.

155. Dragunow M, Faull R. The use of c-fos as a metabolic marker in neuronal pathway tracing. *J Neurosci Methods*. 1989;29(3):261-265. doi:10.1016/0165-0270(89)90150-7

156. Young DM, Fazel Darbandi S, Schwartz G, et al. Constructing and optimizing 3D atlases from 2D data with application to the developing mouse brain. *eLife*. 2021;10:e61408. doi:10.7554/eLife.61408

157. Atlas Thumbnails :: Allen Brain Atlas: Mouse Brain. https://mouse.brain-map.org/experiment/thumbnails/100048576?image_type=atlas. Accessed June 15, 2023.

158. Huston JP, Wagner U, Hasenöhrl RU. The tuberomammillary nucleus projections in the control of learning, memory and reinforcement processes: evidence for an inhibitory role. *Behav Brain Res*. 1997;83(1-2):97-105. doi:10.1016/s0166-4328(97)86052-4

159. Ono T, Nishijo H, Uwano T. Amygdala role in conditioned associative learning. *Prog Neurobiol*. 1995;46(4):401-422. doi:10.1016/0301-0082(95)00008-j

160. Tye KM, Prakash R, Kim SY, et al. Amygdala circuitry mediating reversible and bidirectional control of anxiety. *Nature*. 2011;471(7338):358-362. doi:10.1038/nature09820

161. Roozendaal B, McEwen BS, Chattarji S. Stress, memory and the amygdala. *Nat Rev Neurosci*. 2009;10(6):423-433. doi:10.1038/nrn2651

162. Gallagher M, Chiba AA. The amygdala and emotion. *Curr Opin Neurobiol*. 1996;6(2):221-227. doi:10.1016/s0959-4388(96)80076-6

163. Ma C, Zhong P, Liu D, et al. Sleep Regulation by Neurotensinergic Neurons in a Thalamo-Amygdala Circuit. *Neuron*. 2019;103(2):323-334.e7. doi:10.1016/j.neuron.2019.05.015

164. Wellman LL, Lonart G, Adkins AM, Sanford LD. Regulation of dark period sleep by the Amygdala: A microinjection and optogenetics study. *Brain Res*. 2022;1781:147816. doi:10.1016/j.brainres.2022.147816

165. Hasegawa E, Miyasaka A, Sakurai K, Cherasse Y, Li Y, Sakurai T. Rapid eye movement sleep is initiated by basolateral amygdala dopamine signaling in mice. *Science*. 2022;375(6584):994-1000. doi:10.1126/science.abl6618

166. Machida M, Sweeten BLW, Adkins AM, Wellman LL, Sanford LD. Basolateral Amygdala Regulates EEG Theta-activity During Rapid Eye Movement Sleep. *Neuroscience*. 2021;468:176-185. doi:10.1016/j.neuroscience.2021.06.018

167. Matei M, Bergel A, Pezet S, Tanter M. Global dissociation of the posterior amygdala from the rest of the brain during REM sleep. *Commun Biol*. 2022;5(1):1306. doi:10.1038/s42003-022-04257-0

168. Vardy E, Robinson JE, Li C, et al. A New DREADD Facilitates the Multiplexed Chemogenetic Interrogation of Behavior. *Neuron*. 2015;86(4):936-946. doi:10.1016/j.neuron.2015.03.065

169. Silva BA, Astori S, Burns AM, et al. A thalamo-amygdalar circuit underlying the extinction of remote fear memories. *Nat Neurosci*. 2021;24(7):964-974. doi:10.1038/s41593-021-00856-y

170. Bojarskaite L, Bjørnstad DM, Pettersen KH, et al. Astrocytic Ca2+ signaling is reduced during sleep and is involved in the regulation of slow wave sleep. *Nat Commun*. 2020;11(1):3240. doi:10.1038/s41467-020-17062-2

171. Ingiosi AM, Hayworth CR, Harvey DO, et al. A Role for Astroglial Calcium in Mammalian Sleep and Sleep Regulation. *Curr Biol CB*. 2020;30(22):4373-4383.e7. doi:10.1016/j.cub.2020.08.052

172. Halassa MM, Florian C, Fellin T, et al. Astrocytic modulation of sleep homeostasis and cognitive consequences of sleep loss. *Neuron*. 2009;61(2):213-219. doi:10.1016/j.neuron.2008.11.024

173. Williams RH, Vazquez-DeRose J, Thomas AM, Piquet J, Cauli B, Kilduff TS. Cortical nNOS/NK1 Receptor Neurons are Regulated by Cholinergic Projections From the Basal Forebrain. *Cereb Cortex N Y N 1991*. 2018;28(6):1959-1979. doi:10.1093/cercor/bhx102

174. Williams RH, Vazquez-DeRose J, Nguyen A, Kilduff T. Cortical nNOS/NK1 neurons are regulated by adenosinergic tone. *Neurosci*. 2015.

175. Guttenplan KA, Liddelow SA. Astrocytes and microglia: Models and tools. *J Exp Med*. 2019;216(1):71-83. doi:10.1084/jem.20180200

176. Madisen L, Zwingman TA, Sunkin SM, et al. A robust and high-throughput Cre reporting and characterization system for the whole mouse brain. *Nat Neurosci*.

2010;13(1):133-140. doi:10.1038/nn.2467

177. Vaidyanathan TV, Collard M, Yokoyama S, Reitman ME, Poskanzer KE. Cortical astrocytes independently regulate sleep depth and duration via separate GPCR pathways. *eLife*. 2021;10:e63329. doi:10.7554/eLife.63329

178. Dubey MSR. Restless Legs Syndrome. *Int J Nurs Educ Res*. 2020;8(2):289-291. doi:10.5958/2454-2660.2020.00063.0

179. Berger K, Luedemann J, Trenkwalder C, John U, Kessler C. Sex and the risk of restless legs syndrome in the general population. *Arch Intern Med*. 2004;164(2):196-202. doi:10.1001/archinte.164.2.196

180. Allen RP, Earley CJ. Restless legs syndrome: a review of clinical and pathophysiologic features. *J Clin Neurophysiol Off Publ Am Electroencephalogr Soc*. 2001;18(2):128-147. doi:10.1097/00004691-200103000-00004

181. Jiménez-Jiménez FJ, Alonso-Navarro H, García-Martín E, Agúndez JAG. Genetics of restless legs syndrome: An update. *Sleep Med Rev*. 2018;39:108-121. doi:10.1016/j.smrv.2017.08.002

182. Catoire H, Sarayloo F, Mourabit Amari K, et al. A direct interaction between two Restless Legs Syndrome predisposing genes: MEIS1 and SKOR1. *Sci Rep*. 2018;8(1):12173. doi:10.1038/s41598-018-30665-6

183. Winkelmann J, Schormair B, Lichtner P, et al. Genome-wide association study of restless legs syndrome identifies common variants in three genomic regions. *Nat Genet*. 2007;39(8):1000-1006. doi:10.1038/ng2099

184. Allen RP, Donelson NC, Jones BC, et al. Animal models of RLS phenotypes. *Sleep Med*. 2017;31:23-28. doi:10.1016/j.sleep.2016.08.002

185. Ramar K, Olson EJ. Management of common sleep disorders. *Am Fam Physician*. 2013;88(4):231-238.

186. Sarayloo F, Dion PA, Rouleau GA. MEIS1 and Restless Legs Syndrome: A Comprehensive Review. *Front Neurol*. 2019;10:935. doi:10.3389/fneur.2019.00935

187. Schormair B, Zhao C, Bell S, et al. Identification of novel risk loci for restless legs syndrome in genome-wide association studies in individuals of European ancestry: a meta-analysis. *Lancet Neurol*. 2017;16(11):898-907. doi:10.1016/S1474-4422(17)30327-7

188. Zhang H, Zhang Y, Ren R, et al. Polysomnographic features of idiopathic restless legs syndrome: a systematic review and meta-analysis of 13 sleep parameters and 23 leg movement parameters. *J Clin Sleep Med JCSM Off Publ Am Acad Sleep Med*. 2022;18(11):2561-2575. doi:10.5664/jcsm.10160

189. Lakshminarayanan S, Paramasivan KD, Walters AS, Wagner ML, Patel S, Passi V. Clinically significant but unsuspected restless legs syndrome in patients with sleep apnea. *Mov Disord Off J Mov Disord Soc*. 2005;20(4):501-503. doi:10.1002/mds.20366

190. Wang X, Chou XL, Zhang LI, Tao HW. Zona Incerta: An Integrative Node for Global Behavioral Modulation. *Trends Neurosci*. 2020;43(2):82-87. doi:10.1016/j.tins.2019.11.007

191. Earley CJ, Kuwabara H, Wong DF, et al. The dopamine transporter is decreased in the striatum of subjects with restless legs syndrome. *Sleep*. 2011;34(3):341-347. doi:10.1093/sleep/34.3.341

192. Salminen AV, Silvani A, Allen RP, et al. Consensus Guidelines on Rodent Models of Restless Legs Syndrome. *Mov Disord Off J Mov Disord Soc*. 2021;36(3):558-569. doi:10.1002/mds.28401

193. Dumortier M, Thöni G, Brun JF, Mercier J. Substrate oxidation during exercise: impact of time interval from the last meal in obese women. *Int J Obes 2005*. 2005;29(8):966-974. doi:10.1038/sj.ijo.0802991

194. Silva GE, Goodwin JL, Vana KD, Vasquez MM, Wilcox PG, Quan SF. Restless legs syndrome, sleep, and quality of life among adolescents and young adults. *J Clin Sleep Med JCSM Off Publ Am Acad Sleep Med*. 2014;10(7):779-786. doi:10.5664/jcsm.3872

195. Schattschneider J, Bode A, Wasner G, Binder A, Deuschl G, Baron R. Idiopathic restless legs syndrome: abnormalities in central somatosensory processing. *J Neurol*. 2004;251(8):977-982. doi:10.1007/s00415-004-0475-3

196. Azcoitia V, Aracil M, Martínez-A C, Torres M. The homeodomain protein Meis1 is essential for definitive hematopoiesis and vascular patterning in the mouse embryo. *Dev Biol*. 2005;280(2):307-320. doi:10.1016/j.ydbio.2005.01.004

197. Salminen AV, Garrett L, Schormair B, et al. Meis1: effects on motor phenotypes and the sensorimotor system in mice. *Dis Model Mech*. 2017;10(8):981-991. doi:10.1242/dmm.030080

198. Salminen AV, Schormair B, Flachskamm C, et al. Sleep disturbance by pramipexole is modified by Meis1 in mice. *J Sleep Res*. 2018;27(4):e12557. doi:10.1111/jsr.12557

199. Lyu S, Xing H, Liu Y, et al. Deficiency of Meis1, a transcriptional regulator, in mice and worms: Neurochemical and behavioral characterizations with implications in the restless legs syndrome. *J Neurochem*. 2020;155(5):522-537. doi:10.1111/jnc.15177

200. DeAndrade MP, Johnson RL, Unger EL, et al. Motor restlessness, sleep disturbances, thermal sensory alterations and elevated serum iron levels in

Btbd9 mutant mice. *Hum Mol Genet*. 2012;21(18):3984-3992. doi:10.1093/hmg/dds221

201. Allen RP, Earley CJ, Jones BC, Unger EL. Iron-deficiency and dopaminergic treatment effects on RLS-Like behaviors of an animal model with the brain iron deficiency pattern of the restless legs syndrome. *Sleep Med*. 2020;71:141-148. doi:10.1016/j.sleep.2020.01.024

202. Earley CJ, Allen RP, Connor JR, Ferrucci L, Troncoso J. The dopaminergic neurons of the A11 system in RLS autopsy brains appear normal. *Sleep Med*. 2009;10(10):1155-1157. doi:10.1016/j.sleep.2009.01.006

203. Hirata K, Suzuki K. [Diagnosis and novel treatment approaches in restless legs syndrome: I. Pathophysiology and diagnosis]. *Brain Nerve Shinkei Kenkyu No Shinpo*. 2013;65(10):1185-1197.

204. Bjorness TE, Kelly CL, Gao T, Poffenberger V, Greene RW. Control and Function of the Homeostatic Sleep Response by Adenosine A1 Receptors. *J Neurosci*. 2009;29(5):1267-1276. doi:10.1523/JNEUROSCI.2942-08.2009

205. Gillies MJ, Hyam JA, Weiss AR, et al. The Cognitive Role of the Globus Pallidus interna; Insights from Disease States. *Exp Brain Res*. 2017;235(5):1455-1465. doi:10.1007/s00221-017-4905-8

206. Evarts EV, Wise SP. Basal ganglia outputs and motor control. *Ciba Found Symp*. 1984;107:83-102. doi:10.1002/9780470720882.ch6

Appendices

Supplementary table 1. cFos cell counts from ClearMap automatic cell detection (Chapter 4: Identification of amygdala neurons activated by sleep loss)

n=8-10 per group

Brain region	Manual SD		Treadmill SD		Control ZT4		Manual RS		Treadmill RS		Control ZT6	
	Mean	SEM	Mean	SEM	Mean	SEM	Mean	SEM	Mean	SEM	Mean	SEM
Abducens nucleus	0	0	0	0	0	0	0	0	0	0	0	0
Accessory facial motor nucleus	0	0	0	0	0	0	0	0	0	0	0	0
Accessory olfactory bulb	0	0	0	0	0	0	1	1	0	0	2	1
Accessory supraoptic group	0	0	1	1	0	0	0	0	0	0	0	0
Agranular insular area	1919	248	3693	324	357	57	981	131	987	145	463	95
alveus	296	46	251	26	236	31	291	38	222	28	316	67
amygdalar capsule	75	9	88	9	36	6	58	9	98	12	62	14
Anterior amygdalar area	273	59	634	73	65	15	176	65	121	22	103	26
Anterior cingulate area	492	113	282	77	203	42	253	50	117	29	271	64
anterior commissure	46	16	25	7	10	2	26	4	36	8	20	6
Anterior hypothalamic	96	16	187	25	10	4	43	16	63	15	49	12

nucleus												
Anterior olfactory nucleus	**686**	**97**	**927**	**336**	**31**	**4**	**361**	**105**	**35**	**7**	**86**	**19**
Anterior pretectal nucleus	**22**	**8**	**10**	**3**	**32**	**10**	**31**	**21**	**15**	**3**	**38**	**7**
Anterior tegmental nucleus	**0**	**0**	**0**	**0**	**0**	**0**	**1**	**0**	**0**	**0**	**0**	**0**
Anterodorsal nucleus	**12**	**5**	**2**	**1**	**4**	**1**	**4**	**2**	**3**	**1**	**7**	**1**
Anterodorsal preoptic nucleus	**43**	**8**	**0**	**0**	**2**	**1**	**26**	**9**	**1**	**1**	**26**	**9**
Anterolateral visual area	**487**	**105**	**732**	**135**	**98**	**49**	**185**	**57**	**190**	**47**	**146**	**46**
Anteromedial nucleus	**4**	**3**	**0**	**0**	**2**	**0**	**2**	**1**	**1**	**1**	**3**	**1**
Anteromedial visual area	**751**	**125**	**432**	**61**	**269**	**105**	**442**	**91**	**209**	**66**	**402**	**67**
Anteroventral nucleus of thalamus	**16**	**10**	**2**	**1**	**5**	**2**	**8**	**2**	**3**	**1**	**8**	**2**
Anteroventral periventricular nucleus	**22**	**6**	**60**	**12**	**3**	**1**	**9**	**3**	**12**	**3**	**22**	**14**
Anteroventral preoptic nucleus	**31**	**9**	**56**	**10**	**2**	**1**	**15**	**4**	**11**	**3**	**13**	**6**
arbor vitae	**199**	**41**	**134**	**17**	**251**	**72**	**212**	**56**	**172**	**18**	**246**	**79**
Arcuate hypothalamic nucleus	**63**	**20**	**198**	**16**	**9**	**3**	**23**	**2**	**62**	**13**	**24**	**5**

Area postrema	**0**	**0**	**0**	**0**	**3**	**1**	**0**	**0**	**0**	**0**	**3**	**2**
Barrington's nucleus	**3**	**1**	**0**	**0**	**0**	**0**	**1**	**0**	**0**	**0**	**0**	**0**
Basolateral amygdalar nucleus	**2105**	**126**	**2067**	**191**	**447**	**141**	**1558**	**205**	**913**	**112**	**880**	**254**
Basomedial amygdalar nucleus	**2314**	**88**	**3002**	**267**	**558**	**154**	**1531**	**192**	**1110**	**142**	**890**	**168**
Bed nuclei of the stria terminalis	**289**	**45**	**64**	**14**	**33**	**8**	**230**	**44**	**54**	**12**	**63**	**15**
Bed nucleus of the accessory olfactory tract	**25**	**8**	**66**	**7**	**4**	**3**	**8**	**4**	**9**	**2**	**8**	**2**
Bed nucleus of the anterior commissure	**0**	**0**	**0**	**0**	**0**	**0**	**0**	**0**	**1**	**1**	**0**	**0**
brachium of the inferior colliculus	**94**	**11**	**50**	**6**	**59**	**8**	**79**	**10**	**76**	**12**	**63**	**12**
brachium of the superior colliculus	**52**	**7**	**33**	**5**	**42**	**8**	**51**	**6**	**56**	**12**	**54**	**9**
Caudoputamen	**6123**	**1863**	**1442**	**308**	**4074**	**1400**	**5169**	**1463**	**2745**	**410**	**6302**	**2248**
Central amygdalar nucleus	**830**	**110**	**276**	**51**	**244**	**56**	**768**	**120**	**250**	**44**	**322**	**78**
central canal	**1**	**0**	**1**	**0**	**1**	**0**	**0**	**0**	**0**	**0**	**1**	**0**
Central lateral nucleus of the thalamus	**13**	**5**	**2**	**1**	**3**	**1**	**6**	**2**	**6**	**2**	**9**	**3**
Central linear nucleus raphe	**5**	**2**	**0**	**0**	**2**	**1**	**1**	**0**	**0**	**0**	**2**	**1**

Central medial nucleus of the thalamus	**15**	**6**	**1**	**0**	**3**	**1**	**3**	**2**	**2**	**1**	**6**	**3**
cerebal peduncle	**138**	**15**	**187**	**19**	**136**	**12**	**130**	**16**	**138**	**18**	**164**	**32**
cerebellar commissure	**0**	**0**	**0**	**0**	**0**	**0**	**0**	**0**	**1**	**0**	**1**	**0**
cerebral aqueduct	**120**	**22**	**59**	**16**	**99**	**15**	**106**	**19**	**88**	**23**	**114**	**23**
choroid plexus	**493**	**69**	**655**	**74**	**520**	**89**	**645**	**105**	**525**	**64**	**696**	**95**
cingulum bundle	**73**	**18**	**49**	**21**	**21**	**2**	**40**	**12**	**142**	**43**	**72**	**13**
Claustrum	**457**	**69**	**480**	**43**	**84**	**24**	**203**	**36**	**143**	**13**	**129**	**24**
columns of the fornix	**21**	**4**	**47**	**8**	**3**	**1**	**13**	**5**	**18**	**2**	**8**	**3**
Copula pyramidis	**29**	**10**	**12**	**3**	**40**	**13**	**33**	**10**	**20**	**4**	**48**	**22**
corpus callosum	**279**	**65**	**217**	**47**	**177**	**54**	**216**	**46**	**454**	**145**	**296**	**100**
Cortical amygdalar area	**2458**	**367**	**4264**	**464**	**561**	**129**	**1211**	**254**	**1594**	**230**	**670**	**149**
corticospinal tract	**7**	**5**	**9**	**3**	**2**	**1**	**1**	**0**	**7**	**2**	**2**	**1**
crossed tectospinal pathway	**4**	**1**	**1**	**0**	**3**	**2**	**4**	**1**	**2**	**1**	**4**	**1**
Crus 1	**199**	**41**	**261**	**65**	**253**	**58**	**191**	**50**	**191**	**20**	**231**	**79**
Crus 2	**78**	**15**	**86**	**20**	**108**	**26**	**74**	**15**	**73**	**7**	**76**	**21**
cuneate fascicle	**0**	**0**	**0**	**0**	**0**	**0**	**0**	**0**	**0**	**0**	**0**	**0**

Cuneate nucleus	**6**	**2**	**2**	**1**	**10**	**3**	**5**	**2**	**1**	**0**	**10**	**2**
Cuneiform nucleus	**86**	**19**	**22**	**5**	**32**	**4**	**60**	**20**	**20**	**3**	**67**	**13**
Declive (VI)	**65**	**12**	**60**	**13**	**66**	**13**	**65**	**10**	**76**	**19**	**79**	**10**
Dentate gyrus	**1635**	**245**	**868**	**79**	**876**	**201**	**1388**	**213**	**587**	**39**	**1376**	**354**
Dentate nucleus	**15**	**4**	**13**	**3**	**27**	**7**	**19**	**6**	**22**	**5**	**18**	**5**
Diagonal band nucleus	**53**	**13**	**279**	**37**	**26**	**5**	**31**	**9**	**58**	**7**	**66**	**29**
doral tegmental decussation	**0**	**0**	**0**	**0**	**0**	**0**	**0**	**0**	**0**	**0**	**0**	**0**
dorsal acoustic stria	**0**	**0**	**0**	**0**	**1**	**0**	**0**	**0**	**1**	**0**	**0**	**0**
Dorsal auditory area	**268**	**84**	**756**	**133**	**56**	**24**	**67**	**21**	**173**	**31**	**68**	**22**
Dorsal cochlear nucleus	**139**	**20**	**112**	**19**	**52**	**12**	**65**	**7**	**85**	**19**	**46**	**13**
dorsal fornix	**0**	**0**	**0**	**0**	**0**	**0**	**0**	**0**	**1**	**0**	**0**	**0**
dorsal hippocampal commissure	**27**	**7**	**17**	**8**	**15**	**4**	**18**	**4**	**100**	**51**	**30**	**10**
dorsal limb	**0**	**0**	**2**	**1**	**0**	**0**	**0**	**0**	**0**	**0**	**0**	**0**
Dorsal motor nucleus of the vagus nerve	**1**	**1**	**2**	**1**	**3**	**1**	**1**	**0**	**1**	**1**	**1**	**0**
Dorsal nucleus raphe	**4**	**2**	**0**	**0**	**0**	**0**	**1**	**1**	**0**	**0**	**1**	**0**
Dorsal peduncular	**41**	**10**	**2**	**2**	**14**	**4**	**44**	**11**	**3**	**1**	**18**	**5**

area												
Dorsal premammillary nucleus	**81**	**11**	**115**	**16**	**1**	**0**	**33**	**11**	**30**	**7**	**11**	**3**
dorsal spinocerebellar tract	**2**	**1**	**11**	**2**	**3**	**1**	**7**	**2**	**5**	**1**	**6**	**1**
Dorsal tegmental nucleus	**1**	**1**	**0**	**0**	**0**	**0**	**1**	**0**	**2**	**1**	**0**	**0**
Dorsal terminal nucleus of the accessory optic tract	**2**	**1**	**2**	**1**	**2**	**1**	**2**	**1**	**3**	**1**	**2**	**1**
Dorsomedial nucleus of the hypothalamus	**127**	**15**	**162**	**21**	**9**	**3**	**66**	**23**	**51**	**12**	**81**	**27**
Ectorhinal area/Layer 1	**55**	**14**	**158**	**16**	**16**	**4**	**24**	**5**	**69**	**10**	**17**	**5**
Ectorhinal area/Layer 2/3	**255**	**61**	**657**	**63**	**15**	**5**	**76**	**10**	**219**	**30**	**36**	**12**
Ectorhinal area/Layer 5	**314**	**70**	**673**	**61**	**33**	**12**	**174**	**30**	**317**	**39**	**90**	**20**
Ectorhinal area/Layer 6a	**240**	**41**	**419**	**42**	**48**	**13**	**164**	**21**	**267**	**27**	**85**	**12**
Ectorhinal area/Layer 6b	**15**	**4**	**40**	**4**	**8**	**2**	**13**	**2**	**35**	**6**	**14**	**3**
Edinger-Westphal nucleus	**1**	**0**	**0**	**0**	**1**	**1**	**0**	**0**	**0**	**0**	**1**	**1**
Endopiriform nucleus	**1354**	**127**	**2295**	**212**	**363**	**80**	**828**	**111**	**995**	**108**	**551**	**96**
Entorhinal area	**4005**	**973**	**10578**	**734**	**607**	**113**	**2362**	**346**	**4514**	**366**	**1028**	**189**

external capsule	**278**	**39**	**322**	**29**	**109**	**18**	**192**	**19**	**298**	**36**	**173**	**30**
External cuneate nucleus	**9**	**3**	**10**	**3**	**16**	**6**	**14**	**5**	**4**	**1**	**16**	**6**
external medullary lamina of the thalamus	**3**	**1**	**1**	**0**	**10**	**4**	**8**	**6**	**2**	**1**	**12**	**3**
Facial motor nucleus	**4**	**1**	**44**	**12**	**9**	**3**	**6**	**2**	**8**	**3**	**6**	**3**
facial nerve	**1**	**0**	**2**	**1**	**1**	**0**	**1**	**0**	**1**	**0**	**2**	**1**
fasciculus retroflexus	**3**	**1**	**1**	**0**	**1**	**1**	**2**	**1**	**0**	**0**	**3**	**2**
Fasciola cinerea	**5**	**2**	**5**	**4**	**5**	**2**	**6**	**2**	**3**	**1**	**8**	**2**
Fastigial nucleus	**25**	**20**	**3**	**1**	**5**	**2**	**6**	**2**	**1**	**0**	**6**	**2**
fiber tracts	**380**	**45**	**383**	**38**	**314**	**20**	**371**	**49**	**262**	**20**	**401**	**57**
Field CA1	**3439**	**665**	**1704**	**153**	**1788**	**629**	**2603**	**517**	**1024**	**101**	**2434**	**840**
Field CA2	**91**	**21**	**33**	**5**	**67**	**22**	**104**	**25**	**27**	**5**	**114**	**39**
Field CA3	**1413**	**262**	**984**	**108**	**827**	**187**	**1530**	**324**	**429**	**44**	**1416**	**484**
Fields of Forel	**7**	**2**	**4**	**2**	**7**	**2**	**13**	**10**	**3**	**1**	**9**	**2**
fimbria	**39**	**9**	**55**	**17**	**61**	**9**	**89**	**30**	**34**	**7**	**93**	**17**
Flocculus	**176**	**46**	**633**	**78**	**112**	**18**	**145**	**24**	**219**	**33**	**144**	**32**
Folium-tuber vermis (VII)	**11**	**4**	**3**	**1**	**6**	**3**	**7**	**4**	**2**	**1**	**7**	**4**
fourth ventricle	**248**	**34**	**258**	**43**	**256**	**57**	**224**	**16**	**235**	**29**	**248**	**44**

Fundus of striatum	**196**	**34**	**95**	**17**	**46**	**8**	**151**	**34**	**56**	**8**	**52**	**7**
genu of corpus callosum	**19**	**8**	**13**	**7**	**7**	**2**	**17**	**5**	**44**	**12**	**17**	**3**
genu of the facial nerve	**0**	**0**	**0**	**0**	**0**	**0**	**0**	**0**	**1**	**1**	**0**	**0**
Gigantocellular reticular nucleus	**16**	**4**	**19**	**8**	**13**	**4**	**23**	**7**	**11**	**3**	**21**	**8**
Globus pallidus	**45**	**13**	**42**	**13**	**65**	**17**	**56**	**15**	**53**	**13**	**152**	**90**
Gracile nucleus	**1**	**0**	**0**	**0**	**1**	**0**	**1**	**0**	**0**	**0**	**1**	**1**
Gustatory areas	**340**	**42**	**929**	**113**	**67**	**11**	**223**	**37**	**290**	**44**	**103**	**20**
habenular commissure	**5**	**2**	**7**	**4**	**5**	**2**	**5**	**3**	**5**	**2**	**7**	**3**
Hypoglossal nucleus	**0**	**0**	**1**	**1**	**1**	**0**	**1**	**1**	**1**	**0**	**1**	**0**
Induseum griseum	**14**	**4**	**8**	**4**	**20**	**5**	**24**	**4**	**7**	**1**	**22**	**5**
inferior cerebellar peduncle	**27**	**5**	**46**	**6**	**30**	**5**	**26**	**4**	**46**	**7**	**24**	**7**
Inferior colliculus	**2170**	**398**	**1591**	**250**	**842**	**119**	**1427**	**296**	**1337**	**298**	**1188**	**205**
inferior colliculus commissure	**1**	**0**	**1**	**0**	**0**	**0**	**1**	**1**	**1**	**1**	**1**	**1**
Inferior olivary complex	**2**	**1**	**7**	**2**	**1**	**0**	**0**	**0**	**1**	**0**	**1**	**0**
Inferior salivatory nucleus	**0**	**0**	**0**	**0**	**0**	**0**	**1**	**0**	**0**	**0**	**0**	**0**
Infracerebellar nucleus	**2**	**1**	**0**	**0**	**0**	**0**	**1**	**0**	**0**	**0**	**0**	**0**

Infralimbic area	**167**	**34**	**3**	**1**	**23**	**7**	**150**	**30**	**4**	**1**	**76**	**14**
Interanterodorsal nucleus of the thalamus	**18**	**7**	**0**	**0**	**0**	**0**	**2**	**1**	**1**	**1**	**7**	**3**
Interanteromedial nucleus of the thalamus	**6**	**2**	**0**	**0**	**1**	**0**	**0**	**0**	**0**	**0**	**1**	**1**
Intercalated amygdalar nucleus	**252**	**17**	**186**	**23**	**49**	**13**	**179**	**30**	**102**	**13**	**73**	**16**
Interfascicular nucleus raphe	**14**	**4**	**9**	**3**	**5**	**2**	**7**	**3**	**7**	**2**	**8**	**3**
Intergeniculate leaflet of the lateral geniculate complex	**43**	**13**	**1**	**0**	**22**	**9**	**34**	**11**	**1**	**1**	**31**	**10**
Intermediate reticular nucleus	**15**	**5**	**20**	**9**	**22**	**7**	**18**	**4**	**16**	**7**	**18**	**7**
Intermediodorsal nucleus of the thalamus	**4**	**1**	**1**	**0**	**0**	**0**	**0**	**0**	**1**	**0**	**1**	**1**
internal capsule	**85**	**18**	**98**	**30**	**70**	**17**	**84**	**14**	**144**	**28**	**158**	**78**
Interpeduncular nucleus	**1**	**1**	**0**	**0**	**1**	**0**	**0**	**0**	**0**	**0**	**0**	**0**
Interposed nucleus	**23**	**10**	**14**	**5**	**25**	**9**	**22**	**6**	**18**	**4**	**21**	**9**
Interstitial nucleus of Cajal	**1**	**1**	**0**	**0**	**1**	**1**	**1**	**0**	**0**	**0**	**1**	**0**
Kolliker-Fuse subnucleus	**17**	**6**	**9**	**2**	**16**	**4**	**18**	**8**	**8**	**2**	**16**	**5**
Lateral amygdalar nucleus	**728**	**118**	**369**	**35**	**348**	**88**	**514**	**52**	**396**	**55**	**550**	**144**

Lateral dorsal nucleus of thalamus	**31**	**14**	**13**	**3**	**65**	**27**	**64**	**47**	**14**	**3**	**96**	**33**
Lateral habenula	**8**	**3**	**2**	**1**	**5**	**1**	**3**	**1**	**2**	**1**	**5**	**2**
Lateral hypothalamic area	**621**	**124**	**1086**	**134**	**147**	**25**	**355**	**118**	**403**	**73**	**341**	**63**
lateral lemniscus	**120**	**7**	**225**	**32**	**87**	**9**	**104**	**19**	**125**	**14**	**102**	**19**
Lateral mammillary nucleus	**10**	**5**	**21**	**4**	**5**	**1**	**5**	**2**	**10**	**2**	**9**	**5**
lateral olfactory tract	**30**	**8**	**69**	**13**	**35**	**11**	**44**	**12**	**38**	**6**	**46**	**15**
Lateral posterior nucleus of the thalamus	**40**	**9**	**21**	**5**	**48**	**17**	**54**	**28**	**37**	**7**	**71**	**12**
Lateral preoptic area	**69**	**15**	**154**	**26**	**15**	**6**	**41**	**13**	**68**	**18**	**43**	**18**
lateral recess	**137**	**24**	**140**	**13**	**169**	**29**	**156**	**28**	**128**	**17**	**167**	**36**
Lateral reticular nucleus	**5**	**2**	**34**	**18**	**6**	**2**	**5**	**1**	**7**	**2**	**7**	**4**
Lateral septal nucleus	**292**	**76**	**31**	**13**	**55**	**19**	**139**	**37**	**50**	**11**	**145**	**41**
Lateral terminal nucleus of the accessory optic tract	**5**	**1**	**4**	**1**	**4**	**1**	**4**	**1**	**4**	**1**	**5**	**1**
lateral ventricle	**817**	**151**	**697**	**175**	**916**	**143**	**1053**	**190**	**659**	**115**	**1313**	**262**
Lateral vestibular nucleus	**9**	**3**	**3**	**1**	**15**	**2**	**21**	**14**	**8**	**3**	**16**	**7**

Lateral visual area	**1013**	**162**	**1170**	**200**	**270**	**137**	**492**	**142**	**325**	**77**	**358**	**126**
Laterodorsal tegmental nucleus	**3**	**1**	**1**	**1**	**1**	**0**	**4**	**3**	**2**	**1**	**3**	**1**
Linear nucleus of the medulla	**1**	**0**	**3**	**1**	**1**	**0**	**1**	**0**	**0**	**0**	**1**	**1**
Lingula (I)	**5**	**2**	**4**	**1**	**4**	**2**	**7**	**3**	**6**	**2**	**7**	**2**
Lobule II	**55**	**15**	**8**	**3**	**29**	**11**	**25**	**10**	**16**	**4**	**59**	**15**
Lobule III	**62**	**12**	**25**	**5**	**71**	**22**	**51**	**11**	**28**	**9**	**86**	**30**
Lobules IV-V	**255**	**41**	**171**	**33**	**299**	**73**	**236**	**33**	**169**	**31**	**320**	**79**
Locus ceruleus	**0**	**0**	**0**	**0**	**0**	**0**	**1**	**1**	**0**	**0**	**1**	**0**
Magnocellular nucleus	**51**	**14**	**293**	**50**	**17**	**4**	**40**	**16**	**31**	**7**	**21**	**4**
Magnocellular reticular nucleus	**3**	**1**	**21**	**8**	**1**	**0**	**3**	**2**	**2**	**1**	**1**	**0**
Main olfactory bulb	**32**	**10**	**43**	**23**	**13**	**2**	**19**	**5**	**8**	**2**	**21**	**7**
mammillary peduncle	**8**	**2**	**10**	**1**	**5**	**1**	**8**	**2**	**6**	**2**	**6**	**2**
mammillotegmental tract	**1**	**1**	**0**	**0**	**1**	**1**	**1**	**1**	**0**	**0**	**1**	**0**
mammilothalmic tract	**10**	**2**	**3**	**2**	**1**	**1**	**5**	**3**	**1**	**0**	**9**	**4**
Medial amygdalar nucleus	**1636**	**273**	**2895**	**302**	**281**	**59**	**822**	**239**	**937**	**141**	**641**	**78**
medial corticohypothalmic tract	**1**	**0**	**0**	**0**	**0**	**0**	**0**	**0**	**0**	**0**	**0**	**0**

medial forebrain bundle	**21**	**5**	**29**	**5**	**2**	**1**	**12**	**3**	**11**	**2**	**8**	**3**
Medial geniculate complex	**72**	**15**	**49**	**6**	**82**	**21**	**98**	**43**	**50**	**5**	**90**	**15**
Medial habenula	**13**	**6**	**16**	**6**	**11**	**4**	**9**	**5**	**19**	**4**	**18**	**5**
medial lemniscus	**25**	**4**	**33**	**10**	**17**	**4**	**19**	**7**	**14**	**2**	**25**	**5**
medial longitudinal fascicle	**2**	**1**	**0**	**0**	**1**	**1**	**1**	**1**	**1**	**0**	**1**	**0**
Medial mammillary nucleus	**3**	**1**	**10**	**2**	**1**	**0**	**2**	**1**	**7**	**2**	**2**	**1**
Medial preoptic area	**151**	**25**	**172**	**31**	**10**	**2**	**90**	**24**	**61**	**14**	**85**	**30**
Medial preoptic nucleus	**71**	**17**	**95**	**27**	**7**	**3**	**24**	**9**	**29**	**9**	**26**	**9**
Medial pretectal area	**6**	**3**	**4**	**1**	**7**	**3**	**3**	**1**	**3**	**1**	**5**	**2**
Medial septal nucleus	**17**	**4**	**2**	**1**	**6**	**2**	**11**	**5**	**1**	**1**	**14**	**9**
Medial terminal nucleus of the accessory optic tract	**2**	**0**	**6**	**1**	**3**	**1**	**3**	**0**	**3**	**0**	**2**	**1**
Medial vestibular nucleus	**55**	**12**	**37**	**8**	**95**	**11**	**108**	**58**	**66**	**14**	**81**	**9**
Median eminence	**16**	**6**	**27**	**5**	**6**	**3**	**12**	**4**	**24**	**11**	**12**	**5**
Median preoptic nucleus	**2**	**1**	**2**	**0**	**1**	**0**	**1**	**0**	**3**	**1**	**1**	**0**
Mediodorsal nucleus of	**74**	**21**	**7**	**2**	**6**	**1**	**20**	**6**	**8**	**2**	**18**	**9**

thalamus												
Medullary reticular nucleus	**7**	**2**	**1**	**0**	**13**	**4**	**12**	**5**	**1**	**0**	**10**	**5**
Midbrain reticular nucleus	**349**	**58**	**107**	**19**	**144**	**25**	**281**	**119**	**92**	**18**	**277**	**65**
Midbrain trigeminal nucleus	**2**	**1**	**0**	**0**	**2**	**1**	**2**	**1**	**0**	**0**	**4**	**1**
middle cerebellar peduncle	**109**	**20**	**203**	**17**	**101**	**8**	**103**	**14**	**172**	**17**	**91**	**18**
Motor nucleus of trigeminal	**8**	**3**	**4**	**1**	**12**	**3**	**17**	**7**	**4**	**1**	**11**	**3**
motor root of the trigeminal nerve	**8**	**2**	**16**	**3**	**5**	**1**	**5**	**2**	**14**	**2**	**5**	**1**
nigrostriatal tract	**13**	**3**	**11**	**4**	**8**	**2**	**17**	**7**	**7**	**2**	**13**	**2**
Nodulus (X)	**41**	**27**	**24**	**3**	**17**	**4**	**23**	**7**	**26**	**4**	**28**	**10**
Nucleus accumbens	**710**	**93**	**505**	**79**	**207**	**58**	**555**	**106**	**173**	**37**	**300**	**77**
Nucleus ambiguus	**0**	**0**	**3**	**1**	**1**	**0**	**0**	**0**	**1**	**0**	**1**	**0**
Nucleus incertus	**3**	**1**	**1**	**1**	**0**	**0**	**6**	**4**	**1**	**0**	**1**	**0**
Nucleus of Darkschewitsch	**3**	**2**	**1**	**0**	**2**	**1**	**2**	**1**	**0**	**0**	**1**	**0**
Nucleus of reunions	**29**	**9**	**5**	**4**	**12**	**5**	**19**	**6**	**7**	**2**	**12**	**5**
Nucleus of Roller	**0**	**0**	**0**	**0**	**0**	**0**	**0**	**0**	**0**	**0**	**0**	**0**
Nucleus of the brachium of the	**53**	**11**	**17**	**4**	**6**	**2**	**29**	**8**	**7**	**1**	**33**	**13**

inferior colliculus												
Nucleus of the lateral lemniscus	**76**	**12**	**208**	**35**	**47**	**6**	**68**	**37**	**69**	**7**	**69**	**17**
Nucleus of the lateral olfactory tract	**267**	**53**	**564**	**47**	**38**	**17**	**109**	**37**	**78**	**12**	**45**	**8**
Nucleus of the optic tract	**8**	**2**	**10**	**3**	**4**	**2**	**6**	**1**	**15**	**8**	**9**	**2**
Nucleus of the posterior commissure	**8**	**4**	**2**	**1**	**6**	**3**	**4**	**1**	**2**	**0**	**6**	**3**
Nucleus of the solitary tract	**11**	**3**	**7**	**4**	**10**	**2**	**14**	**6**	**6**	**2**	**9**	**3**
Nucleus of the trapezoid body	**2**	**1**	**28**	**8**	**2**	**1**	**2**	**1**	**8**	**3**	**2**	**1**
Nucleus prepositus	**7**	**3**	**3**	**2**	**6**	**3**	**2**	**1**	**4**	**2**	**4**	**1**
Nucleus raphe magnus	**3**	**1**	**13**	**4**	**3**	**1**	**3**	**1**	**3**	**1**	**3**	**1**
Nucleus raphe obscurus	**1**	**0**	**0**	**0**	**0**	**0**	**0**	**0**	**0**	**0**	**0**	**0**
Nucleus raphe pallidus	**4**	**1**	**15**	**5**	**1**	**1**	**2**	**1**	**5**	**1**	**3**	**2**
Nucleus raphe pontis	**1**	**0**	**0**	**0**	**1**	**0**	**1**	**1**	**0**	**0**	**1**	**0**
Nucleus sagulum	**2**	**1**	**4**	**2**	**1**	**0**	**2**	**1**	**2**	**1**	**3**	**1**
Nucleus x	**3**	**1**	**4**	**1**	**1**	**1**	**1**	**0**	**1**	**1**	**2**	**1**
Nucleus y	**1**	**0**	**1**	**0**	**1**	**0**	**2**	**1**	**1**	**0**	**2**	**1**

oculomotor nerve	**0**	**0**	**1**	**1**	**0**	**0**	**0**	**0**	**1**	**0**	**0**	**0**
Oculomotor nucleus	**0**	**0**	**0**	**0**	**0**	**0**	**0**	**0**	**0**	**0**	**0**	**0**
olfactory nerve layer of main olfactory bulb	**0**	**0**	**0**	**0**	**0**	**0**	**0**	**0**	**0**	**0**	**0**	**0**
Olfactory tubercle	**984**	**255**	**2580**	**375**	**139**	**52**	**588**	**201**	**272**	**58**	**151**	**42**
Olivary pretectal nucleus	**1**	**0**	**1**	**0**	**1**	**0**	**1**	**0**	**1**	**0**	**3**	**1**
optic chiasm	**13**	**8**	**46**	**14**	**14**	**6**	**10**	**3**	**15**	**3**	**14**	**4**
optic tract	**128**	**24**	**148**	**19**	**93**	**13**	**95**	**16**	**90**	**16**	**129**	**18**
Orbital area	**278**	**48**	**103**	**36**	**108**	**15**	**186**	**32**	**83**	**19**	**168**	**27**
Pallidum	**125**	**20**	**239**	**34**	**76**	**13**	**103**	**27**	**112**	**15**	**133**	**29**
Parabigeminal nucleus	**3**	**1**	**3**	**1**	**2**	**0**	**2**	**1**	**2**	**1**	**3**	**1**
Parabrachial nucleus	**69**	**9**	**43**	**7**	**60**	**13**	**72**	**26**	**41**	**9**	**61**	**12**
Paracentral nucleus	**1**	**0**	**0**	**0**	**1**	**0**	**1**	**1**	**0**	**0**	**3**	**1**
Parafascicular nucleus	**5**	**1**	**2**	**1**	**5**	**2**	**4**	**2**	**4**	**1**	**5**	**1**
Paraflocculus	**207**	**35**	**541**	**108**	**183**	**35**	**192**	**14**	**196**	**17**	**175**	**21**
Paragigantocellular reticular nucleus	**7**	**2**	**131**	**32**	**10**	**4**	**7**	**2**	**22**	**6**	**6**	**2**
Paramedian lobule	**59**	**6**	**44**	**9**	**65**	**13**	**47**	**9**	**50**	**3**	**71**	**15**

Parapyramidal nucleus	**0**	**0**	**35**	**10**	**1**	**1**	**0**	**0**	**5**	**2**	**1**	**1**
Parasolitary nucleus	**1**	**0**	**1**	**0**	**1**	**0**	**1**	**1**	**0**	**0**	**2**	**1**
Parastrial nucleus	**6**	**1**	**1**	**0**	**3**	**1**	**8**	**2**	**3**	**1**	**4**	**2**
Parasubiculum	**177**	**27**	**399**	**37**	**105**	**15**	**155**	**39**	**137**	**16**	**120**	**14**
Parasubthalamic nucleus	**88**	**16**	**106**	**19**	**19**	**6**	**77**	**18**	**50**	**10**	**27**	**5**
Parataenial nucleus	**5**	**4**	**0**	**0**	**0**	**0**	**15**	**9**	**0**	**0**	**2**	**1**
Paraventricular hypothalamic nucleus	**43**	**13**	**5**	**2**	**14**	**3**	**22**	**6**	**7**	**2**	**16**	**5**
Paraventricular nucleus of the thalamus	**155**	**49**	**8**	**2**	**14**	**4**	**82**	**24**	**9**	**3**	**58**	**28**
Parvicellular reticular nucleus	**41**	**11**	**93**	**21**	**64**	**18**	**52**	**13**	**42**	**7**	**49**	**25**
Pedunculopontine nucleus	**101**	**21**	**21**	**6**	**29**	**4**	**60**	**25**	**16**	**5**	**57**	**16**
Periaqueductal gray	**621**	**113**	**95**	**15**	**180**	**41**	**298**	**57**	**98**	**20**	**433**	**79**
Peripeduncular nucleus	**37**	**10**	**19**	**3**	**9**	**3**	**21**	**6**	**13**	**2**	**25**	**9**
Perireunensis nucleus	**15**	**4**	**1**	**0**	**3**	**1**	**9**	**3**	**2**	**1**	**8**	**5**
Perirhinal area	**191**	**68**	**574**	**61**	**26**	**3**	**78**	**17**	**248**	**36**	**28**	**8**
Periventricular hypothalamic	**57**	**7**	**110**	**12**	**28**	**4**	**40**	**7**	**45**	**8**	**61**	**17**

nucleus												
Piriform-amygdalar area	**847**	**112**	**1151**	**178**	**196**	**60**	**373**	**53**	**516**	**91**	**180**	**54**
Piriform area	**5846**	**784**	**15139**	**974**	**1078**	**318**	**2424**	**429**	**3804**	**534**	**1059**	**219**
Pontine central gray	**12**	**3**	**6**	**2**	**8**	**3**	**11**	**4**	**7**	**1**	**13**	**4**
Pontine gray	**274**	**109**	**828**	**107**	**45**	**9**	**95**	**50**	**464**	**134**	**77**	**20**
Pontine reticular nucleus	**134**	**33**	**180**	**30**	**156**	**22**	**175**	**65**	**67**	**15**	**157**	**27**
Posterior amygdalar nucleus	**888**	**105**	**1698**	**149**	**119**	**29**	**483**	**84**	**587**	**79**	**250**	**67**
Posterior auditory area	**119**	**30**	**349**	**82**	**22**	**13**	**23**	**6**	**83**	**15**	**33**	**13**
posterior commissure	**3**	**1**	**3**	**1**	**1**	**1**	**2**	**0**	**1**	**0**	**2**	**1**
Posterior complex of the thalamus	**40**	**26**	**12**	**3**	**48**	**17**	**62**	**49**	**17**	**5**	**80**	**30**
Posterior hypothalamic nucleus	**246**	**33**	**89**	**16**	**37**	**12**	**134**	**50**	**38**	**8**	**165**	**43**
Posterior limiting nucleus of the thalamus	**29**	**6**	**4**	**1**	**11**	**4**	**17**	**9**	**7**	**2**	**30**	**9**
Posterior pretectal nucleus	**3**	**1**	**1**	**1**	**2**	**1**	**2**	**1**	**2**	**1**	**7**	**2**
Posterodorsal preoptic nucleus	**1**	**1**	**2**	**1**	**0**	**0**	**1**	**0**	**0**	**0**	**1**	**0**
Posterolateral	**964**	**105**	**1017**	**100**	**310**	**116**	**725**	**76**	**435**	**77**	**394**	**86**

visual area												
posteromedial visual area	**1139**	**194**	**626**	**89**	**413**	**173**	**617**	**141**	**265**	**98**	**623**	**130**
Postpiriform transition area	**751**	**86**	**1757**	**117**	**115**	**40**	**476**	**47**	**715**	**74**	**140**	**38**
Postsubiculum	**95**	**16**	**48**	**10**	**59**	**11**	**84**	**12**	**88**	**15**	**131**	**32**
Precommissural nucleus	**19**	**6**	**3**	**1**	**4**	**2**	**6**	**2**	**3**	**1**	**14**	**5**
Prelimbic area	**283**	**65**	**40**	**15**	**45**	**7**	**168**	**43**	**20**	**5**	**81**	**22**
Preparasubthalamic nucleus	**3**	**1**	**2**	**1**	**2**	**1**	**5**	**1**	**1**	**0**	**1**	**0**
Presubiculum	**187**	**27**	**215**	**26**	**188**	**46**	**188**	**31**	**144**	**16**	**219**	**36**
Primary auditory area	**462**	**93**	**1056**	**230**	**61**	**30**	**79**	**14**	**379**	**67**	**80**	**23**
Primary motor area	**953**	**225**	**974**	**191**	**575**	**64**	**571**	**54**	**529**	**95**	**562**	**91**
Primary somatosensory area	**4079**	**825**	**6490**	**735**	**2109**	**294**	**3054**	**729**	**2040**	**274**	**2033**	**328**
Primary visual area	**9925**	**961**	**6861**	**897**	**3336**	**1306**	**4966**	**1111**	**2172**	**526**	**3220**	**768**
principal mammillary tract	**2**	**1**	**3**	**2**	**1**	**0**	**2**	**0**	**1**	**0**	**2**	**1**
Principal sensory nucleus of the trigeminal	**61**	**13**	**82**	**13**	**86**	**15**	**84**	**36**	**43**	**7**	**62**	**24**
pyramid	**5**	**2**	**19**	**4**	**7**	**2**	**6**	**1**	**5**	**1**	**9**	**4**
Pyramus (VIII)	**13**	**6**	**4**	**4**	**6**	**2**	**6**	**3**	**0**	**0**	**7**	**4**

Red nucleus	**30**	**11**	**4**	**2**	**26**	**9**	**56**	**38**	**7**	**3**	**27**	**7**
Reticular nucleus of the thalamus	**62**	**15**	**38**	**13**	**74**	**18**	**67**	**25**	**35**	**7**	**147**	**44**
Retrochiasmatic area	**17**	**5**	**119**	**16**	**1**	**0**	**4**	**1**	**54**	**13**	**7**	**3**
Retrosplenial area	**3608**	**584**	**3542**	**642**	**971**	**241**	**1967**	**384**	**1662**	**541**	**1313**	**218**
Rhomboid nucleus	**3**	**1**	**0**	**0**	**0**	**0**	**1**	**0**	**1**	**1**	**3**	**1**
root	**2749**	**198**	**2175**	**193**	**2678**	**226**	**2568**	**206**	**1953**	**146**	**3027**	**340**
Rostral linear nucleus raphe	**3**	**1**	**0**	**0**	**2**	**1**	**4**	**3**	**3**	**1**	**3**	**1**
rubrospinal tract	**33**	**4**	**62**	**11**	**20**	**5**	**25**	**11**	**17**	**3**	**30**	**6**
Secondary motor area	**795**	**270**	**1143**	**299**	**351**	**51**	**336**	**32**	**306**	**78**	**336**	**52**
sensory root of the trigeminal nerve	**31**	**8**	**44**	**8**	**27**	**5**	**22**	**4**	**27**	**4**	**35**	**9**
Septofimbrial nucleus	**4**	**1**	**3**	**1**	**2**	**1**	**4**	**2**	**5**	**1**	**4**	**1**
Septohippocampal nucleus	**1**	**1**	**0**	**0**	**0**	**0**	**1**	**0**	**0**	**0**	**1**	**0**
Simple lobule	**291**	**63**	**171**	**35**	**357**	**79**	**291**	**60**	**174**	**29**	**387**	**108**
solitary tract	**0**	**0**	**0**	**0**	**0**	**0**	**0**	**0**	**0**	**0**	**0**	**0**
Spinal nucleus of the trigeminal	**38**	**10**	**83**	**32**	**88**	**32**	**56**	**17**	**36**	**6**	**62**	**29**
spinal tract of the trigeminal nerve	**36**	**16**	**74**	**12**	**32**	**5**	**29**	**5**	**52**	**9**	**29**	**12**

Spinal vestibular nucleus	**31**	**9**	**24**	**5**	**47**	**13**	**50**	**14**	**25**	**2**	**45**	**9**
stria medullaris	**14**	**4**	**5**	**2**	**2**	**1**	**8**	**2**	**6**	**2**	**7**	**1**
stria terminalis	**47**	**11**	**36**	**5**	**19**	**5**	**42**	**11**	**35**	**6**	**51**	**20**
Striatum	**834**	**76**	**579**	**55**	**314**	**59**	**576**	**68**	**333**	**36**	**448**	**83**
Subceruleus nucleus	**0**	**0**	**1**	**0**	**0**	**0**	**1**	**0**	**0**	**0**	**1**	**0**
subependymal zone	**48**	**11**	**40**	**17**	**32**	**7**	**61**	**12**	**40**	**9**	**74**	**18**
Subfornical organ	**1**	**1**	**1**	**0**	**0**	**0**	**2**	**1**	**1**	**0**	**2**	**1**
Subgeniculate nucleus	**4**	**1**	**0**	**0**	**3**	**1**	**4**	**2**	**0**	**0**	**4**	**1**
Subiculum	**416**	**72**	**437**	**45**	**111**	**31**	**253**	**35**	**200**	**15**	**237**	**62**
Sublaterodorsal nucleus	**1**	**1**	**1**	**0**	**3**	**1**	**1**	**1**	**2**	**1**	**3**	**1**
Submedial nucleus of the thalamus	**2**	**1**	**2**	**1**	**1**	**0**	**3**	**1**	**5**	**2**	**4**	**1**
Subparafascicular area	**20**	**8**	**0**	**0**	**1**	**1**	**4**	**1**	**0**	**0**	**9**	**3**
Subparafascicular nucleus	**69**	**15**	**2**	**1**	**8**	**2**	**29**	**10**	**1**	**0**	**35**	**14**
Subparaventricular zone	**12**	**5**	**16**	**5**	**2**	**1**	**5**	**2**	**5**	**1**	**3**	**1**
Substantia innominata	**366**	**84**	**929**	**126**	**78**	**16**	**209**	**70**	**137**	**24**	**106**	**13**
Substantia nigra	**87**	**12**	**222**	**51**	**117**	**16**	**110**	**40**	**121**	**16**	**140**	**34**

Subthalamic nucleus	**14**	**5**	**11**	**3**	**17**	**4**	**25**	**17**	**5**	**1**	**21**	**5**
Superior central nucleus raphe	**21**	**8**	**2**	**1**	**11**	**3**	**19**	**8**	**7**	**3**	**18**	**8**
superior cerebelar peduncles	**11**	**5**	**3**	**2**	**9**	**2**	**7**	**4**	**7**	**3**	**8**	**2**
superior cerebellar peduncle decussation	**1**	**0**	**0**	**0**	**0**	**0**	**1**	**1**	**0**	**0**	**0**	**0**
Superior colliculus	**800**	**154**	**966**	**168**	**393**	**58**	**512**	**111**	**739**	**274**	**573**	**89**
superior colliculus commissure	**3**	**1**	**0**	**0**	**0**	**0**	**1**	**1**	**1**	**0**	**3**	**2**
Superior olivary complex	**48**	**19**	**306**	**41**	**22**	**5**	**20**	**7**	**100**	**14**	**20**	**4**
Superior vestibular nucleus	**14**	**4**	**8**	**2**	**21**	**3**	**28**	**12**	**15**	**3**	**21**	**5**
Supplemental somatosensory area	**1015**	**352**	**2543**	**439**	**450**	**113**	**339**	**58**	**814**	**126**	**379**	**108**
Suprachiasmatic nucleus	**2**	**1**	**17**	**3**	**2**	**1**	**1**	**0**	**9**	**4**	**1**	**0**
Supragenicula te nucleus	**31**	**5**	**8**	**2**	**13**	**4**	**18**	**7**	**12**	**2**	**37**	**6**
Supragenual nucleus	**0**	**0**	**0**	**0**	**0**	**0**	**0**	**0**	**0**	**0**	**0**	**0**
Supramammillary nucleus	**104**	**12**	**182**	**24**	**8**	**3**	**48**	**12**	**90**	**13**	**38**	**13**
supraoptic commissures	**6**	**2**	**10**	**2**	**3**	**1**	**5**	**1**	**7**	**1**	**6**	**1**

Supraoptic nucleus	**10**	**3**	**24**	**5**	**3**	**1**	**5**	**2**	**10**	**2**	**9**	**3**
Supratrigeminal nucleus	**10**	**2**	**5**	**2**	**11**	**1**	**15**	**6**	**3**	**1**	**10**	**3**
Taenia tecta	**244**	**29**	**301**	**77**	**36**	**8**	**182**	**44**	**22**	**4**	**55**	**13**
Tegmental reticular nucleus	**31**	**6**	**58**	**14**	**16**	**6**	**24**	**11**	**21**	**5**	**18**	**5**
Temporal association areas	**1186**	**213**	**2388**	**325**	**125**	**54**	**396**	**70**	**835**	**132**	**294**	**90**
third ventricle	**196**	**46**	**205**	**62**	**122**	**23**	**234**	**76**	**166**	**20**	**292**	**80**
trapezoid body	**20**	**5**	**59**	**10**	**25**	**8**	**20**	**3**	**35**	**4**	**32**	**7**
Triangular nucleus of septum	**8**	**2**	**11**	**3**	**4**	**2**	**9**	**4**	**13**	**2**	**9**	**2**
trochlear nerve	**2**	**1**	**0**	**0**	**2**	**1**	**2**	**1**	**1**	**1**	**2**	**1**
Trochlear nucleus	**0**	**0**	**0**	**0**	**0**	**0**	**0**	**0**	**0**	**0**	**0**	**0**
Tuberal nucleus	**130**	**24**	**592**	**49**	**40**	**8**	**65**	**9**	**232**	**29**	**66**	**9**
Tuberomammillary nucleus	**38**	**7**	**129**	**10**	**21**	**2**	**33**	**5**	**55**	**8**	**34**	**6**
uncinate fascicle	**2**	**1**	**1**	**0**	**1**	**0**	**2**	**1**	**1**	**1**	**2**	**1**
Uvula (IX)	**23**	**9**	**2**	**1**	**8**	**2**	**9**	**4**	**4**	**1**	**7**	**2**
Vascular organ of the lamina terminalis	**0**	**0**	**1**	**0**	**1**	**0**	**1**	**0**	**0**	**0**	**2**	**1**
Ventral anterior-lateral complex of the thalamus	**18**	**13**	**2**	**1**	**25**	**12**	**33**	**31**	**7**	**3**	**47**	**18**

Ventral auditory area	**583**	**94**	**1111**	**176**	**59**	**25**	**133**	**22**	**410**	**65**	**92**	**31**
Ventral cochlear nucleus	**91**	**32**	**264**	**57**	**52**	**8**	**50**	**7**	**161**	**33**	**58**	**19**
ventral hippocampal commissure	**3**	**1**	**1**	**1**	**1**	**0**	**3**	**1**	**1**	**0**	**4**	**2**
Ventral medial nucleus of the thalamus	**17**	**3**	**2**	**1**	**12**	**6**	**16**	**9**	**3**	**2**	**37**	**13**
Ventral part of the lateral geniculate complex	**249**	**71**	**6**	**2**	**132**	**33**	**209**	**56**	**10**	**3**	**201**	**51**
Ventral posterolateral nucleus of the thalamus	**34**	**23**	**5**	**2**	**134**	**67**	**129**	**120**	**8**	**4**	**144**	**53**
Ventral posteromedial nucleus of the thalamus	**187**	**153**	**9**	**3**	**463**	**226**	**429**	**408**	**18**	**7**	**529**	**223**
Ventral premammillary nucleus	**59**	**11**	**130**	**15**	**1**	**0**	**27**	**13**	**41**	**11**	**19**	**5**
ventral spinocerebellar tract	**18**	**4**	**47**	**7**	**18**	**3**	**24**	**5**	**21**	**3**	**32**	**9**
Ventral tegmental area	**56**	**7**	**96**	**22**	**12**	**3**	**29**	**8**	**32**	**7**	**29**	**8**
ventral tegmental decussation	**6**	**3**	**0**	**0**	**1**	**1**	**5**	**3**	**1**	**1**	**3**	**1**
Ventral tegmental nucleus	**0**	**0**	**0**	**0**	**0**	**0**	**0**	**0**	**0**	**0**	**0**	**0**

Ventrolateral preoptic nucleus	**19**	**10**	**34**	**11**	**2**	**1**	**12**	**4**	**14**	**3**	**13**	**6**
Ventromedial hypothalamic nucleus	**82**	**13**	**242**	**31**	**4**	**1**	**42**	**12**	**81**	**17**	**46**	**12**
vestibular nerve	**21**	**5**	**28**	**4**	**11**	**3**	**16**	**2**	**34**	**8**	**17**	**10**
Visceral area	**415**	**81**	**1040**	**113**	**81**	**24**	**232**	**58**	**386**	**54**	**120**	**32**
Zona incerta	**114**	**20**	**31**	**10**	**121**	**29**	**139**	**74**	**34**	**8**	**189**	**35**

Supplementary table 2. cFos cell counts from ClearMap automatic cell detection (Chapter 6: Phenotypic assessment and neural activity mapping of MEIS1 point mutation mice)

n=5-7 per group

Brain region	$Meis1^{R272H/R272H}$ ZT0		$Meis1^{R272H/R272H}$ ZT12		WT ZT0		WT ZT12	
	Mean	SEM	Mean	SEM	Mean	SEM	Mean	SEM
Abducens nucleus	0	0	1	1	0	0	0	0
Accessory facial motor nucleus	0	0	0	0	0	0	0	0
Accessory olfactory bulb	1	1	0	0		0	0	0
Accessory supraoptic group	1	0	1	1	1	1	0	0
Agranular insular area	571	110	555	116	405	66	538	45
alveus	215	23	237	28	228	34	274	30
amygdalar capsule	32	6	44	7	27	6	61	13
Anterior amygdalar area	140	35	143	20	71	10	85	8
Anterior cingulate area	254	28	376	52	265	47	356	39
anterior commissure	15	4	13	2	10	2	11	2
Anterior hypothalamic nucleus	69	19	100	35	56	18	77	27

Anterior olfactory nucleus	**83**	**27**	**167**	**30**	**58**	**14**	**94**	**25**
Anterior pretectal nucleus	**43**	**12**	**193**	**80**	**80**	**15**	**55**	**22**
Anterior tegmental nucleus	**0**	**0**	**2**	**1**	**1**	**0**	**1**	**0**
Anterodorsal nucleus	**9**	**3**	**35**	**12**	**13**	**5**	**16**	**7**
Anterodorsal preoptic nucleus	**10**	**4**	**43**	**9**	**8**	**7**	**22**	**6**
Anterolateral visual area	**174**	**46**	**231**	**28**	**148**	**47**	**249**	**89**
Anteromedial nucleus	**6**	**1**	**19**	**8**	**7**	**3**	**4**	**1**
Anteromedial visual area	**372**	**78**	**498**	**52**	**359**	**49**	**319**	**78**
Anteroventral nucleus of thalamus	**10**	**3**	**28**	**11**	**11**	**5**	**18**	**11**
Anteroventral periventricular nucleus	**6**	**2**	**22**	**7**	**15**	**5**	**15**	**6**
Anteroventral preoptic nucleus	**2**	**1**	**27**	**7**	**4**	**2**	**15**	**4**
arbor vitae	**508**	**106**	**346**	**36**	**504**	**48**	**346**	**68**
Arcuate hypothalamic nucleus	**17**	**4**	**65**	**17**	**21**	**10**	**43**	**6**
Area postrema	**6**	**1**	**6**	**1**	**6**	**3**	**2**	**1**

Barrington's nucleus	**2**	**1**	**4**	**1**	**1**	**0**	**1**	**0**
Basolateral amygdalar nucleus	**544**	**83**	**588**	**64**	**315**	**60**	**630**	**119**
Basomedial amygdalar nucleus	**767**	**144**	**801**	**96**	**435**	**79**	**709**	**145**
Bed nuclei of the stria terminalis	**106**	**28**	**91**	**14**	**49**	**9**	**68**	**17**
Bed nucleus of the accessory olfactory tract	**6**	**2**	**10**	**3**	**6**	**1**	**8**	**3**
Bed nucleus of the anterior commissure	**0**	**0**	**0**	**0**	**0**	**0**	**0**	**0**
brachium of the inferior colliculus	**56**	**7**	**47**	**10**	**48**	**4**	**59**	**18**
brachium of the superior colliculus	**51**	**6**	**51**	**6**	**71**	**10**	**40**	**12**
Caudoputamen	**1195**	**499**	**2722**	**592**	**1639**	**629**	**2110**	**256**
Central amygdalar nucleus	**299**	**55**	**260**	**68**	**164**	**30**	**181**	**25**
central canal	**1**	**1**	**1**	**0**	**0**	**0**	**1**	**1**
Central lateral nucleus of the thalamus	**9**	**3**	**39**	**14**	**11**	**4**	**9**	**5**
Central linear nucleus raphe	**2**	**1**	**4**	**2**	**2**	**1**	**3**	**1**
Central medial nucleus of the thalamus	**4**	**1**	**12**	**3**	**4**	**1**	**4**	**1**

cerebal peduncle	**202**	**15**	**146**	**19**	**194**	**17**	**136**	**35**
cerebellar commissure	**3**	**2**	**2**	**2**	**6**	**5**	**1**	**0**
cerebral aqueduct	**139**	**26**	**90**	**11**	**120**	**29**	**105**	**21**
choroid plexus	**675**	**30**	**652**	**72**	**691**	**63**	**767**	**126**
cingulum bundle	**77**	**31**	**117**	**22**	**57**	**14**	**76**	**21**
Claustrum	**146**	**42**	**237**	**40**	**74**	**17**	**235**	**46**
columns of the fornix	**10**	**2**	**13**	**2**	**12**	**2**	**11**	**2**
Copula pyramidis	**115**	**31**	**47**	**7**	**130**	**27**	**60**	**21**
corpus callosum	**143**	**28**	**190**	**33**	**175**	**23**	**164**	**15**
Cortical amygdalar area	**1034**	**263**	**732**	**79**	**711**	**86**	**553**	**81**
corticospinal tract	**3**	**1**	**4**	**2**	**4**	**2**	**4**	**2**
crossed tectospinal pathway	**4**	**1**	**15**	**6**	**8**	**3**	**9**	**3**
Crus 1	**499**	**53**	**379**	**35**	**474**	**77**	**406**	**77**
Crus 2	**208**	**27**	**112**	**18**	**194**	**25**	**116**	**34**
cuneate fascicle	**1**	**0**	**0**	**0**	**3**	**2**	**1**	**0**
Cuneate nucleus	**15**	**3**	**8**	**2**	**14**	**4**	**12**	**5**
Cuneiform nucleus	**59**	**20**	**86**	**16**	**70**	**10**	**48**	**14**

Declive (VI)	**203**	**31**	**144**	**20**	**231**	**48**	**155**	**43**
Dentate gyrus	**663**	**86**	**949**	**89**	**828**	**141**	**942**	**209**
Dentate nucleus	**50**	**15**	**52**	**14**	**60**	**11**	**40**	**13**
Diagonal band nucleus	**49**	**12**	**60**	**16**	**52**	**10**	**34**	**12**
doral tegmental decussation	**0**	**0**	**1**	**0**	**0**	**0**	**0**	**0**
dorsal acoustic stria	**0**	**0**	**0**	**0**	**1**	**0**	**1**	**0**
Dorsal auditory area	**91**	**20**	**59**	**12**	**74**	**12**	**113**	**33**
Dorsal cochlear nucleus	**88**	**16**	**65**	**10**	**103**	**8**	**71**	**15**
dorsal fornix	**0**	**0**	**0**	**0**	**0**	**0**	**0**	**0**
dorsal hippocampal commissure	**22**	**6**	**29**	**7**	**37**	**8**	**21**	**6**
dorsal limb	**0**	**0**	**0**	**0**	**0**	**0**	**0**	**0**
Dorsal motor nucleus of the vagus nerve	**4**	**1**	**5**	**1**	**6**	**1**	**9**	**8**
Dorsal nucleus raphe	**3**	**2**	**13**	**5**	**4**	**1**	**3**	**1**
Dorsal peduncular area	**19**	**6**	**21**	**3**	**13**	**3**	**16**	**4**
Dorsal premammillary nucleus	**23**	**10**	**47**	**15**	**17**	**6**	**42**	**12**

dorsal spinocerebellar tract	**3**	**1**	**9**	**4**	**10**	**5**	**7**	**3**
Dorsal tegmental nucleus	**2**	**1**	**6**	**3**	**1**	**0**	**1**	**1**
Dorsal terminal nucleus of the accessory optic tract	**4**	**1**	**3**	**1**	**5**	**2**	**3**	**1**
Dorsomedial nucleus of the hypothalamus	**52**	**15**	**135**	**30**	**55**	**14**	**90**	**16**
Ectorhinal area/Layer 1	**27**	**7**	**22**	**4**	**27**	**4**	**38**	**6**
Ectorhinal area/Layer 2/3	**31**	**10**	**36**	**8**	**16**	**5**	**55**	**15**
Ectorhinal area/Layer 5	**72**	**14**	**136**	**21**	**52**	**12**	**166**	**33**
Ectorhinal area/Layer 6a	**95**	**12**	**146**	**23**	**71**	**17**	**203**	**46**
Ectorhinal area/Layer 6b	**11**	**3**	**14**	**3**	**17**	**4**	**20**	**6**
Edinger-Westphal nucleus	**3**	**2**	**2**	**1**	**5**	**2**	**0**	**0**
Endopiriform nucleus	**488**	**50**	**781**	**121**	**383**	**68**	**776**	**151**
Entorhinal area	**1087**	**167**	**1373**	**159**	**777**	**98**	**1699**	**290**
external capsule	**101**	**6**	**165**	**22**	**119**	**23**	**194**	**37**
External cuneate nucleus	**16**	**3**	**17**	**6**	**18**	**5**	**7**	**1**

external medullary lamina of the thalamus	**15**	**6**	**25**	**3**	**14**	**6**	**10**	**4**
Facial motor nucleus	**17**	**1**	**17**	**5**	**18**	**4**	**22**	**13**
facial nerve	**2**	**1**	**4**	**2**	**3**	**1**	**3**	**1**
fasciculus retroflexus	**4**	**1**	**5**	**2**	**4**	**1**	**2**	**1**
Fasciola cinerea	**6**	**2**	**3**	**1**	**5**	**2**	**6**	**2**
Fastigial nucleus	**28**	**6**	**24**	**9**	**15**	**5**	**9**	**3**
fiber tracts	**359**	**5**	**357**	**21**	**361**	**42**	**303**	**43**
Field CA1	**936**	**109**	**1088**	**142**	**1052**	**249**	**1568**	**225**
Field CA2	**72**	**11**	**91**	**7**	**80**	**19**	**102**	**19**
Field CA3	**885**	**136**	**1123**	**117**	**1083**	**253**	**1051**	**96**
Fields of Forel	**12**	**3**	**51**	**18**	**27**	**7**	**17**	**5**
fimbria	**80**	**12**	**60**	**7**	**83**	**18**	**114**	**41**
Flocculus	**190**	**41**	**127**	**22**	**152**	**21**	**168**	**34**
Folium-tuber vermis (VII)	**55**	**16**	**45**	**15**	**68**	**9**	**28**	**5**
fourth ventricle	**325**	**25**	**307**	**42**	**440**	**82**	**320**	**76**
Fundus of striatum	**48**	**11**	**46**	**6**	**26**	**3**	**41**	**2**
genu of corpus callosum	**8**	**4**	**14**	**5**	**11**	**3**	**16**	**9**

genu of the facial nerve	**0**	**0**	**1**	**1**	**1**	**0**	**1**	**0**
Gigantocellular reticular nucleus	**17**	**4**	**83**	**33**	**55**	**12**	**29**	**12**
Globus pallidus	**44**	**9**	**64**	**12**	**51**	**15**	**46**	**9**
Gracile nucleus	**11**	**6**	**2**	**1**	**8**	**3**	**3**	**2**
Gustatory areas	**95**	**14**	**119**	**34**	**105**	**29**	**126**	**19**
habenular commissure	**5**	**2**	**3**	**1**	**8**	**4**	**8**	**3**
Hypoglossal nucleus	**3**	**1**	**3**	**2**	**9**	**3**	**2**	**1**
Induseum griseum	**17**	**8**	**19**	**5**	**15**	**6**	**18**	**4**
inferior cerebellar peduncle	**33**	**5**	**30**	**4**	**32**	**5**	**33**	**7**
Inferior colliculus	**1352**	**202**	**1197**	**153**	**1335**	**141**	**1199**	**336**
inferior colliculus commissure	**2**	**1**	**1**	**0**	**2**	**2**	**2**	**1**
Inferior olivary complex	**3**	**1**	**2**	**1**	**6**	**2**	**6**	**4**
Inferior salivatory nucleus	**1**	**0**	**1**	**0**	**0**	**0**	**0**	**0**
Infracerebellar nucleus	**1**	**1**	**3**	**1**	**3**	**1**	**0**	**0**
Infralimbic area	**64**	**21**	**83**	**16**	**37**	**10**	**68**	**23**
Interanterodorsal nucleus of the	**3**	**1**	**15**	**6**	**2**	**1**	**5**	**3**

thalamus								
Interanteromedial nucleus of the thalamus	**1**	**0**	**3**	**1**	**2**	**0**	**2**	**1**
Intercalated amygdalar nucleus	**66**	**10**	**61**	**9**	**34**	**7**	**46**	**12**
Interfascicular nucleus raphe	**8**	**3**	**11**	**2**	**11**	**2**	**6**	**1**
Intergeniculate leaflet of the lateral geniculate complex	**32**	**6**	**36**	**7**	**32**	**11**	**33**	**11**
Intermediate reticular nucleus	**32**	**5**	**54**	**20**	**77**	**21**	**46**	**22**
Intermediodorsal nucleus of the thalamus	**1**	**1**	**2**	**0**	**1**	**0**	**2**	**1**
internal capsule	**67**	**13**	**96**	**11**	**72**	**12**	**61**	**12**
Interpeduncular nucleus	**2**	**1**	**2**	**1**	**1**	**1**	**3**	**1**
Interposed nucleus	**58**	**16**	**60**	**12**	**94**	**15**	**33**	**11**
Interstitial nucleus of Cajal	**1**	**0**	**5**	**3**	**1**	**1**	**1**	**0**
Kolliker-Fuse subnucleus	**29**	**7**	**45**	**8**	**42**	**11**	**29**	**13**
Lateral amygdalar nucleus	**252**	**27**	**256**	**36**	**202**	**64**	**362**	**63**
Lateral dorsal nucleus of thalamus	**93**	**39**	**248**	**66**	**133**	**56**	**82**	**26**

Lateral habenula	**8**	**3**	**21**	**7**	**12**	**3**	**8**	**4**
Lateral hypothalamic area	**414**	**87**	**492**	**83**	**448**	**105**	**343**	**56**
lateral lemniscus	**123**	**15**	**129**	**14**	**118**	**11**	**114**	**24**
Lateral mammillary nucleus	**10**	**2**	**9**	**3**	**8**	**2**	**8**	**2**
lateral olfactory tract	**45**	**8**	**41**	**11**	**55**	**13**	**39**	**13**
Lateral posterior nucleus of the thalamus	**82**	**22**	**160**	**36**	**130**	**25**	**75**	**22**
Lateral preoptic area	**33**	**9**	**39**	**7**	**28**	**7**	**31**	**4**
lateral recess	**219**	**27**	**225**	**23**	**235**	**45**	**214**	**14**
Lateral reticular nucleus	**24**	**12**	**36**	**18**	**16**	**8**	**10**	**5**
Lateral septal nucleus	**157**	**75**	**171**	**39**	**104**	**12**	**123**	**43**
Lateral terminal nucleus of the accessory optic tract	**7**	**2**	**5**	**1**	**2**	**1**	**5**	**2**
lateral ventricle	**1203**	**81**	**894**	**115**	**896**	**70**	**1257**	**324**
Lateral vestibular nucleus	**42**	**20**	**55**	**8**	**51**	**14**	**36**	**17**
Lateral visual area	**453**	**134**	**680**	**83**	**324**	**97**	**636**	**193**
Laterodorsal tegmental nucleus	**7**	**3**	**17**	**6**	**9**	**3**	**6**	**2**

Linear nucleus of the medulla	**3**	**2**	**8**	**3**	**7**	**3**	**3**	**1**
Lingula (I)	**9**	**3**	**4**	**1**	**15**	**10**	**7**	**4**
Lobule II	**111**	**33**	**72**	**15**	**96**	**23**	**67**	**23**
Lobule III	**208**	**50**	**169**	**42**	**183**	**28**	**136**	**46**
Lobules IV-V	**567**	**80**	**548**	**70**	**571**	**77**	**472**	**131**
Locus ceruleus	**1**	**0**	**3**	**1**	**2**	**1**	**1**	**1**
Magnocellular nucleus	**52**	**11**	**40**	**9**	**31**	**11**	**30**	**7**
Magnocellular reticular nucleus	**1**	**0**	**7**	**4**	**4**	**2**	**9**	**4**
Main olfactory bulb	**36**	**17**	**21**	**6**	**35**	**9**	**29**	**10**
mammillary peduncle	**9**	**2**	**9**	**2**	**6**	**1**	**6**	**2**
mammillotegmental tract	**2**	**1**	**1**	**1**	**0**	**0**	**1**	**0**
mammilothalmic tract	**3**	**0**	**21**	**6**	**6**	**2**	**15**	**5**
Medial amygdalar nucleus	**672**	**135**	**747**	**95**	**493**	**68**	**509**	**70**
medial corticohypothalmic tract	**0**	**0**	**0**	**0**	**0**	**0**	**0**	**0**
medial forebrain bundle	**11**	**3**	**10**	**3**	**8**	**3**	**8**	**2**
Medial geniculate	**124**	**36**	**140**	**20**	**166**	**47**	**94**	**36**

complex								
Medial habenula	**26**	**8**	**11**	**2**	**19**	**6**	**24**	**8**
medial lemniscus	**32**	**7**	**67**	**20**	**55**	**8**	**39**	**12**
medial longitudinal fascicle	**2**	**1**	**6**	**3**	**3**	**1**	**2**	**1**
Medial mammillary nucleus	**2**	**1**	**2**	**1**	**4**	**2**	**1**	**0**
Medial preoptic area	**27**	**5**	**157**	**36**	**32**	**14**	**96**	**26**
Medial preoptic nucleus	**10**	**2**	**62**	**28**	**13**	**3**	**27**	**7**
Medial pretectal area	**4**	**1**	**6**	**1**	**4**	**1**	**2**	**1**
Medial septal nucleus	**22**	**5**	**22**	**4**	**17**	**5**	**9**	**3**
Medial terminal nucleus of the accessory optic tract	**6**	**1**	**4**	**1**	**6**	**2**	**3**	**1**
Medial vestibular nucleus	**155**	**37**	**293**	**79**	**259**	**26**	**150**	**64**
Median eminence	**11**	**3**	**10**	**4**	**11**	**6**	**10**	**4**
Median preoptic nucleus	**1**	**1**	**1**	**1**	**1**	**1**	**2**	**1**
Mediodorsal nucleus of thalamus	**22**	**6**	**62**	**15**	**25**	**8**	**26**	**10**
Medullary reticular nucleus	**21**	**5**	**14**	**5**	**28**	**10**	**20**	**14**

Midbrain reticular nucleus	**282**	**64**	**697**	**174**	**403**	**65**	**307**	**94**
Midbrain trigeminal nucleus	**3**	**2**	**7**	**1**	**5**	**2**	**4**	**2**
middle cerebellar peduncle	**149**	**18**	**109**	**19**	**163**	**20**	**113**	**35**
Motor nucleus of trigeminal	**28**	**5**	**42**	**12**	**50**	**12**	**21**	**8**
motor root of the trigeminal nerve	**7**	**2**	**5**	**1**	**7**	**2**	**5**	**2**
nigrostriatal tract	**20**	**3**	**25**	**4**	**18**	**5**	**15**	**2**
Nodulus (X)	**99**	**19**	**56**	**12**	**125**	**42**	**67**	**28**
Nucleus accumbens	**173**	**36**	**210**	**36**	**160**	**25**	**150**	**31**
Nucleus ambiguus	**2**	**1**	**1**	**0**	**1**	**1**	**1**	**1**
Nucleus incertus	**2**	**1**	**13**	**4**	**3**	**1**	**3**	**2**
Nucleus of Darkschewitsch	**2**	**1**	**7**	**2**	**4**	**1**	**3**	**2**
Nucleus of reunions	**21**	**4**	**26**	**8**	**13**	**4**	**18**	**5**
Nucleus of Roller	**0**	**0**	**0**	**0**	**1**	**1**	**0**	**0**
Nucleus of the brachium of the inferior colliculus	**10**	**3**	**16**	**7**	**9**	**2**	**15**	**7**
Nucleus of the lateral lemniscus	**115**	**25**	**188**	**35**	**161**	**23**	**100**	**40**

Nucleus of the lateral olfactory tract	**92**	**24**	**90**	**13**	**48**	**15**	**59**	**15**
Nucleus of the optic tract	**23**	**8**	**38**	**12**	**37**	**9**	**12**	**4**
Nucleus of the posterior commissure	**4**	**2**	**16**	**5**	**10**	**2**	**7**	**4**
Nucleus of the solitary tract	**29**	**4**	**44**	**7**	**38**	**11**	**35**	**22**
Nucleus of the trapezoid body	**5**	**4**	**7**	**4**	**6**	**3**	**1**	**1**
Nucleus prepositus	**2**	**1**	**15**	**7**	**10**	**3**	**7**	**3**
Nucleus raphe magnus	**6**	**2**	**7**	**3**	**8**	**1**	**7**	**3**
Nucleus raphe obscurus	**0**	**0**	**0**	**0**	**2**	**1**	**1**	**1**
Nucleus raphe pallidus	**4**	**4**	**6**	**2**	**6**	**3**	**3**	**3**
Nucleus raphe pontis	**2**	**0**	**4**	**2**	**2**	**1**	**0**	**0**
Nucleus sagulum	**5**	**2**	**4**	**1**	**7**	**1**	**4**	**2**
Nucleus x	**3**	**1**	**4**	**1**	**3**	**1**	**1**	**1**
Nucleus y	**4**	**2**	**4**	**1**	**4**	**1**	**3**	**1**
oculomotor nerve	**1**	**0**	**0**	**0**	**0**	**0**	**0**	**0**
Oculomotor nucleus	**1**	**1**	**5**	**2**	**2**	**1**	**2**	**1**

olfactory nerve layer of main olfactory bulb	**1**	**0**	**0**	**0**	**0**	**0**	**0**	**0**
Olfactory tubercle	**274**	**83**	**176**	**41**	**174**	**59**	**154**	**36**
Olivary pretectal nucleus	**2**	**1**	**8**	**4**	**7**	**4**	**4**	**1**
optic chiasm	**10**	**3**	**10**	**5**	**10**	**3**	**7**	**3**
optic tract	**123**	**11**	**69**	**6**	**116**	**25**	**65**	**14**
Orbital area	**142**	**29**	**199**	**26**	**98**	**12**	**113**	**21**
Pallidum	**82**	**11**	**108**	**10**	**80**	**11**	**54**	**7**
Parabigeminal nucleus	**4**	**1**	**1**	**0**	**3**	**1**	**2**	**1**
Parabrachial nucleus	**92**	**32**	**172**	**20**	**117**	**20**	**112**	**50**
Paracentral nucleus	**3**	**1**	**10**	**5**	**4**	**2**	**3**	**2**
Parafascicular nucleus	**7**	**3**	**32**	**14**	**9**	**3**	**9**	**6**
Paraflocculus	**214**	**35**	**186**	**32**	**286**	**99**	**188**	**39**
Paragigantocellular reticular nucleus	**14**	**2**	**32**	**11**	**19**	**4**	**28**	**14**
Paramedian lobule	**127**	**33**	**79**	**16**	**144**	**26**	**88**	**22**
Parapyramidal nucleus	**0**	**0**	**2**	**1**	**2**	**1**	**3**	**2**
Parasolitary nucleus	**3**	**1**	**3**	**1**	**2**	**1**	**2**	**1**

Parastrial nucleus	**8**	**4**	**11**	**2**	**5**	**3**	**4**	**2**
Parasubiculum	**185**	**40**	**119**	**21**	**126**	**18**	**180**	**43**
Parasubthalamic nucleus	**78**	**11**	**68**	**13**	**77**	**21**	**31**	**5**
Parataenial nucleus	**12**	**5**	**10**	**6**	**3**	**3**	**1**	**1**
Paraventricular hypothalamic nucleus	**44**	**9**	**49**	**15**	**44**	**10**	**28**	**6**
Paraventricular nucleus of the thalamus	**113**	**21**	**123**	**20**	**102**	**25**	**92**	**25**
Parvicellular reticular nucleus	**94**	**12**	**85**	**21**	**108**	**18**	**67**	**30**
Pedunculopontine nucleus	**45**	**15**	**135**	**23**	**71**	**23**	**65**	**21**
Periaqueductal gray	**404**	**96**	**860**	**180**	**509**	**86**	**587**	**135**
Peripeduncular nucleus	**9**	**3**	**14**	**5**	**11**	**2**	**13**	**4**
Perireunensis nucleus	**5**	**2**	**20**	**6**	**8**	**2**	**14**	**4**
Perirhinal area	**35**	**6**	**60**	**12**	**37**	**5**	**54**	**4**
Periventricular hypothalamic nucleus	**54**	**8**	**75**	**22**	**63**	**12**	**74**	**18**
Piriform-amygdalar area	**358**	**100**	**240**	**23**	**296**	**76**	**211**	**52**

Piriform area	**1903**	**300**	**2021**	**282**	**1472**	**330**	**1802**	**385**
Pontine central gray	**21**	**6**	**34**	**11**	**25**	**9**	**22**	**7**
Pontine gray	**185**	**37**	**292**	**58**	**238**	**52**	**109**	**28**
Pontine reticular nucleus	**199**	**23**	**535**	**158**	**308**	**72**	**245**	**61**
Posterior amygdalar nucleus	**287**	**76**	**192**	**44**	**184**	**28**	**183**	**34**
Posterior auditory area	**32**	**7**	**24**	**4**	**18**	**4**	**44**	**14**
posterior commissure	**1**	**1**	**3**	**1**	**2**	**1**	**2**	**1**
Posterior complex of the thalamus	**69**	**32**	**201**	**67**	**102**	**40**	**44**	**17**
Posterior hypothalamic nucleus	**144**	**27**	**328**	**50**	**119**	**28**	**243**	**41**
Posterior limiting nucleus of the thalamus	**25**	**7**	**32**	**6**	**29**	**8**	**20**	**7**
Posterior pretectal nucleus	**4**	**2**	**26**	**9**	**17**	**7**	**9**	**4**
Posterodorsal preoptic nucleus	**0**	**0**	**1**	**0**	**0**	**0**	**0**	**0**
Posterolateral visual area	**589**	**141**	**714**	**49**	**310**	**84**	**603**	**131**
posteromedial visual area	**614**	**133**	**799**	**71**	**617**	**72**	**584**	**165**

Postpiriform transition area	**175**	**30**	**120**	**15**	**142**	**27**	**139**	**42**
Postsubiculum	**122**	**21**	**77**	**9**	**133**	**20**	**118**	**27**
Precommissural nucleus	**7**	**2**	**19**	**4**	**7**	**2**	**10**	**4**
Prelimbic area	**99**	**35**	**130**	**30**	**48**	**11**	**109**	**36**
Preparasubthalamic nucleus	**5**	**1**	**5**	**1**	**5**	**2**	**2**	**0**
Presubiculum	**208**	**25**	**124**	**23**	**213**	**29**	**217**	**44**
Primary auditory area	**137**	**27**	**54**	**12**	**74**	**15**	**149**	**58**
Primary motor area	**985**	**116**	**820**	**174**	**805**	**103**	**692**	**164**
Primary somatosensory area	**3768**	**456**	**3330**	**520**	**3262**	**252**	**2728**	**492**
Primary visual area	**4443**	**1264**	**5899**	**452**	**3540**	**824**	**3989**	**960**
principal mammillary tract	**3**	**2**	**4**	**1**	**4**	**2**	**2**	**0**
Principal sensory nucleus of the trigeminal	**139**	**37**	**205**	**40**	**194**	**51**	**109**	**50**
pyramid	**7**	**2**	**13**	**5**	**32**	**7**	**15**	**9**
pyramidal decussation	**1**	**0**	**0**	**0**	**1**	**1**	**1**	**0**
Pyramus (VIII)	**53**	**13**	**31**	**11**	**57**	**14**	**28**	**10**
Red nucleus	**39**	**16**	**261**	**101**	**95**	**32**	**67**	**28**

Reticular nucleus of the thalamus	**106**	**34**	**206**	**25**	**135**	**41**	**100**	**36**
Retrochiasmatic area	**4**	**2**	**10**	**6**	**7**	**3**	**13**	**7**
Retrosplenial area	**1911**	**331**	**2080**	**206**	**1822**	**156**	**1736**	**251**
Rhomboid nucleus	**3**	**1**	**4**	**1**	**2**	**1**	**2**	**1**
root	**3368**	**184**	**3138**	**220**	**3555**	**236**	**3095**	**359**
Rostral linear nucleus raphe	**6**	**2**	**9**	**4**	**9**	**1**	**1**	**0**
rubrospinal tract	**29**	**4**	**53**	**10**	**39**	**5**	**38**	**10**
Secondary motor area	**572**	**99**	**556**	**129**	**508**	**109**	**550**	**140**
sensory root of the trigeminal nerve	**52**	**13**	**42**	**8**	**60**	**13**	**45**	**17**
Septofimbrial nucleus	**6**	**1**	**4**	**1**	**3**	**1**	**5**	**2**
Septohippocampal nucleus	**1**	**0**	**0**	**0**	**1**	**0**	**0**	**0**
Simple lobule	**708**	**119**	**651**	**45**	**611**	**154**	**570**	**145**
solitary tract	**0**	**0**	**0**	**0**	**0**	**0**	**1**	**0**
Spinal nucleus of the trigeminal	**116**	**23**	**100**	**17**	**168**	**23**	**109**	**59**
spinal tract of the trigeminal nerve	**44**	**9**	**48**	**6**	**75**	**6**	**44**	**21**
Spinal vestibular nucleus	**65**	**12**	**91**	**21**	**97**	**8**	**50**	**12**

stria medullaris	**8**	**2**	**8**	**3**	**6**	**1**	**12**	**4**
stria terminalis	**32**	**5**	**29**	**7**	**31**	**5**	**46**	**12**
Striatum	**319**	**31**	**382**	**45**	**262**	**31**	**344**	**20**
Subceruleus nucleus	**2**	**0**	**6**	**3**	**3**	**1**	**3**	**2**
subependymal zone	**40**	**9**	**43**	**17**	**63**	**25**	**56**	**21**
Subfornical organ	**2**	**1**	**0**	**0**	**3**	**3**	**1**	**1**
Subgeniculate nucleus	**8**	**1**	**8**	**1**	**9**	**4**	**5**	**2**
Subiculum	**140**	**19**	**201**	**18**	**145**	**31**	**256**	**58**
Sublaterodorsal nucleus	**4**	**1**	**10**	**2**	**7**	**3**	**3**	**1**
Submedial nucleus of the thalamus	**4**	**1**	**8**	**4**	**5**	**1**	**7**	**4**
Subparafascicular area	**6**	**3**	**22**	**7**	**2**	**1**	**11**	**6**
Subparafascicular nucleus	**25**	**5**	**43**	**8**	**22**	**5**	**19**	**6**
Subparaventricular zone	**18**	**7**	**8**	**4**	**10**	**3**	**9**	**3**
Substantia innominata	**188**	**38**	**121**	**18**	**110**	**25**	**109**	**21**
Substantia nigra	**239**	**14**	**233**	**33**	**300**	**24**	**230**	**88**
Subthalamic nucleus	**27**	**8**	**62**	**12**	**34**	**15**	**24**	**4**

Superior central nucleus raphe	**18**	**6**	**43**	**15**	**27**	**12**	**27**	**8**
superior cerebelar peduncles	**19**	**7**	**34**	**8**	**22**	**4**	**18**	**9**
superior cerebellar peduncle decussation	**0**	**0**	**1**	**0**	**0**	**0**	**0**	**0**
Superior colliculus	**1017**	**168**	**1211**	**258**	**1294**	**295**	**860**	**174**
superior colliculus commissure	**2**	**1**	**2**	**1**	**1**	**0**	**1**	**1**
Superior olivary complex	**61**	**28**	**114**	**40**	**63**	**13**	**59**	**26**
Superior vestibular nucleus	**49**	**24**	**73**	**12**	**77**	**23**	**50**	**25**
Supplemental somatosensory area	**845**	**158**	**596**	**180**	**514**	**46**	**670**	**182**
Suprachiasmatic nucleus	**11**	**5**	**4**	**2**	**5**	**2**	**5**	**4**
Supragenicula te nucleus	**29**	**6**	**24**	**5**	**34**	**6**	**18**	**4**
Supragenual nucleus	**0**	**0**	**1**	**0**	**1**	**0**	**0**	**0**
Supramammillary nucleus	**40**	**10**	**68**	**15**	**35**	**8**	**57**	**4**
supraoptic commissures	**5**	**1**	**3**	**1**	**5**	**2**	**3**	**2**
Supraoptic nucleus	**8**	**3**	**9**	**2**	**9**	**3**	**8**	**3**

Supratrigeminal nucleus	**24**	**4**	**36**	**8**	**36**	**8**	**22**	**8**
Taenia tecta	**71**	**29**	**86**	**14**	**50**	**9**	**58**	**12**
Tegmental reticular nucleus	**29**	**7**	**118**	**43**	**64**	**12**	**44**	**15**
Temporal association areas	**231**	**44**	**320**	**47**	**134**	**31**	**534**	**167**
third ventricle	**172**	**21**	**142**	**33**	**143**	**21**	**265**	**90**
trapezoid body	**30**	**7**	**26**	**12**	**43**	**16**	**21**	**9**
Triangular nucleus of septum	**7**	**2**	**2**	**1**	**2**	**1**	**8**	**4**
trochlear nerve	**2**	**1**	**3**	**1**	**4**	**1**	**1**	**0**
Trochlear nucleus	**0**	**0**	**1**	**0**	**0**	**0**	**0**	**0**
Tuberal nucleus	**73**	**9**	**120**	**22**	**86**	**21**	**79**	**8**
Tuberomammillary nucleus	**45**	**10**	**61**	**11**	**51**	**5**	**39**	**5**
uncinate fascicle	**4**	**1**	**2**	**1**	**3**	**2**	**1**	**1**
Uvula (IX)	**78**	**8**	**31**	**6**	**110**	**43**	**42**	**11**
Vascular organ of the lamina terminalis	**0**	**0**	**1**	**1**	**1**	**1**	**1**	**0**
Ventral anterior-lateral complex of the thalamus	**58**	**35**	**226**	**82**	**79**	**39**	**39**	**20**
Ventral auditory area	**91**	**14**	**73**	**15**	**66**	**13**	**166**	**48**

Ventral cochlear nucleus	**124**	**21**	**79**	**10**	**109**	**17**	**80**	**31**
ventral hippocampal commissure	**3**	**2**	**1**	**0**	**2**	**1**	**3**	**2**
Ventral medial nucleus of the thalamus	**22**	**9**	**108**	**41**	**41**	**9**	**25**	**11**
Ventral part of the lateral geniculate complex	**285**	**43**	**328**	**40**	**276**	**60**	**205**	**20**
Ventral posterolateral nucleus of the thalamus	**164**	**79**	**339**	**73**	**235**	**110**	**108**	**56**
Ventral posteromedial nucleus of the thalamus	**480**	**244**	**1096**	**221**	**725**	**324**	**345**	**175**
Ventral premammillary nucleus	**8**	**3**	**42**	**12**	**12**	**5**	**41**	**11**
ventral spinocerebellar tract	**20**	**6**	**21**	**5**	**29**	**6**	**20**	**9**
Ventral tegmental area	**45**	**8**	**78**	**16**	**59**	**15**	**57**	**23**
ventral tegmental decussation	**2**	**2**	**3**	**1**	**2**	**1**	**2**	**1**
Ventral tegmental nucleus	**1**	**1**	**2**	**1**	**1**	**1**	**0**	**0**
Ventrolateral preoptic nucleus	**2**	**1**	**13**	**3**	**4**	**1**	**6**	**2**

Ventromedial hypothalamic nucleus	**19**	**4**	**58**	**13**	**36**	**15**	**47**	**9**
vestibular nerve	**32**	**9**	**14**	**2**	**21**	**2**	**19**	**11**
Visceral area	**103**	**17**	**119**	**34**	**133**	**15**	**128**	**25**
Zona incerta	**209**	**28**	**319**	**38**	**261**	**52**	**126**	**35**

List of publications

1. Submitted to SLEEP on 13th of July, 2023:
   Manuscript ID: SLEEP-2023-0560
   Title: A patient-enriched MEIS1 coding variant causes a restless legs syndrome-like phenotype in mice
   Contributing Authors: **Leu, Chia-Luen**; Lam, Daniel D.; Salminen, Aaro; Wefers, Benedikt; Becker, Lore; Garrett, Lillian; Rozman, Jan; Wurst, Wolfgang; Hrabe, Martin; Hölter, Sabine M.; Winkelmann, Juliane; Williams, Rhiannan

   This study was supported by internal funding (Helmholtz Munich) to JW; and by the ERC under the European Union's Horizon 2020 Research and Innovation Program Grant Agreement No. 715933 to RHW.

2. Peer reviewed abstracts submitted to SfN 2022:

   (Poster presentation in November 2022, San Diego, USA)

   CL Leu[1,2], M Hessel[1], E Voggenreiter[1], M Miller[1], RH Williams[1#]

   [1]Helmholtz Zentrum München, [2]Technical University of Munich

   [#]corresponding author

   Sleep deprivation methodology and cortical dynamics

   Sleep is an important behavior that all animals need to sustain life. Sleep is regulated by a two-process model, the circadian rhythm and the sleep homeostat. In sleep homeostasis, the drive to sleep increases with sustained arousal and dissipates with sleep onset. Circadian rhythm affects when sleep onset can easily occur. Our understanding of circadian components for sleep is evolving yet how the brain senses sleep need or which brain regions are directly involved in the sleep homeostat is more elusive. Nevertheless, to study the sleep homeostat researchers must induce sleep loss, normally in experimental animals. The gold standard method is gentle handling by a trained researcher for a defined period of time to evoke sleep deprivation (SD). However, the technique varies between sleep laboratory, involves significant researcher - animal interaction which can lead to stress effects on the animal or diminished concentration of the researcher. We therefore examined how manual SD compared a treadmill-induced sleep loss in C57Bl6J mice (male and female).

   Mice were implanted with abdominal telemeters (HD-X02, DataSciences Inc) for wireless EEG and EMG capture. Following post-operative recovery, mice were subjected to 4h and 6h SD periods manually or by walking on a treadmill (speed $\leq$ 3cm/s). Assessment of total SD and delta power in recovery sleep were carried out. Additionally we performed further technical comparisons to assess the similarity of SD modalities,

namely 1) whole brain activity mapping using c-FOS expression as an indicator for cellular activity, 2) calcium imaging of cortical neurons via microendoscope recordings, and 3) PiezoSleep screen to compare pressure sensor detection of vigilance states to EEG. Through these different analyses we found that while trained researchers can ensure consistent sleep loss during sleep deprivation periods (90-95%), treadmill evoked sleep loss was more efficient and easier to implement. Secondly, whole brain mapping revealed similarities in brain regions activated in SD between manual- or treadmill-induced sleep loss but also subtle differences. Nevertheless, overall the robustness and ease of treadmill-induced sleep loss may prove an important methodology for adoption for researchers of sleep homeostasis.

Research supported by ERC under the European Union's Horizon 2020 Research and Innovation Program Grant Agreement No. 715933 to RHW.

DD Lam[1,2], CL Leu[1,2], M Hessel[1], IK Deligiannis[3], E Voggenreiter[1], CP Martinez-Jimenez[2,3], RH Williams[1#]

[1]Helmholtz Zentrum München, [2]Technical University of Munich, [3]Helmholtz Pioneer Campus

[#]corresponding author

ANAS: Amygdala Neurons Activated by Sleep deprivation

Given the ubiquity of sleep loss and its profound negative effects on health, well-being, and productivity, there is a pressing social and economic need to develop new therapeutic strategies to improve the quality of sleep. Effective sleep aids require understanding which brain centres contribute to sleep homeostasis and govern the delicate balance between sleep need and sleep drive.

We applied whole brain activity mapping from C57Bl/6J mice (male and female; n=8/cohort, age 24 ± 9 weeks old) subjected to 4h manual sleep deprivation (SD), 4h SD and 2h recovery sleep (RS), or undisturbed time-matched controls (C4, or C6 respectively). Brain regions were parcellated based on the Allen Brain Atlas and the number of c-FOS+ nuclei in each brain region computed. Next single nucleus RNA seq (snRNA-seq) was performed on cortical and amygdala samples from male C57Bl/6J mice (n= 6; 2 pooled replicates) after 6h manual SD, 6h SD and 30 min RS or undisturbed time-matched control at C6. After sample processing, cells are clustered and annotated to a reference atlas. Expression of *Fos* and other immediate early genes between cells were compared across sleep conditions using two-tailed Kruskal-Wallis tests with Dunn's post-test analyses.

Quantification of c-FOS expression after optical clearing indicated

increased expression patterns during SD in the amygdala and specific subregions compared to RS or control groups. We did not observe statistically significant changes in any brain region following RS. These initial results permitted follow-up snRNAseq on amygdala and cortical regions to identify precisely molecularly defined cell types activated by perturbations of sleep homeostasis. Functional follow-up *in vivo* will reveal which are likely to be involved in sensing or responding to these perturbations to affect behaviour and vigilance state.

Research supported by ERC under the European Union's Horizon 2020 Research and Innovation Program Grant Agreement No. 715933 to RHW.

3. Peer reviewed abstract submitted to IRLSSG 2022 Annual Meeting:

(Oral presentation in June 2022, Charlotte, USA)

DD Lam*[1,2] , CL Leu*[1,2], E Voggenreiter[1], A. Salminen[1, 2], C Tiringer[1], J Merl[3], S Hauck[3], B Wefers[1], W Wurst[1], A Salminen[1,2], J Winkelmann[1,2], RH Williams[1#]

[1]Helmholtz Zentrum München, [2]Technical University of Munich, [3] Proteomics core facility Helmholtz Zentrum München

***equal contribution; [#]corresponding author**

A mouse model of RLS with aberrant cortical rhythms

Aim: Using a reverse translational approach we aimed to generate a preclinical mouse model of RLS to identify brain regions that may be implicated in disease etiology and new therapeutic targets for intervention.

Methods: We generated a mouse model carrying a *MEIS1* loss-of-function coding variant, G815A, which is ~7-fold more prevalent in RLS patients. Homozygous *Meis1*G815A mice were fully viable and developed a late (middle aged) onset circadian hyperactivity consistent with RLS. This hyperactivity was only apparent in females (concordant with the increased prevalence in women) and occurred around the onset of the rest period. We next performed multimodal characterisation of these mice, including proteomics, transcriptomics, neuronal activity mapping and EEG.

Results: We observed alterations in EEG spectral composition, and sleep-wake activity recapitulating known phenomena seen in RLS. We found perturbation of the daily rhythm in brain-wide neuronal activity, and specific perturbation of the daily rhythm in the cortical proteome compared to the subcortex. Because *MEIS1* is expressed in the embryonic forebrain, we conclude that it sculpts cortical development,

with the G815A variant predisposing cortical physiology to circadian disruption.

Research supported by ERC under the European Union's Horizon 2020 Research and Innovation Program Grant Agreement No. 715933 to RHW, and internal funding (Helmholtz Munich) to JW.